UNIVERSITY OF SOUTHAMPTON
FACULTY OF ENGINEERING AND PHYSICAL SCIENCES
ENERGY TECHNOLOGY GROUP

ELECTROCHEMICAL ENGINEERING ASPECTS OF A DIRECT BOROHYDRIDE FUEL CELL

by

Abdulaziz Abdulkarim M. Abahussain

supervised by
Dr. Carlos Ponce de León and Professor Frank C. Walsh

Thesis for the Degree of Doctor of Philosophy

Southampton, United Kingdom
April 2020

UNIVERSITY OF SOUTHAMPTON

Abstract

FACULTY OF ENGINEERING AND PHYSICAL SCIENCES
ENERGY TECHNOLOGY GROUP
Doctor of Philosophy

ELECTROCHEMICAL ENGINEERING ASPECTS OF A DIRECT BOROHYDRIDE FUEL CELL

Abdulaziz A. M. Abahussain

Fuel cells (FCs) are clean power sources for both large-scale and portable applications, as they provide a viable method to convert the chemical energy of fuel directly into electrical energy. The most developed FC is the $H_2\|O_2$ system, which uses hydrogen as fuel. However, issues have been observed with the use of hydrogen, such as sourcing, the safety of handling and storage problems. Direct borohydride fuel cells (DBFCs) are liquid FCs that address some of these issues. They are composed of both BH_4^- fuel, which oxidises at the anode, and hydrogen peroxide (or O_2), which reduces at the cathode. Their many advantages, such as their high theoretical specific energy (up to 17 kW h kg^{-1}) and high theoretical cell voltage (up to 3.02 V), have attracted increasing interest. Borohydride is also available in a solid state (sodium borohydride, $NaBH_4$) or as an aqueous electrolyte up to 30 weight percent (wt.%), where it remains unchanged in a strong alkaline solution with a half-life of around 270 days at pH 13.9 (25 ^{o}C). Moreover, the final product of the borohydride oxidation reaction (BOR) is metaborate ($NaBO_2$), which is not harmful to the environment and can be reused to produce sodium borohydride again. Finally, borohydride FCs can operate under ambient conditions and in an air-free environment, which makes them more convenient for portable and anaerobic applications (such as in space and underwater). The main challenges to their commercialisation, however, are the selectivity of the anode catalysts and their substrate materials. Many publications have investigated noble metals (e.g. platinum, gold, palladium, etc.) as candidate materials, but none have found an anode catalyst able to meet the needs of both high catalytic activity towards BH_4^- oxidation and low activity towards its hydrolysis. Experimentally, Pt catalysts have shown a higher activity rate (by a factor of 10) and lower onset potential of BH_4^- oxidation compared to Au. Bimetallic electrocatalysts (e.g. Au-Pt, Pt-Ni, Pt-Zn) have also presented considerable cell performance in contrast to single-metal catalysts. As $Pt_{0.75}$-$Ir_{0.25}$/Ti and $Pt_{0.25}$-$Ir_{0.75}$/Ti anode catalysts have not been studied in DBFCs, this research considers them. Employing 3D electrode materials, such as reticulated metals, is expected to enhance the reactants' mass transport, avoid channel blocking, fully utilise the active sites, minimise the amount of noble metal required and thus simultaneously reduce electrode costs and increase cell power output. Moreover, optimising the operational conditions (temperature, reactant compositions, background materials, flow rate, etc.) of DBFCs will improve their performance. Therefore, the aim of this research is to investigate approaches to increase the overall performance and efficiency of a DBFC with the following research objectives: investigate the use of Pt-Ir alloys supported by titanium as anode materials for DBFCs; discover the optimal anode geometry among different 3D electrode materials by determining the volumetric mass-transfer coefficient using a limiting-current technique; and find the maximum power density of a DBFC using the optimal electrode through manipulation of operating conditions and electrolyte compositions. $Pt_{0.75}$-$Ir_{0.25}$/Ti and $Pt_{0.25}$-$Ir_{0.75}$/Ti anode catalysts have been characterised and evaluated, $Pt_{0.75}$-$Ir_{0.25}$/Ti being the most effective electrode for direct $NaBH_4$ oxidation. Its reaction parameters – including the activation energy (E_a^{app}), the charge-transfer coefficient (α), the total number of electrons exchanged (z), the heterogeneous rate constant (k_a) of the BH_4^- oxidation process and reaction order (β) – were 18.6 kJ mol^{-1}, 0.59, 5.3, 0.40 cm s^{-1} and 0.87, respectively. Among 3D electrode materials, the fine mesh showed the best performance. Finally, the operating conditions were discovered to have a significant influence on the cell power density. For example, the cell performance showed a dependence on the operating temperature, that is, the reaction kinetics at the anode and cathode were promoted when it rose. The peak power density also increased dramatically, from 93 to 162 mW cm^{-2} (~75%), when the temperature elevated from 25 to 65 ^{o}C.

Keywords: borohydride oxidation, 3D electrode, iridium, limiting current, mass transport, platinum, porous electrode, operating conditions.

Table of Contents

List of Tables

List of Figures

List of Publications

Published papers

1. A. Abahussain, C. Ponce de León, A. and F. C. Walsh, "Mass-transfer measurements at porous 3D Pt-Ir/Ti electrodes in a direct borohydride fuel cell", *Journal of The Electrochemical Society*, 165 (3): F198-F206, 2018.*

Papers in progress

1. A. Abahussain, C. Ponce de León, A. and F.C. Walsh, "Titanium supported Pt-Ir alloy anode (75:25 and 25:75) for direct borohydride fuel cells", *Electrochimica Acta*.
2. A. Abahussain, C. Ponce de León, A. and F.C. Walsh, "Effect of operating conditions and anode structure on direct $NaBH_4 \| H_2O_2$ fuel cell performance" *Journal of The Electrochemical Society*.

Conferences

1. A. Abahussain, C. Ponce de León, F. C. Walsh, "Improvement of direct borohydride fuel cells", EngSci PGR conference, Southampton, November 2016.
2. A. Abahussain, C. Ponce de León, F. C. Walsh, "Mass-transfer measurements of 3D Pt-Ir/Ti Electrodes in a direct borohydride fuel cells", 11th European Symposium on Electrochemical Engineering, Prague, June 2017.
3. A. Abahussain, C. Ponce de León, F. C. Walsh, "Pt-Ir/Ti anode for direct borohydride fuel cell", International flow Battery Forum, Lausanne, July 2018.

Author's Declaration

I, Abdulaziz A. Abahussain, declare that this thesis entitled: **Electrochemical Engineering Aspects of a Direct Borohydride Fuel Cell,** and the work presented in it are my own, and have been generated by me as the result of my own original research. I confirm that:

- This work was done wholly or mainly while in candidature for a research degree at this University;
- Where any part of this thesis has previously been submitted for a degree or any other qualification at this University or any other institution, this has been clearly stated;
- Where I have consulted the published work of others, this is always clearly attributed;
- Where I have quoted from the work of others, the source is always given. With the exception of such quotations, this thesis is entirely my own work;
- I have acknowledged all main sources of help;
- Where the thesis is based on work done by myself jointly with others, I have made clear exactly what was done by others and what I have contributed myself;
- Parts of this work have been published in peer-reviewed journals, as marked by the symbol * in the List of Publications.

Signed:

Date:

Acknowledgements

I would like to express my sincere gratitude to my supervisor, Dr Carlos Ponce de León Albarran, for his generosity and support. He has been dynamic, open-minded, patient and motivational, and his continuous guidance has deeply inspired me. Dr Carlos was always welcoming and available to discuss my results. He was approachable and even sympathetic to the personal issues that students may have. He sets an excellent example for those of us who would like to become better supervisors by encouraging and facilitating his students' exploration of new ideas.

I also give my sincere thanks and appreciation to my co-supervisor, Professor Frank C. Walsh, for sharing his great vision, vast experience, helpful comments and invaluable advice throughout my PhD programme.

It was a great privilege and honour to work and study under their supervision, and this project would not have been achieved without their support. I wish to thank both for their empathy and friendship. I truly enjoyed this journey, and I am convinced that it was largely possible because of the advanced laboratories and the excellent Energy Research Group that Frank and Carlos have set up at the University of Southampton.

I am extremely thankful to Dr Julian Wharton for his valuable comments on my 9th and 18th reports. I also extend thanks to my colleagues for their useful discussions and support during the lab work, including special thanks to my friends that I have met in the laboratory: Fernando Arenas, Bader Alshamery, Rachel Mckerracher, Christian, Sayed, Krishna, Horacio, Nicolás and many more in the university and among visiting students. I am deeply grateful to many friends in Riyadh, who have kept in touch while I have been abroad. They are caring and supportive, especially Awad Al-Waridah and Mohammed Al-Gahtani.

I would like to acknowledge my employer, King Saud University, for granting me this scholarship, and I want to thank the Ministry of Education and the Saudi Cultural Bureau in London for their support during my study in the United Kingdom.

Above all, I must admit that none of my studies nor my career would have been possible without the support of my God and family. I am deeply grateful to my wife, Ashwaq, for her understanding, patience, continuing support, encouragement and endless love throughout my PhD programme. For many months, I could not give enough time to my family, especially to my three sons, Rayyan, Abdulkarim and my little boy Abdulrahman, who was born when I started my programme. We have experienced many blissful moments and overcome some challenging adventures together.

My sincere thanks and heartfelt gratitude go to my beloved parents, Abdulkarim and Monyrah, for their prayers, love, caring and sacrifice to reach this point and prepare me for my future. I give many thanks to all my brothers and sisters. They are always supporting and encouraging to me – most of the time.

Abdulaziz Abdulkarim M. Abahussain

This work is dedicated to:
My wife, who supported me through this study,
to my parents,
and to my three sons;
words cannot express my deepest love, appreciation and gratitude.

Abbreviations

Abbreviation	**Meaning**
2D	Two-dimensional
3D	Three-dimensional
AEM	Anion exchange membrane
BET	Brunauer-Emmett-Teller
BOR	Borohydride oxidation reaction
CAD	Computer-aided design
CE	Counter electrode
CEM	Cation exchange membrane
CTAB	Cetyltrimethylammonium bromide
CV	Cyclic voltammetry
DBFC	Direct borohydride fuel cell
DBHPFC	Direct borohydride–hydrogen peroxide fuel cell
DMFC	Direct methanol fuel cell
DFT	Density functional theory
EC	Electrochemical–chemical
ECE	Electrochemical–chemical–electrochemical
FC	Fuel cell
FeTMPP	Tetramethoxyphenyl prophyrin
HER	Hydrogen evolution reaction
HOR	Hydrogen oxidation reaction
IBFC	Indirect borohydride fuel cell
LSV	Linear sweep voltammetry
LWD	Long-way distance between connected knots of diamond
MEA	Membrane electrode assembly
OCP	Open-circuit potential
PEM	Proton-exchange membrane
ppi	Linear pores per inch
PVD	Physical vapour deposition
PTFE	Polytetrafluoroethylene
RDE	Rotating disc electrode

rpm	Revolutions per minute
RVC	Reticulated vitreous carbon
SCE	Saturated calomel electrode
SDS	Sodium dodecyl sulphate
SEM	Scanning electron microscopy
SHE	Standard hydrogen electrode
SWD	Short way distance between connected knots of diamond
TEAH	Tetraethylamonium hydroxide
TP	Turbulence promoter
Wt.%	Weight percent

Symbols

Symbol	Meaning	Units
A	Geometrical surface area of electrode	cm^2
A_e	Active electrode area per unit electrode volume	cm^{-1}
A_x	Cross-sectional area of electrode	cm^2
A_i	Arrhenius pre-exponential factor	
B	Breadth of rectangular flow channel	cm
c	Bulk concentration	mol cm^{-3}
c_E	Concentration at the electrode surface	mol cm^{-3}
D	Diffusion coefficient of borohydride ions	cm^2 s^{-1}
d_e	Equivalent diameter of flow channel	cm
E	Electrode potential	V
E^o	Formal potential	V
E_{cell}	Cell potential	V
E_{cell}^o	Standard cell potential	V
E_P	Oxidation peak potential	V
E_{ac}^o	Standard activation energy for charge transfer	kJ mol^{-1}
E_a^{app}	Apparent activation energy for charge transfer	kJ mol^{-1}
F	Faraday constant = 96485	C mol^{-1}
G	Gibbs free energy	J mol^{-1}
I	Current	A
I_L	Limiting current	A
I_p	Peak current	A
j	Current density	A cm^{-2}
j_o	Exchange current density	A cm^{-2}
j_L	Limiting current density	A cm^{-2}
j_P	Peak current density	A cm^{-2}
k_m	Mass-transfer coefficient	cm s^{-1}
k_s	Standard heterogeneous rate constant	cm s^{-1}
k_a	Heterogeneous rate constant	cm s^{-1}
L	Electrode length	cm
L_e	Dimensionless length	dimensionless

m	Particle mass	g
M_w	Molar mass	g mol^{-1}
n_a	Number of electrons involved in the rate-determining step	
n_e	Number of electrodes	dimensionless
P	Power density	W cm^{-2}
q	Charge density	μC cm^{-2}
Q	Electrical charge	C
Q_V	Volumetric flow rate	cm^{3} s^{-1}
Re	Reynolds number	dimensionless
R	Universal gas constant = 8.314	J K^{-1} mol^{-1}
r	Reaction rate	mol dm^{-3} s^{-1}
S	Channel height/depth	cm
Sc	Schmidt number	dimensionless
Sh	Sherwood number	dimensionless
T	Temperature	K
t	Time	s
t_i	Positive intercept of the squared time axis	s$^{1/2}$
v	Mean linear flow velocity of electrolyte	cm s^{-1}
V_e	Electrode volume	cm^{3}
y	A reaction constant	A cm mol^{-1}
z	Total number of electrons exchanged	dimensionless
Z	Frequency factor	depends on order

Greek symbols

α	Charge transfer coefficient	dimensionless
β	Reaction order	dimensionless
ν	Kinematic viscosity of electrolyte	cm^{2} s^{-1}
υ	Potential scan rate	V s^{-1}
ω	Rotation rate	rad s^{-1}
η	Overpotential	V
κ	Electrolytic conductivity	S cm^{-1}
τ	Theoretical residence time	s
δ	Limiting current enhancement factor	dimensionless

Chapter 1: Introduction

1.1. Fuel cells as a source of energy

There is a global concern about energy security because of the expected decrease in oil production [1] and increase in fossil-fuel consumption due to the world's growing population, both of which could contribute to global warming. The world population was approximately 7.7 billion in 2019 and has reached up to seven-fold over the last 200 years with an expected growth of 11 billion by the end of the 21st century [2]. The consumption of fossil-fuel to power vehicles was estimated to be around 18.3 million barrels/day by 2040 [3]. Burning fossil fuels is also possibly the main source of atmospheric carbon dioxide, which contributes to air pollution. Accordingly, the development of clean, efficient energy technology is a crucial step towards secure energy supplies. Researchers should look for alternative approaches that generate power from environmentally friendly sources.

Fuel cells (FCs) convert the chemical energy of fuels directly into electrical energy. Many consider them an attractive source of green, safe and efficient energy, meaning that FCs will likely play a vital role in humanity's future. The theoretical specific energy of $H_2\|O_2$ FC is about 33 kW h kg^{-1} [4] (three times higher than that of gasoline, 11 kW h kg^{-1}) [5], coupled with a considerable efficiency 50-60% in comparison to combustion engines (<25%) [6]. They can generate power for both small and large applications, such as light transportation systems, and constitute a promising replacement for batteries in portable applications.

Currently, the most developed FC is the $H_2\|O_2$ system, which uses hydrogen fuel because it provides a clean, rich energy source from natural gas or via electrolysis [7]. However, the use of this flammable gas (in > 4% air) in FCs has several issues, including sourcing, safe handling, efficient storage [8] [9] and transport. Moreover, hydrogen has a very low energy-per-volume basis, meaning that it requires a large volume to store it; for example, a 180 dm^3 pressurised tank is required to store a mere 5 kg of hydrogen at 34 MPa (5000 psi) of pressure [10]. An alternative approach is to replace the gaseous H_2 with a liquid fuel as a hydrogen carrier. With this method, the same amount of hydrogen in a 35 weight percent (wt.%) sodium borohydride ($NaBH_4$) solution could be stored in only a 65 dm^3, non-pressurised tank [10].

The most promising types of FCs are thus direct liquid FCs, which have higher energy densities, uncomplicated structures, compact fuel tanks, fast recharging capabilities and are easier to store and transport [11]. The most common liquid fuel is usually a type of alcohol, such as ethanol or methanol [11] [12]. The latter is used in a direct methanol fuel cell (DMFC); however, this system has persistent problems, such as methanol crossover, anode poisoning (from carbon monoxide), low power densities and toxicity [7] [12]. Moreover, alcohol cells require delicate operating conditions, such as highly managed temperature, humidity and impurity levels [13]. Further information and discussion of many direct liquid FCs, including direct methanol, ethanol, ethylene glycol, glycerol, formic acid, dimethyl ether, hydrazine acid and borohydride FCs can be found in a new review article [11]. Chemical hydrides, such as lithium borohydride ($LiBH_4$) and $NaBH_4$, are suitable liquid hydrogen carriers, as they can be fed into a borohydride FC. Even though lithium borohydride has a higher hydrogen content (18.5 wt.%) than $NaBH_4$, it needs extreme temperatures (~ 600–650 ^{o}C) and pressures (~ 70–350 bar) to decompose and release H_2 [14] [15], but $NaBH_4$ is more stable, easier to handle and can operate in ambient conditions [16].

$NaBH_4$ is produced from boron mines, 70% of which are in Turkey [17] [18], and the distance between Turkey and Saudi Arabia is around 420 mile. Between 1930 and 1940, the University of Chicago produced the first batch of borohydride compounds. Later, the government requested the University to study more chemical hydrides for war purposes, leading to the discovery of uranium borohydride [19] [20]. Currently, $NaBH_4$ is used as a reducing agent for chemical compounds, as a bleaching agent for paper manufacturing and as a cooling solution [21] [22] [23].

1.2. The motivation for the direct borohydride fuel cell

Direct borohydride fuel cells (DBFCs) are a promising, novel source of energy due to their many advantages. They have a higher theoretical cell potential, faster anodic oxidation rates [13] and higher theoretical power densities than direct ethanol and direct methanol FCs, as shown in Table 1.1 [24]. DBFCs can generate a higher theoretical specific energy: up to 17 kW h kg^{-1} when using H_2O_2 as an oxidant and up to 9.3 kW h kg^{-1} with O_2, which is at least *ca.* three times of the theoretical specific energy of methanol FCs (6.09 kW h kg^{-1}) [25], two times that of ethanol FCs (8.04 kW h kg^{-1}) [26] and about half of that from $H_2\|O_2$ FC systems (33 kW h kg^{-1} but without a storage vessel) [4]. DBFCs also have a far higher energy density than the secondary batteries. For example, Li-ion batteries – one of the most advanced types – can only generate 0.2 kW h kg^{-1} [27]. It is claimed [28] that DBFCs could also provide ten times the density (1000 W h kg^{-1} out of 2580 W h kg^{-1}, theoretically) of space batteries (i.e. Li batteries).

Table 1.1. Different theoretical energies for some fuels with oxidants at 298 K and 1 atm.

Fuel	Oxidant	Theoretical cell potential / V	Theoretical specific energy / kW h kg^{-1}	Electrons exchanged / e$^-$ mol^{-1} of fuel
$NaBH_4$	H_2O_2 (in acidic)	3.02	17 [29]	8
$NaBH_4$	O_2	1.64	9.3 [25]	8
Ethanol (C_2H_5OH)	O_2	1.144 [30]	8.04 [26]	12
Methanol (CH_3OH)	O_2	1.21 [31]	6.08 [25]	6
H_2	O_2	1.23 [31]	32.9 [4]	2

Borohydride FCs can operate under ambient conditions, making them more convenient for some portable applications, such as nomad electronic devices. Another advantage of sodium borohydride is its availability as a solid or diluted in water up to 30 wt.%, where it remains unchanged in a strong alkaline mix with a half-life of around 270 days at pH 13.9 (25 °C) [32] [33] [34]. Additionally, ethanol and methanol usually release carbon dioxide when used as fuel, while the sodium borohydride FC does not produce any [35]. Finally, the final product of borohydride oxidation is metaborate, which is recyclable and environmentally safe [36]. $NaBH_4$ has a high weight percentage of hydrogen (10.6 wt.%) kept in a safe, innocuous form [37].

Borohydride FCs can be divided into two types. The first is the DBFC, which oxidises liquid fuel containing $NaBH_4$ directly at the anode surface. The second type is the indirect borohydride fuel cell (IBFC), which contains a separate reactor that generates high-purity hydrogen from $NaBH_4$ to feed a conventional $H_2 \| O_2$ FC [38]. The next chapter thoroughly explains both types. Sodium borohydride is typically dissolved in water with up to a 30 wt.% concentration of high-concentrate sodium hydroxide (≥ 2 mol dm^{-3}) and is used as the anolyte in a DBFC. In a typical cell, this solution is coupled with the reduction of oxygen (pure or contained in the air) or a solution of hydrogen peroxide in acid (or alkaline media). Different anode catalysts for DBFCs include noble metals (Au, Pt, Pd Os, Ag and Ru), non-precious metals (Ni and Cu) and alloys, which can be used to oxidise $NaBH_4$.

1.3. Research challenges

Even though Indig and Snyder [39] were the first scholars to explore the DBFC in the early 1960s, research is still in an early stage, since many challenges and issues remain unsolved. Various studies of DBFCs have been done on half-cells (a conventional three-electrode cell), single and multiple [28] cells. However, the ideal theoretical power density, at which eight (or close to eight) electrons transfer, has not been achieved with a cost-effective material. The critical issue is the hydrolysis of BH_4^- (at low potential) that leads to hydrogen evolution during the electrochemical oxidation of BH_4^- at the anode catalyst sites. Another issue is the crossover of borohydride ions to the cathode electrode through the membrane, which causes the deactivation of cathode catalysts and low utilisation of fuel [40]. Accordingly, finding appropriate, cost-effective materials for cathode that are inactive towards borohydride oxidation also need to be developed to make DBFCs reliable and more efficient energy sources [41] [12]. The greatest issue, however, is the anode material and its design structure [two-dimensional (2D) *vs.* three-dimensional (3D)], which has not been investigated in sufficient depth. There is a lack of consideration from an electrochemical engineering perspective, such as the characterisation of mass transport in the DBFC. These issues need to be addressed to make DBFCs competitive on the market.

1.4. Opportunities for developing direct borohydride fuel cell

Many aspects of DBFCs remain to be investigated before they can compete against other FC technologies, such as the following:

- Designing 3D anode structures to improve the efficiency of the anode to extract higher power density, increase durability and reduce the anode cost.
- Suppressing the hydrogen evolution rate from the hydrolysis reaction of borohydride ions, which occurs in parallel with borohydride oxidation. Using surfactants can inhibit the mechanism that triggers hydrogen evolution and promotes the direct oxidation of borohydride ions.
- Developing an efficient and cost-effective cathode catalyst to increase the reduction rate of O_2 (or H_2O_2) that is not active towards the borohydride reaction.
- Finding a highly efficient membrane material able to balance the chemical ions and maintain the pH level in both anolyte and catholyte solutions. The membrane needs to be developed to minimise the borohydride ion crossover at high BH_4^- concentrations.
- Improving DBFC performance by optimising the operating conditions, such as flow velocity, reactant concentration, temperature, background material and its concentration, etc.
- Discovering the optimal design of the flow field for a plate electrode to increase the mass transport of reactants.

1.5. Aims and objectives

The core aim of this research is to investigate approaches to increase the overall performance and efficiency of DBFCs. Therefore, this project focuses on the following objectives:

- Evaluation of titanium-supported Pt-Ir alloys as anode materials for DBFCs. The reaction behaviour of BH_4^- oxidation at these electrodes is investigated by determining the catalyst parameters, including the activation energy, E_a^{app}, the standard heterogeneous rate constant, k_s, the heterogeneous rate constant, k_a, the number of electrons exchanged in the reaction, z, the charge transfer coefficient, α, the mass-transport coefficient, k_m, by electrochemical measurements in a half-cell arrangement and the power density output of a single DBFC to find an adequate electrocatalytic material for borohydride oxidation.

- Design and construction of a single DBFC to evaluate the performance of different 3D anode structures (such as mesh, micromesh, fine mesh and felt) to discover the optimal anode geometry for DBFCs by obtaining the volumetric mass-transfer coefficient using the limiting-current technique.
- Investigation of the effects of various operating conditions and electrolyte compositions to maximise the power density of DBFCs using the optimum anode material determined previously.

1.6. Thesis outline

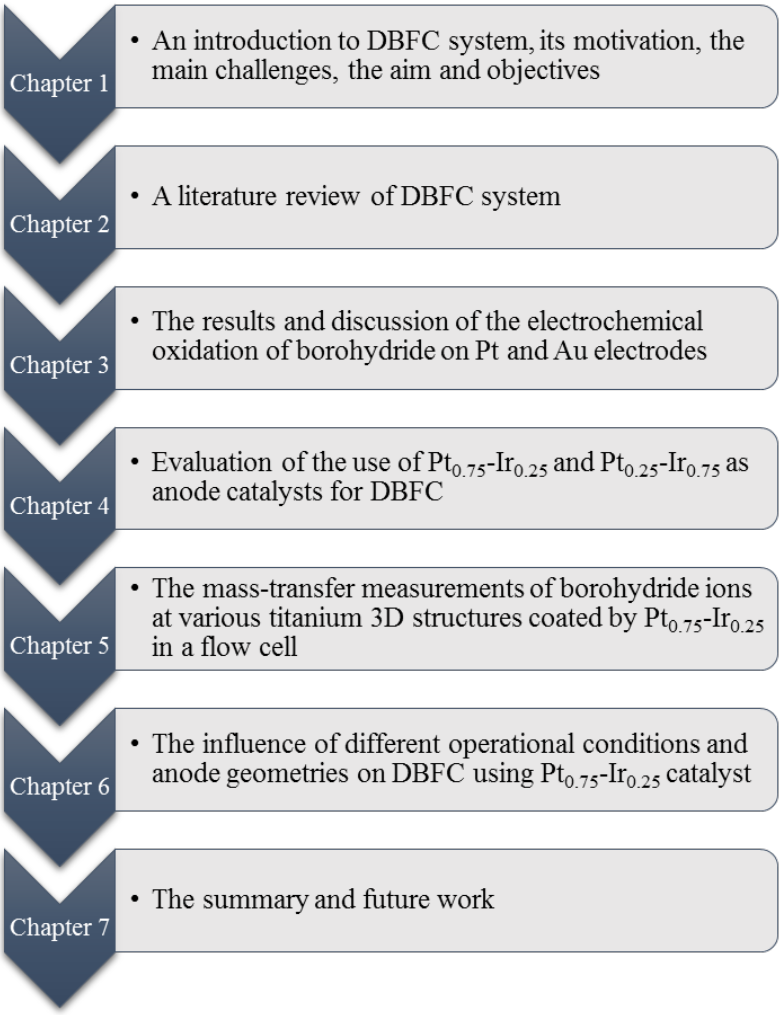

Chapter 1
- An introduction to DBFC system, its motivation, the main challenges, the aim and objectives

Chapter 2
- A literature review of DBFC system

Chapter 3
- The results and discussion of the electrochemical oxidation of borohydride on Pt and Au electrodes

Chapter 4
- Evaluation of the use of $Pt_{0.75}$-$Ir_{0.25}$ and $Pt_{0.25}$-$Ir_{0.75}$ as anode catalysts for DBFC

Chapter 5
- The mass-transfer measurements of borohydride ions at various titanium 3D structures coated by $Pt_{0.75}$-$Ir_{0.25}$ in a flow cell

Chapter 6
- The influence of different operational conditions and anode geometries on DBFC using $Pt_{0.75}$-$Ir_{0.25}$ catalyst

Chapter 7
- The summary and future work

Chapter 2: Literature Review

2.1. Borohydride fuel cells

This section explains the two types of borohydride FCs in detail. As hydrogen storage is an impediment to a hydrogen economy [42], chemical hydrides, especially sodium borohydride ($NaBH_4$), can offer a solution with their high storage density of hydrogen, up to 6.5 wt.% hydrogen in an aqueous solution of 30 wt.% $NaBH_4$, as the latter has a high hydrogen content (10.6 wt.%) [43].

The first process, then, uses borohydride fuel as an indirect hydrogen carrier [the indirect borohydride fuel cell (IBFC)]. It could be stored as an aqueous solution in a tank, for instance, to supply a catalytic hydrogen reactor (e.g. a packed-bed tubular reactor [43]) and produce pure hydrogen, as shown in Figure 2.1. The process involves a heat exchanger to cool down the H_2 stream and the side products, like water, which are further removed by a splitter. The hydrogen gas passes through a silica-packed bed to dry the residual moisture and is fed into a conventional $H_2 \| O_2$ proton-exchange membrane (PEM) FC. This system is the most common process to generate pure hydrogen from $NaBH_4$ [43] [12]. However, it has been reported that the estimated cost of pure H_2 generated by reforming natural gas is about 130 times (US$ 2 kg^{-1} H_2) lower than that of H_2 produced from $NaBH_4$ (US$ 260 US kg^{-1} H_2), and if the H_2 is generated by electrolysis using wind power, even 50 times lower (US$ 5 kg^{-1} H_2) [22]. The high cost of $NaBH_4$ could explain this price difference; however, its cost is expected to fall in the future, which will make the borohydride system more attractive for power generation. It was reported [22] in 2006 to be about US$ 55 kg^{-1}, and it has been claimed that its price could reach US$ 1 kg^{-1} in the next few years (from 2006). However, that seems impossible, as BH_4^- production depends on hydrogen (H_2) gas. The second process uses borohydride directly. This method has received considerable attention over the last decade because it offers numerous advantages as an alternative to the well-known FCs, such as $H_2 \| O_2$ and direct methanol FCs. Figure 2.2 illustrates a typical process of creating DBFCs that uses $NaBH_4 \| H_2O_2$, where the most significant factors of using borohydride as a fuel are its high theoretical power density and cell voltage.

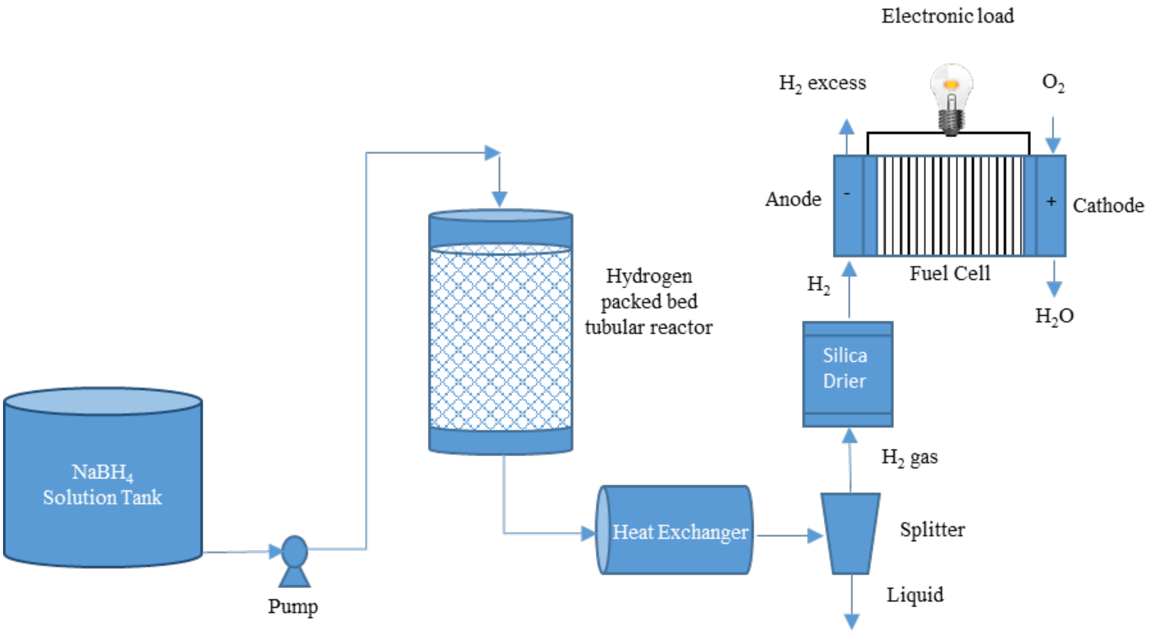

Figure 2.1. The IBFC scheme involves a hydrogen generator that feeds $NaBH_4$ into a $H_2\|O_2$ FC [43] [12].

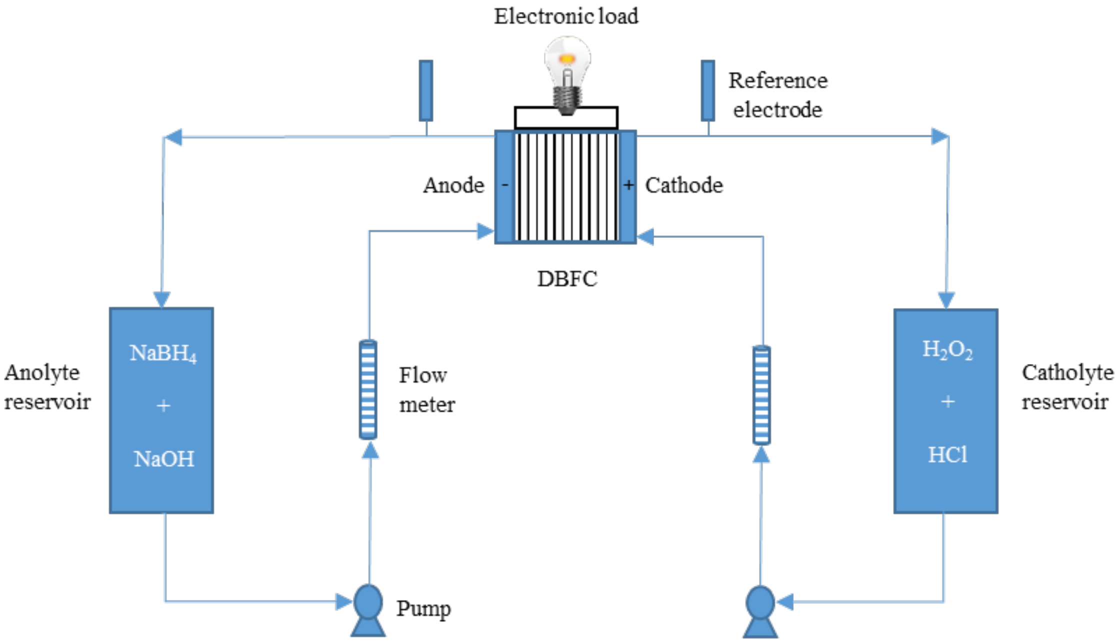

Figure 2.2. The flow diagram of the DBFC, where $NaBH_4$ is oxidised directly using hydrogen peroxide as an oxidant [29].

In this process, the direct oxidation of borohydride ions in an alkaline solution can theoretically release eight electrons at an equilibrium standard potential of -1.24 V *vs.* SHE, which provides a theoretical equilibrium cell potential of 1.64 V or 3.02 V when using O_2 or H_2O_2 oxidising agents, respectively [29].

In such a system, sodium borohydride solution is transferred by a variable speed pump into the anode compartment to diffuse through the liquid diffusion layer, where sodium borohydride oxidises in the presence of water at the anode catalyst to produce sodium metaborate ($NaBO_2$), protons and electrons [24]. The protons pass through the ion exchange membrane towards the cathode side, while the electrons transport along the external circuit to the cathode electrode. On the cathode surface, both electrons and protons react with hydrogen peroxide (H_2O_2) to produce water. See the Membrane section (2.4) for more detail about the function of the membrane in a borohydride FC. The next section explains the reactions occur at the cathode and the anode.

2.2. Reactions taking place in DBFCs

2.2.1. The reaction occurring at the anode

Complete oxidation of borohydride ions in an aqueous alkaline solution can occur directly at a wide range of anode catalysts to release, in theory, a maximum of eight electrons. The electro-oxidation (irreversible) reaction of BH_4^- is as follows:

$$BH_4^- + 8OH^- \rightarrow BO_2^- + 6H_2O + 8e^- \qquad E^o_{Anode} = -1.24\ vs.\ \text{SHE} \tag{2.1}$$

The main issue for the DBFCs is the hydrolysis of BH_4^-, which occurs at the same time as the direct oxidation reaction, causing hydrogen evolution and generating hydroxy borohydride intermediate [44], as shown in the following reactions Eq. (2.2) and Eq. (2.3). The good news is that half of the hydrogen gas comes from water and the other half comes from sodium borohydride, as it is a 'water-splitting' agent [23] [45].

$$BH_4^- + H_2O \leftrightarrow BH_3(OH)^- + H_2 \tag{2.2}$$

$$BH_3(OH)^- + H_2O \rightarrow BO_2^- + 3H_2 \tag{2.3}$$

Due to hydrogen presence, the anode potential acquires a mixed potential value, combining the direct oxidation of borohydride ions, as seen in Eq. (2.1) with the hydrogen oxidation reaction, Eq. (2.4). Thus, the anode voltage ranges usually from -1.24 to -0.828 V *vs.* SHE, depending on the anode material and fuel concentration [46].

$$H_2 + 2OH^- \rightarrow 2H_2O + 2e^- \qquad E^o_{Anode} = -0.828\ vs.\ \text{SHE} \qquad (2.4)$$

Because of the competition between the two reactions, oxidation of borohydride and its hydrolysis may reduce the coulombic efficiency. Larminie and Dicks [47] mentioned that it is possible to increase the direct oxidation of BH_4^- and force hydrogen molecules to oxidise rapidly using a state-of-the-art, 3D electrode that can liberate eight electrons. In addition, if the concentration of borohydride in the anolyte solution is low and sodium hydroxide is high, the homogeneous hydrolysis reaction can be slowed down [47]. Even though 3D electrodes can provide a high active area per unit electrode volume and lower catalyst loading [48], resulting in reduced fuel-cell costs, the hydrolysis rate might increase because the large surface area is exposed to the borohydride ions. Therefore, this research carefully studies this subject (effect of the anode structure, see Chapter 5).

The exact mechanism of borohydride electro-oxidation is still not completely defined and requires further investigation [49] [7]. It is experimentally shown that the behaviour of borohydride electro-oxidation also depends on the electrocatalyst material. This section describes the present understanding of the reaction mechanism. In the first step, the transfer of one electron is followed by the formation of a BH_4^* (adsorbed), and its immediate decomposition, which is the second step. A third step is a further electron transfer: an electrochemical–chemical–electrochemical (ECE) reaction sequence. Mirkin et al. [50] used two Au microelectrodes (12.5 and 50 μm) in CV experiments that applied the fast-potential scan rate (up to 3×10^4 V s^{-1}) in a solution containing 0.01 mol dm^{-3} $NaBH_4$ in 1.0 mol dm^{-3} NaOH. The authors suggested that the ECE steps for the oxidation of borohydride ions on Au electrodes occurred as follows:

$$BH_4^- - e^- \leftrightarrow BH_4^* \qquad \text{(E)} \qquad (2.5)$$

$$BH_4^* + OH^- \leftrightarrow BH_3^- + H_2O \qquad \text{(C) Fast reaction} \qquad (2.6)$$

$$BH_3^- - e^- \leftrightarrow BH_3 \qquad \text{(E)} \qquad (2.7)$$

The intermediate monoborane (BH_3), which is formed in the ECE sequence, undergoes further reactions to liberate six electrons out of eight in total and are thought to take place in a rapid electrochemical reaction. These steps were suggested for Au catalyst; the oxidation of borohydride on Pt has even less information [49] [51] perhaps because it was thought that Au is the ideal catalyst for BOR ($8e^-$ and no hydrolysis) [51]. Elder and Hickling [52] among others, proposed a different reaction pathway for the oxidation of borohydride on Pt [53] [54] [55] [56]. Elder and Hickling showed that Pt catalyses the evolution of H_2 gas through polarisation conditions and open-circuit potential (OCP) [52] [53]. Concha et al. [57] [56] used in situ mass spectrometry - a physical technique - Fourier Transform Infrared Reflectance (FTIR) to monitor B–H and B–O bond regions on Au [57] and Pt [56] (Pd by similar study [58]) electrodes during a positive sweep of electrode potential in 1 M $NaBH_4$ + 1 M NaOH. The authors presented different possible scenarios in the light of FTIR spectroscopy's results for Au and Pt. In regard to Pt [56], it would flow chemical–electrochemical (CE) reaction sequence and the heterogeneous hydrolysis of BH_4^- occured at low potential but the products (H_2 and BH_3OH^-) do not block the surface as no quantitative formation of hydrogen was shown, which suggested a fast electro-oxidation of the them [56].

Recently in 2018, Olu et al. [59] investigated the BOR using differential electrochemical mass spectrometry on 5, 50 and 500 mmol dm^{-3} $NaBH_4$ on Au and Pt electrocatalysts. They combined their results with data from some chosen literature reviews which studied the intermediate species generated in the BOR process using different electrochemical techniques to propose a microkinetic model of the BOR for both electrocatalysts. The suggested reaction mechanisms can be seen in Figure 2.3. The model considers the general behaviour of H_2 generation during the BOR. The reaction pathway of the BOR depends on the potential region, available active sites and borohydride concentration. Two distinct mechanisms were suggested on Pt and Au catalysts:

1- Fully-dissociative adsorption of BH_4^- into BH_{ads} and $3H_{ads} + e^-$ which is expected to be at low potential values ($\sim E < -0.27$ V *vs.* SHE, i.e. before metal oxide region) using low BH_4^- concentration (< 10 mmol dm^{-3}). This mechanism likely takes place on Pt (the red-coloured arrows represent the reaction steps that can occur only on Pt), which demands free active sites to proceed (four Pt sites/BH_4^- adsorption). The BH_{ads} formed (a stable molecule on Pt) would get oxidised slowly – in the presence of OH^- adsorption at high potential – to produce BOH_{ads} and then again to form the final product BO_2^- (4-5e^- process). The H_2 gases occur from the adsorbed H* ions on Pt surface followed by hydrogen oxidation reaction (HOR) simultaneously with BOR.

2- Partially-dissociative pathway is proposed for Pt and Au electrodes at high potential; in this case, BH_4^- electro-oxidises to $BH_{3,ads}$ intermediate, and then $BH_{3,ads}$ can react in four different ways:
   a. Desorbs as BH_3OH^- to the solution
   b. Self-dehydrogenates to form $BH_{ads} + H_2$
   c. Dissociates into $BH_{ads} + 2H_{ads}$ (only with Pt and requires more free Pt active sites)
   d. Oxidises with OH^- to produce BH_{ads}

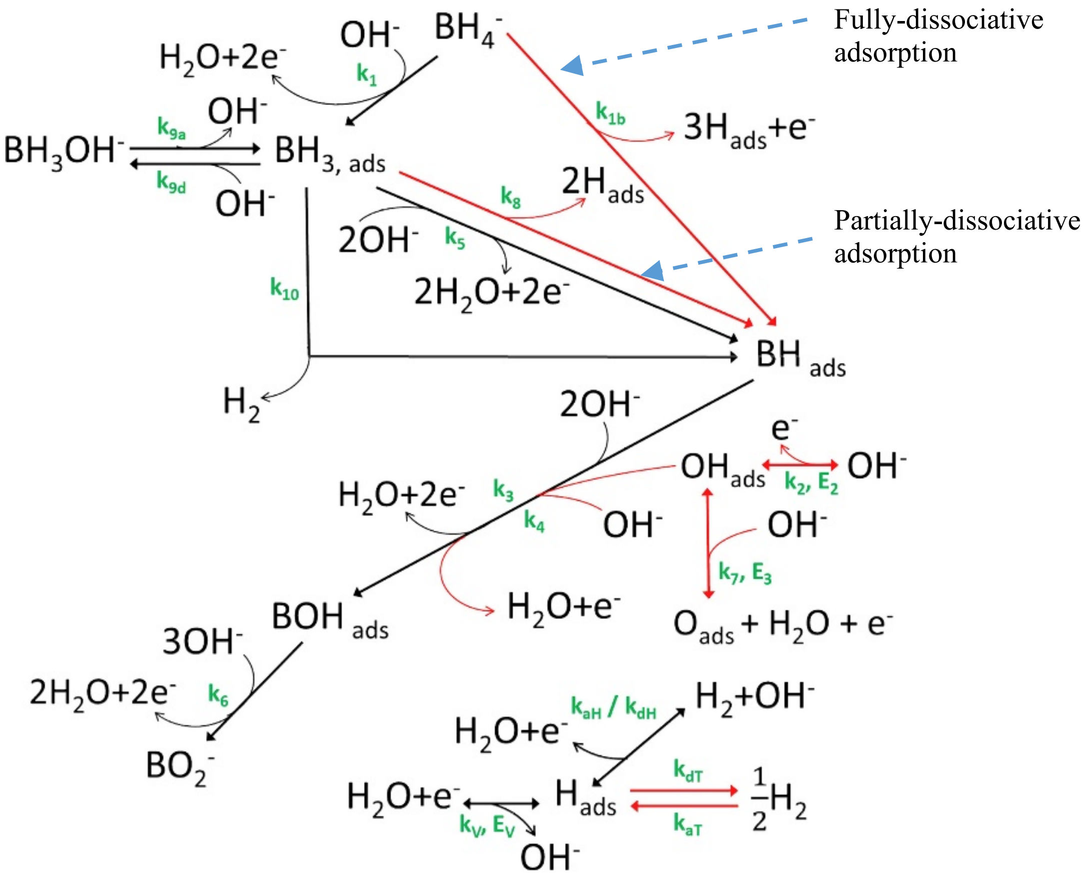

Figure 2.3. Tentative borohydride oxidation reaction pathways for Pt and Au catalysts proposed by Olu et al. [59], red-coloured arrows represent the reaction steps that can occur only on Pt.

In general, the partially-dissociative pathway for Pt and Au electrodes is less demanding in catalyst sites. Hydrogen might be produced from a self-dehydrogenate reaction (b pathway) on both Pt and Au electrodes to form BH_{ads}, and this is the least demanding mechanism in free active sites, but it would reduce the power efficiency. Moreover, if high borohydride content is used (> 50 mmol dm^{-3}), BH_{ads} can block the Pt sites even at low potential (E < -0.27 *vs.* SHE), and the partially-dissociative mechanism becomes predominant. However, optimising borohydride concentration appears to be essential in such a case.

The most of the proposed reaction schemes are uncertain, and these steps are still subject to speculation [12 56 57 60 51]. It has been observed that the reaction pathway of this multi-step process could not only vary based on the anode material but also on the operational conditions [61 44] (i.e. the pH and the ratio of alkali to fuel concentration $[OH^-]/[BH_4^-]$ [62]) which make the system complicated.

2.2.2. The reaction taking place at the cathode

Oxygen and hydrogen peroxide are the most common oxidants that have been used for cathodic reaction in DBFCs. The oxygen reaction at a cathode surface in an alkaline electrolyte is as follows:

$$2O_2 + 4H_2O + 8e^- \rightarrow 8OH^- \qquad E^o_{cathode} = 0.4 \text{ V } \textit{vs.} \text{ SHE} \qquad (2.8)$$

The mechanism of the cathodic reaction of oxygen is complicated, and it contains the formation of intermediates such as H_2O_2 and metal oxide, which reduces the activity of the catalysts [63]. The overall reaction of the DBFC with oxygen as the oxidant is shown below:

$$NaBH_4 + 2O_2 \rightarrow NaBO_2 + 2H_2O \qquad E^o_{cell} = 1.64 \text{ V} \qquad (2.9)$$

When hydrogen peroxide is the oxidant – which is suitable for anaerobic applications, such as space and underwater vehicles [29 28] – both the power density and cell efficiency are higher due its faster reduction rate and higher cell voltage [24]. Furthermore, from an operational point view, feeding the combination of liquid into DBFC is technically better than using liquid and gas because of a reduced requirement for compressing the gas, ease of storage and heat removal [28]. The electro-reduction of H_2O_2 in alkaline media at the cathode can be written as the following:

$$4H_2O_2 + 8e^- \rightarrow 8OH^- \qquad E^o_{cathode} = 0.87 \text{ V } vs. \text{ SHE} \qquad (2.10)$$

The theoretical cell potential, in this case, is 2.11 V, and the net cell reaction can be expressed as the following [29]:

$$4HO_2^- + BH_4^- \rightarrow 4OH^- + BO_2^- + 2H_2O \qquad E^o_{cell} = 2.11 \text{ V} \qquad (2.11)$$

It is highly likely that H_2O_2 decomposes at the cathode catalyst to generate water and oxygen, as shown in Eq. (2.12), and that the latter is reduced electrochemically at the cathode surface, as seen in Eq. (2.8) [63].

$$H_2O_2 \rightarrow H_2O + 1/2O_2 \qquad (2.12)$$

Cathode potential depends on the pH level of the oxidant; Eqs. (2.13) and (2.14) show the relationships of oxygen and hydrogen peroxide, respectively [64] [65] [66].

$$E_{O_2} = 1.23 - 0.059 \text{ pH} \qquad (2.13)$$

$$E_{H_2O_2} = 1.78 - 0.059 \text{ pH} \qquad (2.14)$$

As the pH of the electrolyte decreases, the cathode potential increases and the rate of H_2O_2 decomposition decreases at the cathode interface [64]. If the cathodic reactions take place in an acidic solution (i.e. pH tending to zero), the possibility of direct reduction of hydrogen peroxide raises, see Eq. (2.15). However, in an alkaline media (i.e. pH tending to 14), H_2O_2 would decompose to O_2 followed by its reduction, as expressed by Eq. (2.16) and Eq. (2.17), respectively [63].

$$4H_2O_2 + 8H^+ + 8e^- \rightarrow 8H_2O \qquad E^o_{cathode} = 1.78 \text{ V } vs. \text{ SHE} \qquad (2.15)$$

$$4H_2O_2 \rightarrow 4H_2O + 2O_2 \qquad (2.16)$$

$$2O_2 + 8H^+ + 8e^- \rightarrow 4H_2O \qquad E^o_{cathode} = 1.23\text{V } vs. \text{ SHE} \qquad (2.17)$$

Therefore, based on acidity of the hydrogen peroxide solution in the catholyte, the theoretical OCP value alters between 1.64 V [Eq. (2.1) + (2.8)], and 3.02 V [Eq. (2.1) + (2.15)] [65]. The overall cell reaction of a $NaBH_4 \| H_2O_2$ is the following [67]:

$$NaBH_4 + 4H_2O_2 \rightarrow NaBO_2 + 6H_2O \qquad E^o_{cell} = 3.02 \text{ V} \qquad (2.18)$$

2.3. Electrode materials

2.3.1. Anode catalyst materials

Finding a suitable anodic catalyst for the oxidation of BH_4^- is a subject that has been widely studied. Platinum, palladium and nickel all show high catalytic activity towards both the electro-oxidation of BH_4^- and its hydrolysis [61] [49] [68]. That means, the selectivity towards borohydride still needs to be improved to enhance the overall efficiency of the fuel cell (FC). Gold and silver catalysts are also present good activity for BH_4^- electro-oxidation, but their kinetic reaction parameters are slower by far than, for example, platinum. Despite the high activity of these metals, their high cost presents a serious restriction to the commercialisation of DBFCs. Many studies have thus been done with noble metal alloys, such as Pt-Au [69] [70] and Pd-Ir [71] [72], as they show more activity than single noble metals. Other materials that have been investigated to reduce cell cost include the following: non-noble metal materials (Zn, Cu, Co) and their alloys (Pt-Zn [73], Pd-Cu [74] [75], AB_2: $Zr_{0.9}Ti_{0.1}Mn_{0.6}V_{0.2}Co_{0.1}Ni_{1.1}$ [64]); non-metallic materials, such as mesoporous, nitrogen-rich carbon [76]; and catalytic polymeric electrodes [77]. The activity and durability of these materials, however, are still questionable.

A conductive polymer material has been considered by Bayatsarmadi et al. [77] as an anode for DBFCs. They investigated the use of conducting polymer Poly (3,4-ethylene-dioxythiophene) for the oxidation of BH_4^- and the reduction of H_2O_2. The polarisation curves showed a maximum power density of about only 7.5 mW cm^{-2} and a cell voltage of approximately 0.4 V at a current density load of 20 mA cm^{-2}. The DBFC was contained an anolyte solution of 1 mol dm^{-3} $NaBH_4$ in 4 mol dm^{-3} NaOH, on the cathode side, 5 mol dm^{-3} of H_2O_2 in 0.75 mol dm^{-3} H_2SO_4 separated by a cationic membrane (Fumsep FKB). The cell was examined at room temperature (23 °C). The results imply that the performance of the polymer electrode is very low. The (long-time) durability test of polymer electrodes needs to be investigated for their ability to survive in a strong alkaline (pH ~14, for an anode) and acidic medium (pH ~0, for a cathode).

The application of non-noble metals and their alloys in DBFCs have been reported in many publications. Nickel [61] [68] [78] [79] [80] [81] and its binary alloys [82] [78] [69] [83] [80] [84] were investigated via electrochemical measurements for their electrocatalytic activity towards borohydride oxidation in an alkaline medium. Liu et al. [61] found Ni to be a suitable catalyst for DBFC. The OCP for a Ni electrode presented higher potential than Pt and Pd electrodes; however, the oxidation reaction of borohydride on a Ni electrode can release only four electrons, whereas the other 50% of the borohydride turned into hydrogen gas. Çelikkan et al. [45] investigated the oxidation of $NaBH_4$ on Au, Pt, Pd and Ni electrodes, but they found that Ni was inactive for the direct oxidation of BH_4^-, which contradicts the results of Liu et al.[61].

Santos et al. [82] fabricated Ni alloys, including $Ni_{0.90}$-$Dy_{0.10}$, $Ni_{0.95}$-$Dy_{0.05}$, $Ni_{0.90}$-$Sm_{0.10}$ and $Ni_{0.95}$-$Sm_{0.05}$, for borohydride oxidation reaction (BOR). The study revealed that $Ni_{0.95}$-$Dy_{0.05}$ was the most active catalyst and $Ni_{0.90}$-$Sm_{0.10}$ showed the lowest activity for BOR. No data about power densities was found in the three studies for Ni and its alloys. However, Ma et al. [85] reported a peak power density of 77 mW cm^{-2} for a DBFC consisting of a Ni-Pd/C (25:1, 1 mg metal cm^{-2}) composite anode and a Pt/C (1 mg metal cm^{-2}) cathode separated with Nafion® 212 membrane. The anolyte was 1.32 mol dm^{-3} $NaBH_4$ in 2.5 mol dm^{-3} NaOH, and its flow rate was 5 mL min^{-1}, while the oxidant was humidified O_2 at 0.15 mL min^{-1} at 28 °C. At an elevated temperature of 60 °C, the peak power density reached up to 167 mW cm^{-2}.

Non-noble alloys as anode materials, such as AB_2 alloy ($Zr_{0.9}Ti_{0.1}Mn_{0.6}V_{0.2}Co_{0.1}Ni_{1.1}$), were considered by Li et al. [64]. The authors obtained 100 mW cm^{-2} from a $NaBH_4 \| O_2$ system (with 4 cm^2 of active area) at a high temperature of 50 °C (with no data at room temperature). Pt/C was used as a cathode material, and the two electrodes were separated by Nafion® 117. The concentration of the fuel solution was 2.64 mol dm^{-3} $NaBH_4$ in 5 mol dm^{-3} NaOH, and the flow rate was 0.2 dm^3 min^{-1}. This alloy, which is a mixing of alloy powder pasted onto Ni foam, was originally used in Ni-MH batteries (as a negative electrode) [86]. It is expected that AB_2 can also absorb the evolved H_2 during the operation [64].

Silver catalysts have been investigated by several groups of researchers [62 87 88 89]. Chatenet et al. [62] studied the direct electro-oxidation of borohydride on Ag and Au (a 10 wt.% catalyst loaded on Vulcan XC72) supported either on bulk and polycrystalline or nano-dispersed over carbon (all from E-Tek). The authors used a rotating disk–electrode (RDE) technique, linear sweep voltammetry (LSV) and cyclic voltammetry (CV) with a scan rate ranging from 5–200 mV s^{-1} to quantify the reaction kinetics and determine the kinetics parameters, which consist of the Tafel slope (± 2.3 $RT/\alpha zF$) [90] and the exchange current density. The oxidation of borohydride was carried out under an argon atmosphere and bubbled into the electrolyte solution during the experiments. An electrolyte solution of 1.0 mol dm^{-3} $NaBH_4$ in 0.01 mol dm^{-3} NaOH was used. The NaOH concentration was quite low. The suggested [3 17 91] NaOH concentration is around 5 mol dm^{-3} to avoid borohydride decomposition, specifically at high BH_4^- concentration. The geometrical area of the anode electrode was 0.28 cm^2. The authors used the Levich equation [Eq. (2.19)] to determine the number of electrons exchanged in the reaction, z, of the Ag and Au electrodes.

$$j_L = \frac{0.62\, zFD^{2/3}c}{\nu^{1/6}}\, \omega^{0.5} \tag{2.19}$$

Where j_L is the limiting anodic current density (A cm^{-2}), F is Faraday's constant (96485 C mol^{-1}), D is the diffusion coefficient (cm^2 s^{-1}), c is the bulk concentration (mol cm^{-3}), ω is the rotation rate (rad s^{-1}) and ν is kinematic viscosity (cm^2 s^{-1}). The diffusion coefficient of BH_4^- ions was taken from a different study in which it had been fixed to be of 1.6 × 10^{-5} cm^2 s^{-1} to obtain z from the Levich slope of limiting current *vs.* the square root of rotation speeds. Ag/C and Au/C anodes were able to deliver 7.5 electrons, but Ag/C showed slower kinetics parameters than the Au electrode. Duan et al. [89] prepared Ag/C, Cu_1-Ag_1/C, Cu_2-Ag_1/C, Cu_4-Ag_1/C and Cu/C nanoparticles (0.35 mg cm^{-2}) on glass carbon (3 mm in diameter) for $NaBH_4 \| H_2O_2$ cell. The anolyte was a 0.1 mol dm^{-3} $NaBH_4$ in 2 mol dm^{-3} NaOH, and the catholyte was a 2 mol dm^{-3} HCl in 4.5 mol dm^{-3} H_2O_2. The anode of Cu_2-Ag_1/C provided the best performance of all the studied catalysts, but its peak power density was only 6 mW cm^{-2} (17.27 mW mg^{-1}) at a current density of 9.7 mA cm^{-2} (27.8 mA mg^{-1}). The peak power density of Ag/C was 1.5 mW cm^{-2} (4.31 mW mg^{-1}), indicating that Ag materials have very low activity towards BH_4^- oxidation.

Gold [92] [87] [70] [93] [94] and gold alloys [69] [70] [83] [95] [96] [97] [98] [99] have been investigated extensively by a number of studies. Gyenge [49] studied the oxidation of borohydride ions on gold and platinum electrodes. Seven electrons were calculated on Au, which is consistent with the value reported by Amendola et al. [91]. Çelikkan et al. [45] investigated the oxidation of $NaBH_4$ on Au, Pt, Pd and Ni electrodes and found similar results as Gyenge. Au catalysts have been recognized as effective, the main reason being their inactivity towards the hydrolysis of BH_4^-. However, in 2010, the results of Chatenet et al. [100] contradicted those found by previous reports, as they used online mass spectrometry to detect the H_2 yield during borohydride oxidation on Au electrodes and found that the amount of hydrogen is not negligible, as the authors [100] have reported. Another study made similar conclusion here [93]. Au is thus no longer thought to be faradaic-efficient for the electrochemical oxidation of borohydride ions. Therefore, another reaction kinetic pathway for the oxidation of borohydride on Au should be suggested. In another study, palladium was compared with an Au electrode; the latter showed a lower cell performance [24].

Ponce de León et al. [29] ran a filter-press flow cell of $NaBH_4 \| H_2O_2$ with an electrode area of 64 cm^2. Borohydride oxidation occurred on Au supported by a carbon felt electrode (0.5 mg Au cm^{-2}), while the Pt/porous carbon paper (4 mg cm^{-2}) was employed as a cathode. The anolyte consisted of 6.6 mol dm^{-3} $NaBH_4$ + 6 mol dm^{-3} NaOH, with 1 mol dm^{-3} H_2O_2 + 1 mol dm^{-3} HCl as a catholyte. The authors used a high concentration of $NaBH_4$ and a higher flow rate of 95 ± 5 L h^{-1} than the average conditions reported in the literature. At 20 ^{o}C and a current density of 31.8 mA cm^{-2}, the maximum power density and cell voltage were around 34 mW cm^{-2} and 1.06 V, respectively. Cao et al. [101] prepared Au/Ni-foam electrodes with 3D structures (5 cm^2) that served as both the anode and the cathode for a $NaBH_4 \| H_2O_2$ cell. The cell delivered about 42 mW cm^{-2} at 25 ^{o}C in an anolyte solution of 0.1 mol dm^{-3} $NaBH_4$ + 2 mol dm^{-3} NaOH and a catholyte solution of

2 mol dm^{-3} NaOH + 0.5 mol dm^{-3} H_2O_2, and membrane Nafion® 115 was used to divide the cell.

Palladium materials [61] [102] [103] [58] [104] and its alloys [71] [105] [106] [72] [75] [107] are some of the best materials for DBFCs. Liu et al. [61] considered Pd/C and Pt/C as potential electrocatalysts for DBFCs. They supposed that the reaction mechanism of borohydride oxidation depends on the reaction conditions and the electrocatalyst's nature. Both Pt and Pd showed some similarities in terms of H_2 evolution behaviour; however, the evolution decreased and almost stopped under special conditions, such as a low concentration of $NaBH_4$ and a large electrode current load. For example, the authors observed that a higher fuel efficiency – between six and, ideally, eight electrons – could be achieved on both Pt and Pd at a low concentration (< 1.5 mol cm^{-3}) of borohydride ions with a high anodic current (4 A, 0.8 A cm^{-2}), as opposed to four electrons when a high concentration of BH_4^- and a low current were used. Cheng et al. [108] explored the performance of Au, Pt, Ag, Pd and Ni electrodes for BH_4^- oxidation. They fabricated the membrane (Nafion® 117) electrode assemblies (MEAs) of the five anodes supported by carbon (Vulcan XC-72R with a 2 mg metal catalyst cm^{-2}). The Pt and Au electrodes demonstrated substantially better durability than the Pd, Ag and Ni at a current load of 20 mA cm^{-2} (25 °C) and 50 mA cm^{-2} (70 °C) for a 50-h test period, as can be seen in Figure 2.4.

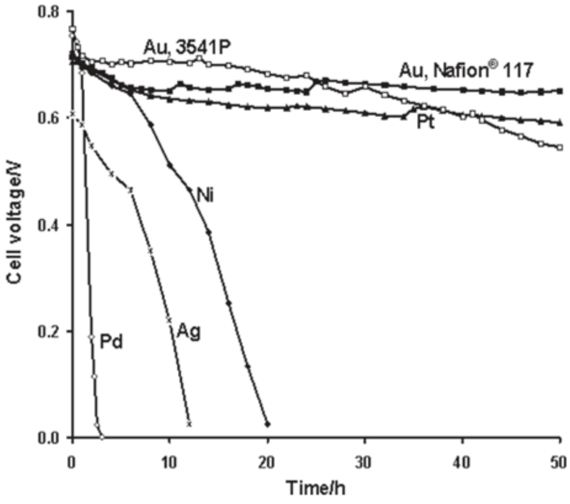

Figure 2.4. The stability test of different anodes electrodes in $NaBH_4$‖O_2 FCs at a 50 mA cm^{-2} current load and a temperature of 70 °C [108]. The anolyte contained 1.32 mol dm^{-3} $NaBH_4$ in 2.5 mol dm^{-3} NaOH with a flow rate of 0.01 dm^3 min^{-1}. The cathode was Pt/C separated by Nafion® 117 membrane, and the oxidant was O_2 (200 cm^3 min^{-1}).

The test used a solution of 1.32 mol dm^{-3} $NaBH_4$ in 2.5 mol dm^{-3} NaOH with a flow rate of 0.01 dm^3 min^{-1}. The cathode was Pt/C separated by Nafion® 117 membrane, and the oxidant was O_2 (200 cm^3 min^{-1}). Nevertheless, if one must choose between Pt and Pd for BOR, Pt is the more economical material while still suiting DBFCs reasonably well, as it costs around 50% less (£629 oz^{-1}) than Pd (£1203 oz^{-1}, metalsdaily.com, 2019).

For iridium [66] and iridium alloys [69 71 72 109], there is little research on their uses for anodic oxidation in DBFCs. Kiran et al. [66] studied Ir supported on Vulcan XC72R carbon (catalyst loading 0.5 mg cm^{-2}) as an anode and Pt/C as a cathode (2 mg cm^{-2}) with a Nafion® 117 membrane in a $NaBH_4 \| H_2O_2$ system. The concentration of the electrolyte on the anode and cathode sides were 2.64 mol dm^{-3} $NaBH_4$ in 2.5 mol dm^{-3} NaOH (anolyte flow rate: 1.35 cm^3 min^{-1}) and 2.2 mol dm^{-3} H_2O_2 in 1.5 mol dm^{-3} H_2SO_4 (catholyte flow rate: 2.1 cm^3 min^{-1}), respectively. The power density was 140 mW cm^{-2} with 165 mA cm^{-2} at 80 °C. They conducted polarisation experiments to oxidise BH_4^- ions on bimetallic rhodium-iridium alloy (Rh-Ir/C) under the same conditions, and the power density reached up to 270 mW cm^{-2} at a load current density of 290 mA cm^{-2}. The cyclic voltammograms (50 mV s^{-1}, 25 °C) of different borohydride concentrations (0.01 and 0.1 mol dm^{-3} $NaBH_4$ + 1 mol dm^{-3} NaOH) on Ir/C showed only one oxidation peak at -0.32 V *vs.* Hg/HgO (~ -0.18 V *vs.* SHE). The hydrogen oxidation peak did not appear because they ran the experiments at high potentials. The authors speculated that the direct oxidation of BH_4^- ions caused this peak (at -0.18 V *vs.* SHE). However, the peak is not close to the DBFC anode potential, and the Ir/C electrode is known as a good catalyst for H_2 evolution as well. Nevertheless, the performance of the Ir/C anode reported by Kiran et al. implies that Ir could be a possible choice for the BOR (as an alloy). As few studies have investigated the use of Ir alloy materials for DBFCs, they have been considered in the current work for further research.

Pt electrocatalysts [49 70 110 111 112 59 55] and Pt alloys [69 70 73 110 113 114 115 116 117 118 119] have been substantially investigated as promising anode materials for DBFCs. The first study of using Pt anode was reported by Jasinski dating back to 1965 [120 69]. The Pt was deposited on Ni mesh and provided a good cell potential of 0.87 V at 100 mA cm^{-2} and 45 °C. After that many research groups have investigated of its use for DBFC, however in 2006, Gyenge [49] examined the oxidation of borohydride ions on Au and Pt electrodes, and the

Pt was more active towards both the catalytic hydrolysis and the direct oxidation of the borohydride, revealing that the heterogeneous rate constant of Pt is ten times larger (1.86 cm s^{-1}) than that of Au (0.14 cm s^{-1}). The study also found that Pt, in the presence of thiourea (TU) additive (1.5×10^{-3} mol dm^{-3}), inhibits hydrogen evolution reaction (HER) but negatively affects the oxidation performance (by reducing the current). Gyenge [49] [69] concluded that, even though Pt provides half of the specific anode capacity (A h $g^{-1}_{NaBH_4}$) as Au, it is an effective catalyst for BH_4^- oxidation.

In another study, Gyenge et al. [69] also synthesised colloidal Pt and Pt alloys – Pt-Au, Pt-Ni and Pt-Ir (1:1 atomic ratio, 5 mg cm^{-2}) supported by Vulcan XC72R (20 wt.% metal) – and fixed them onto glassy carbon disk electrodes (3 mm). They also experimented with a commercial Pt-Ru anode electrode. A single DBFC with a 5 cm^2 geometrical area was tested using a 2 mol dm^{-3} $NaBH_4$ in 2 mol dm^{-3} NaOH solution and a Nafion® 117 membrane, where an O_2 gas diffusion electrode was loaded on the cathode side by a Pt catalyst (4 mg cm^{-2}). The anolyte flow rate was 50 cm^3 min^{-1}, and the oxygen flow rate was 200 cm^3 min^{-1} (2.7 atm). The operational temperature was either 298 K (25 °C) or 333 K (60 °C). Figure 2.5 shows the polarisation curves of all studied electrodes for DBFCs at 25 °C; as it illustrates, Pt-Ir and Pt-Ni were the most effective anodes, demonstrating the highest cell voltage at any applied current density. For instance, the cell potential with Pt:Ir (50:50) was around 0.1 V (10 mW cm^{-2}) and 0.53 V (53 mW cm^{-2}) at a current density load of 100 mA cm^{-2} for 25 °C and 60 °C, respectively. These outcomes were better than the power densities of Au and Au-Pd electrodes under similar conditions, which were recorded by Atwan et al. including Gyenge [94] in a previous study. Observations [69] suggest that, by increasing the temperature, cell performance improves dramatically with all catalysts.

The chronopotentiometry test represents an electrode voltage at a specific current load on an FC; chronopotentiometry experimental data were reported for all Pt alloys by the same research group [69]. The electrochemical measurements were made in a solution of 0.5 mol dm^{-3} $NaBH_4$ in 2 mol dm^{-3} NaOH at a 10 mA cm^{-2} current load at 25 °C. The tests revealed that, beside being the most stable, the Pt-Ir anode had the narrowest gap (0.08 V) between the OCP and the steady-state operating potential, followed by Pt-Ni, Pt-Au and Pt (0.45 V). Additionally, Pt-Ir presented multiple oxidation peaks in the CV experiments [at -

0.71, -0.51, and -0.13 V *vs.* SHE] at the most negative potentials, meaning that they have the most potentially favourable kinetics of all the electrode materials that were reported in the study. The Pt-Ir alloy also exhibited a more significant oxidation peak at potentials > -0.26 V *vs.* SHE than the Pt-Ni alloy. Finally, the direct oxidation of borohydride on Pt nanoparticles with a concentration > 0.1 mol dm^{-3} performed better than H_2 oxidation.

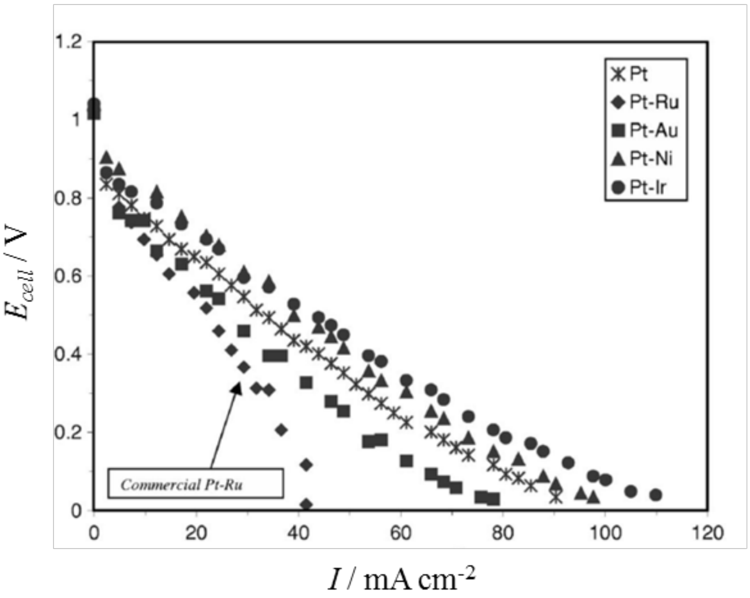

Figure 2.5. The polarisation curve of a DBFC at 298 K comparing the anode catalysts Pt-Ir, Pt, Pt-Au, Pt-Ni and Pt-Ru with an anode catalyst load of 5 mg cm^{-2} in 2 mol dm^{-3} $NaBH_4$ in 2 mol dm^{-3} NaOH, a cathode electrode (Pt) load of 4 mg cm^{-2}, an anolyte flow rate of 50 cm^3 min^{-1} and an oxygen flow rate of 200 cm^3 min^{-1} at 2.7 atm [69].

The authors proposed that the borohydride oxidation mechanism of the Pt-Ir catalyst follows a chemical–electrochemical (CE) process between -0.26 and -0.06 V *vs.* SHE. They concluded that the reaction mechanism of borohydride oxidation on Pt-Ir cannot be satisfactorily explained and needs to be investigated further.

Figure 2.6 presents the “volcano plot” of hydrogen oxidation/evolution reactions (HOR/HER) for the exchange current densities and free energy (the hydrogen metal bond strength) on monometallic surfaces, where the currents were measured in both acidic and alkaline electrolytes by Durst et al. [121]. The Pt and Ir catalysts plotted at the top of the volcano indicate higher activity towards HOR/HER, and the binding energy between surface and adsorbates exhibits neither poor adsorption of the species nor difficulty in releasing the final product (not poisoning the active sites) [122] [123]. Therefore, it is more likely that H_2 gas may occur from BH_4^- hydrolysis and would oxidise rapidly on these two metals. The figure also displays that Pt, Ir and Pd have less reactivity to H_2 in alkaline media (around two orders of magnitude) compared to acidic solutions, and they are more influenced by the pH level of a solution than non-noble metal catalysts (Ni, Cu, etc.). The authors [121] reported that using Pt-group metal (Pt, Pd, Ir and Rh) electrodes is still considered an effective choice for hydrogen oxidation in base electrolytes.

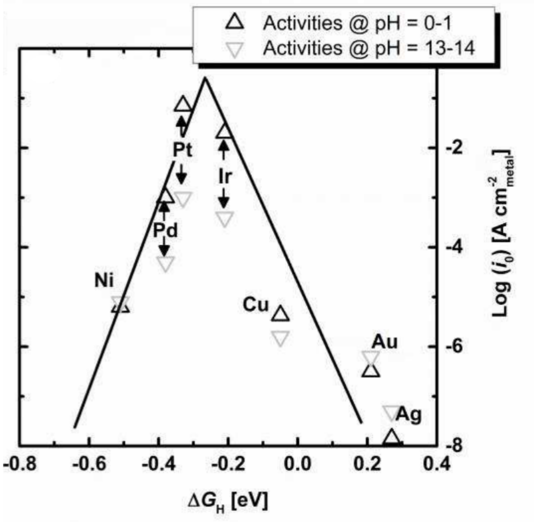

Figure 2.6. A “volcano plot” presenting the logarithm of exchange current densities for H_2 oxidation/evolution carried out in acidic and alkaline electrolytes on monometallic surfaces by [121].

The thickness of the active layer should also be considered, as it might affect the reaction pathway of borohydride ions. Concha and Chatenet [110] synthesised Pt nanoparticles (10 wt.% catalyst loaded on Vulcan XC72) to be examined in a 1 mmol dm^{-3} $NaBH_4$ in 0.1 mol dm^{-3} NaOH. The catalysts were nanodispersed on glassy carbon electrodes with catalytic layers of different thicknesses. The authors used a 3 µm active layer (which is relatively thick) to obtain nearly eight electrons, and they observed that z depends on the thickness; with the thin layers, in contrast, the number of transferred electrons decreased (e.g. z was approximately 2 at a thickness < 1 µm). They anticipated that the thick layer offers sufficient residence time for the molecules, resulting in a complete hydrogen oxidation reaction (HOR) and/or a borohydride oxidation reaction, which increases the number of electrons transferred. However, it seems also that the activity increased because the deposition time increased, which creates a greater coverage area for the catalyst on the electrode surface.

From the previous research, it seems that Ir metal and its alloys show significant activity towards BH_4^- oxidation even though there are few publications with these catalysts. In particular, the bimetallic Pt-Ir showed remarkable kinetic parameters and high electrode performance in contrast to Pt, Au, Ag, Pd and their alloys. Nevertheless, to the best of the author's knowledge, only one report [69], which was published in 2006, has investigated the use of Pt-Ir (50:50) for DBFCs. Therefore, this study investigates Pt-Ir alloy, however, in detail with different metal ratios (Pt:Ir; 75:25, 25:75) to accomplish its research objectives, namely, the effects of anode substrate design and various operating conditions on the overall efficiency and power density of DBFCs. Table 2.1 summarises some of the related electrocatalytic materials that have been investigated by different research groups as potential anode catalysts for DBFC.

2.3.2. Cathode catalyst materials

Most studies of DBFCs are focused on anodes because $H_2 \| O_2$ FC studies have largely covered the development of cathode materials. Cathode efficiency plays a significant role in the performance of DBFCs [24 124 125 126]. Cheng et al. [108] investigated different cathode materials, including Pt, Ni and Ag, using Au as an anode (all electrodes: 2 mg metal cm^{-2}) for $NaBH_4 \| O_2$ FCs using 1.32 mol dm^{-3} $NaBH_4$ fuel and 0.2 L min^{-1} O_2 (1 atm) divided by Nafion® 117 at an elevated temperature of 85 ^{o}C. The results revealed that the Pt/C cathode presented the best power density (more than 72 mW cm^{-2}), which is more than double the power densities of Ni and Ag catalysts under the same conditions. In the same study, the authors performed a durability test – which is essential from a practical point of view – on Pt, Ag, Ni, and Pd using a current load of 50 mA cm^{-2} at 70 ^{o}C [108], as shown in Figure 2.7. The data suggest that Pt is significantly more stable than other cathode catalysts at 70 ^{o}C, which led Pt to be selected as a cathode for this project. Generally, as the authors concluded [108], Pt is considered the best cathode electrode for commercial FCs, oxygen reduction, high electronic conductivity and stability; however, its high cost might limit the competitiveness of DBFCs in the FC market [108].

Table 2.1. A selection of the DBFC data and performance results with different anode and cathode catalysts.

Anode material (catalyst loading / mg cm^{-2})	**Cathode material (catalyst loading / mg cm^{-2})**	**Membrane**	**T °C**	**Oxidant (flow / cm^3 min^{-1})**	**Fuel and concentration (flow / cm^3 min^{-1})**	**Power density / mW cm^{-2}**	**Ref.**
$Pt_{0.75}$-$Ir_{0.25}$/Ti plate (2)	Pt/Ti mesh (2)	Nafion® 115	25	2 M H_2O_2 1.5 M H_2SO_4	0.5 M $NaBH_4$ 4 M NaOH	93	This work
$Pt_{0.75}$-$Ir_{0.25}$/Ti plate (2)	Pt/Ti mesh (2)	Nafion® 115	65	2 M H_2O_2 1.5 M H_2SO_4	0.5 M $NaBH_4$ 4 M NaOH	162	This work
$Pt_{0.50}$-$Ir_{0.5}$/C (5)	Pt/C(4)	Nafion® 117	25	O_2 (200)	2.0 M $NaBH_4$ 2.0 M NaOH	22	69
$Pt_{0.75}Zn_{0.25}$/C (4.5)	Pt/C (4.5)	Nafion® 117	25	2 M H_2O_2 0.5 H_2SO_4	1.0 M $NaBH_4$ 3.0 M NaOH	66	73
$Pt_{0.75}Sn_{0.25}$/C (4.5)	Pt/C (4.5)	Nafion® 117	25	2 M H_2O_2 0.5 H_2SO_4	1.0 M $NaBH_4$ 3.0 M NaOH	74	117
$Pt_{0.67}Cu_{0.33}$/C (4.5)	Pt/C (4.5)	Nafion® 117	25	2 M H_2O_2 0.5 H_2SO_4	1.0 M $NaBH_4$ 3.0 M NaOH	53	127
$Pt_{0.75}Co_{0.25}$/C (4.5)	Pt/C (4.5)	Nafion® 117	25	2 M H_2O_2 0.5 H_2SO_4	1.0 M $NaBH_4$ 3.0 M NaOH	69	128
Pt-Pd	Pd-Ir (10)	Nafion® 117	25	0.04 M H_2O_2 1.0 H_2SO_4	0.01M $NaBH_4$ 1.0 M NaOH	55	129
Pt/ Nanoporous carbon (4)	Au/XC- 72	Nafion® 117	25	2 M H_2O_2 0.5 H_2SO_4	1.0 M $NaBH_4$ 3.0 M NaOH	55	130
Pt/C(4.5)	Pt/C(4.5)	Nafion® 117	25	2 M H_2O_2 0.5 H_2SO_4	1.0 M $NaBH_4$ 3.0 M NaOH	43	117
Pt/C (0.7)	Pt/C(0.7)	Nafion® 117	25	2 M H_2O_2 0.5 H_2SO_4	1.0 M $NaBH_4$ 3.0 M NaOH	43	73
Au/C felt (0.5)	Pt/C (4)	Nafion® 117	20	1 M H_2O_2 1 M HCl	6.6 M $NaBH_4$ 6.0 M NaOH	34	29
Au/Ti mesh (2)	Pt/C (2)	Nafion® 117	85	O_2 (200)	1.3 M $NaBH_4$ 2.5 M NaOH (10)	81	87
Au/C (1.4) nanoparticles	Pt mesh	Nafion® 212	20	4.5 M H_2O_2 2.0 M HCl	0.5 M $NaBH_4$ 2.0 M NaOH	30	83
Au/Ni-foam	Au/Ni-foam	Nafion® 115	25	2 M NaOH 0.5 M H_2O_2	0.1 M $NaBH_4$ 2.0 M NaOH	42	101
Ag/Ti mesh (2)	Pt/C (2)	Nafion® 117	85	O_2 (200)	1.3 M $NaBH_4$ 2.5 M NaOH (10)	58	87
Ni-Au/C (1.4) nanoparticles	Pt mesh	Nafion® 212	20	4.5 M H_2O_2 2.0 M HCl	0.5 M $NaBH_4$ 2.0 M NaOH	74	83
Pd/C (2)	Pt/C (2)	Nafion® 117	85	O_2	1.3 M $NaBH_4$ 2.5 M NaOH	90	108
Ni + Pd/C (1)	Pt	Nafion® 212	28	O_2 (0.15)	1.3 M $NaBH_4$ 2.5 M NaOH (5)	77	85

$Co(OH)_2$-PPy-BP (10)	CoOOH-PPy-C	Nafion® 117	25	O_2 (10)	1.3 M $NaBH_4$ 2.5 M NaOH	101	[131]
AB_2 alloy	Pt/C	Nafion® 117	85	O_2	2.6 M $NaBH_4$ 5.0 M NaOH	180	[64]
AB_5 (39)	Au	Nafion® 961	25	2.0 M H_2O_2 1.5 M H_2SO_4 0.1 M H_3PO_4	1.1 M $NaBH_4$ 5.0 M NaOH (10)	50	[132]
Poly (3,4-ethylenedi-oxythiophene)	Poly (3,4-ethylenedi-oxythiophene)	Fumsep FKB	23	5 M H_2O_2 0.75 H_2SO_4	1 M $NaBH_4$ 4 M NaOH	7.5	[77]

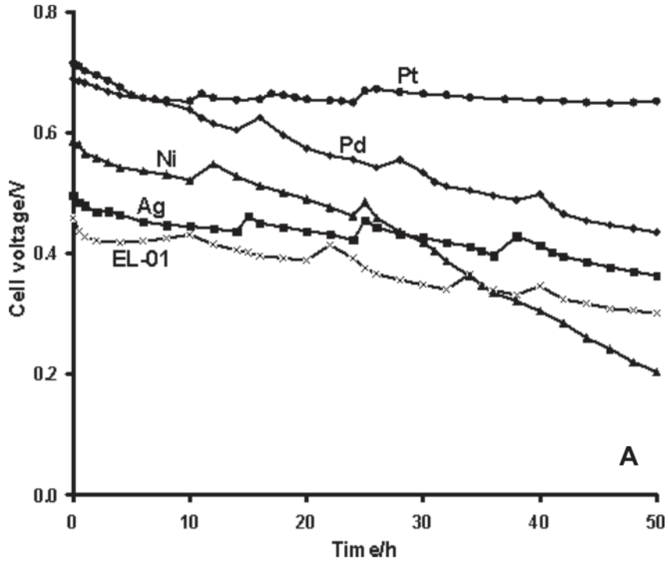

Figure 2.7. The durability tests of different cathode materials in a $NaBH_4\|O_2$ FC at a 50 mA cm^{-2} current load and a temperature of 70 °C [108]. The anolyte contained 1.32 mol dm^{-3} $NaBH_4$ in 2.5 mol dm^{-3} NaOH with a flow rate of 0.01 dm^3 min^{-1}. The cathode was Pt/C separated by Nafion® 117 membrane and the oxidant was O_2 (200 cm^3 min^{-1})

Therefore, non-noble electrocatalyst cathodes, such as iron tetramethoxyphenyl porphyrin (FeTMPP), were evaluated and showed a higher cell power performance than either Ag and Ni, that is, up to 65.3 mW cm^{-2} [133]. However, the cell with the FeTMPP cathode exhibited lower activity and stability compared to those observed with the Pt cathode [133]. Recently, Lin et al. [134] synthesised a low-cost catalyst for the cathode: polypyrrole modified carbon supported FeS (FeS-PPy-BP) in alkaline media for a $NaBH_4\|O_2$ FC. The open cell voltage was 0.92 V, and the maximum power density of the cell was around 79 mW cm^{-2} at 30 °C. Pt/C (5 mg Pt cm^{-2}) was employed as an anode in 1.3 mol dm^{-3} $NaBH_4$ + 2.5 mol dm^{-3} NaOH and 100 mL min^{-1} O_2 under 0.2 MPa. Since the use of H_2O_2 in DBFC at the cathode compartment provides higher open-circuit voltages and higher power density than O_2, many papers have studied the effectiveness of various cathode materials for hydrogen peroxide. Gu et al. [24] examined a potential catalyst for a direct borohydride‖hydrogen peroxide FC using Pourbaix diagrams to guide the experimental testing. Pourbaix diagrams represent the thermodynamically stable form of an element as a function of the potential and pH of a given environment [135]. The authors used activated carbon cloth as a supporting material since it has a higher surface area than carbon powder or paper [24]. They recognised that Au was an effective cathode catalyst material for a $NaBH_4$‖H_2O_2 FC using a serpentine, bipolar plate. However, they did not consider the electrode cost. The experiments showed, in another paper [28], that using H_2O_2 as an oxidant in the direct oxidation of BH_4^- can provide a cell voltage 30% higher than conventional H_2‖O_2 FCs because, as discussed in section 2.2.2, the reduction potentials of O_2 [Eq. (2.8)] and H_2O_2 [Eq. (2.15)] are 0.4 V and 1.78 V *vs.* SHE, respectively.

2.4. Membrane

The membrane separator is an integral part of a DBFC. It allows the transport of selected ions and prevents the crossover of borohydride towards the cathode, which can activate borohydride decomposition and might deactivate the cathode sites by forming metaborate on the cathode surface. Many properties should be considered when selecting a membrane, such as conductivity, thickness, mechanical strength, ion exchange capacity [35] and equilibrium water content [108]. The latter is required during DBFC operation to protect membranes from drying, as membrane hydration is essential for ion migration. Cheng et al. [108], for example, reported that a 3541P membrane can absorb a higher amount of water (45% [136] equilibrium water content) than the Nafion® 117 (19%), meaning that a 3541P membrane would function well with a high current density and with unhumidified O_2. The cell temperature also affects the properties of a membrane; membrane conductivity will increase if temperature increases, which can improve the cell current output [137]. However, it also dries the membrane and changes the water balance, causing its resistance to rise and thus decreasing cell efficiency [138]. Ideally, a healthy balance can be achieved.

There are two kinds of membranes: the anion exchange membrane (AEM) and the cation exchange membrane (CEM), both of which have been examined for use in DBFCs. Figure 2.8 shows different schematic diagrams of a direct borohydride system which exhibits how the ions exchange in AEM and CEM membranes. AEMs, as illustrated in Figure 2.8a), allow hydroxyl ions (OH^-) to transport from the cathode compartment to the anode compartment, maintaining the alkalinity of the anolyte at a high level, which helps stabilise the borohydride ions. However, unlike CEMs, AEMs suffer from the migration of borohydride ions (BH_4^-) in the opposite direction of OH^- ions. CEMs prevent the crossover of BH_4^- ions, which allows the efficient transport of sodium ions (Na^+ or K^+) from the anode to the cathode compartment to preserve the charge balance: see Figure 2.8b) [12].

The most common membrane in FCs is CEMs, particularly Nafion®, because of their mechanical strength, chemical stability [35] [139], commercially availability [63] and higher ion conductivity than AEMs [139]. Their long-term stability, however, has not been studied, especially at high temperatures [29] [12] for alkaline electrolytes in FCs. The drawback of a CEM (Na^+ transfer) in DBFCs is that it may decrease the alkali concentration in the anolyte compartment which, in a longer-term operation, makes borohydride unstable [63] [12]. The thickness of the membrane also affects the cell performance, as thin membranes show low ohmic and charge-transfer resistances [139] [63], resulting in high cell efficiency despite the increase in BH_4^- crossover. Liu et al. [139] discovered the polarisation curves of different Nafion® membranes, including NRE-211 (25.4 μm), 112 (51 μm), 115 (127 μm) and 117 (183 μm). Their results showed that thinner membranes increase maximum power density, with the best performance presented by NRE-211. The cell performance of Nafion® 115 was similar to that of Nafion® 117 for the borohydride FC.

Conversely, another study done by Li et al. [64] found that Nafion® 117 leads to better cell performance than Nafion® 112 (51 μm), as Nafion® 117 exhibits considerable resistance to borohydride crossover. One of the challenges in DBFCs is to decrease the ion transport resistance in the cell. As Na^+ is larger than H^+, it may face higher resistance than that in the PEM FC. However, Liu et al. [139] noted that the ohmic losses are not literally related to the membrane thickness; rather, it is primarily affected by electrolyte resistance.

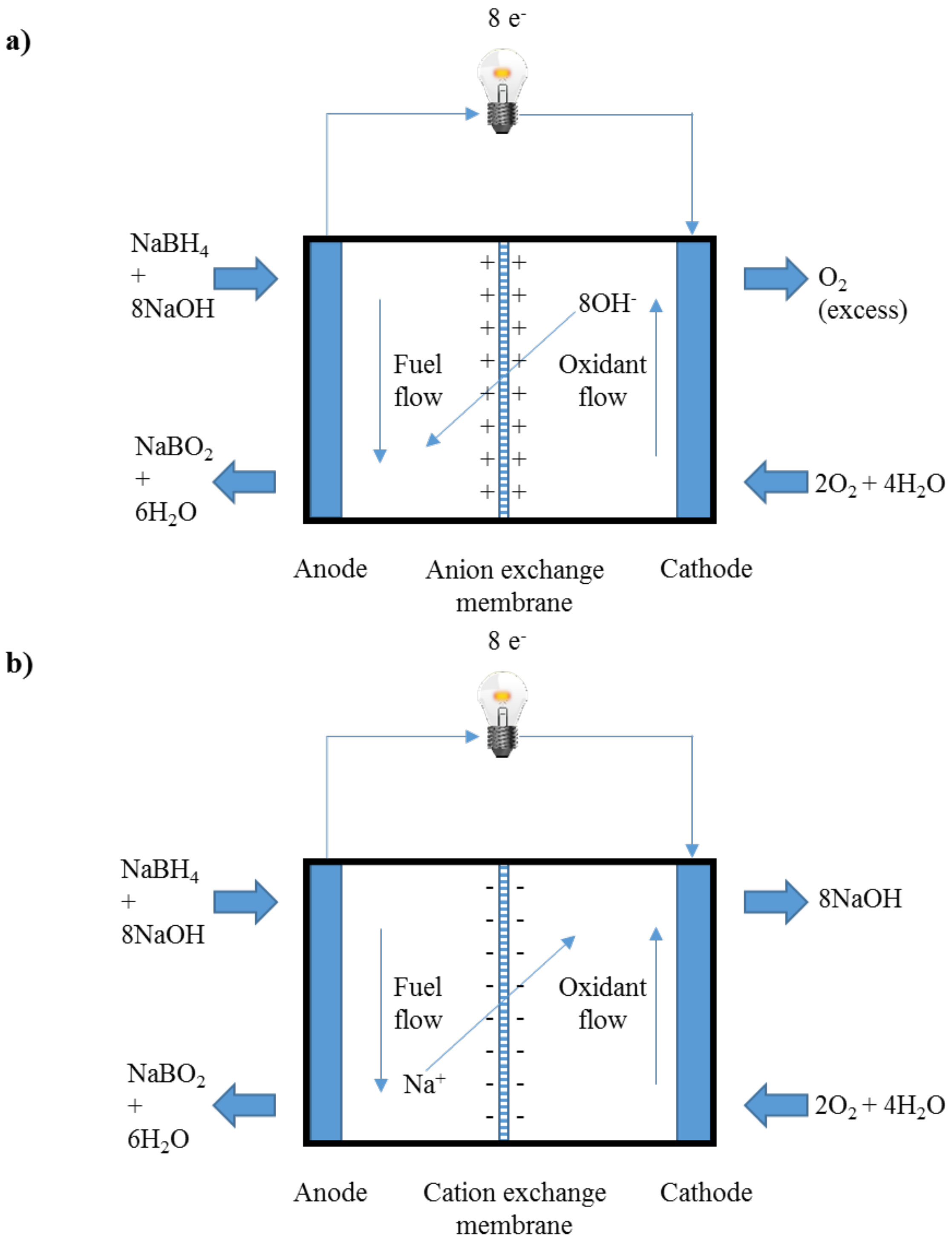

Figure 2.8. Different schematic diagrams of a direct borohydride fuel cell separated by a) anion exchange membrane and b) cation exchange membrane.

Šljukić et al. [140] have published a report with the following title question: “Anion- or Cation-Exchange Membranes for $NaBH_4 \| H_2O_2$ Fuel Cells?” They studied the impact of membrane types on $NaBH_4 \| H_2O_2$ cell power output, comparing two commercial ion-exchange membranes, including an AEM (AMI-7001S) and a CEM (CMI-7000S). Several performance tests revealed that CEMs have significant performance advantages over AEMs. Therefore, the cation exchange membrane, namely, the Nafion® 115 membrane, has been chosen for this project.

2.5. The influence of the operational variables of DBFCs

2.5.1. Effects of temperature

One of the main advantages of DBFCs is their capability to generate power at or near room temperature, which makes them appropriate for mobile applications. Cheng and Scott [138] studied the effect of temperature (from 25 to 85 ^{o}C) on the performance of a $NaBH_4 \| O_2$ FC in which the catalyst loading was 2 mg cm^{-2} for both of anode (Au/C) and cathode (Pt/C). The fuel concentration was 1.32 mol dm^{-3} $NaBH_4$ in 2.5 mol dm^{-3} NaOH. The authors observed that the elevated temperature had a manifest influence on the performance and power density of the DBFC (see Figure 2.9). They attributed this improvement to the enhancement of the mass transfer of the reactants, the faster kinetics of borohydride oxidation and the higher conductivity of the electrolytes [141] [138] [142] [143]. For example, the maximum conductivity recorded for the fuel solution at 85 ^{o}C was about three times greater than at 25 ^{o}C. However, increasing the temperature might also adversely affect cell performance by enhancing BH_4^- crossover and its hydrolysis (H_2 evolution), reducing the fuel utilisation and the number of active sites on the cathode surface because of increased metaborate formation. Moreover, as discussed in the Membrane section, higher temperatures can dehydrate the membrane, which would also increase its resistance.

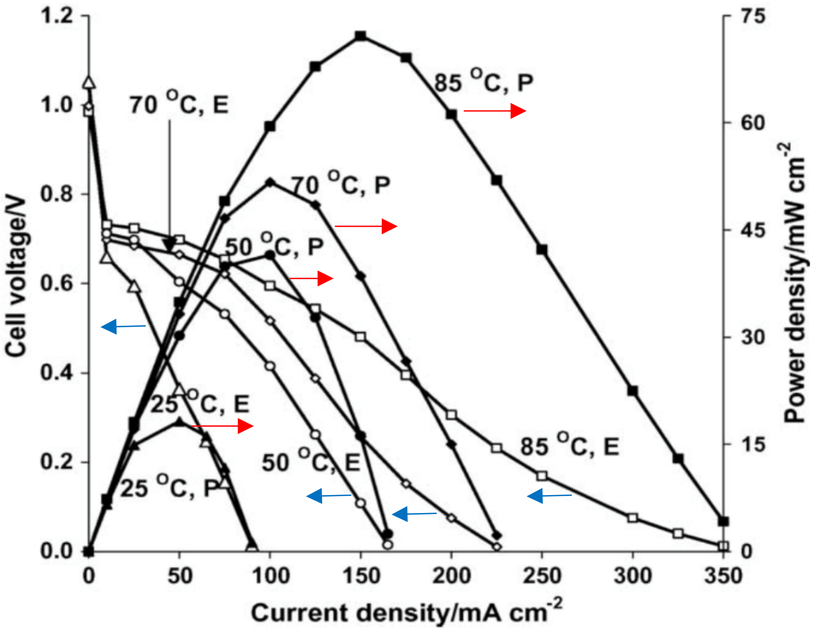

Figure 2.9. The influence of temperature on the performance of a NaBH4/O2 FC. Catalyst loading: 2 mg cm^{-2}; anode: Au/C; cathode: Pt/C; concentration of the fuel: 1.32 mol dm^{-3} NaBH4 in 2.5 mol dm^{-3} NaOH [138].

2.5.2. Effects of reactant concentrations

Changing the concentration of $NaBH_4$ and NaOH affects the performance of DBFCs. Cheng and Scott [138] recognised that the OCP of DBFCs improved by concentrating BH_4^-, a finding which validates the Nernst equation[144]:

$$E = E^o + \frac{RT}{8F}\, ln \frac{(c_{BH_4^-}) \times (c_{OH^-}^{8})}{(c_{BO_2^-})} \tag{2.20}$$

Where E^o is the formal standard electrode potential (-1.24 V *vs.* SHE), R is the universal gas constant (8.314 J mol^{-1} K^{-1}), T is temperature (K), F is Faraday's constant (96485 C mol^{-1}) and c is the bulk concentration of borohydride (mol cm^{-3}). The Nernst equation could be used to determine the electrode potential (E) of the electro-oxidation/reduction reaction under non-standard equilibrium conditions.

As BH_4^- concentration rises, the power density improves due to the enhancement of both the fuel mass transfer and the electro-oxidation of borohydride; however, a higher concentration of $NaBH_4$ may increase the crossover rate of BH_4^- to the cathode side, which is what Cheng and Scott [138] observed and which agrees with Li et al.'s [40] findings. It also leads to higher hydrogen evolution, reducing the fuel utilisation [12]. The catalyst loading limits the current density and thus further raises the borohydride concentration might be a disadvantage.

In addition, regarding the effect of NaOH, Li et al. [40] reported that its concentration should not affect the cell voltage, as it does not involve the cell reaction [Eq. (2.9)] but that it would reduce the mobility of the charge carrier (Na^+) in the anolyte solution. As a result, the cell polarisation would be dominated by the anolyte viscosity, especially at higher current densities. Increasing the NaOH concentration would increase the anolyte viscosity, which hinders the movement of borohydride ions towards the anode catalyst sites [145] and decreases the mobility of Na^+ to the cathode compartment, which would reduce the cell's performance [138] [18]. The concentration should therefore be optimised in view of the cost of the fuel and cell performance [12]. Chatenet et al. [62] reported that the $[OH^-]/[BH_4^-]$ ratio has a great influence on the reaction kinetics, as 8 OH^- ions are required for each BH_4^- ion, where the suggested ratio should be 100 times and more in this process. An optimal NaOH concentration of 5 mol dm^{-3} was proposed by Celik et al. [17] for the DBFC system. However, it seems that the optimal concentration also depends on the electrode materials and the other operating parameters; as the current study concludes, it is around 4 mol dm^{-3} (see Chapter 6).

As the NaOH concentration affects the diffusion of the reactants, Wang et al. [146] have obtained an empirical polynomial equation [Eq. (2.21)] that can be used to determine the BH_4^- diffusion coefficient, D ($cm^2\ s^{-1}$), without knowing the borohydride concentration or the electron number involved in the anode reaction.

$$D = 2.01 \times 10^{-5} - 3.65 \times 10^{-6} x + 2.25 \times 10^{-7} x^2 \tag{2.21}$$

Where x is the NaOH concentration in mol dm^{-3} ranging from 0.5 to 6 mol dm^{-3} at 30 ^{o}C. The authors applied chronoamperometry experiments on a spherical Au electrode fused to the tip of a glass tube. They found that the temperature dependence of D can be described (by the Arrhenius equation) for a NaOH concentration of 2 mol dm^{-3} as: 5.57×10^{-3} exp(-15.2 kJ/RT).

2.5.3. Effects of fuel and oxidant flow rate

DBFCs are also affected by the anolyte and catholyte flow rates. Celik et al. [17] applied different flow rates during the oxidation of a $NaBH_4$‖air (humidified) FC using Pd/C (10 wt.%) as an anode and Pt/C (10 wt.%) as a cathode separated by a Nafion® 117 membrane. The fuel concentration was 1.0 mol dm^{-3} $NaBH_4$ in 5 mol dm^{-3} NaOH and the flow rate of the solution was 2 cm^{3} min^{-1} at 25 ^{o}C. The authors detected a small improvement in the power density by increasing the flow rate; for example, when the flow rate of the oxidant increased from 10 to 150 cm^{3} min^{-1}, the power density increased from 8.5 to 10.1 mW cm^{-2}. It should be mentioned that, when the air is used as an oxidant, carbonate is formed due to the CO_2 associated with ambient air, which could affect both the electrode and solution [138 147].

Cheng and Scott [138] also experimented with different flow rates of fuel (5, 10 and 100 cm^{3} min^{-1}) and observed only a 3.5% improvement in the power density when the flow rate was changed from 10 to 100 cm^{3} min^{-1}. They concluded that higher fuel flow rates provide better mass transport and alleviate possible blocking of the channel by product accumulation. Accordingly, operating DBFCs at a lower flow rate is more economical, since its influence is relatively small [148]. Moreover, a higher flow rate increases the risk of leakage because of additional stresses on the cell, especially on the tubes, the electrode and the sealing materials; on the other hand, a higher fuel rate ensures uniform distribution of the reactants (avoiding dead zones) and might improve the mass transport by removing the hydrogen gas [12]. In short, the operating conditions deeply influence the performance of FC systems. Therefore, they have been considered in this research by using a practical DBFC and studying their effects on its performance (see Chapter 6).

2.6. Effects of electrode geometry

Noble metals presented higher performance of the electro-oxidation of $NaBH_4$, but they would increase the cost of DBFCs. Most studies on the DBFC have used microstructures, meaning that the catalysts are usually supported by carbon powder, or they have used 2D electrodes [88]. Using 3D electrodes has several advantages. For example, reticulated metals allow full utilisation of the active sites, minimising the amount of noble metal required and thus reducing electrode costs [102]. A porous, 3D electrode also substantially increases the rate of electrocatalytic reaction because it offers a high surface area and develops turbulent flow, which enhances the mass-transport conditions close to the electrode surface [149]. 3D electrodes also increase the space-time yield, raising the efficiency of the FC. Finally, they prevent the active sites from absorbing gas bubbles and becoming blocked by facilitating the release of by-product gases, such as H_2 and O_2 [101] [102].

Different reticulated materials have been used to build 3D electrodes, including nickel [102], Cu [150], reticulated vitreous carbon (RVC) [88] and titanium [87]. Several 3D electrode geometries are commercially available, such as felt, foam, sponge and mesh. One example is the RVC material illustrated in Figure 2.10, which is characterised by the number of pores per linear inch (ppi). To study the influence of pore size on the electro-oxidation rate of BH_4^-, Ponce de León et al. [88] experimented with the oxidation of borohydride ions on RVC of various ppis coated with Au nanoparticles using the sputtering method – which is the physical vapour deposition (PVD) of a catalyst – and different exposure times. The authors observed that increasing both the Au deposition time and the porosity of the RVC electrodes led to higher performance of the electrode. The average efficiency of the charge transfer was between 87 and 98%; they attributed this variation to uneven current and potential distribution on the 3D electrodes, which suggests that the thickness of the RVC electrode and its coating quality need to be optimised [88]. Low et al. [151] tested Au nanoparticles supported by the nanotubular titanate (NT) oxide electrodes (Figure 2.11) to examine the oxidation of borohydride ions. The Au-coated titanium oxide nanotube array offered approximately double the electrical charge of a Au/commercial carbon felt electrode (E-TEK) in agreement with the results of Santos et al. (AuCo/TiO2-NTs) [152] and Ponce de León et al. [153] (Au/NT). Titanate oxide nanotubes offer a large surface area with a reliable, low-cost technique [151]. However, in the reported data of Ponce de León et al. [153], the onset potential of BH_4^- oxidation was shifted by 0.3 and 0.33 V towards positive values compared to the Au foil and the Au/C, respectively, under the same conditions.

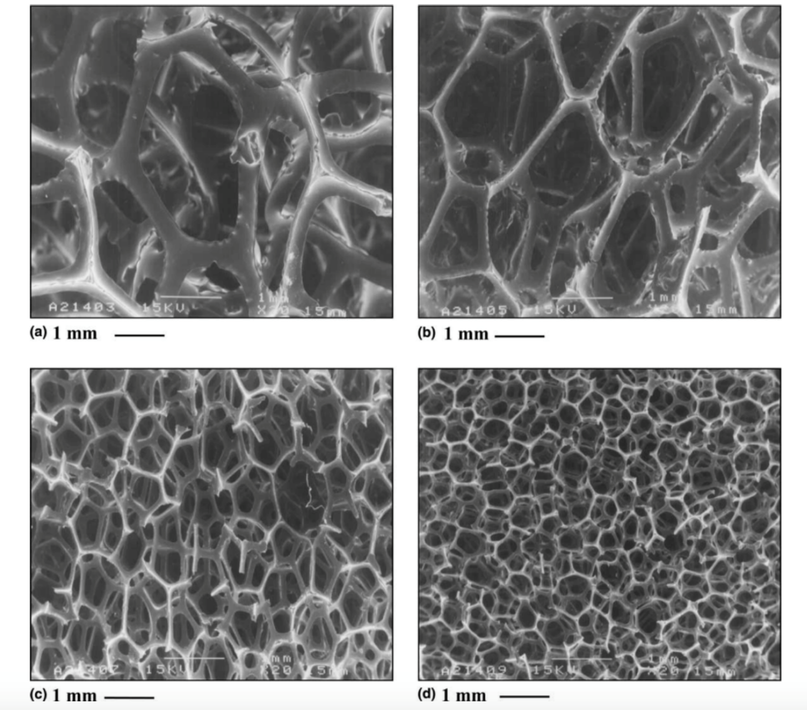

Figure 2.10. SEM micrographs of reticulated vitreous carbon (RVC) samples: (a) 10, (b) 30, (c) 60 and (d) 100 ppi [154].

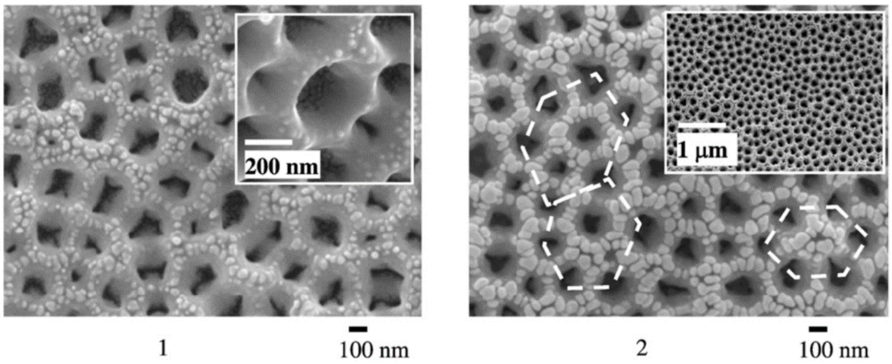

Figure 2.11. Surface morphology of two Au-coated TiO_2 electrodes with a different sputtering time 1): 10 min and 2): 30 min [151].

Cheng and Scott [87] investigated the oxidation of borohydride ions on Au and Ag anodes that were supported by titanium mesh in a DBFC. The two anodes were coated with 2 mg cm^{-2} metal using the reported thermal deposition method [155]. The membrane electrode assembly (MEA) was fabricated with a Nafion® 117 membrane separating the selected anode and the Pt/C cathode and was assembled between two graphite blocks with parallel flow channels to provide a 4 cm^{-2} active area. The fuel concentration was 1.32 mol dm^{-3} $NaBH_4$ in 2.5 mol dm^{-3} NaOH with a fuel flow rate of 0.01 dm^3 min^{-1} and 0.2 dm^3 min^{-1} of oxidant (O_2) at 85 °C. The DBFC, employing Ti mesh supporting Au and Ag anodes, exhibited remarkable current densities – up to 50% higher and power densities up to 20% higher (81.4 and 51 mW cm^{-2} for Au/Ti mesh and Ag/Ti mesh, respectively) – than those of the same anodes supported by carbon, as can be seen in Figure 2.12. Titanium materials are promising alternative catalyst supporters because of their many advantages, such as given acceptable conductivity, high mechanical and electrochemical stability, open structure and ease of manufacturing [63]. Most of the studies on DBFCs have focused on 2D electrodes substrates, and, to the best of the author's knowledge, no publication has studied the performance of different 3D Ti structures or characterises the mass-transport parameters of them for DBFCs. Therefore, this study uses 3D titanium materials, including a flat electrode, as substrates because of their many advantages mentioned above. The core objective of using 3D Ti structures is to improve the performance of the DBFC by finding the most efficient electrode structure (2D or 3D) regardless of the catalyst.

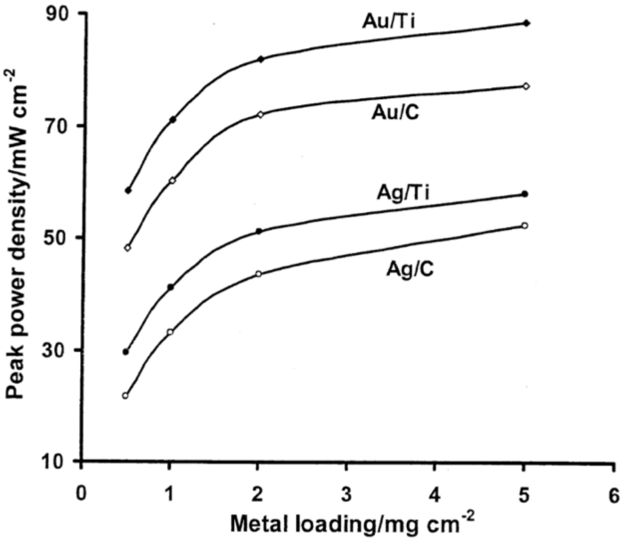

Figure 2.12. The power densities *vs.* metal loading for anode catalysts with 4 cm^{-2} of active area; Au and Ag in a $NaBH_4 \| O_2$ FC; Nafion® 117 membrane; a fuel concentration of 5 wt.% (1.32 mol dm^{-3}) $NaBH_4$ in 10 wt.% (2.5 mol dm^{-3}) NaOH; a fuel flow rate of 0.01 dm^3 min^{-1}; O_2 as the oxidant; a flow rate of 0.2 dm^3 min^{-1}; and a temperature of 85 °C [87].

2.7. Effects of surfactants in DBFCs

One of the most challenging aspects of DBFCs is minimising the hydrolysis reaction to avoid the oxidation of hydrogen gas, which lowers the number of electrons and causes a mixed cell potential. The formation of hydrogen gas in a running DBFC not only minimises the efficiency of fuel utilisation but can also create a safety hazard. The hydrogen evolution depends mainly on the electrode material and the fuel concentration. Liu et al. [61] studied the hydrogen generation behaviours in Ni, Pd/C and Pt/C anode electrodes using different anodic currents and different fuel concentrations. Surprisingly, the results demonstrated that the Pt electrode generated the lowest hydrogen evolution rate, which supported the selection of a Pt catalyst for the current study. All anode catalysts in Liu et al.'s study showed a dramatic increase at high current, especially for Ni; see Figure 2.13 for the solution of 1.02 mol dm^{-3} $NaBH_4$ in 6 mol dm^{-3} NaOH. The results also showed that a significant amount of hydrogen is generated when the initial concentration of borohydride is increased.

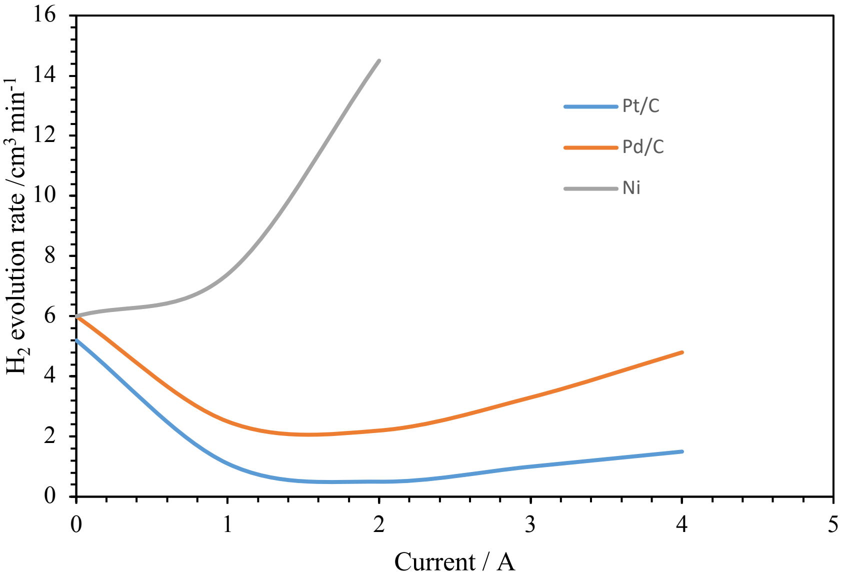

Figure 2.13. The hydrogen evolution rate *vs.* the applied anode current on Pt, Pd and Ni electrodes at 1.02 mol dm^{-3} $NaBH_4$ at 30 °C [61].

The hydrogen generation issue can be solved in two different ways: the use of a suitable anode material that favours borohydride oxidation instead of the hydrolysis reaction or the use of surfactants to inhibit the hydrogen generation [156].

Few papers have reported on the use of additives to suppress the H_2 evolution [156] [157] [158] [159] [37] [49] [160] [161]. Merino-Jimenez et al. [156] analysed the kinetics of borohydride oxidation both in the presence and the absence of surfactants, using rotating and static gold disc electrodes in a conventional three-electrode cell. Three surfactants were selected: alkoxylated ether (non-ionic) Triton X-100, sodium dodecyl sulphate (SDS; anionic, i.e. it contains anionic functional groups, e.g. sulphate and phosphate) and FC4430 (non-ionic). Harvey [162] described SDS as "[having] a long-chain hydrophobic (tail) and an ionic functional group, providing a negatively charged (head)". The experimental results of Merino-Jimenez et al. [156] showed that the SDS surfactant in 3 mol dm^{-3} NaOH (no $NaBH_4$) is not electroactive in a potential range of -0.8 to 0.6 V *vs.* Hg/HgO (-0.66 to 0.74 V *vs.* SHE); meaning that all the increased CV's peaks in the presence of $NaBH_4$ with SDS were due to BOR. The authors concluded that SDS was a promising inhibitor, since it improved the diffusion coefficient of borohydride, the limiting current and the kinetic constant. The authors also mentioned that the concentration of SDS should not exceed 0.001 wt.%; otherwise, it partially blocks the active sites and reduces the current density. The use of the other non-ionic surfactants, Triton X-100 and FC4430, showed a decrease in the current density. Thiourea (TU) and tetraetylammonium hydroxide (TEAH) have been reported as suggested inhibitors for hydrogen evolution [49] [159], but Demirci [158] argued that TU acts as a poison for the anode active sites, since TU is an organic sulphur compound and thus may absorb on the electrode surface. Gyenge [49] found that, in the presence of TEAH, the H_2 oxidation peak still existed and shifted by 0.3 V in the positive direction, while only the peak of direct oxidation of borohydride was observed in the presence of TU, although the current was lower than without it. Surfactants may enhance the fuel utilisation efficiency and coulombic efficiency of DBFCs; however, future work is needed to determine the long-term stability and the chance of catalyst poisoning in a solution containing a surfactant.

Generally, it is believed that surfactants play an essential role in the inhibition of corrosion, improvements in reaction rates and the performance of FCs and batteries [163]. For example, cetyltrimethylammonium bromide (CTAB) can influence and modify electrode properties [157]. Alternatively, Jamard et al. [161] suggested that it is better to optimise the catalyst loading rather than adding surfactants to the fuel solution, which leads to high utilisation of the fuel and maximises the power density, possibly improving the durability of the electrodes and the efficiency of the cell. The current study uses SDS additive because of its suppression of the H_2 evolution in a single borohydride flow cell, as most of the studies were performed in the half-cell configuration that Merino-Jimenez et al. [156] used.

2.8. The recycling process of sodium metaborate to sodium borohydride

Sodium borohydride ($NaBH_4$) is a promising chemical substance for hydrogen storage for PEM FCs and DBFCs. The by-product of $NaBH_4$ reactions (hydrolysis or oxidation) is metaborate ($NaBO_2$), which can be recycled back into $NaBH_4$ many ways [164] [165] [166] [167] [168]. One of the challenges that limits DBFC and IBFC technologies is this costly and inefficient process of recycling. However, Chen et al. [167] recently reported a cost-effective, efficient process to regenerate $NaBH_4$ by high-energy ball milling the $NaBO_2+2H_2O$ or $NaBO_2+4H_2O$ with MgH_2 to achieve 90% or 88% yields of borohydride, respectively, at 25 ^{o}C and 1 atm. High-energy ball milling synthesises $NaBH_4$ through the reaction of the mixed powder of Mg/MgH_2 and $NaBO_2$ at 25 ^{o}C [165]. Magnesium hydride (MgH_2) is used as a reducing agent to transform H^- into $NaBO_2$ [165] [168]. The experimental details can be seen in various studies [165] [168]. The raw material of magnesium hydride is very costly, however, which might raise the overall cost of the recycling system [166]. Nevertheless, finding a cost-effective recycling process for the magnesium oxide byproduct to MgH_2 and minimising milling energy requirements would make this a good choice; that has been suggested by Dow Chemical Company (top manufacturer of $NaBH_4$, reported in 2010) [169]. Çelikkan et al. [45] studied some patents for reconverting $NaBO_2$ to $NaBH_4$, revealing that the electrochemical process (see this patent [170]) is the most economical, promising method. Metaborate could also be utilised in other processes. For example, Kibar and Akın [171] discovered a novel way of producing a high added-value chemicals via the carbonation reaction of metaborate and carbon dioxide (at 400 °C), as the latter is a controversial greenhouse gas. In conclusion, there appears to be progress on regenerating $NaBH_4$ or reusing its by-products in other systems, but further investigation is essential to provide a simple, economic recycling system to make borohydride FCs more attractive to the market.

2.9. The limiting current technique and mass-transfer coefficient

The idea of the limiting current technique is based on driving the electrochemical reaction to the upper bound of its rate, where it is limited by mass transport [172]. The limiting current is a crucial design parameter, as it represents the maximum rate for a particular electrode. Furthermore, it is a useful technique for mass-transport studies because mass-transport coefficients can be calculated accurately from the experimental plot of current versus applied potential [172]. According to Faraday's law, the kinetic rate of an electrochemical process, r_1, depends on the current, I, a number of exchange electrons, z, and on the Faraday constant, F [149] (96485 C mol^{-1}):

$$r_1 = \frac{I}{zF} \tag{2.22}$$

The rate of component transfer, r_2, can also be defined by the following equation:

$$r_2 = k_m A\ (c - c_E) \tag{2.23}$$

Where k_m (cm s^{-1}) is the mass-transfer coefficient, A (cm^2) is the active electrode area and c and c_E (mol cm^{-3}) are the concentration of the controlled species in bulk and at the electrode surface, respectively. When the current reaches its limit, c_E becomes zero, r_1 and r_2 are equal, and so I takes the value I_L, which can be determined from the V-I plot (i.e. Figure 2.14). As a result, in this situation, the value of k_m can be easily calculated from the following equation [172]:

$$k_m = \frac{I_L}{zFAc} \tag{2.24}$$

Determining the overall rate of mass transfer is used to evaluate the performance of an electrochemical reactor, which can be determined by calculating the mass-transport coefficient, k_m, from the evaluated limiting current, I_L (A), under mass-transport controlled conditions [173]. Under these conditions, the reaction depends on the product of the mass-transfer coefficient, k_m (cm s^{-1}), and the active electrode area, A (cm^2) [173].

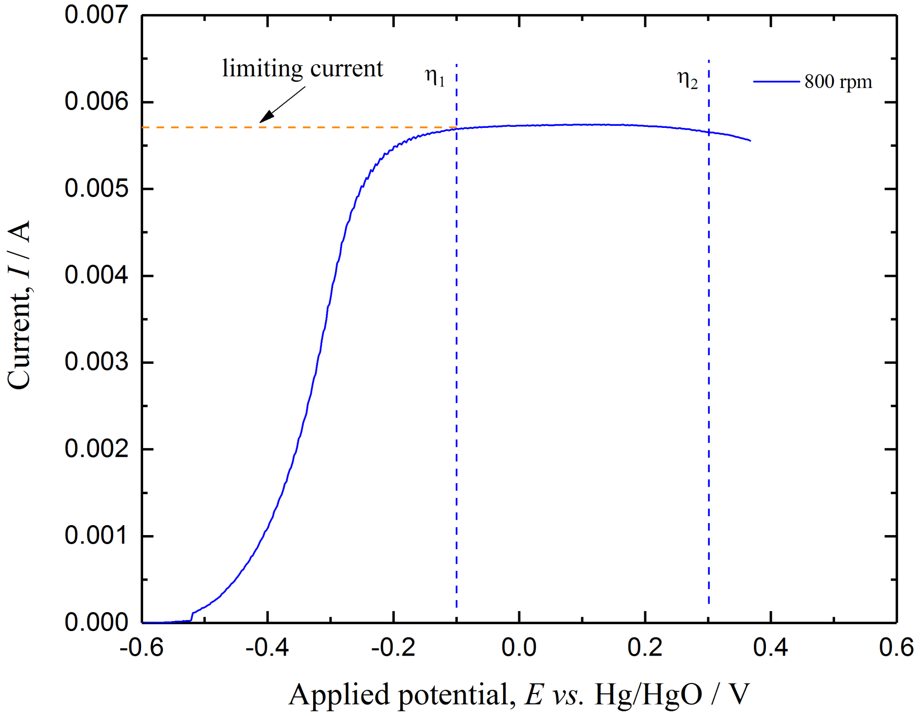

Figure 2.14. The LSV of a solution containing 0.018 mol dm^{-3} in $NaBH_4$ in 2 mol dm^{-3} NaOH using a gold planar electrode and a rotation rate of 800 rpm at 23 °C (the data is from the current work).

Evaluation of k_m by the limiting current technique can also be used to study the performance of two or more electrochemical cells which have similar conditions to select the one most suitable for a particular process [172]. The experimental conditions have to be set under known electrolyte concentrations, where the process operates at a constant temperature and within a constant geometric electrode area [174]. Overall, the limiting current is proportional to a range of main experimental variables, such as the electrode area (A), the reactant concentration (c) and the mean linear flow velocity of the electrolyte (v) at a controlled temperature based on the following equation [175]:

$$I_L \ \alpha \ Azc \ Fv^x \tag{2.25}$$

There are many techniques to determine the limiting current. The most common one is the potential sweep method. In this method, linear sweep voltammetry (LSV) can be used to obtain the polarisation curve by changing one of the mentioned variables. However, a more convenient option is the potential step technique, in which the potential is stepped from a low potential to one in the mass transfer region [175], as shown in Figure 2.14 between η_1 and η_2. In the borohydride process, in which the electro-oxidation mechanism is sophisticated and might involve the direct oxidation of borohydride ions, BH_3OH^- and H_2 form from the hydrolysis reaction [69]. In this case, it is preferable to control the potential at a selected value and incrementally step the electrolyte flow rate or borohydride concentration.

Walsh [175] reported the following factors that cause non-uniformity in the limiting current distribution and which might show a fluctuation in limiting current measurements:

- The difference in flow rate due to local turbulence, gas evolution or flow pulsation.
- The difference in surface roughness due to electrode manufacturing and the catalyst deposition method.
- The electrode structure (especially 3D electrode materials), causing non-uniformity in the potential distribution.

For porous electrode materials, it is hard to determine the active electrode area (A) [176], and the real electrochemical active area is much lower than the surface area that can be determined by the Brunauer-Emmett-Teller (BET) method [177], which was published in 1938 [178]. In this method, the surface area is determined by obtaining the amount of liquid nitrogen (at ~77 K) adsorbed isothermally on a solid surface, assuming a completed monolayer in a close-packed state [179]. Therefore, for the 3D electrode, many authors have suggested using k_mA_e (s^{-1}) as one product so that it is not necessary to know the value of the area separately [176 149 175 180]. A_e is defined as the active electrode area per unit of electrode volume ($cm^2\ cm^{-3}$), V_e, i.e. [175 181 180] the following:

$$A_e = \frac{A}{V_e} \tag{2.26}$$

The combining of Eq. (2.24) and Eq. (2.26) leads to the electrode performance factor ($k_m A_e$), which can be named the 'volumetric mass-transport coefficient':

$$k_m A_e = \frac{I_L}{zFcV_e} \tag{2.27}$$

The goal is usually to maximise A_e to achieve a compact electrochemical reactor [180]. By assuming a mass-transport rate control, the volumetric mass-transport coefficient can be evaluated in two ways: 1) by determining the limiting current that could be obtained from a certain electrode or 2) by measuring the depletion of active species with time [175 182]. The latter method is slower, more difficult and inconvenient [182]. Accordingly, in this project, the first approach was used to evaluate different 3D electrode geometries. The characterisation of an electrode and the evaluation of its coefficients are important to obtain the dimensionless parameters during cell scale-up. As a result, the cell size and its corresponding investment can be determined.

2.10. Dimensionless parameters

The most common design used in industrial electrochemical reactors is a flow-through parallel plate reactor which is approximate to a rectangular channel [175] (see Figure 2.15). The geometry of the rectangular flow channel is usually characterised by the equivalent (hydraulic) diameter, d_e, the dimensionless length group, L_e, and the aspect channel ratio, γ, which is the channel's height, S, over its width, B (Figure 2.15) [175]:

$$d_e = \frac{2BS}{B+S} \tag{2.28}$$

$$L_e = \frac{d_e}{L} \tag{2.29}$$

$$\gamma = \frac{S}{B} \tag{2.30}$$

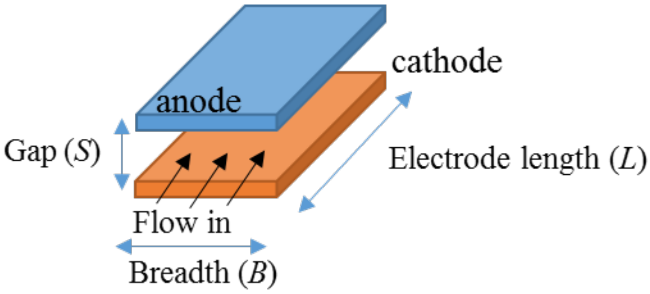

Figure 2.15. A sketch of the flow through a rectangular channel.

In the mass-controlled region, a convective-diffusion mode was assumed, i.e. both the velocity gradient (external mechanical force by a pump) and concentration gradient (physical force) contributed to mass transport [175]. Thus, the mean linear electrolyte flow velocity past the electrode surface, v (cm s^{-1}), can be calculated from the following:

$$v = \frac{Q_V}{\varepsilon A_x} \tag{2.31}$$

Where Q_V (cm^3 s^{-1}) is the electrolyte volumetric flow rate, ε is the volumetric porosity of the porous electrode and A_x (BS) is the cross-sectional area (cm^2) of the electrode. The mass transport in electrochemical cells can be explicitly expressed by the dimensionless groups, named the Sherwood (Sh), Reynolds (Re) and Schmidt (Sc) [149 175] numbers, which can be described by a dimensionless group correlation [149 175]:

$$Sh = aRe^{b}Sc^{0.33} \tag{2.32}$$

Where a and b are empirical constants dependent upon both electrode geometry and flow conditions [175]. The dimensionless groups can be defined as:

$$Sh = \frac{k_m d_e}{D} \tag{2.33}$$

$$Re = \frac{v d_e}{\nu} \tag{2.34}$$

$$Sc = \frac{\nu}{D} \tag{2.35}$$

Where D (cm^2 s^{-1}) is the diffusion coefficient of the electroactive species, and v (cm^2 s^{-1}) is the kinematic viscosity of the electrolyte. One of the measurement techniques (mentioned previously) to determine the limiting current, I_L, is to vary the mean linear electrolyte flow velocity while the potential is held constant within the limiting current region [175]. In this work, the chronoamperometry measurement, at +0.20 *vs.* Hg/HgO (0.34 V *vs.* SHE), was used to determine the I_L *vs.* different electrolyte velocities. It is useful to obtain the volumetric mass-transport coefficient, $k_m A_e$, as a function of linear flow velocities for both 3D and flat electrodes, which were then fitted to Eq. (2.36) [183], where p and q are empirical constants that can be used to characterise various electrodes:

$$k_m A_e = p v^q \tag{2.36}$$

Several studies have investigated the performance of three-dimensional materials using the mass-transfer coefficient. Brown et al. [184] have used the reduction of cupric ions to Cu metal to characterise the mass-transport properties of six types of plastic mesh turbulence promoters. The authors noted that the limiting current is not only increased by the faster electrolyte linear flow but also that the increased turbulence at the electrode surface has a significant effect on it. Moreover, using mesh turbulence promoters (TPs) had a strong influence on the current distribution, smoothing out the current within the reactor. In another study [185], the authors analysed the relationship between the mass-transport coefficient and the mean linear flow velocity both with and without a TP in a parallel plate electrolyser using a number of patterns of a segmented line made from Cu. The TPs increased the average mass-transport coefficient by 1.7 to 3.8, while the pressure drop in the reactor was small. The turbulence promoters also reduced the variation of the current distribution by about 30%.

In another publication [183], the same authors also explored the performance of different 3D materials in an FM01-LC reactor using the reduction of ferricyanide ions as a model reaction. The examined electrodes were nickel materials, including two types of expanded metal mesh (both short and long diagonal arrangements), twin grid, a fine nickel mesh and a stacked grid and foam (see Figure 2.16). The two expanded meshes differed only in the orientation to the flow; the short diagonal arrangement doubled the effect of the long diagonal arrangement. However, in another study conducted by Leroux and Coeuret [186], the factor was only 1.4 for similar materials. Both articles considered 45 ppi nickel foam; however, the empirical constant of the linear flow velocity ($k_m A_e = p v^q$) was $q = 0.49$ in Leroux and Coeuret’s study, while Brown et al. found it to be 0.7. Brown et al. attributed this to the difference in their cell design, which did not have an entry (or calming) zone to allow for a well-developed flow at the entry and the exit to the solution reservoir, possibly affecting the mass-transport correlation equations of the electrode. Brown et al. [183] also reported a less than 20% increase in the pressure drop when the 3D electrode materials were used.

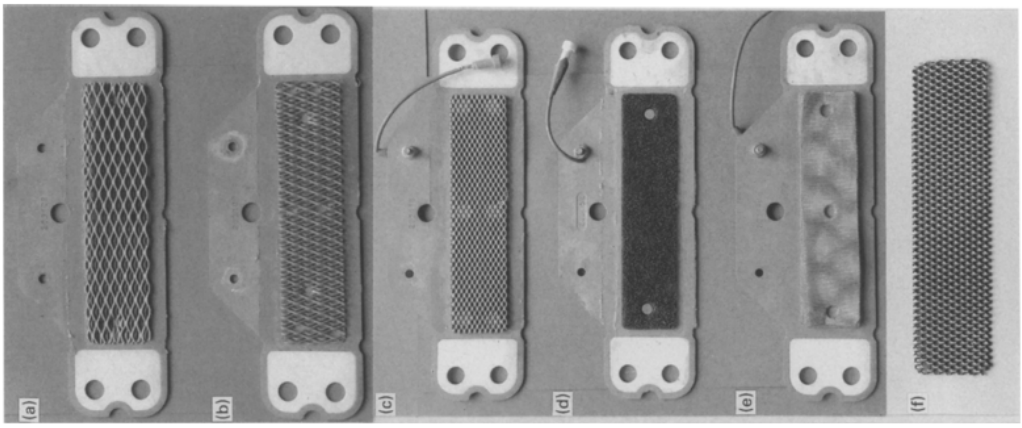

Figure 2.16. Photographs of 3D nickel electrodes that were examined in a FM01-LC reactor using the reduction of ferricyanide ions: a) expanded nickel type 197V, b) 197H, c) twin grid, d) foam, e) stacked nets and f) stacked grids [183].

2.11. Conclusion

In summary, the DBFC is a promising, novel source of energy due to its high theoretical specific energy that can reach up to 17 kW h kg^{-1} (at room temperature). It has at least *ca.* three times of the theoretical specific energy density of methanol FCs and two times that of ethanol FCs, not to mention secondary batteries (e.g. Li-ion batteries, which can have only 0.2 kW h kg^{-1}).

The current review indicates that high concentrations of borohydride can provide more current density; however, they also lead to anodic poisoning, BH_4^- hydrolysis and its crossover to the cathode compartment, which reduces fuel efficiency and poisons the cathode. It is essential that sodium hydroxide is present in the anolyte solution to prevent BH_4^- from decomposing and to increase the solution conductivity. However, higher concentrations of NaOH increase the electrolyte viscosity, which reduces the transport of borohydride towards the anode and of sodium ions towards the cathode. Furthermore, adding surfactants to the anolyte (such as SDS) would help with inhibiting the H_2 evolution; however, it might block and poison the catalyst sites at high concentrations. In brief, optimising the operating parameter is essential to maximise the cell power density.

Polymer materials presented a modest performance (7.5 mW cm^{-2}) compared to non-noble metals and their alloys, such as Ni. However, borohydride oxidation on the Ni electrode can release only four electrons and demonstrated higher hydrolysis rates than

Pd and Pt, the latter being the lowest in terms of the H_2 evolution rate. Au is no longer considered faradaic efficient for the electrochemical oxidation of borohydride ions, as the online mass spectrometry detected a non-negligible amount of H_2 yield during borohydride oxidation on Au electrodes. The Pt catalyst presented faster kinetic reaction parameters by far than Au, where the heterogeneous rate constant of Pt is ten times larger (1.86 cm s^{-1}) than Au (0.14 cm s^{-1}). Pt and Pd showed some similarities in terms of H_2 evolution; however, Pt demonstrated substantially better durability than the Pd, Ag and Ni catalysts at various current loads. Additionally, Pt as a raw material costs roughly 50% less (£629 oz^{-1}) than Pd (£1203 oz^{-1}). Pt-Ir alloy (50:50, 2D structure) formed a more effective anode than Pt-Au, Pt-Ni or Pt-Ru, demonstrating the highest cell voltage at any applied current density. The chronopotentiometry tests revealed that the Pt-Ir anode had the narrowest gap (0.08 V) between the OCP and the steady-state operating potential, followed by Pt-Ni, Pt-Au and Pt (0.45 V); it also formed the most stable anode. Pt-Ir exhibited oxidation peaks at the most negative potentials, which meant the most potentially favourable kinetics of all electrode materials that have been reported in the study [69].

3D electrode materials provide a high surface area and develop turbulent flow, both of which can increase the rate of electrocatalytic reaction. They can also increase the mass-transport rate and space-time yield, cause full utilisation of the active sites and minimise the amount of noble metal required, which leads to both lower electrode costs and higher DBFC efficiency. Titanium materials are promising alternative catalyst supporters because of their many advantages, such as given acceptable conductivity, high mechanical and electrochemical stability, open structure and ease of manufacturing.

From the cited research, Ir and its alloys showed a significant activity towards the BH_4^- oxidation, although few publications studying this material have been found. Pt-Ir bimetallic (1:1) showed remarkable kinetic parameters and high electrode performance in contrast to Pt, Au, Ag, Pd and their alloys. Therefore, Pt-Ir alloys have been nominated to be investigated thoroughly with new metal ratios (Pt:Ir; 75:25, 25:75) to evaluate various 3D Ti anode substrates and the influence of operating conditions to improve the overall efficiency and power density of DBFCs.

Chapter 3: Oxidation of Borohydride on Platinum and Gold

The objective of the chapter is to study the kinetic reaction and the electrochemical behaviour of borohydride ions in alkaline solutions. This chapter presents the experimental electrochemical results of comparative cyclic voltammetry (CV) and linear sweep voltammetry (LSV) of borohydride oxidation on Au and Pt electrodes using a typical three-electrode cell.

3.1. Electrochemical experiments

3.1.1. The electrochemical behaviour of borohydride on Au and Pt

The chemicals that have been used in all experiments are sodium borohydride, 98% (12–13 mm pellets, Acros Organics) and sodium hydroxide, 98% (pellets, Merck KGaA). All water used is deionised water (5 µS cm^{-1}) using the Purite Fusion 160 BP water purification system. A planar gold (0.125 cm^2, Pine Research Instrumentation) and platinum disk electrodes (0.071 cm^2, Eco Chemie) were examined in a conventional three-electrode cell, as seen in Figure 3.1. A platinum mesh (1 cm^2 geometrical area) served as a counter electrode, while mercury/mercury oxide (Hg/HgO, 1.0 mol dm^{-3} KOH, Radiometer Analytical, XR440) was selected to be the reference electrode. Electrochemical measurements were performed by a potentiostat/galvanostat (Autolab). The Autolab brand (Metrohm AG, the Netherlands) is controlled by a computer and operated by advanced electrochemical system software (NOVA 2.0). Cyclic voltammograms were carried out (-1.0 to +0.6 V *vs.* Hg/HgO) at different scan rates from 10–100 mV s^{-1} in an anolyte solution containing 0.03 mol dm^{-3} $NaBH_4$ in 2.0 mol dm^{-3} NaOH at 295 K. The counter electrode was immersed in 6.0 mol dm^{-3} NaOH and separated by a cation exchange membrane, Nafion® 115 (Dupont Co, USA, 127 µm thick). In each experiment, the Pt and Au electrodes were polished to a mirror finish with alpha alumina paste (0.3 µm particle size) for 50 s, followed by thorough washing with distilled water before being introduced into an ultrasonic bath for 3 minutes.

3.1.2. Determination of the diffusion coefficient of the borohydride ions

The typical three-electrode cell (Figure 3.1) was used to evaluate the diffusion coefficient of BH_4^- in a solution consisted of 3.75 mmol dm^{-3} $NaBH_4$ + 6 mol dm^{-3} NaOH on the gold rotating disk electrode (RDE) using a Compact Pine Rotator. The gold electrode was selected due to its inactivity towards the hydrogen oxidation reaction. A graphite rod (5 mm diameter, 150 mm length, Alfa Aesar, 99%) was employed as a counter electrode instead of Pt mesh. Nafion® membrane was absent in these experiments because BH_4^- does not oxidise on the graphite material, unlike Pt. Linear voltammograms were performed at different rotation speeds (ω = 500, 1000, 1500, 2000, 2500 and 3000 rpm) at a 40 mV s^{-1} scan rate and potential range between -0.8 and 0.2 V *vs.* Hg/HgO at 296 K.

3.1.3. Monitoring of borohydride in aqueous solutions by a voltammetric method

An electrochemical test could be used to detect the BH_4^- concentration in a solution; therefore, cyclic voltammetry was employed to determine the peak current for different borohydride concentrations using the potentiostat. The electrochemical measurements were carried out in the three-electrode cell (Figure 3.1). The gold RDE was chosen due to its well-defined signal. The graphite rod served as a counter electrode, and the reference electrode was Hg/HgO. The CV scan rate was 100 mV s^{-1} with a potential range of -1.0 to 0.3 V *vs.* Hg/HgO with a 10 mV potential step at 296 K. Different borohydride concentration solutions were examined (20, 15, 7.5, 3.75, 1.875, 0.938 and 0 × 10^{-3} mol dm^{-3} $NaBH_4$) in 2.0 mol dm^{-3} NaOH. The test was done five times for each solution. The solution was stirred for five seconds and left for ten seconds between each CV measurement. The plot of borohydride concentration *vs.* peak current was performed to determine the borohydride concentration in a solution at any time.

3.1.4. Stability of borohydride in aqueous solutions using LSV

The stability of borohydride ions was studied by applying LSV in the three-electrode cell containing 1.75 dm^3 of 0.02 mol dm^{-3} $NaBH_4$ in 2 mol dm^{-3} NaOH (see Figure 3.2). The counter electrode was the graphite rod, and the potential was swept from 1 to 0.2 V *vs.* Hg/HgO with a 25 mV s^{-1} scan rate on a gold working electrode (2 mm diameter).

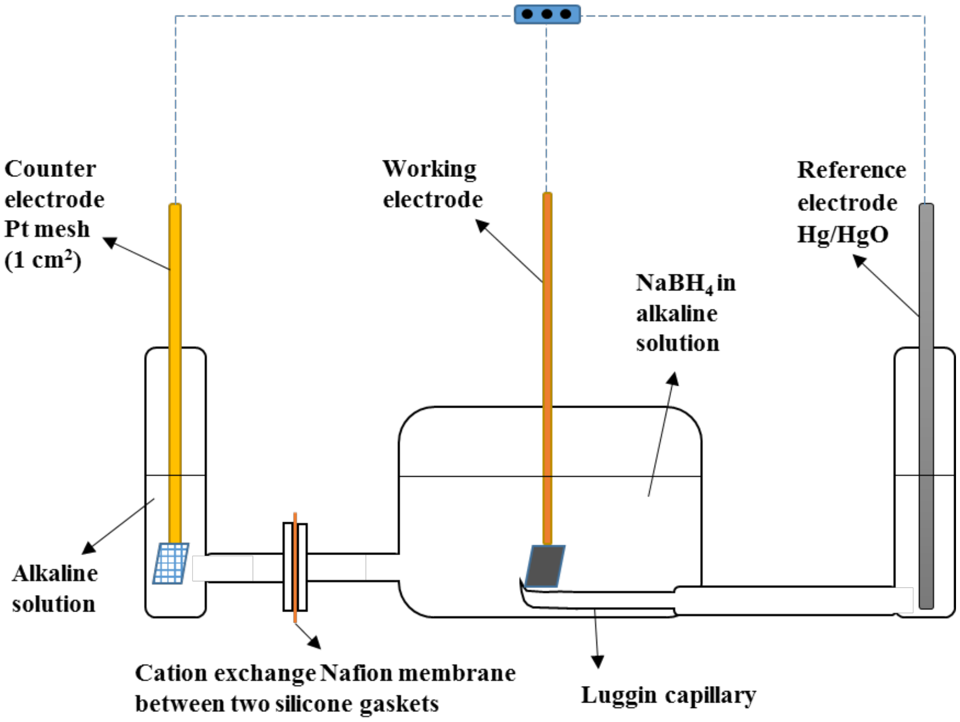

Figure 3.1. A typical three-electrode cell. Pt or Au planar is the working electrode in $NaBH_4^+$ 2.0 mol dm^{-3}, platinum mesh (1 cm^2 geometrical area) is the counter electrode in 6.0 mol dm^{-3} and the reference electrode is Hg/HgO (1.0 mol dm^{-3} KOH).

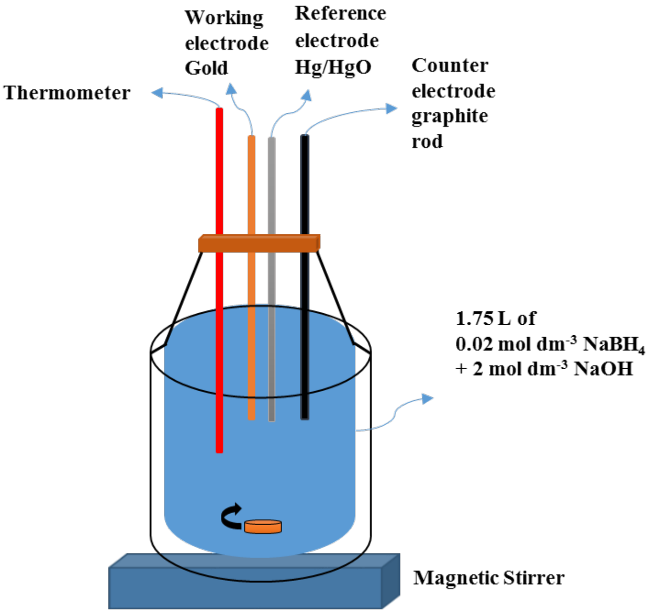

Figure 3.2. The setup for borohydride ion stability to apply an LSV *vs.* time. The potential swept from 1 to 0.2 V *vs.* Hg/HgO with a 25 mV s^{-1} scan rate. The gold working electrode and the graphite counter electrode were contained in a tank containing 1.75 dm^3 of 0.02 mol dm^{-3} $NaBH_4$ + 2 mol dm^{-3} NaOH at 23 ± 1 °C.

The peak current was recorded every 15 minutes for 15 h of continuous operation using the potentiostat. The total number of LSV measurements was 62 runs at 23 ± 1 ºC.

3.2. Results and discussion

3.2.1. Cyclic voltammetry on Pt and Au electrodes

The planar Pt (0.071 cm^2) and Au (0.125 cm^2) electrodes were tested in the conventional three-electrode cell (Figure 3.1) to understand the kinetic reaction and the electrochemical behaviour of borohydride ions in an alkaline solution. Figure 3.3a-b shows the forward scan of cyclic voltammograms (-1.0 to +0.6 V *vs.* Hg/HgO) of Pt and Au electrodes, which revealed three peaks (a1, a2 and a3), while only one peak (c1) was observed on the backwards scan. Many authors have observed these peaks, although disagreements persist [49 119 83 187 51 188 37]. The explanation below is taken from the literature and helps for understanding the experimental results of this research.

Figure 3.3a) shows the cyclic voltammogram of 2 mol dm^{-3} NaOH (with the absence of BH_4^-) on Pt. A single anodic peak was observed at a potential of about -0.85 V *vs.* Hg/HgO and with a 0.5 mA cm^{-2} current density. This peak was attributed to the ionisation of hydrogen bonded to Pt which was generated because of the cathodic discharge of water [189 49 37 110]. In the case of the presence of BH_4^-, a peak (a1) was observed at -0.4 V *vs.* Hg/HgO and 20 mA cm^{-2}, which is a superior value than the ionisation of hydrogen peak. The formation of wave a1 was at onset potential of *ca.* -0.85 V, according to Figure 3.3a) (inset), which could be attributed to the electro-oxidation of H_2 ($2e^-$) and/or BH_3OH^- ($3e^-$) [Eq. (3.2), Eq. (3.3)] that occurred by the hydrolysis of borohydride ions [Eq. (3.1)] on the Pt electrode surface. A similar peak was observed by Gyenge [49] at approximately -0.81 V *vs.* Hg/HgO at 25 mV s^{-1} and 25 ºC. Concha and Chatenet [110] found it to be around -0.59 V *vs.* Hg/HgO on Pt/C nanoparticles but at 100 mV s^{-1} in 1 mmol dm^{-3} + 0.1 mol dm^{-3} NaOH (25 ºC).

$$BH_4^- + H_2O \leftrightarrow BH_3OH^- + H_2 \quad (3.1)$$

$$H_2 + 2OH^- \rightarrow 2H_2O + 2e^- \quad (3.2)$$

$$BH_3OH^- + 3OH^- \rightarrow BO_2^- + 3/2\,H_2 + 2H_2O + 3e^- \quad (3.3)$$

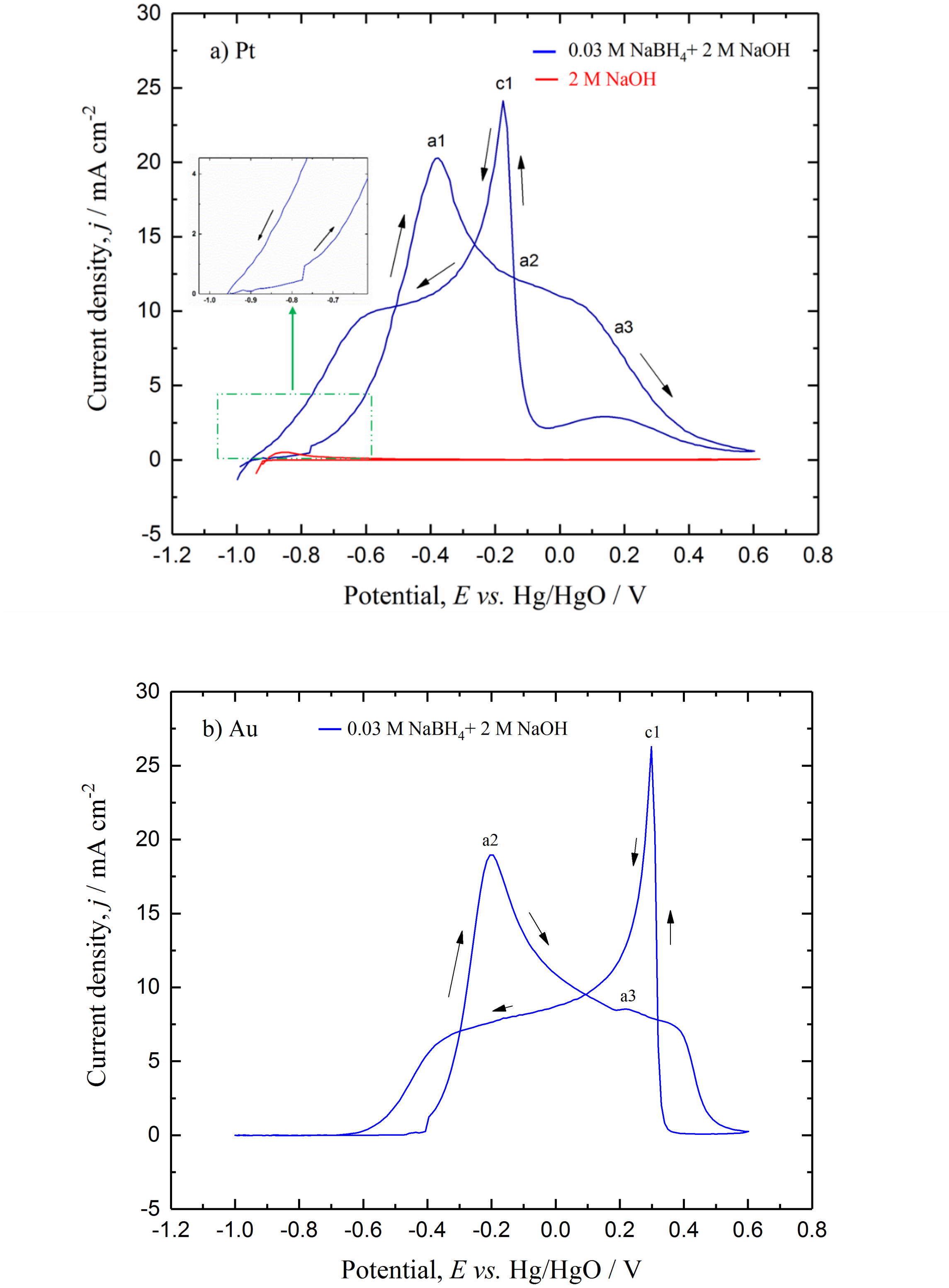

Figure 3.3. The typical cyclic voltammogram on a) Pt and b) Au electrodes. The solution consisted of 0.03 mol dm^{-3} $NaBH_4$ in 2.0 mol dm^{-3} NaOH at a 10 mV s^{-1} scan rate and 295 K. The red curve is for 2 mol dm^{-3} NaOH (background) without $NaBH_4$ on the Pt electrode.

The oxidation of borohydride on Pt is presented in the entire potential window (from -0.95 to +0.6 V *vs.* Hg/HgO, Figure 3.3a), which suggests that both H_{ads} and $BH_{4\,ads}^{-}$ contribute to the anodic current – reported by Lam and Gyenge [190] – even at lower potential [110]. Peak a1 was absent in the cyclic voltammetry wave of the gold electrode, Figure 3.3b), due to the non-catalytic nature of Au catalysts towards hydrogen oxidation but the heterogeneous hydrolysis of BH_4^- still exist [100] [59]. In the same figure, there is an anodic peak (a2) at -0.23 V for the Au electrode and a shoulder between -0.25 and 0.05 V *vs.* Hg/HgO for the Pt electrode seen in Figure 3.3a). These are reported in the literature to directly oxidise borohydride ions, according to Eq. (3.4), which was observed at -0.14 V *vs.* Hg/HgO (10 V s^{-1} scan rate) for Au electrode, while the anodic peak of Pt was at -0.09 *vs.* Hg/HgO (25 mV s^{-1}) [49]. Atwan et al. [94] obtained a wide wave between -0.5 and 0.05 *vs.* Hg/HgO (100 mV s^{-1}) on a colloidal Au electrode. All the authors tested the electrodes at 295 K (in the same concentrations of current work), but Atwan et al. examined at 298 K. This peak (a2) is important for the DBFC, as eight electrons are expected to be released at this range of potential.

$$BH_4^- + 8OH^- \rightarrow BO_2^- + 6H_2O + 8e^- \qquad E^o = -1.24 \text{ } vs. \text{ SHE} \qquad (3.4)$$

It is also expected that the intermediate product [$BH_3(OH)^-$], from Eq. 3.1, goes under further electro-oxidation [Eq. (3.3)] and/or hydrolysis occurring wave a3 (see Figure 3.3a-b) according to the following equation [49]:

$$BH_3OH^- + 3H_2O \overset{Pt}{\rightarrow} B(OH)_4^- + 3H_2 \qquad (3.5)$$

Above 0.6 V *vs.* Hg/HgO, the Au and Pt show a deactivation towards BOR because of the metal-oxide formation on their surfaces [110] [191]. Finally, in Figure 3.3a-b, an additional peak (c1) is revealed on the reverse scan, which is also possibly due to the electro-oxidation of the adsorbed intermediate product [$BH_3(OH)^-$] of borohydride oxidation [Eq. (3.3)] on the partially oxidised Pt and Au surfaces [49]. Martins et al. [37] attributed this peak to the oxidation of BH_4^- in agreement with the results of density functional theory (DFT) [192], as the hydroxyl species are reduced from the metal surface.

Rostamikia and Janik [193] [192] studied the mechanism of the BOR over Pt(111) and Au(111) using DFT methods. The results of DFT recommend a1 peak (shown in Figure 3.3a) with a Pt electrode due to the competition between the BOR and HOR at low potentials (< -0.4 V *vs.* Hg/HgO), which would affect the cell efficiency. The BH_4^- reaction in this case could follow the fully-dissociative adsorption pathway [193] [192] and presented by Olu et al. [59], using the microkinetic model in Figure 2.3 (similar technique for Au(111) was also done [194]). The adsorption of the BH_4^- to the Pt sites take places with the dissociation of 3B–H bonds, producing $3H_{ads}$ and BH_{ads} species; however, the activation of B–H bonds over the Au surface requires a substantial overpotential where the adsorption rate is sluggish at low overpotentials. The electrooxidation reaction mechanism over Au that caused peak a2 (a shoulder with Pt) is likely based on the partially-dissociative adsorption of BH_4^- to form $BH_{3,ads}$, where the latter would self-dehydrogenated to evolve to hydrogen gas [59] or undergo further oxidation with OH^- species until reaching the final product (BO_2^-) at high potentials. The declines (a3) that appear in Figure 3.3a-b are due to the adsorbed hydroxide that was formed on the metal electrodes and hydroxyl groups poisoning the surface (reducing the current density), preventing further BOR. The formation of surface hydroxide/oxide on Pt and Au is reduced, freeing more sites for the oxidation of BH_4^- to cause the large cathodic peak (c1), suggested by the DFT results [192] [193]. In general, not only the electrocatalyst type would affect the borohydride oxidation behaviour, the nature of the electrode (e.g. Pt surface structure) may also affect the reaction mechanism as it can be seen in these two studies [111] [55].

The cyclic voltammograms of a solution of 0.03 mol dm^{-3} $NaBH_4$ in 2.0 mol dm^{-3} NaOH using the Pt and Au electrodes, are shown in Figure 3.4a) and Figure 3.4b), respectively. Increasing the scan rate raises the anodic peak current density (a1, a2 and a3) shifts the peak potential towards more positive potentials for both Pt and Au electrodes, which agrees with the cited studies [69] [94] [37]. This shifting nature of the peak potential is typical of the irreversible electrochemical process [82]. The Pt planar electrode produced a higher current density from BH_4^- oxidation at a much lower potential in contrast to the Au results (see Figure 3.4), which agrees with the findings of Elder and Hickling [195]. For example, at a scan rate of 100 mV s^{-1}, the current density reached up to 54 mA cm^{-2} at -0.29 V for Pt, while it was about 41 mA cm^{-2} (32% lower) at -0.13 V for Au. Similar observation by other research groups has been reported for Pt [33] [104] and Au [196] [191] [197].

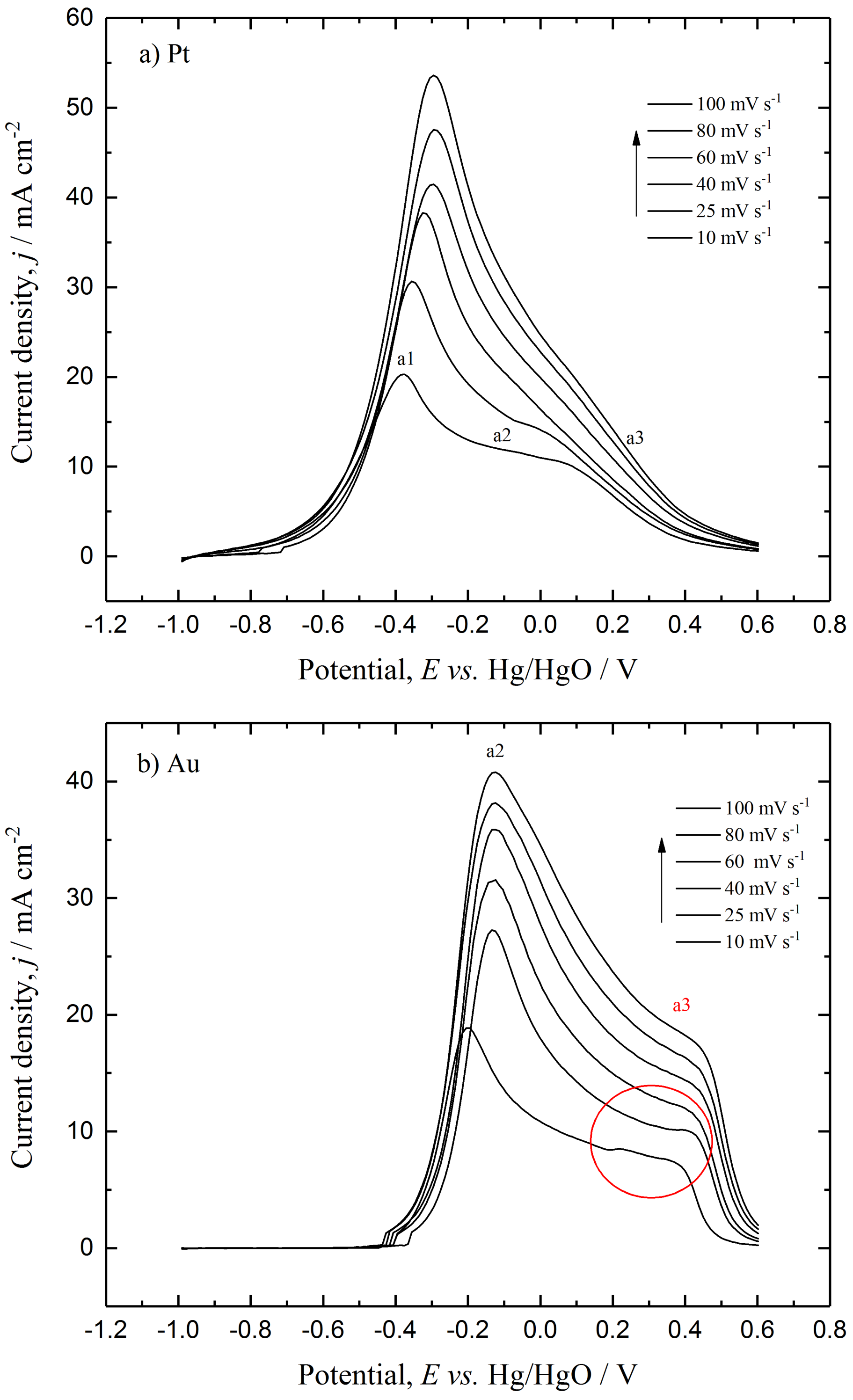

Figure 3.4. The cyclic voltammogram (forward scan) of 0.03 mol dm^{-3} $NaBH_4$ in 2 mol dm^{-3} NaOH on a) Pt and b) Au disk electrodes at different scan rates and 295 K.

3.2.2. Determination of the diffusion coefficient of borohydride anion using Au

LSVs were applied to determine the diffusion coefficient of BH_4^- using the Levich equation, as seen in Eq. (3.6). The diffusion coefficient can be obtained from the slope of the limiting current density, j_L (A cm^{-2}), and the square root of the rotation speed of the rotating electrode [144].

$$j_L = \frac{0.62\, zFD^{2/3}c}{v^{1/6}}\, \omega^{0.5} \qquad (3.6)$$

Where z is number of electrons that transfer, F is Faraday's constant (96485 C mol^{-1}), D is the diffusion coefficient (cm^2 s^{-1}), c is the bulk concentration (mol cm^{-3}), ω is the rotation rate (rad s^{-1}) and v is the kinematic viscosity (cm^2 s^{-1}), its value being reported in the literature as approximately 0.02 cm^2 s^{-1} [198]. The number of electrons was assumed to be 7.7, a number obtained by Wang et al. [146] using a gold RDE and a solution containing 0.02 mol dm^{-3} $NaBH_4$ in 6 mol dm^{-3} NaOH at 30 °C. This equation is valid when the system is mass-transport limited [6]. Chatenet et al. [198] reported that the limiting current plateau of the borohydride oxidation, like the chronoamperometric and Levich techniques, cannot be reached above 0.01 mol dm^{-3} $NaBH_4$ in solution. Moreover, Cheng and Scott [92] indicated that an increase in the rotation rate caused an increase in the current; however, with a further increase in rotation rates, the diffusion limiting currents were not well-defined due to the high irreversibility of BH_4^- oxidation.

Figure 3.5 shows LSVs of BH_4^- oxidation in the gold RDE at different rotation rates in a solution containing 3.75 mmol dm^{-3} $NaBH_4$ in 6 mol NaOH. At a negative potential below -0.4 V, the current was completely limited by the kinetics of electron transfer, while above -0.3 V it was affected by the mass transport of BH_4^- species. The limiting current increases with the rotation speed means that the kinetic is limited by the borohydride diffusion. The electrochemical signals are flatter as the rotation rate decreased. The calculated diffusion coefficient was $0.52 \pm 0.06 \times 10^{-5}$ cm^2 s^{-1} at 23 °C, which was obtained from the Levich slope of the j_L vs. $\omega^{0.5}$ plot, as shown in Figure 3.6. The D result was near to that recorded by Wang et al [146] of $0.66 \pm 0.03 \times 10^{-5}$ cm^2 s^{-1} at 30 °C (see Figure 3.7). The difference was about 12%, which could be attributed to the difference in operating temperature, the method and the experimental setup that were used to determine the diffusion coefficient.

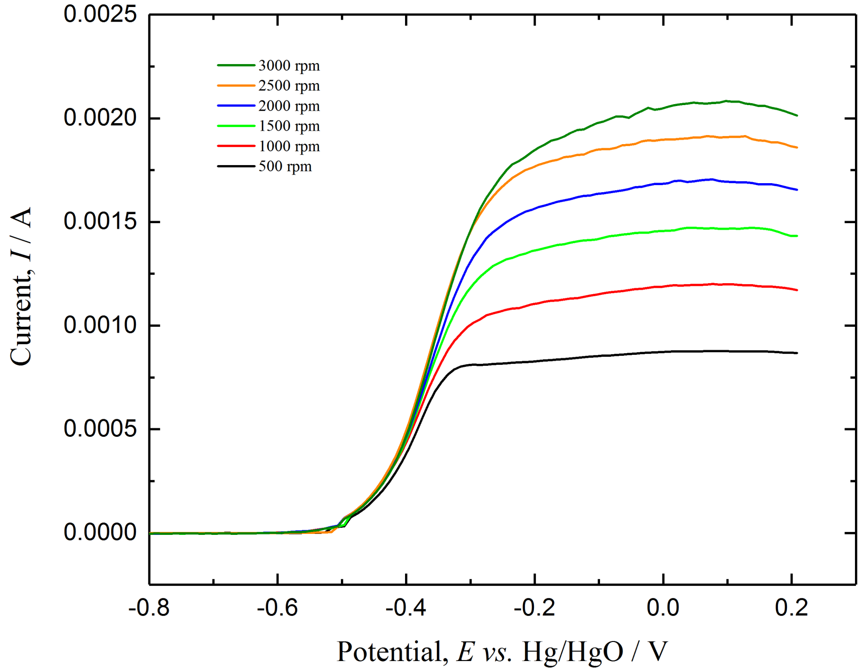

Figure 3.5. The LSV of 3.75×10^{-3} mol dm^{-3} $NaBH_4$ in 6 mol NaOH on a gold RDE (0.125 cm^2) in a three-electrode cell. Graphite was used as a counter electrode. 40 mV s^{-1} was the scan rate and the potential ranged between -0.8 and 0.2 V *vs.* Hg/HgO at 296 K.

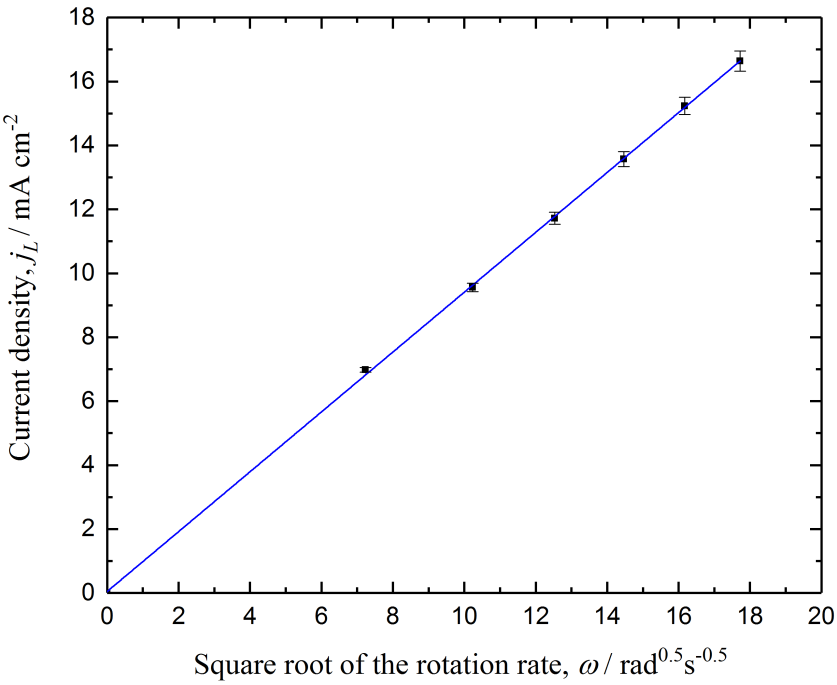

Figure 3.6. The Levich plot for Eq. (3.6) of 3.75 mmol dm^{-3} in 6 mol dm^{-3} NaOH on a Au RDE (0.125 cm^2) at a scan rate 40 mV s^{-1} with different rotation rates at 296 K.

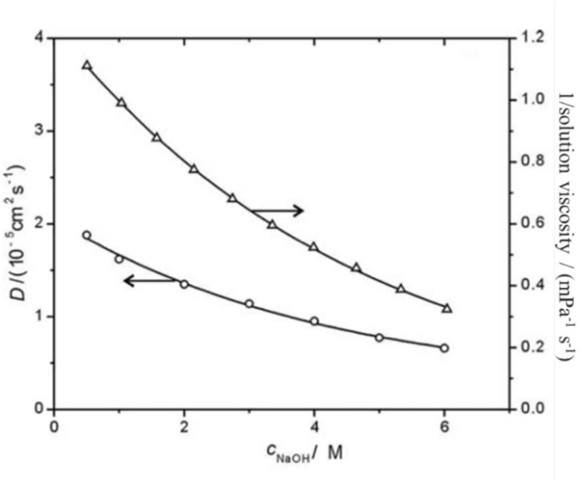

Figure 3.7. The diffusion coefficient in NaOH concentration and 1/solution viscosity at 30 °C [146]. In the current study, $D = 0.52 \pm 0.06 \times 10^{-5}$ cm^2 s^{-1} in 6 mol dm^{-3} NaOH at 23 °C, being about 12% lower than the results of Wang et al. [146].

Wang et al. applied a chronoamperometry technique using a spherical Au electrode fused to the tip of a glass tube. The diffusion coefficient should have one value only, so uncertainties in determination method could cause different values. The Levich method might lead to inaccuracy while calculating the diffusion coefficient of BH_4^- ions due to the fact that the *z*-value is usually assumed, and electrolyte kinematic viscosity should be known. Moreover, a boron-oxide film is expected to form at the RDE surface – which is possibly behind the irreproducibility of the limiting current measurements – while using the rotating ring-disc electrode technique is suggested to obtain an accurate *D* value for the current system, reported by Chatenet et al.[198]. Therefore, in this research, the *D* value is taken from the literature.

3.2.3. The voltammetric method to determine borohydride concentration

In order to quantify the concentration of sodium borohydride in an alkaline solution, a family of cyclic voltammograms was carried out in alkaline aqueous solutions using a gold working electrode. The electrode materials should be inactive towards BH_4^- hydrolysis and the oxidation-reduction of any other species in the solution in the oxidation potential range of borohydride [199]. Mirkin and Bard have been using a voltammetric method using a gold electrode since 1991 [200]. The gold catalyst was found to be the most suitable material for the analytical determination of borohydride because of its well-defined signal, unlike, for example, Ni, Pd or Pt [200] [199] [201]. In addition, the gold electrode is quite stable with a low level of background current in the potential region of borohydride oxidation [200]. It was also found in this project that the peak current decreases with increased cycling, see Figure 3.8a). This behaviour has been observed by many authors and discussed thoroughly by Tokash and Macdonald, but they could not offer a conclusive explanation [202]. The authors attributed this to either the stagnation of reaction products close to the electrode or adsorption of an intermediate (boron-oxide film) on a gold surface. Finkelstein et al. [112] demonstrated the poisoning behaviour of Pt and Au electrodes and suggested a cleaning potential or 'self-cleaning potential' at -0.2 V *vs.* Ag/AgCl for Pt, freeing it of both surface hydrides and oxide or hydroxide while enhancing the one-borohydride reaction mechanism. From the current project, it was observed that some small bubbles appeared on the electrode surface which sometimes block the surface while sweeping the potential for a series of cycling; however, mixing the solution would remove the bubbles and refreshes the solution close to the electrode. Therefore (after many trials), this issue – current decreases with increased cycling – has been successfully solved by stirring the RDE electrode for about 5 s and waiting for 10 s to allow the solution to settle down for the next cycle, as can be shown in Figure 3.8b) where the five cycles are almost identical.

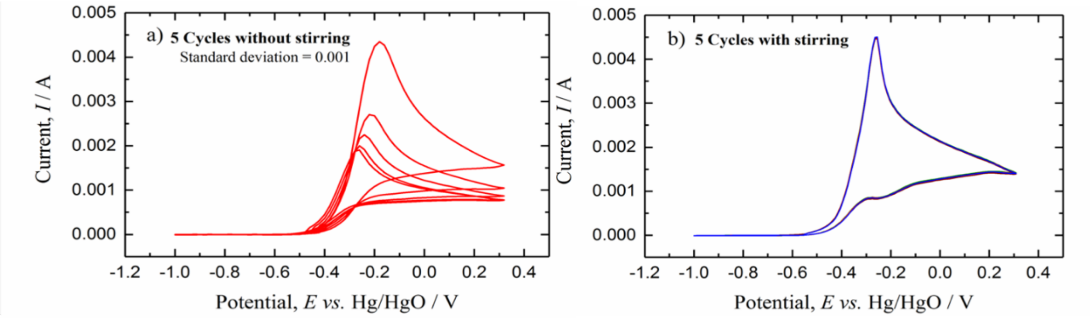

Figure 3.8. The cyclic voltammogram for 0.03 mol dm^{-3} $NaBH_4$ in 2.0 mol dm^{-3} NaOH on a planar gold electrode (0.125 cm^2) at a scan rate of 100 mV s^{-1} at 296 K.

Figure 3.9 shows five repeated cyclic voltammograms of six different borohydride concentrations (ranging from 0.94 to 20 mmol dm^{-3}). The potential sweep was between -1.0 and 0.3 V *vs.* Hg/HgO at a scan rate of 100 mV s^{-1} and at 296 K. To prevent the hydrolysis of the borohydride, all solutions contained 2 mol dm^{-3} NaOH. The calibration curve of the borohydride concentration *vs.* the peak current is presented in Figure 3.10, which shows the increase in the peak current with borohydride concentration. The empirical relation [$I_p = 0.182\ c_{BH_4^-}$] between the peak current (mA) and the borohydride concentration was obtained, which is valid for a concentration ranging from 0 to 20 mmol dm^{-3}.

A further increase in borohydride concentration might lead to a wide fluctuation of the peak current, which explains why, according to the best of the author's knowledge, most studies report a concentration of $NaBH_4$ less than 20×10^{-3} mol dm^{-3}. This phenomenon has also been observed in this project; for example, see Figure 3.9 for 20×10^{-3} mol dm^{-3} $NaBH_4$. However, the average of the five peaks was fitted nicely to the calibration curve. The fluctuation could refer to the significant bubbling that occurred close to the electrode surface during the electrochemical measurements, even though the gold electrode was used. This may be due to the increase in borohydride concentration, which, in turn, increases the hydrolysis rate. Colominas et al. [203] speculated that these bubbles are hydrogen formed by hydrolysis; because the oxidation reaction consumes OH^-, the concentration of OH^- decreases at the gold-solution interface.

3.2.4. Sodium borohydride stability

The stability of borohydride ions in an aqueous solution is vital for mass-transport studies (see Chapter 5) to select a solution composition which ensures that borohydride is stable during experiments. The LSV, using the setup and conditions described in Section 3.1.4, was carried out in a tank containing 1.75 dm^3 of 0.02 mol dm^{-3} $NaBH_4$ + 2 mol dm^{-3} NaOH to determine the peak current at every 15 minutes using a gold electrode (2 mm diameter). Figure 3.11 shows all the obtained peaks *vs.* time, and the average peak current over the 15-h test period being evaluated as 0.774 mA by taking the mean of 62 peaks. The average standard deviation of the samples was 0.024, and the average error was around 5%, which suggests that this method is highly reliable to detect BH_4^- stability in any aqueous solution. The borohydride is stable in 2 mol dm^{-3} NaOH over a 15-h test period. Colominas et al. [203] examined 0.1×10^{-3} mol dm^{-3} $NaBH_4$ (low concentration) in 2 mol dm^{-3} NaOH for a 19-day test period using CV and a gold electrode (6 mm diameter). The authors concluded that $NaBH_4$ is stable over that period as well.

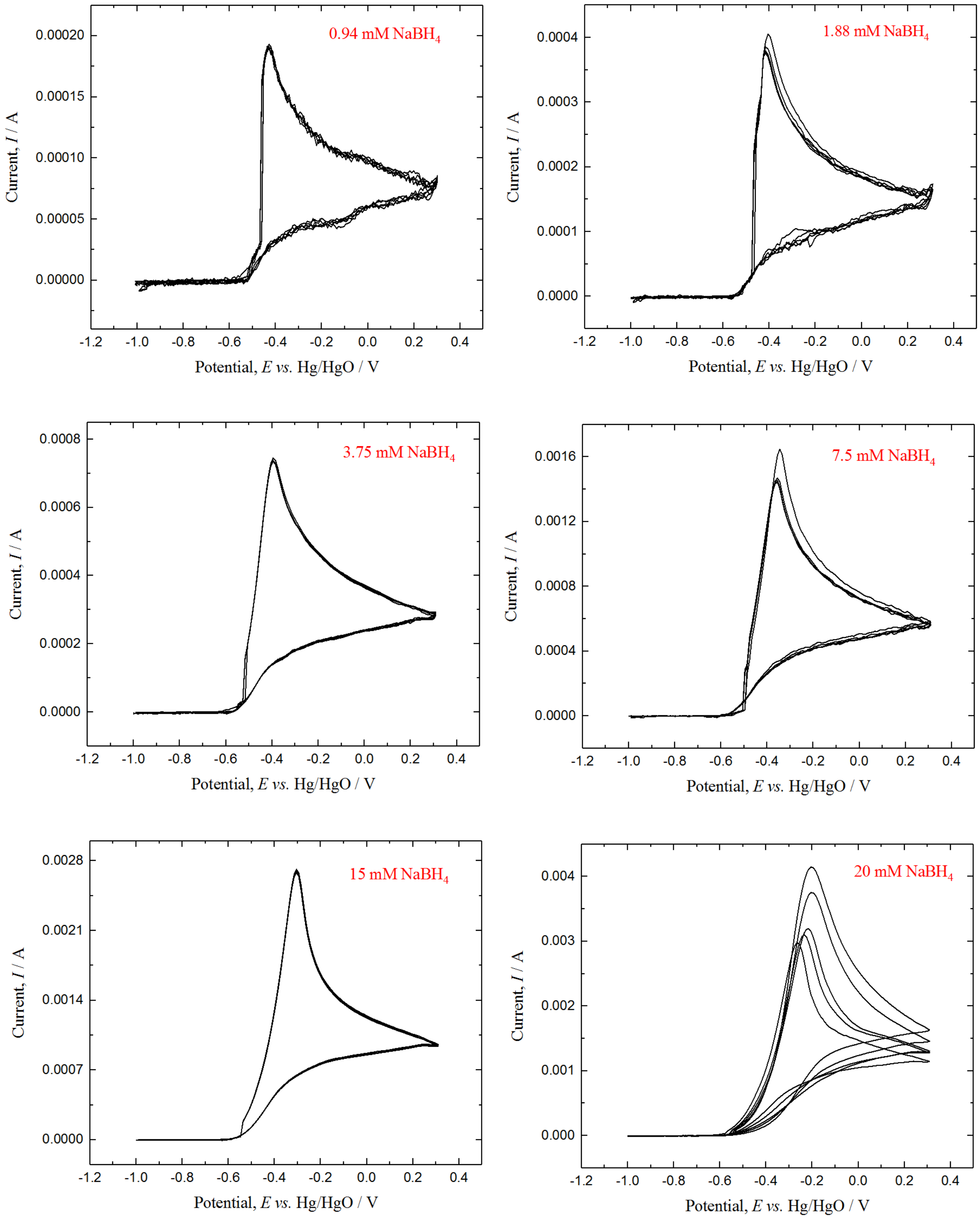

Figure 3.9. Cyclic voltammograms (5 times) for *x* mol dm^{-3} NaBH4 in 2.0 mol dm^{-3} NaOH on a gold electrode (0.125 cm^2) at a scan rate of 100 mV s^{-1} at 296 K.

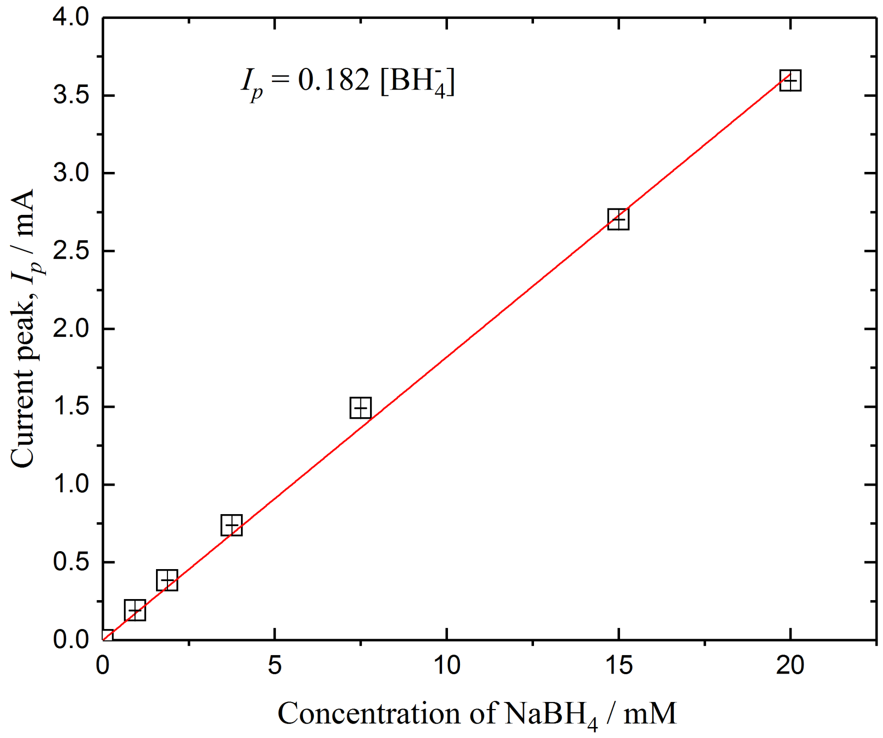

Figure 3.10. The current peak *vs.* borohydride ion concentration in 2 mol dm^{-3} NaOH using a static planar gold electrode (0.125 cm^2). The scan rate was 100 mV s^{-1}, and the scan ranged from -1.0 to 0.3 V *vs.* Hg/HgO at 296 K.

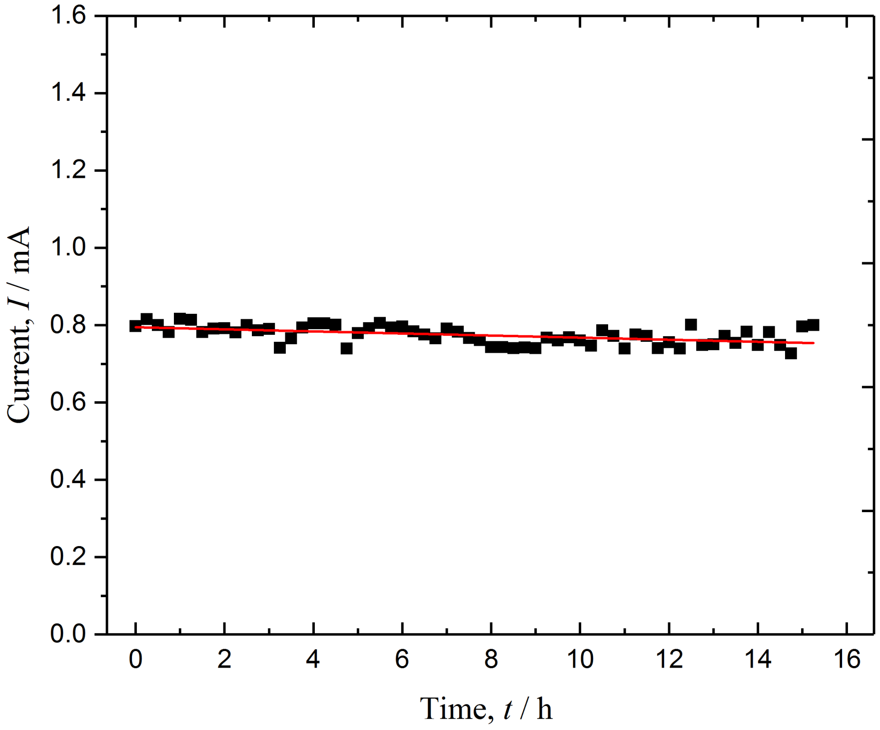

Figure 3.11. The stability of borohydride ions. These are the 62 current peaks of linear sweep voltammetry *vs.* time. The potential swept from 1 to 0.2 V *vs.* Hg/HgO at a 25 mV s^{-1} scan rate. The gold working electrode (2 mm diameter) and the graphite counter electrode were in a tank containing 1.75 dm^3 of 0.02 mol dm^{-3} $NaBH_4$ + 2 mol dm^{-3} NaOH at 23 ± 1 °C.

3.3. Conclusion

The kinetic reactions and the electrochemical behaviour of borohydride ions in the alkaline solution were investigated by applying CV and LSV experiments on gold and platinum electrodes using a typical three-electrode cell. The Pt electrode revealed three peaks (a1, a2 and a3) for the forward scan, but Au showed only two (a2 and a3). Peak a1 is attributed to the competition between BOR and HOR at low potentials on Pt because of the fully-dissociative adsorption of BH_4^- to $3H_{ads}$ and BH_{ads}, while a2 shows partial dissociation. The shoulder a3 showed a decrease in the current density due to the hydroxyl groups poisoning the metal surfaces, which in turn prevented further BOR. The increased scan rate increases the anodic peak current density (a1, a2 and a3) and shifts the peak potential towards more positive potentials for both Pt and Au electrodes, which is typical of the irreversible electrochemical process.

The diffusion coefficient was found to be $0.52 \pm 0.06 \times 10^{-5}$ cm^2 s^{-1} at 23 °C, which was close to the reported data using a different method (chronoamperometry) [146]. In this project, it was obtained from the Levich slope of the j_L *vs.* $\omega^{0.5}$ plot for a low concentration of 3.75 mmol dm^{-3} $NaBH_4$ in 6 mol NaOH.

A cyclic voltammogram was used to quantify the sodium borohydride in alkaline aqueous solutions. A gold working electrode was used, as the gold catalyst is the most suitable material for analytical determinations of borohydride because of its well-defined signal and the low level of background current in the potential region of borohydride oxidation. Further increasing the borohydride concentration might cause the current peak to fluctuate widely. The calibration curve of the peak current *vs.* the borohydride ion concentration was prepared to monitor the fuel concentration in the aqueous electrolyte. It was found that stirring a solution for about 5 s and waiting for 10 s to allow the solution to settle down for the next cycle is a good technique to overcome the decreases of the peak current with increased cycling during CV experiments for a Au electrode.

The stability of borohydride ions in an aqueous solution was studied using LSV on a gold electrode (2 mm diameter) over a 15-h test period. The result suggested that borohydride is stable in 2 mol dm^{-3} NaOH.

The Pt planar electrode presented a higher current density from BH_4^- oxidation at a much lower potential than the Au electrode. It is well-known from the experimental results that bimetallic transition metals have demonstrated higher electrocatalytic activity and selectivity than the corresponding monometallic catalysts [95]. Therefore, the next chapter aims to investigate Pt-Ir alloys in detail, as they are expected to be promising anodes for borohydride system.

Chapter 4: Platinum-Iridium Alloy Anodes for Direct Borohydride Fuel Cells

This chapter studies the electrochemical behaviour of two Pt-Ir alloys (75:25, 25:75) compositions towards the borohydride oxidation in alkaline media by means of linear sweep voltammetry and chronoamperometry using a conventional three-electrode cell. The kinetic parameters to evaluate the two electrocatalysts involved the charge transfer coefficient, the number of exchanged electrons, the standard heterogeneous rate constant, the heterogeneous rate constant, the reaction order and the mass-transport coefficient. The effects of these anodic electrocatalysts on the performance of a direct borohydride–hydrogen peroxide fuel cell was investigated as well.

4.1. Introduction

Noble metals, such as gold [49] [94] [153], enable the transfer of a large number of electrons during the oxidation of borohydride ions. However, many authors have demonstrated that the oxidation on gold is much slower than on platinum [49] [204] [51] [100] [142]. Gyenge et al. [49] have reported that the heterogeneous rate constant was about ten times larger on Pt/thiourea (1.86 cm s^{-1}) than on Au (0.14 cm s^{-1}) using chronoamperometry tests. Finkelstein et al. [51] have also observed that Pt has faster reaction kinetics (0.029 cm s^{-1}) than Au (0.012 cm s^{-1}) using RDE experiments (Koutecky´-Levich equation) but the values of the heterogeneous rate constants and activation energies were lower than those obtained by the Gyenge group for both catalysts. The performance of Pt-Ir electrocatalysts was only studied by Gyenge et al. [69] (this has been revised previously in the literature review chapter). The group used Pt-Ir metal colloids with a 50:50 composition supported on Vulcan XC72R (20 wt.% metal, 5 mg cm^{-2} catalyst loading) in a 5 cm^2 geometrical area single fuel cell. However, the Pt-Ir of 75:25 and 25:75 have not been investigated as potential electrocatalysts for direct borohydride fuel cells (DBFCs). The goal of this chapter is to study the fundamental electrochemical kinetics of the borohydride oxidation reaction on these Pt-Ir/Ti alloys by a variety of electrochemical techniques and then evaluate their performance in a single practical DBFC.

4.2. Experimental preparation

4.2.1. Electrode preparation and characterisation

All electrocatalysts included Pt and bimetallic Pt_x-Ir_x used in this chapter and the rest of the thesis were supported by titanium materials in which they were cut and spot-welded in-house and coated by a commercial supplier (Magneto Special Anodes B.V). In this study, a Ti plate (0.9 mm thick, 99.7%, Alfa Aesar) was coated with $Pt_{0.75}$-$Ir_{0.25}$ and $Pt_{0.25}$-$Ir_{0.75}$ alloys to be employed as a working electrode in both a conventional three-electrode cell and a flow cell with exposed projected areas of 1 cm^2 and 9 cm^2 (20 × 45 mm), respectively. The typical procedure used by the manufacturer is the ceramic coating method of Pt-IrO_2 which was performed for all anode electrodes using paint-stove cyclic. The Ti material was cleaned and etched, and a thin layer of the liquid precursor was applied onto the surface with a roller. After evaporation of the solvent, the layer was activated at an elevated temperature in a stove; after cooling down, this process was repeated until the required coating loading has been achieved (1 g m^{-2} per cycle). The catalyst loading was 2 mg cm^{-2} of the Pt + Ir alloy. For the counter electrode, a Pt/Ti mesh was requested from the same supplier (3 mm sheet thickness, 2 mm strand width, 12.5 mm LWD, 7.0 mm SWD); see Figure 4.1 for the geometrical standard of a mesh. A seeding layer was applied, as described above, to prepare the Pt/Ti mesh cathode (2 mg Pt cm^{-2}); after that, the Pt was applied galvanically in an aqueous, high-alkaline plating bath (as received from the manufacturer); the details of this method have been also described by Chandler et al. [205].

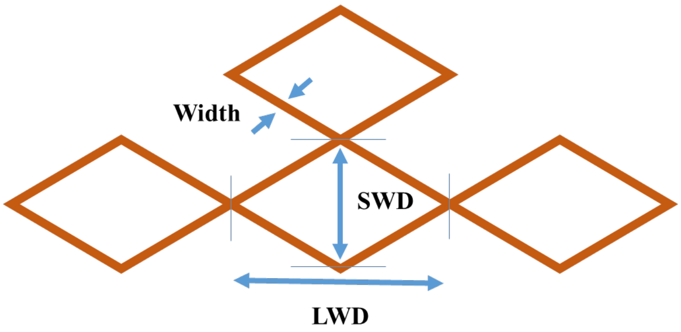

Figure 4.1. The top view of a mesh. The standard dimension abbreviations are 'long way distance between connected knots of the diamond' (LWD) and 'short way distance between connected knots of the diamond' (SWD).

The surface morphology and composition of the prepared electrocatalysts were characterised using scanning electron microscopy (SEM) and energy dispersive X-ray spectroscopy (EDS) analysis using a JSM-6500F field emission electron microscope (JEOL Inc, USA). The inductively coupled plasma-optical emission spectrometers (ICP-OES) method is widely used for inorganic chemical analysis (e.g. all metals). Therefore, the alloys' composition of Pt_x-Ir_x were also confirmed by using ICP-OES (Varian 720ES, USA). 5 g were scratched from the coated layer of one side of the 9 cm^2 electrode while the other side was kept for the electrochemical measurements. The samples then were sent to a commercial laboratory (MEDAC Ltd, UK) to be analysed. Nitric acid (69%, ARISTAR grade for trace analysis) was used to digest the metals and prepare them for the analysis.

4.2.2. Half-cell tests

The electrochemical characterisation of the two electrocatalysts, that is, the Pt-Ir/Ti plates (Pt:Ir: 75:25 and 25:75, 1 cm^2), was carried out in a typical three-electrode cell shown in Figure 4.2 using the potentiostat (Autolab, Metrohm AG, the Netherlands). The counter electrode, Pt mesh (1 cm^2 geometric area), was immersed in 6 mol dm^{-3} NaOH, and the cathode compartment was separated by the cation exchange membrane (CEM) Nafion® 115. All measured potentials in this research were *vs.* Hg/HgO (1 mol dm^{-3} KOH, Radiometer Analytical, XR440) which was used as a reference electrode. In each experimental borohydride oxidation, fresh $NaBH_4$ (99%, powder, Sigma-Aldrich) solutions were prepared immediately prior to measurements to avoid loss of BH_4^- due to its hydrolysis during solution storage. Different linear and cyclic voltammograms were performed (from -1.0 to 0.6 V *vs.* Hg/HgO) using a family of scan rates from 25 to 1000 mV s^{-1} in an electrolyte containing 0.03 mol dm^{-3} $NaBH_4$ in 2 mol dm^{-3} NaOH at 294 K (21±1 ^{o}C). In order to obtain the borohydride oxidation reaction (BOR) kinetic parameters, different concentrations of BH_4^- (0.01–0.2 mol dm^{-3}) were prepared. Short chronoamperometry experiments (0.4 seconds each) were carried out by shifting the electrode potential from the open-circuit potential (OCP) value to -0.2, 0.0 and +0.2 V *vs.* Hg/HgO. The influence of the operation temperature on borohydride oxidation was studied with a temperature range of 298–338 K (25–65 ^{o}C) using chronoamperometry tests (at +0.2 V *vs.* Hg/HgO, for 50 seconds). A thermostatic water bath was employed to control the solution temperature for all experiments.

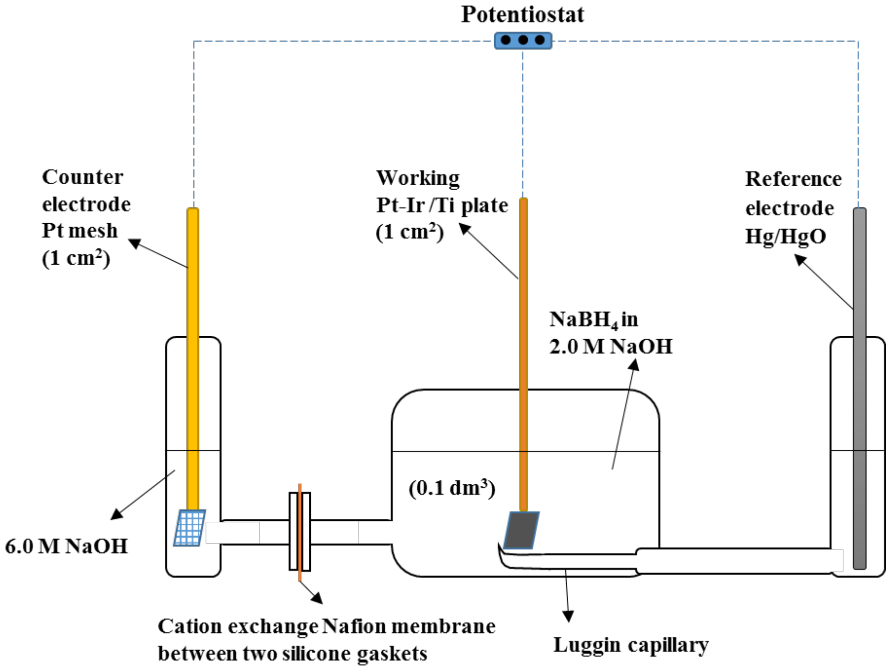

Figure 4.2. A three-electrode cell with a Pt-Ir/Ti plate as the working electrode (1 cm^2) in *x* mol dm^{-3} $NaBH_4$ + 2.0 mol dm^{-3} NaOH, Pt mesh (1 cm^2, geometrical area) as the counter electrode in 6.0 mol dm^{-3} and Hg/HgO (1.0 mol dm^{-3} KOH) as the reference electrode.

4.2.3. The preparation of a single flow cell

The electrochemical flow cell compartments shown in Figure 4.3 were designed using 3D computer-aided design (CAD, Solidworks® software) and manufactured using acrylic polymer; the cell included two endplates, two current collectors (holders) and two electrolyte channel frames. Interchangeable electrodes were used with projected areas of 9 cm^2. The cathode electrode (No. 4 in Figure 4.3) was spot-welded onto a titanium plate (No. 3) to ensure adequate electrical contact. The current collector (holder for both cathode and anode) frame (No. 2) was grooved (1 mm in depth) to maintain the level of the electrode as equivalent to the flow level into a rectangular channel (No. 5), avoiding any causes of turbulent flow. The width of the (grooved) current collector (No. 2) is 10 mm wider than the flow channel breadth (20 mm, Figure 4.3) to hold the electrode, which is stuck, between the flow frame and the current collector frame so that it will not come loose while the connector adapter (a 4 mm male-to-female connector) is screwed in, making contact with the current collector Ti plate (No. 3). The flow channel plate (5) has been designed to allow a smooth distribution of the electrolyte at the entrance to the rectangular channel. A black silicone sealant paste (158, Acc Silicones) was used to seal the current collector's Ti plate and frame. To seal the cell compartments, a silicone gasket (PAR Group Ltd, UK) 0.5 mm thick (*ca.* 0.4 mm compressed) was installed between each part. The cell was divided by a Nafion® 115 CEM (Dupont Co, USA) to separate the anode and cathode compartments. Finally, all compartments were rearranged, compressed and tightened with six M4 steel screws.

4.2.4. Experiments with the single flow cell

Chronoamperometry and cell polarisation measurements of borohydride oxidation were carried out using the setup in Figure 4.4. The hydraulic circuit of the experimental arrangement can be seen in Figure 4.5. The Autolab digital potentiostat was connected to the platinum alloy/titanium working electrode with an exposed area of 9 cm^2, while a platinised titanium (Pt/Ti) mesh was used as a counter electrode (8.55 cm^2, geometrical area). The counter electrode compartment was supported by one turbulence promoter (TP). The TP was inert polypropylene mesh (1.3 mm thickness, 8.0 mm LWD and 6.8 mm SWD) as shown in Figure 4.6. The two compartments were separated by a CEM (Nafion® 115). Polytetrafluoroethylene (PTFE) tubing (1 mm internal diameter) was fitted at the anode compartment to serve as a Luggin capillary to measure the anode potential *vs.* the reference electrode (Hg/HgO). A peristaltic pump (323S/D, Watson-Marlow) with two heads was used to recirculate and control the electrolyte flow rate into the working and counter electrode compartments. The pump was calibrated before it was used (see the calibration curve on Appendix I). The mean linear flow rates were the same in the working and counter electrode compartments. To smooth out the flow pulsation during the experiments, pressure pulse dampeners were fitted to the hydraulic circuit. A thermostatic water bath was used to control the electrolyte temperature.

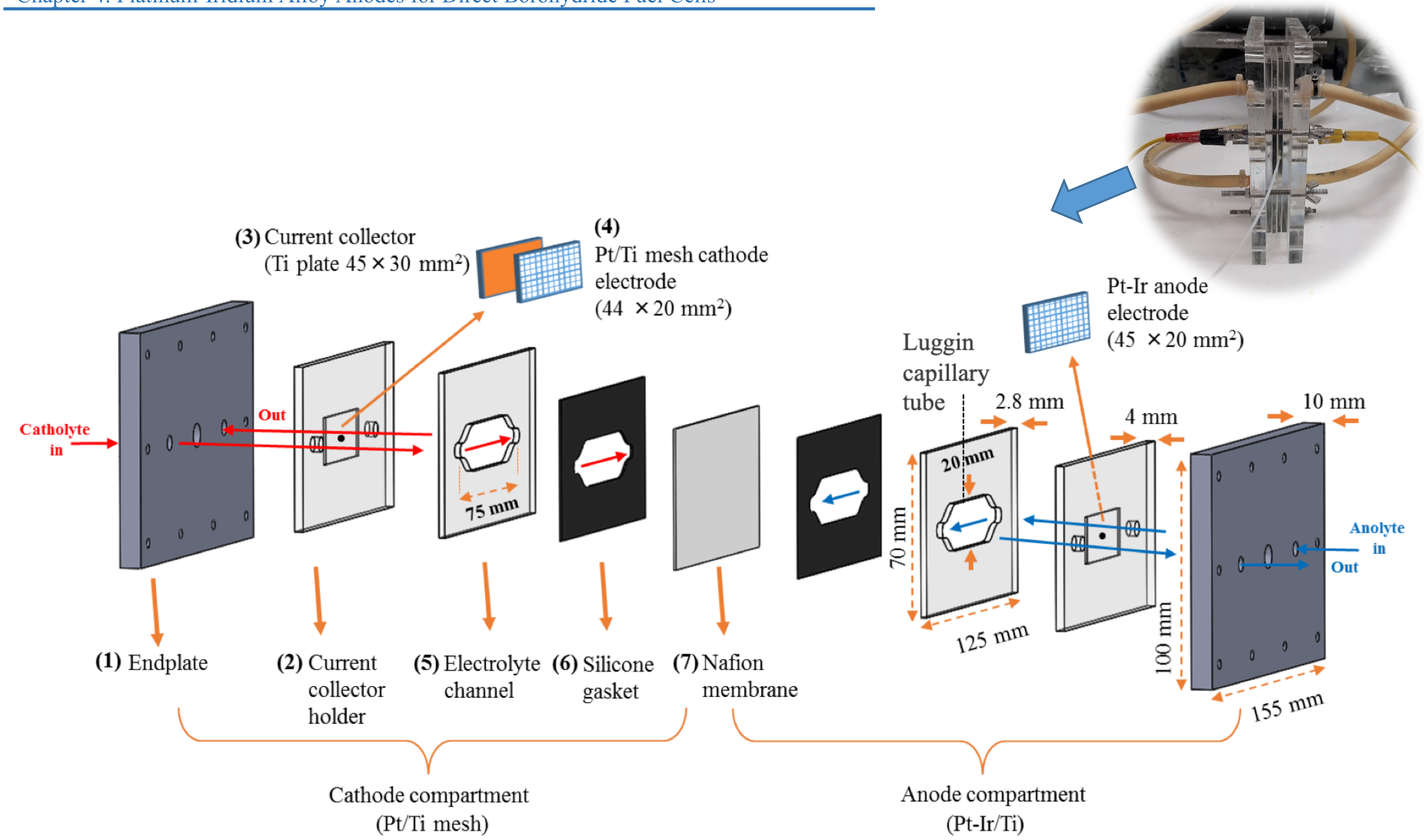

Figure 4.3. An expanded view of the designed single DBFC.

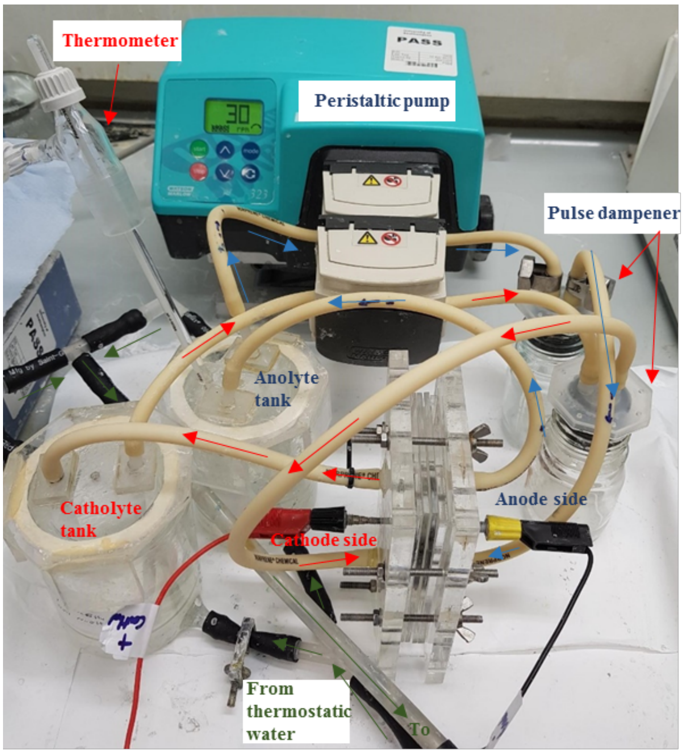

Figure 4.4. The schematic diagram of the experimental setup for the DBFC.

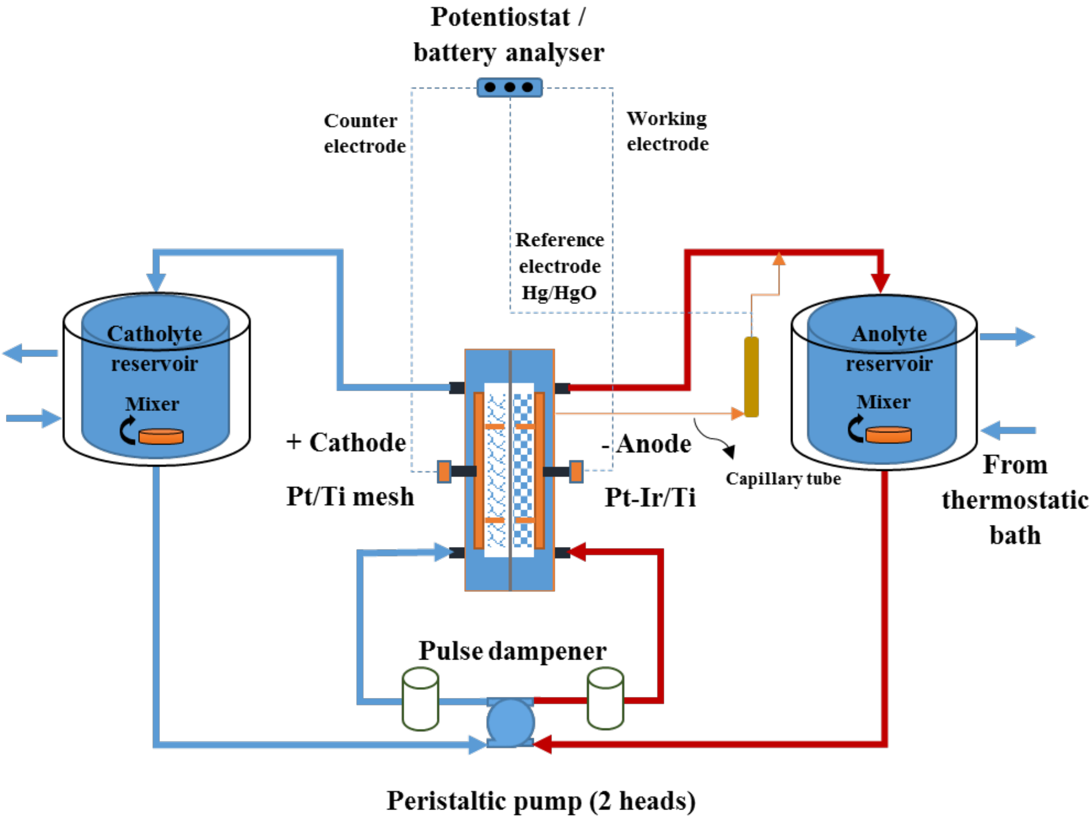

Figure 4.5. The flow diagram for the single flow cell to carry out the electrochemical measurements at the Pt-Ir anodes

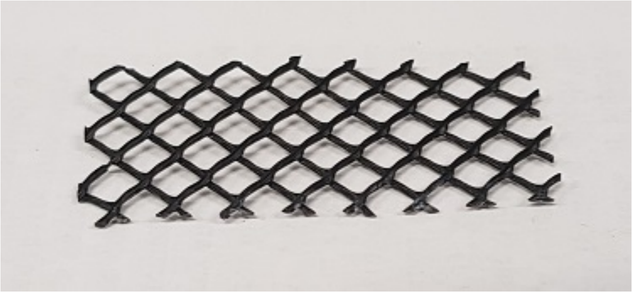

Figure 4.6. A plastic mesh turbulence promoter used in the flow cell above.

In order to study the effect of the electrolyte flow velocity, chronoamperometry was used on both Pt-Ir/Ti working electrodes (75:25, 25:75) to measure the limiting current *vs.* time (s) at linear flow velocities ranging from 1 to 10 cm s^{-1}. The electrode potential was stepped from the OCP to +0.2 V *vs*. Hg/HgO (40 seconds) in an electrolyte of 0.01 mol dm^{-3} $NaBH_4$ and 2 mol dm^{-3} NaOH (0.18 dm^3) at 298 K. The counter electrode compartment contained 2 mol dm^{-3} NaOH (0.18 dm^3). The limiting current values were obtained based on the average of ten records at 25 to 35 s. Each chronoamperometry measurement was repeated three times at each flow velocity, and the average limiting current was obtained *vs.* mean linear flow velocity.

The performance and stability of the DBFC were evaluated using a BST8-A3 battery analyser (MTI, USA) on the single flow cell shown in Figure 4.5. The cell potential and power density *vs.* current density were measured for the two Pt-Ir anode electrodes with 9 cm^2 geometric areas. The rate of applied current density was 5 mA cm^{-2} min^{-1} from 0 to 250 mA cm^{-2}. The anolyte composition was 1 mol dm^{-3} $NaBH_4$ in 4 mol dm^{-3} of NaOH (0.2 dm^3), and the corresponding catholyte was composed of 1 mol dm^{-3} H_2O_2 in 1 mol dm^{-3} HCl (0.2 dm^3). The polarisation curve was performed at 298 and 333 K (25 and 60 ^{o}C), and the mean linear fluid velocity was 3 cm s^{-1}. Using the same electrolyte compositions, the cell stability was examined for a short-term period (80 min) at a permanent current density of 25 mA cm^{-2}. The temperature was maintained at room temperature and the fluid velocity at 1 cm s^{-1}.

4.3. Results and discussion

4.3.1. Characterisation of the Pt-Ir alloys

The SEM micrographs of Pt-Ir alloys with nominal compositions of $Pt_{0.75}$-$Ir_{0.25}$ and $Pt_{0.25}$-$Ir_{0.75}$ are presented in Figure 4.7 (a, b) and (c, d), respectively. Figure 4.7a) and c) has a lower magnification (×25, 1 mm scale), than Figure 4.7b) and d) (×150, 100 μm scale). The homogeneity and rough surface can be seen in these pictures (b and d), which could be beneficial to the mass transport of the electrolyte components. The $Pt_{0.25}$-$Ir_{0.75}$ image (d) shows an agglomeration of the alloy material that may provide a larger active area than the $Pt_{0.75}$-$Ir_{0.25}$. However, more hydrogen evolution would be expected in that case.

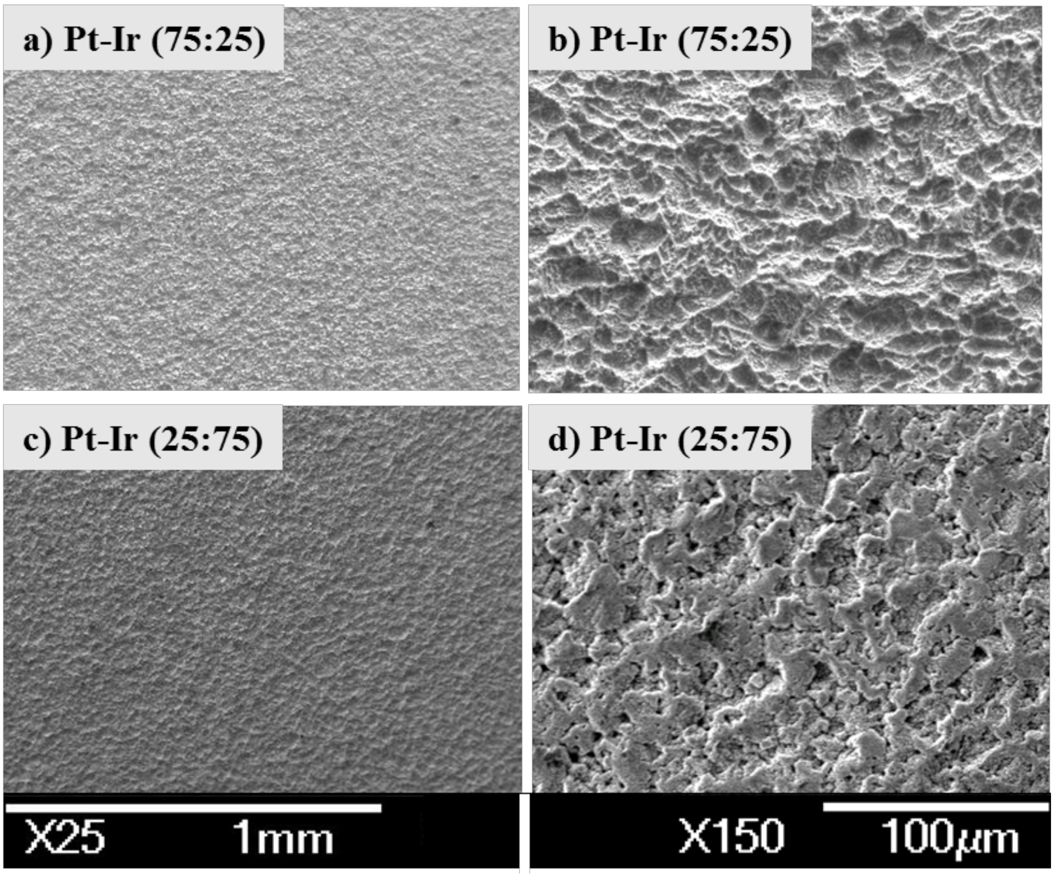

Figure 4.7. The SEM images of Pt-Ir alloys (a, b) $Pt_{0.75}$-$Ir_{0.25}$ and (c, d) $Pt_{0.25}$-$Ir_{0.75}$ deposited on Ti plate.

Elemental analysis was carried out using EDS, showing the average phase of Pt:Ir to have an atomic ratio of 76:24 and 16:84 for $Pt_{0.75}$-$Ir_{0.25}$ and $Pt_{0.25}$-$Ir_{0.75}$, respectively. It can be seen that the average ratios of these alloys are slightly different (1.3% for $Pt_{0.75}$-$Ir_{0.25}$)

especially with $Pt_{0.25}$-$Ir_{0.75}$ (12%) than the nominal values. For the rest of this thesis, $Pt_{0.75}$-$Ir_{0.25}$ and $Pt_{0.25}$-$Ir_{0.75}$ electrodes would represent the atomic compositions that were obtained from the EDS analysis, which were calculated from nine random quantitative measurements of different spots on each electrode, see Appendix II. The standard deviation of the EDS composition values of the nine spots was less than one, indicating good homogeneity of the coated materials.

Figure 4.8a) and b) show the Pt and Ir EDS maps, respectively, in the prepared alloys, are evenly distributed throughout. The colour density of the Ir (red dots) clearly reflects its composition, unlike the Pt (yellow dots).

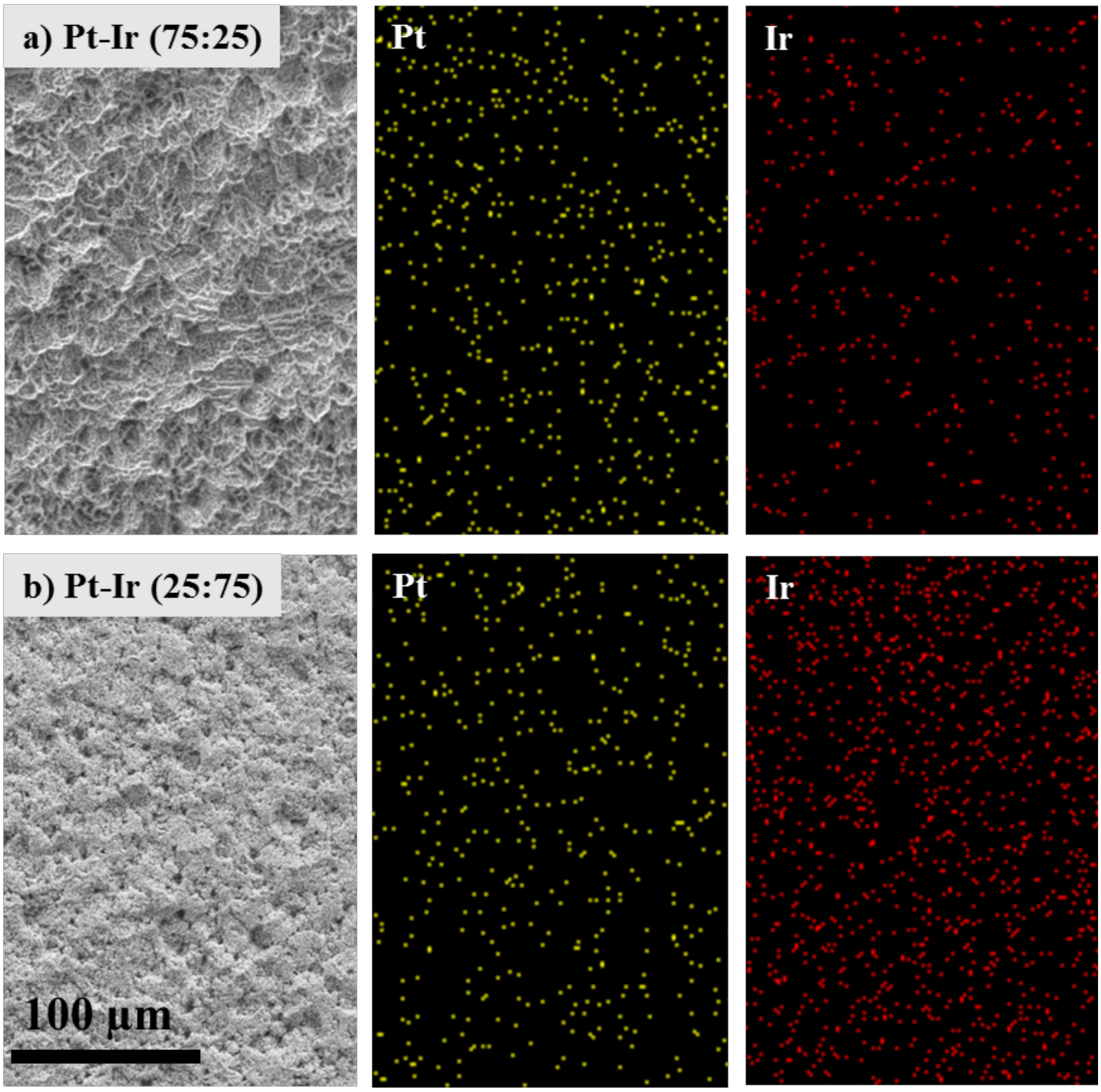

Figure 4.8. The EDS map of the two anode electrodes: $Pt_{0.75}$-$Ir_{0.25}$/Ti and $Pt_{0.25}$-$Ir_{0.75}$/Ti.

The variety of Pt presence in the two spots of 75:25 and 25:75 electrodes was confirmed by calculating the percentage of the area of platinum (the yellow dots, Figure 4.8, Pt) in each image using image-processing and analysis software (ImageJ, National Institutes of Health, USA). The results showed that (Pt) approximately covered 5.3% [in Figure 4.8a), Pt] and 2.5% [Figure 4.8b), Pt] for $Pt_{0.75}$-$Ir_{0.25}$ and $Pt_{0.25}$-$Ir_{0.75}$, respectively, which indicated that the amount of Pt distributed on $Pt_{0.75}$-$Ir_{0.25}$ surface for this spot is more than twice of that on $Pt_{0.25}$-$Ir_{0.75}$. As EDS analysis might be affected by the surface texture because the beams will be reflected in different angles if the surface is not smooth. That could result in different compositions for the measured elements. Therefore, each sample was analysed four times, from 0^o, 90^o, 180^o and 270^o at the same spot. The Pt:Ir compositions were obtained and the standard deviation of Pt:Ir compositions turned out to be negligible (about 0.3%), meaning the element compositions that were determined using the EDS method can be considered for Pt-Ir alloys (see Appendix III for the raw data). Newbury and Ritchie [206] answered the following question: 'Is scanning electron microscopy/energy dispersive X-ray spectrometry (SEM/EDS) quantitative?' They reported that SEM/EDS analysis results could match the electron-excited wavelength dispersive spectrometry output except for H, He and Li (with low atomic numbers).

Nevertheless, for Pt_x-Ir_x compositions in this project, the wavelength dispersive spectrometry method was carried out using inductively coupled plasma-optical emission spectrometers (ICP-OES, Varian 720ES, USA), and different digestion methods for the materials were applied. However, some material remained undigested, which is presumably Ir, as it is notoriously difficult to digest. The results of this method were not close to the EDS results. The alloy compositions obtained using ICP-OES were 86:14 and 28:72 for $Pt_{0.75}$-$Ir_{0.25}$ and $Pt_{0.25}$-$Ir_{0.75}$, respectively; as the reader may notice, the Ir composition is always less than the expected percentage, possibly due to the remaining amount of undigested Ir metal.

4.3.2. Oxidation of borohydride ions at Pt-Ir alloy electrodes

Figure 4.9a) and b) show a family of linear voltammetry at different scan rates (25–1000 mV s^{-1}) of borohydride oxidation on $Pt_{0.75}$-$Ir_{0.25}$ and $Pt_{0.25}$-$Ir_{0.75}$, respectively. The background current densities – the orange curves – of Pt_x-Ir_x/Ti electrodes were apparently very low; for that reason, they have been ignored in this project. The two anodes showed similar behaviour, exhibiting four oxidation peaks a1, a2, a3 and a4 at an approximately equivalent potential range.

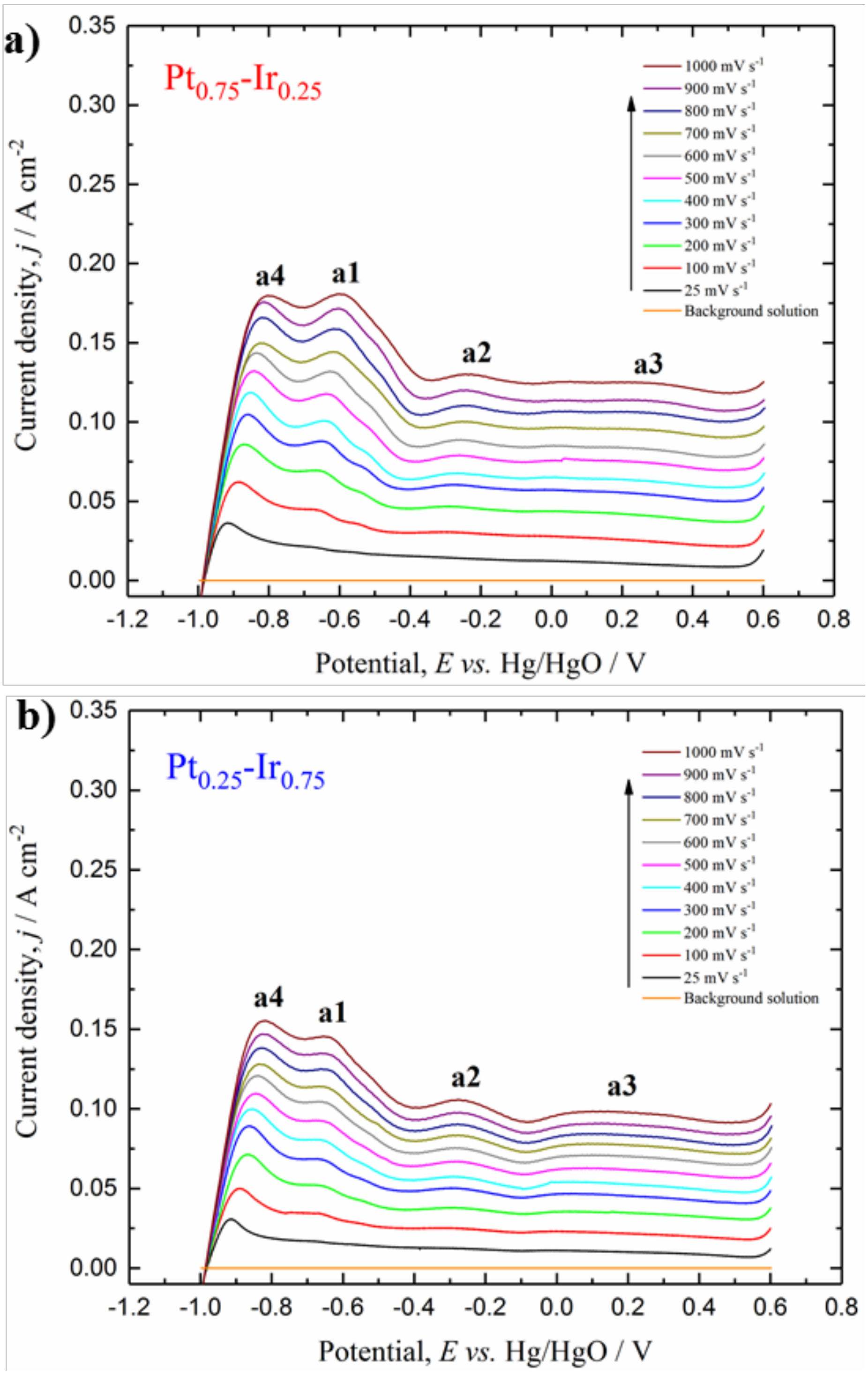

Figure 4.9. The linear voltammograms of BH_4^- oxidation on Pt-Ir alloy catalysts deposited on Ti plate (1 cm^2) using the three-electrode cell at 294 K (21 ± 1 °C). The inset legend indicates different scan rates using 0.03 mol dm^3 $NaBH_4$ + 2 mol dm^3 NaOH.

At OCP the hydrogen bubbles evolving from the surface of the catalyst was clearly observed as a result of heterogeneous hydrolysis of BH_4^-; even with the presence of concentrated NaOH. Jusys and Behm [70] reported that, at OCP conditions for the Pt electrode, a mixed potential would be formed from a competition between the partial BOR and water reduction (HER) that occur simultaneously and release hydrogen. As the hydrolysis of borohydride [Eq. (2.2) + (2.3)] and the direct oxidation reaction expected to occur simultaneously in the presence of Pt, the two waves a1 and a4 emerged around -0.65 V and -0.90 V *vs.* Hg/HgO on Pt-Ir alloy catalysts, respectively. The peak a1 due to the electro-oxidation of the intermediate product, $BH_3(OH)^-$ [Eq. (3.3)], while a4 due to the hydrogen oxidation [Eq. (2.4)] [69 49 119]. The small shoulder a2 was located in the range between -0.4 and -0.1 V where the direct electro-oxidation of borohydride is expected [69]. This a2 peak was near Gyenge et al.'s [69] findings for $Pt_{0.5}$-$Ir_{0.5}$ [the range between -0.4 and 0.0 *vs.* Hg/HgO (2 mol dm^{-3} NaOH)]. It is also likely that the intermediate product [$BH_3(OH)^-$], undergoes further electro-oxidation [Eq. (3.3)] and/or hydrolysis at wave a3 [Eq. (2.3)] [49]. The mechanism of borohydride oxidation is still under discussion; moreover, the BH_4^- oxidation on Pt_x-Ir_x needs further investigation. However, Olu et al. [59] recently proposed different reaction pathways, that depend on borohydride concentration and the onset potential on both Pt and Au (seen in Figure 2.3 and discussed in Chapter 2). For the Pt-Ir CVs shown on Figure 4.9 at low potentials < -0.4 V, a fully-dissociative adsorption of BH_4^- into BH_{ads} to release $3H_{ads} + e^-$ likely occurred (the 4-5e^- process), while the partially-dissociative pathway is suggested (BH_4^- electro-oxidises to $BH_{3,ads}$ intermediate) at higher potentials. The Pt_x-Ir_x catalysts appear very active towards the HOR (peak a1 and a4) due to the fully-dissociative adsorption of BH_4^-, which would definitely cause a reduction in the coulombic efficiency of the electrodes. Pt is well known for its activity towards water reduction at potentials below the hydrogen reversible potential causing HER of water and producing a huge current, meaning that there would be a small chance for the BOR at these potentials. Consequently, the DBFC with Pt alloys should be run at higher potentials.

With increasing scan rates, the peak potentials shifted slightly towards more positive values in all alloys, as the BOR involves the slow, irreversible electron transfer process [88]. The produced current densities with Pt_x-Ir_x/Ti were superior; for example at a 100 mV s^{-1} scan rate, the current densities (mA cm^{-2}) of 30.7 (75:25) and 25.3 (25:75) [at a2: -0.31 V *vs.* Hg/HgO (1.0 mol dm^{-3} KOH)] were observed. Even though Gyenge et al. [69]

examined Pt-Ir (50:50, 20 wt.% metal load) colloidal catalysts at a higher temperature (298 K), the current density was only 10 mA cm^{-2} for 100 mV s^{-1} [peak a2: -0.28 V *vs.* Hg/HgO (2 mol dm^{-3} NaOH)]. This value was lower by far than those obtained by Pt_x-Ir_x/Ti in this study, although the hydrogen evolution was higher on both Pt_x-Ir_x/Ti anodes (see a4 in Figure 4.9) due to the higher activity of Pt and Ir towards the hydrolysis of borohydride. The current density of $Pt_{0.75}$-$Ir_{0.25}$ always surpassed the current density observed for $Pt_{0.25}$-$Ir_{0.75}$ at any scan rate, but the latter presented slightly more negative potentials at high scan rates. It indicates that the electrode with more Ir content favours the borohydride oxidation at lower potentials in good agreement with [66]. For example, the peak current densities (at 200 mV s^{-1} and peak a2) were 47 (-0.30 V) and 38 (-0.30 V) mA cm^{-2} for $Pt_{0.75}$-$Ir_{0.25}$ and $Pt_{0.25}$-$Ir_{0.75}$, respectively, while 130 (-0.23 V) and 106 (-0.28 V) mA cm^{-2} were recorded at 1000 mV s^{-1}.

Figure 4.10 illustrates the oxidation performance of BH_4^- by using a potential linear sweep of 100 mV s^{-1} using $Pt_{0.75}$-$Ir_{0.25}$/Ti (1 cm^2) and Au (0.125 cm^2) electrodes. The $Pt_{0.75}$-$Ir_{0.25}$ electrode presented 25% less peak current density (31 mA cm^{-2}) than the maximum current density obtained from the Au electrode (41 mA cm^{-2}) at the peak potential (a2: -0.13 V *vs.* Hg/HgO). Nevertheless, in the expected region of direct BH_4^- oxidation (-0.42 to +0.50 V *vs.* Hg/HgO), the area under the I-V curve of the $Pt_{0.75}$-$Ir_{0.25}$ catalyst was approximately 35% higher (28 mA cm^{-2} V) than the area obtained from the Au electrode (21 mA cm^{-2} V) under the same potential range. Moreover, the Pt-Ir catalyst could oxidise BH_4^- at lower potential in contrast to Au, indicating that $Pt_{0.75}$-$Ir_{0.25}$ is a far better material for borohydride oxidation. A similar observation has been reported for platinum, palladium, and nickel [195] [62]. However, the hydrogen oxidation peak was not presented in the case of the Au electrode as it is relatively inactive towards H_2 oxidation, unlike the $Pt_{0.75}$-$Ir_{0.25}$ electrode; Figure 4.10 shows a hydrogen oxidation peak (a4) at -0.85 V *vs.* Hg/HgO. This issue can be resolved by using additives that can suppress borohydride hydrolysis. The potential window at which the borohydride oxidation occurs, as well as the peaks, could be different in each electrode. It would be useful to confirm the performance of these catalysts by evaluating the cell power output of these electrodes using, for example, a single DBFC.

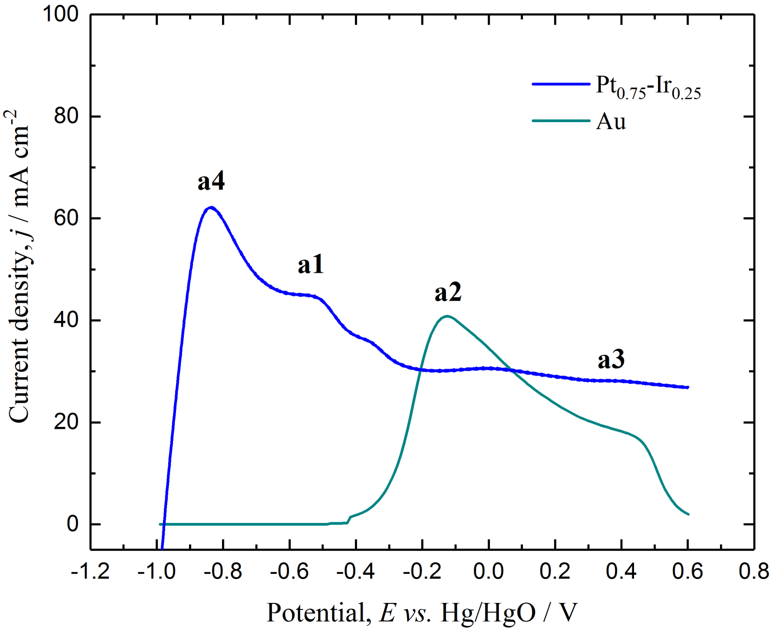

Figure 4.10. The potential linear sweeps of 0.03 mol dm^{-3} $NaBH_4$ in 2.0 mol dm^{-3} NaOH on Pt-Ir and Au disk electrodes at a 100 mV s^{-1} scan rate at 294 K.

4.3.3. The charge transfer coefficient

As suggested before in this chapter, the current density of the peak a2, *j*, between -0.4 and -0.1 V *vs.* Hg/HgO was attributed to the direct oxidation of borohydride ions to release 8 electrons [49]. That potential window was claimed an interesting domain for DBFCs [69], but this is too high for the reaction. Figure 4.9 shows that the increasing scan rate, υ, in the two anodes leads to a marked shift of the oxidation peak potential, E_p, of the peak a2, which is accompanied by a rise of the current density with no significant change of the curve shape, typical of an irreversible process [207]. Bard and Faulkner [208] reported that Eq (4.1) could be applied for the *z*-electron transfer of an irreversible heterogeneous process when the rate-determining first step involves one-electron transfer [i.e. a pure electrochemical (E) step [209]], which is more likely in the borohydride oxidation systems, as considered by many studies [88 119 207 210]. In this case, the following equation can be used to analyse the dependence of the electrode peak potential, E_p (V), on the potential scan rate, υ (V s^{-1}) [208]:

$$E_p = E^o + \frac{RT}{(1\text{-}\alpha)n_a F}\left[0.78 + ln\left(\frac{D_{BH_4^-}^{1/2}}{k_s}\right) + ln\left(\frac{(1\text{-}\alpha)n_a F\upsilon}{RT}\right)^{1/2}\right] \quad (4.1)$$

Where E^o is the formal potential (-1.24 V *vs.* SHE), R is the universal gas constant (8.314 J K^{-1} mol^{-1}), T is the temperature (K), F is Faraday's constant (96485 C mol^{-1}), α is the charge transfer coefficient (ranging from 0 to 1), n_a is the number of electrons involved in the rate-determining step (the most likely value being 1) [49 119 207 150], D is the diffusion coefficient of BH_4^- (cm^2 s^{-1}), and k_s is the standard heterogeneous rate constant (cm s^{-1}). Rearranging Eq (4.1) results in the following linear equation:

$$E_p = E^o + \frac{RT}{(1\text{-}\alpha)n_aF}\left[0.78 + \ln\left(\frac{D_{BH_4^-}^{1/2}}{k_s}\right) + 0.5\ln\left(\frac{(1\text{-}\alpha)n_aF}{RT}\right)\right] + \frac{RT}{2(1\text{-}\alpha)n_aF}\ln \upsilon \tag{4.2}$$

Where the charge transfer coefficient, α, can be calculated from the slope of E_p *vs.* $\ln(\upsilon)$ for the peak a2 (Figure 4.11):

$$The\ slope = \frac{RT}{2(1\text{-}\alpha)n_aF} \tag{4.3}$$

The values of α were 0.59 and 0.42 for the BH_4^- oxidation process on the catalysts of $Pt_{0.75}$-$Ir_{0.25}$ and $Pt_{0.25}$-$Ir_{0.75}$, respectively. In most electrochemical systems, α lies between 0.3 and 0.7 [208]. Its value being higher than 0.5 in the case of $Pt_{0.75}$-$Ir_{0.25}$ implies that the system is irreversible, suggesting a low energy barrier to the oxidation process that requires less overpotential to generate a more substantial current [208 144 82]. The α value (0.42) of the $Pt_{0.25}$-$Ir_{0.75}$ electrode suggested that its oxidation reaction is somewhat less favoured and required additional energy for the anodic oxidation [82] than $Pt_{0.75}$-$Ir_{0.25}$. The average transfer coefficient values obtained here agree with Gyenge [49] and with Finkelstein et al.'s [51] findings that the α value was 0.55 with a Pt ring-disk electrode (3 mm diameter, 5 mmol dm^{-3} $NaBH_4$ in 1 mol dm^{-3} NaOH, 298 K). Gyenge found that the α value was equal to 0.67 for the BH_4^- electro-oxidation on the Pt disk electrode (1 mm diameter) in the presence of thiourea (TU) (1.5×10^{-3} mol dm^{-3}) in 0.03 mol dm^{-3} $NaBH_4$ in 2 mol dm^{-3} NaOH at 295 K.

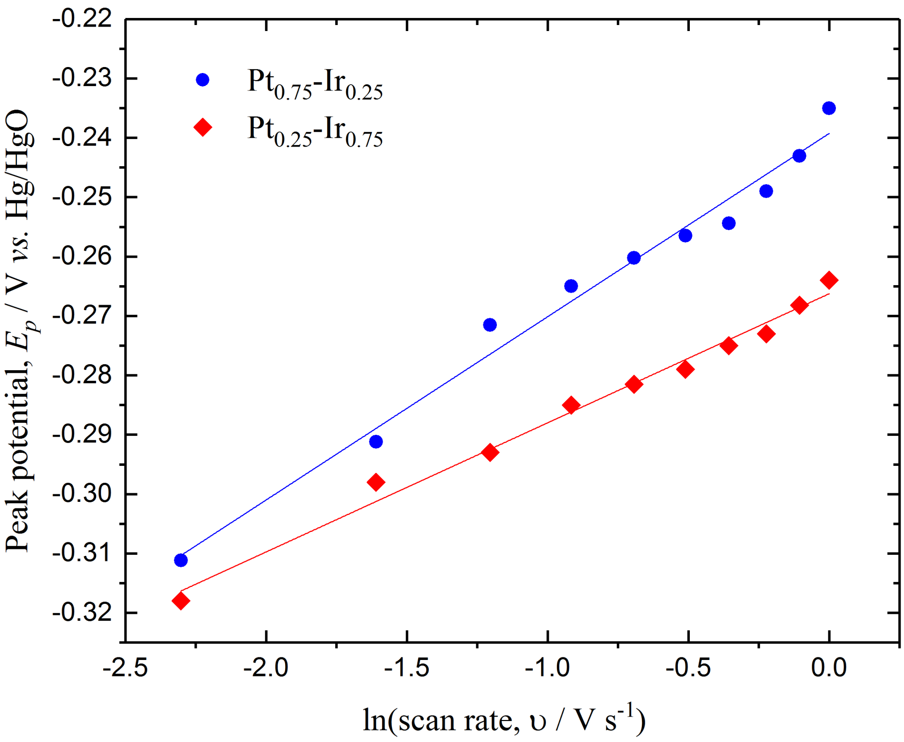

Figure 4.11. The peak potentials *vs.* ln [scan rate, υ] using Eq (4.1) of Pt_x-Ir_x/Ti electrodes (1 cm^2) in 0.03 mol dm^{-3} $NaBH_4$ + 2 mol dm^{-3} NaOH recorded at 294 K for peak a2.

Santos et al. [207] obtained α values of 0.75, 0.76, 0.78 and 0.81 for Pt, Pt-Ho, Pt-Sm and Pt-Ce (all alloys ratios around 1:1), respectively. They used a similar electrolyte composition (0.03 mol dm^{-3} $NaBH_4$ in 2 mol dm^{-3} NaOH), but the temperature was different (298 K). Sljukic et al. [119] found that α values can be affected, not only by anode materials, but also by the electrolyte concentration and the operating temperature. Similar observations have been published [63 211]. For example, α values fell from 0.87 to 0.68 for $Pt_{0.75}$-$Co_{0.25}$/C and from 0.93 to 0.80 for $Pt_{0.75}$-$Ni_{0.25}$/C when the temperature increased from 298 to 338 K [119]. With concentrations of borohydride of 0.01, 0.03 and 0.06 mol dm^{-3}, the α values (at 298 K) were 0.83, 0.91 and 0.77, respectively [119]. The α values in the present work were close to Gyenge's [49] results and within the range of most electrochemical systems (0.3–0.7) [208]. However, they were lower than those of Santos et al. [207] and Sljukic et al. [119], possibly because of different electrode materials (Pt_x-Ir_x supported on Ti plate) and operating temperatures.

4.3.4. Number of exchanged electrons

Figuring out the total number of electrons exchanged, *z*, is an essential aspect of the borohydride oxidation process. Figure 4.12 shows the observed increase of peak a2 current density, j_p (A cm^{-2}), with the square root of the scan rate, $\upsilon^{0.5}$ (V s^{-1})$^{0.5}$, for Pt_x-Ir_x/Ti electrodes. The variation of j_p with respect to υ can be described by the following modified Randles-Sevcik equation for irreversible processes [208] [144]:

$$j_p = 2.99\times10^5[(1-\alpha)\,n_a]^{1/2}zcD^{1/2}\upsilon^{1/2} \tag{4.4}$$

Where *z* is the total number of exchanged electrons during BH_4^- oxidation, *c* is the bulk concentration of BH_4^- (mol cm^{-3}), and *D* is the diffusion coefficient (cm^2 s^{-1}) of borohydride ion towards the anode surface. As explained previously (Chapter 3), the diffusion coefficient value falls as the NaOH concentration rises (since a highly viscous solution reduces the borohydride mobility [138] [18]), as seen in Figure 3.7. In 2005, Wang et al. [146] [159] published an expression that could be used to evaluate *D*, which describes its temperature dependence based on the well-known Stokes-Einstein relation [$D = f(T)$] (requires the solution viscosity) using a gold electrode in 2 mol dm^{-3} NaOH solution (the concentration used in this work). The authors found that changing the temperature from 293 to 333 K (20-60 °C) can present good linearity of *D* corresponding to *T*:

$$D = 5.57\times10^{-3}e^{\frac{-15.2\times10^3}{RT}} \tag{4.5}$$

For the present work, using Eq. (4.5), the calculated *D* value was 1.12 × 10^{-5} cm^2 s^{-1} at 294 K. The total number of electrons exchanged on Pt_x-Ir_x/Ti anodes for borohydride electro-oxidation can be determined from the slope of the linear fitting of j_p *vs.* $\upsilon^{0.5}$ using Eq. (4.4), as shown in Figure 4.12. The calculated values of *z* were 7.5 and 5.2 electrons for $Pt_{0.75}$-$Ir_{0.25}$ and $Pt_{0.25}$-$Ir_{0.75}$, respectively. However, Chatenet et al. [198] indicated in 2009 that the diffusion coefficients should be *ca.* twice as large as those generally reported in the literature, as some of their techniques (such as Levich) have led to *z* value above 8e$^-$ which is not accepted from a thermodynamic point of view. The authors [198] used a transit-time technique of rotating ring-disk Au electrode, which does not need *z* value or BH_4^- concentration unlike the Levich equation, as seen in Eq. (3.6). Thus, the calculated value of D was multiplied by 2 ($D = 2.23 \times 10^{-5}$ cm^2 s^{-1}), and, in this case, z values became more reasonable: 5.3 and 3.7 of $Pt_{0.75}$-$Ir_{0.25}$ and $Pt_{0.25}$-$Ir_{0.75}$, respectively. Table 4.1 summarises these values.

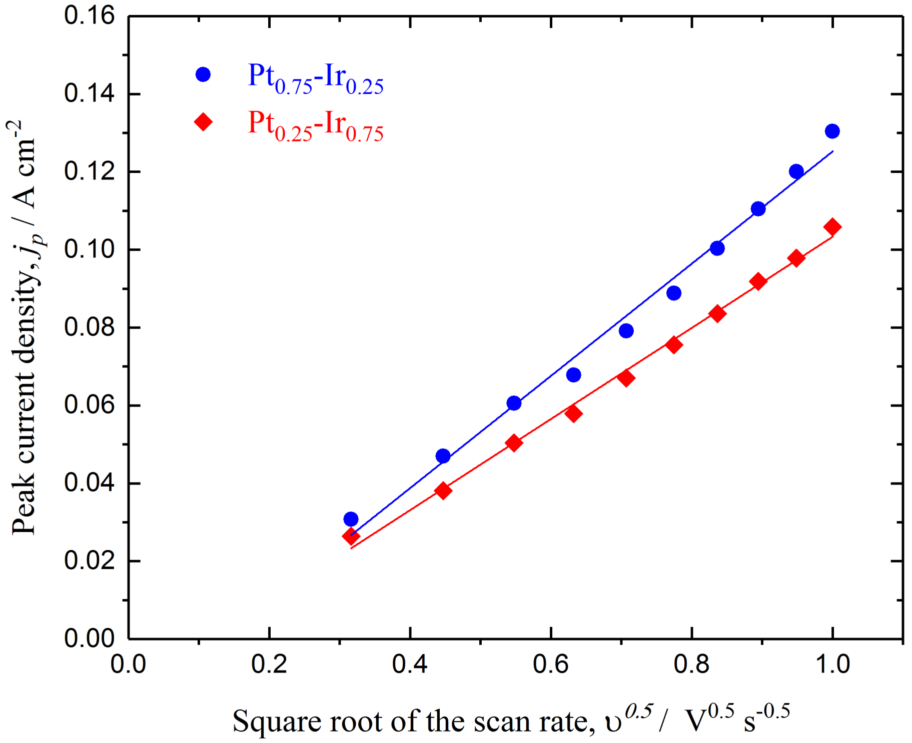

Figure 4.12. The current density peak (peak a2 from Figure 4.9) *vs.* the square root of the scan rate with a Pt_x-Ir_x/Ti plate in 0.03 mol dm^{-3} $NaBH_4$ + 2 mol dm^{-3} NaOH recorded at 294 K.

Table 4.1. The total number of electrons exchanged, z, using different parameters. The solution contained 0.03 mol dm^{-3} + 2 mol dm^{-3} NaOH, at 294 K:

Pt_x-Ir_x/Ti	$D_{BH_4^-}$, cm^2 s^{-1} 1.12×10^{-5}	$D_{BH_4^-}$, cm^2 s^{-1} 2.23×10^{-5}
75:25	7.5	5.3
25:75	5.2	3.7

To the best of the author's knowledge, Pt_x-Ir_x/Ti figures have not yet been reported in the literature. Elder and Hickling [52] (in 1962) and others [39] have reported that the number of electrons exchanged on a Pt electrode is between 2 and 4, which agrees well with many recent studies of the BOR on Pt electrodes, namely, that up to 4 electrons are liberated [49] [62] [45]. It was also found that $z = 4$ [69] [49] and $z = 2.5$ [207] for the Pt catalyst using the same experimental setup as the present work. It can be concluded that, in the present work, $Pt_{0.75}$-$Ir_{0.25}$ alloy shows good coulombic efficiency for the BOR compared to monometallic Pt.

Sljukic et al. [119] found that *z* could decrease when the borohydride concentration [61] and the temperature of the solutions increases. For example, they evaluated the oxidation of BH_4^- on $Pt_{0.75}Co_{0.25}/C$ in 0.03 and 0.06 mol dm^{-3} $NaBH_4$ and found that the number of electron interchanged was 3.4 e^- and 1.8 e^-, respectively. They also studied the effects of various temperatures on the number of exchanged electrons in the electro-oxidation process, and they concluded that increasing the temperature would decrease the *z* value. For example, when the temperature increased for experiments using $Pt_{0.75}Co_{0.25}/C$ electrode from 25 to 65 ^{o}C, the *z* values fell from 4.5 to 1.7. The reduction in *z* at elevated temperatures might be linked to the hydrolysis of borohydride, which can be observed in the formation of gas bubbles in electrolytes at higher concentrations and temperatures [119]. Another effect on the number of electrons is the concentration of the supporting electrolyte, for example, increasing the NaOH concentration can suppress the hydrolysis, resulting in a greater number of exchanged electrons. Molina and Chatenet [33], for instance, found that the *z* value when using a Pt electrode increased from 2.9 to 5.5 when NaOH concentration was changed from 0.1 to 1 mol dm^{-3} in 0.01 $NaBH_4$ at 298 K.

4.3.5. The standard heterogeneous rate constant

It is possible to evaluate the standard heterogeneous rate constant, k_s (cm s^{-1}), of the BOR at Pt_x-Ir_x/Ti anodes by using the data obtained from the LSVs, as seen in Figure 4.9. For irreversible systems, the peak potential is typically shifting (for an oxidation) towards a positive potential with the scan rate [208]. Therefore, the following expression has been driven by Bard and Faulkner [208] to describe the relationship between the peak current density, j_p (A cm^{-2}), and the peak potential, E_p (V), for an electrochemical system:

$$j_p = 0.227zFck_s \exp\left\{\left(\frac{(1-\alpha)n_aF}{RT}\right)\left(E_p - E^o\right)\right\} \tag{4.6}$$

By rearranging Eq. (4.6), the following linear equation can be obtained:

$$\ln j_p = \ln(0.227zFck_s) + \frac{(1\text{-}\alpha)n_aF}{RT}\left(E_p\text{-}\ E^o\right) \tag{4.7}$$

The interception of ln j_p *vs.* (E_p - E^o) was used to determine the value of k_s for each electrode using the data shown in Figure 4.13. Many studies have used this method [209] [88] [82] to determine k_s values as it is applicable for borohydride electro-oxidation process. The obtained values of k_s for the BH_4^- oxidation on the two catalysts were 0.1×10^{-10} and 5×10^{-15} cm s^{-1} for $Pt_{0.75}$-$Ir_{0.25}$ and $Pt_{0.25}$-$Ir_{0.75}$, respectively. This result indicates that the oxidation reaction is faster by far on $Pt_{0.75}$-$Ir_{0.25}$ than on $Pt_{0.25}$-$Ir_{0.75}$ catalysts, which has the slowest rate. Ponce de León et al. [88] reported the same order of magnitude for k_s (9×10^{-10} cm s^{-1}) for a Ag porous sponge material using a similar approach to determine k_s. The values of k_s here indicate that the borohydride oxidation process is a sluggish system, likely due to its multistep electron reaction mechanisms and the complexity of the reactions, unlike simple electron-transfer processes in the range of 1 to 10 cm s^{-1} [208]. Bard and Faulkner [208] mentioned that the values of k_s with lower than 10^{-9} cm s^{-1} for different kinds of electrochemical systems have been found by many studies [212] [213] [214] [215]. Santos et al. [207], nevertheless, evaluated Pt, Pt-Ce, Pt-Sm and Pt-Ho (Holmium, atomic number 67) and discovered average k_s values of 2.6×10^{-7}, 1.2×10^{-7}, 2.2×10^{-6} and 1.2×10^{-5} cm s^{-1}, respectively, meaning that the Pt-Ho alloy showed relatively higher oxidation kinetics than the Pt-Ce alloy.

The k_s values were higher in order of magnitude compared to the current results; which could be related to the materials nature and the method of calculations. The authors extracted k_s values from (a different method) chronopotentiogram measurements (13 mA cm^{-2}) by using the same concentrations used here but at a higher temperature of 298 K. In theory and it is an empirical fact that, in most electrode materials, the k_s values increase with elevated electrolyte temperature, as can be seen from the well-known Arrhenius Eq. (4.8), where Z is a constant known as the frequency factor and E^o_{ac} (kJ mol^{-1}) is the standard activation energy (energy barrier) for charge transfer [208].

$$k_s = Z\ exp\left(-\frac{E^o_{ac}}{RT}\right) \tag{4.8}$$

Therefore, a further study was carried out by Sljukic et al. [119] revealed that elevating the solution temperature from 298 to 338 K (25–65 °C) increases k_s values from 6.8×10^{-4} to 3.62×10^{-3} cm s^{-1} for Pt/C, from 1.2×10^{-5} to 1.1×10^{-2} cm s^{-1} for $Pt_{0.75}Ni_{0.25}$/C, and from 2.1×10^{-5} to 4.6×10^{-2} cm s^{-1} for $Pt_{0.75}Co_{0.25}$/C electrodes, which are similar conclusions as another study that used a gold electrode (25–65 °C) [216].

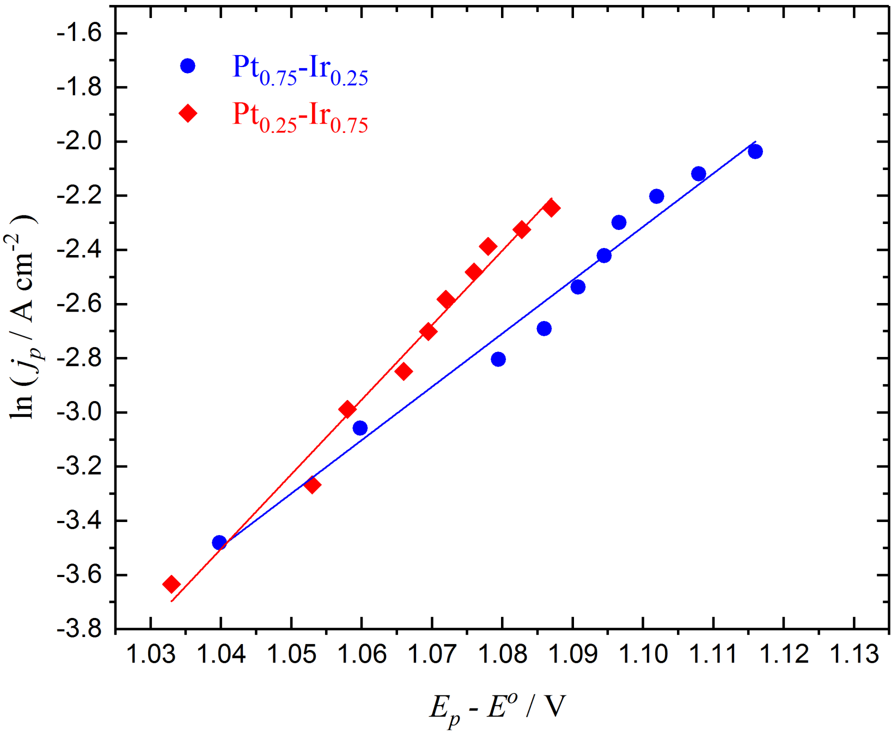

Figure 4.13. A plot of $\ln j_p$ *vs.* $(E_p - E^o)$, for Eq. (4.7) with Pt_x-Ir_x/Ti electrodes (1 cm^2) in 0.03 mol dm^{-3} $NaBH_4$ + 2 mol dm^{-3} NaOH at 294 K.

4.3.6. The heterogeneous rate constant

The heterogeneous rate constant of the electron-transfer reaction depends on the applied potential [208]. The electron transfer control most likely occurs at an early transient regime (the beginning of the current transient) [144]. At that regime, the heterogeneous rate constant of BH_4^- electro-oxidation, k_a (cm s^{-1}), was evaluated using chronoamperometry over a very short time period (< 1 s). Figure 4.14 demonstrates the short chronoamperometry results (40 ms), where the potential stepped from the OCP to +0.2 V *vs.* Hg/HgO on Pt_x-Ir_x/Ti electrodes in 0.03 mol dm^{-3} $NaBH_4$ in 2 mol dm^{-3} NaOH. The figure shows a higher activity of $Pt_{0.75}$-$Ir_{0.25}$ than $Pt_{0.25}$-$Ir_{0.75}$.

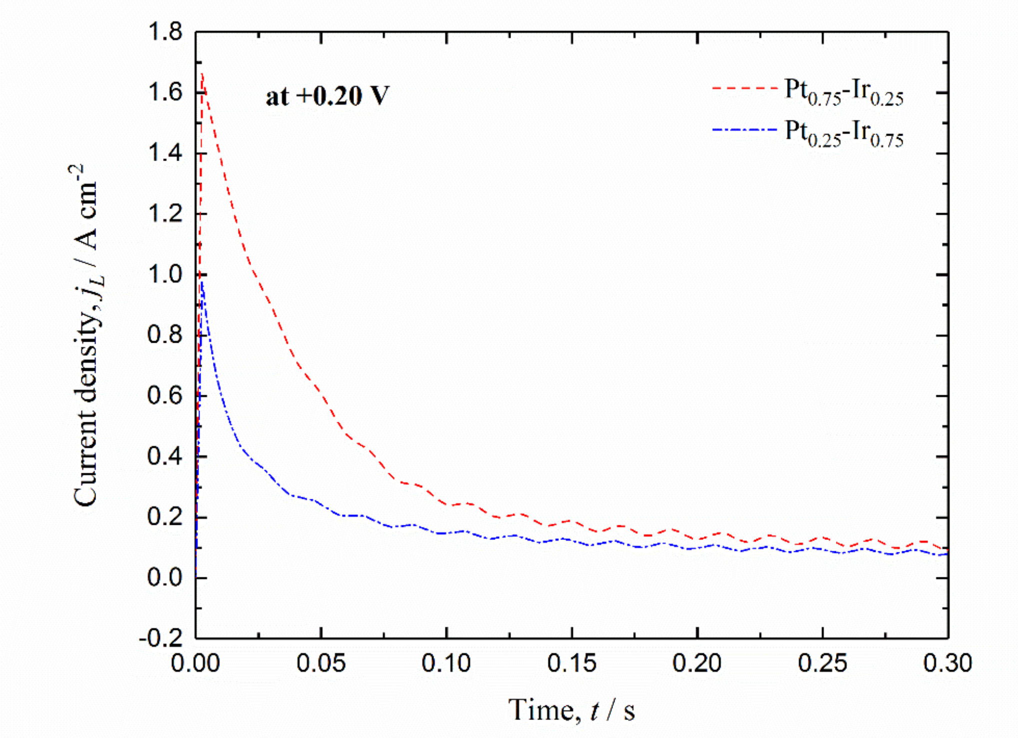

Figure 4.14. Chronoamperometry (from OCP to +0.2 V *vs.* Hg/HgO, 40 ms) of 0.03 mol dm^{-3} NaBH$_4$ in 2 mol dm^{-3} NaOH in the three-electrode cell using different Pt-Ir alloys (1 cm^2). Pt mesh was the counter, and the temperature was controlled at 294 K (21 ±1 ºC).

The values of the heterogeneous kinetic rate constant, k_a, for borohydride oxidation over Pt$_x$-Ir$_x$/Ti electrodes at certain potentials can be obtained from the cumulative charge, Q(C), with overtime ^{208}, as the following equation expresses:

$$Q(t) = zFAck_a\left(\frac{2t^{1/2}}{H\pi^{1/2}} - \frac{1}{H^2}\right) \tag{4.9}$$

where H can be defined as follows

$$H = \frac{\pi^{1/2}}{2t_i^{1/2}} \tag{4.10}$$

Here, $t_i^{1/2}$ is the positive intercept on the $t^{1/2}$ axis employing a shorter linear extrapolation, as seen in Figure 4.15a), which shows a linear plot of the cumulative charge (Q) *vs.* $t^{1/2}$ for Pt$_x$-Ir$_x$/Ti anodes. With H in hand, the k_a value can be calculated from the intercept or the slope [$2zFAck_a/(H\pi^{1/2})$], which was chosen here; see Eq. (4.9). As the kinetic rate constant depends on the electrode potential, the short chronoamperometry experiments were also repeated with potentials (where the direct oxidation of BH_4^- is expected) of 0.0 and -0.2 V *vs.* Hg/HgO (see j_L *vs.* t in Appendix IV), the results of which (Q *vs.* $t^{1/2}$) are illustrated in Figure 4.15b) and Figure 4.15c), respectively. The total number of electrons exchanged, z, for the two electrodes has been taken from Table 4.1 [5.3 e^- (75:25) and 3.7 e^- (25:75)].

Accordingly, Table 4.2 shows the rate constants for the anodic reaction at different potentials, where $Pt_{0.75}$-$Ir_{0.25}$ and $Pt_{0.25}$-$Ir_{0.75}$ presented average reaction rates of 0.39 and 0.53 cm s^{-1}, respectively, at any potential between -0.2 and +0.2 V *vs.* Hg/HgO. In the case of the $Pt_{0.25}$-$Ir_{0.75}$ electrode, the Cottrellian response (diffusion-controlled) was dominant, and the highest values of k_a were for this electrode.

Table 4.2. The heterogeneous rate constant, k_a cm s^{-1}, of borohydride oxidation on Pt_x-Ir_x/Ti electrodes at different potentials at 294 K.

Electrode	*E vs.* Hg/HgO		
	-0.2	0.0	+0.2
$Pt_{0.75}$-$Ir_{0.25}$	0.40 ±0.01	0.37 ±0.01	0.38 ±0.01
$Pt_{0.25}$-$Ir_{0.75}$	0.55 ±0.05	0.64 ±0.09	0.41 ±0.11

This method has been discussed thoroughly by Bard, Faulkner [208] and Pletcher [144]. Gyenge [49] applied it experimentally using Pt and Au disk electrodes at 0.0 V *vs.* Ag/AgCl, KCl_{std}, in a similar electrolyte solution (0.03 mol dm^{-3} $NaBH_4$ in 2 mol dm^{-3}) but with additive of 1.5 × 10^{-3} mol dm^{-3} Thiourea (TU) (to suppress the hydrolysis) at room temperature (295 K). The author found that Pt has a higher $k_a = 1.86$ cm s^{-1} than a Au electrode (0.14 cm s^{-1}) at 0 V *vs.* Ag/AgCl (KCl_{std}). Finkelstein et al. [51] applied the Koutecky-Levich equation using the voltammograms of BH_4^- obtained from an RDE. They reported significantly lower values – 0.029 and 0.012 cm s^{-1} for Pt and Au, respectively – than those found for Pt-Ir alloy electrodes. This finding could be attributed to differences in the reaction mechanism or experimental and calculation techniques.

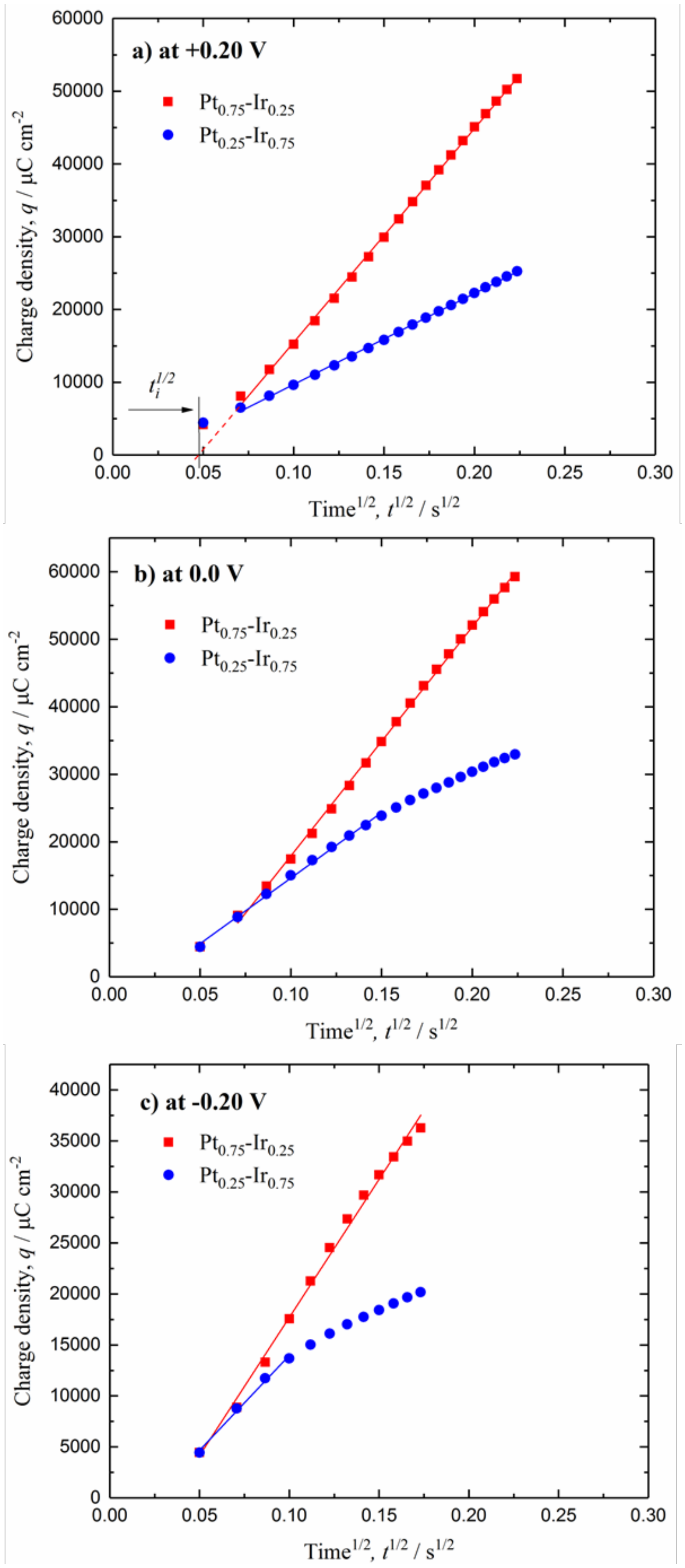

Figure 4.15. The charge density *vs.* time$^{1/2}$ for the two Pt_x-Ir_x electrodes (1 cm^2) at a) +0.20, b) 0.0 and c) -0.2 V *vs.* Hg/HgO. The data was obtained from the chronoamperometry measurements under similar conditions as the previous figure.

4.3.7. The activation energy – the influence of temperature

The activation energy can express the prospect of using thermal energy to overcome an energy barrier [208] to proceed with a reaction process. Evaluation of apparent activation energies, E_a^{app} (kJ mol^{-1}), of the two alloys for the oxidation of borohydride ions was made using chronoamperometry tests at different temperatures (25–65 °C), as shown in Figure 4.16. The activation energies were determined by applying the other form of the Arrhenius equation [Eq. (4.11)] [119] [82] [217]:

$$ln j_L = ln A_i - \frac{E_a^{app}}{RT} \qquad (4.11)$$

Where A_i is the Arrhenius pre-exponential factor [82]. E_a^{app} was determined from the fitting data of the limiting current densities, j_L, at +0.2 V *vs.* Hg/HgO *vs.* the reciprocal temperatures, $1/T$, as seen in Figure 4.17, for each electrode. E_a^{app} values were calculated to be 18.6 and 28.0 kJ mol^{-1} for borohydride oxidation at $Pt_{0.75}$-$Ir_{0.25}$ and $Pt_{0.25}$-$Ir_{0.75}$, respectively. This result means that $Pt_{0.75}$-$Ir_{0.25}$ required less thermal energy than the $Pt_{0.25}$-$Ir_{0.75}$ catalyst to surmount the energy barrier of BH_4^- oxidation. Sljukic et al. [119] obtained values of 20, 25 and 34 kJ mol^{-1} for $Pt_{0.75}Ni_{0.25}$/C, $Pt_{0.75}Co_{0.25}$/C and Pt/C, respectively, using a similar electrolyte composition, revealing the advantages of the bimetallic Pt alloy over monometallic Pt.

Oliveira et al. [218] tested a polypyrrole-carbon (5–35 wt.% carbon) decorated with Pt nanoparticles and found that the values of E_a^{app} range from 10 to 18 kJ mol^{-1} but using cyclic voltammetries (j_p *vs.* $1/T$) at 50 mVs^{-1} in 0.03 mol dm^{-3} $NaBH_4$ + 2 mol dm^{-3} NaOH at 25-65 °C. Many other materials have also been evaluated; for example, Ni alloys presented values of 18, 23 and 31 kJ mol^{-1} for borohydride oxidation on $Ni_{0.95}Dy_{0.05}$, $Ni_{0.90}Dy_{0.10}$ and $Ni_{0.95}Sm_{0.05}$, respectively [82], which was determined from chronoamperometric curves recorded in 0.03 mol dm^{-3} $NaBH_4$ in 2 mol dm^{-3} NaOH. Santos and Sequeira [209] reported significantly higher values (40–72 kJ mol^{-1}) for a gold disc electrode [0.03 mol dm^{-3} $NaBH_4$ at -0.5 to +0.5 V *vs.* saturated calomel electrode (SCE)] than those obtained for Pt_x-Ir_x (present work), however, Cheng and Scott [92] applied linear sweep voltammograms on a Au rotating disk electrode (25-70 °C, 1000 rpm) and it found that the apparent activation energy to be 27 kJ mol^{-1}. Recently, Oliveira et al. [217] found it to be around 29 kJ mol^{-1} for Pt-Cu/nanoalloys and mesoporous carbon nitride.

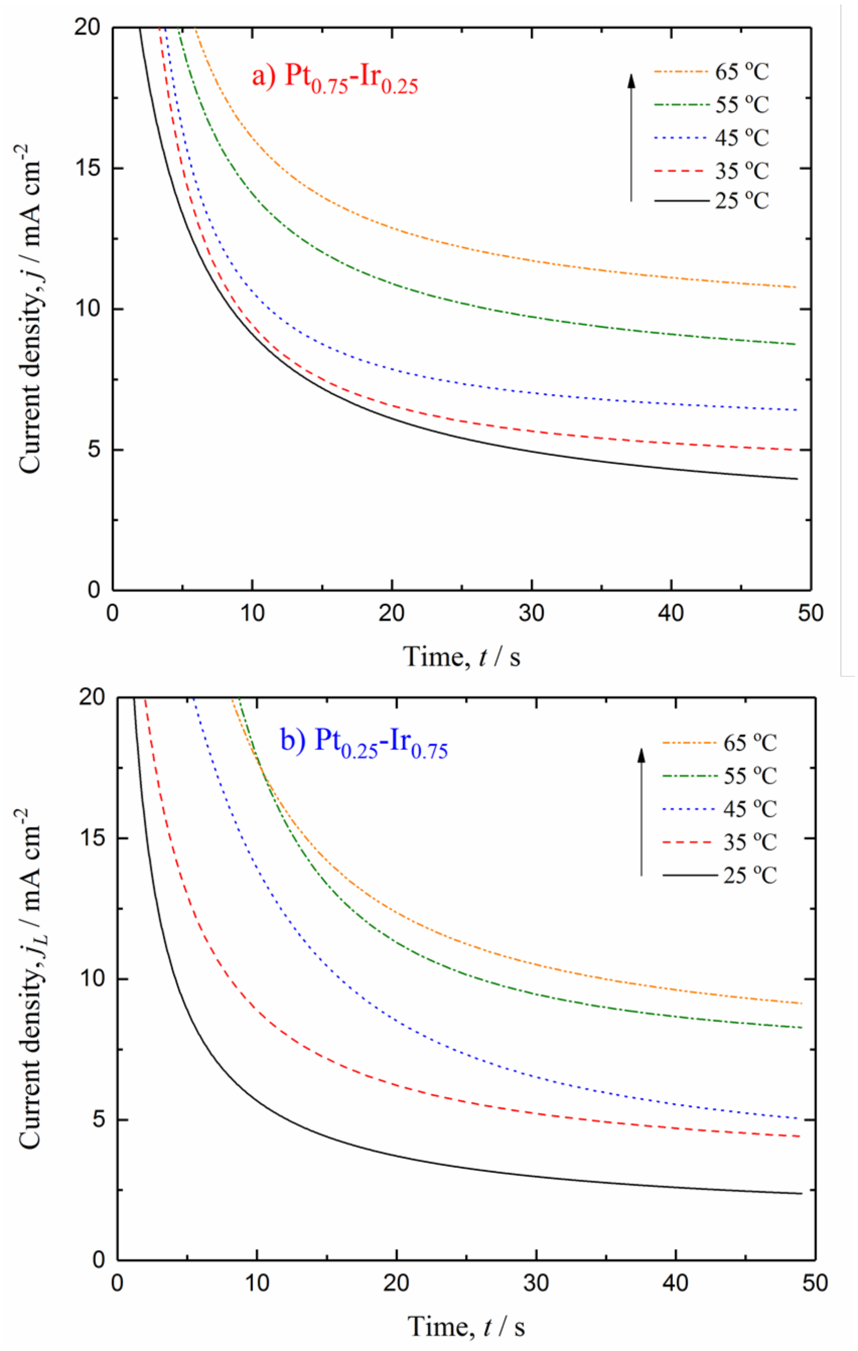

Figure 4.16. Chronoamperometry (at +0.2 V *vs.* Hg/HgO, 50 s) at different temperatures using a three-electrode cell. The electrolyte consisted of 0.01 mol dm^{-3} $NaBH_4$ in 2 mol dm^{-3} NaOH (0.1 dm^{-3}), the anode was Pt_x-Ir_x/Ti (1 cm^2) and the counter electrode was Pt mesh.

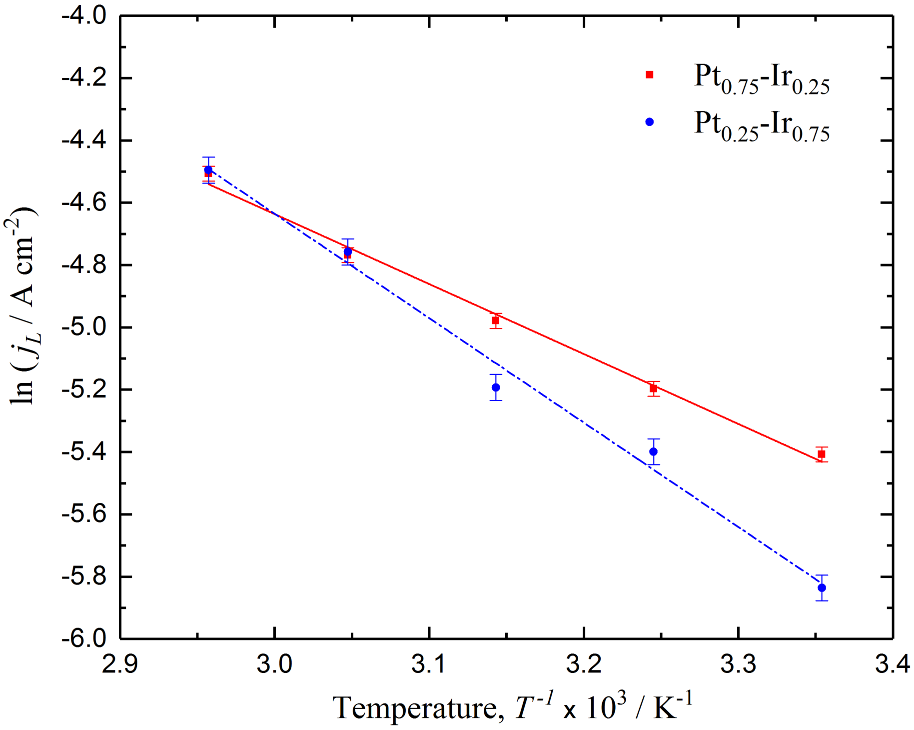

Figure 4.17. Arrhenius plots for the $Pt_{0.75}$-$Ir_{0.25}$ and $Pt_{0.25}$-$Ir_{0.75}$ catalyst electrodes (1 cm^2).

4.3.8. The reaction order – the influence of concentration

Figure 4.18a) and b) show the linear sweep voltammograms at 100 mV s^{-1} scan rate, from -1 V to 0.6 V *vs.* Hg/HgO for borohydride oxidation on $Pt_{0.75}$-$Ir_{0.25}$, and $Pt_{0.25}$-$Ir_{0.75}$ electrodes in an electrolyte containing BH_4^- ranging from 0.01-0.2 mol dm^{-3} concentration. The current densities increased linearly with borohydride concentration. It can be seen that the peak potential for borohydride oxidation shifted to more positive values as the BH_4^- concentration increased. This behaviour, as was suggested by Sljukic et al. [119], Santos and Sequeira [209], is due to the longer time required to achieve full depletion of borohydride ions when there is a higher concentration at the electrode surface. O_2 evolution was observed at higher positive potentials (> +0.6 V *vs.* Hg/HgO) for both electrodes. At positive potentials > +0.2 V and higher BH_4^- concentrations (> 0.1 mol dm^{-3}), $Pt_{0.75}$-$Ir_{0.25}$ showed superior activity towards BH_4^- oxidation, providing a high current densities (seen in Figure 4.18a), possibly due to the increase of [BH_4^-] as it cannot be from an oxygen evolution reaction. For the $Pt_{0.25}$-$Ir_{0.75}$ electrode at the highest concentration of 0.2 mol dm^{-3}, as seen in Figure 4.18b), the peak potential shifted to the positive direction but the peak current was lower at a low potential, which means probably that the electrode with a higher content of Ir favours the borohydride oxidation than H_2 oxidation at BH_4^- concentration ≥ 0.2 mol dm^{-3}.

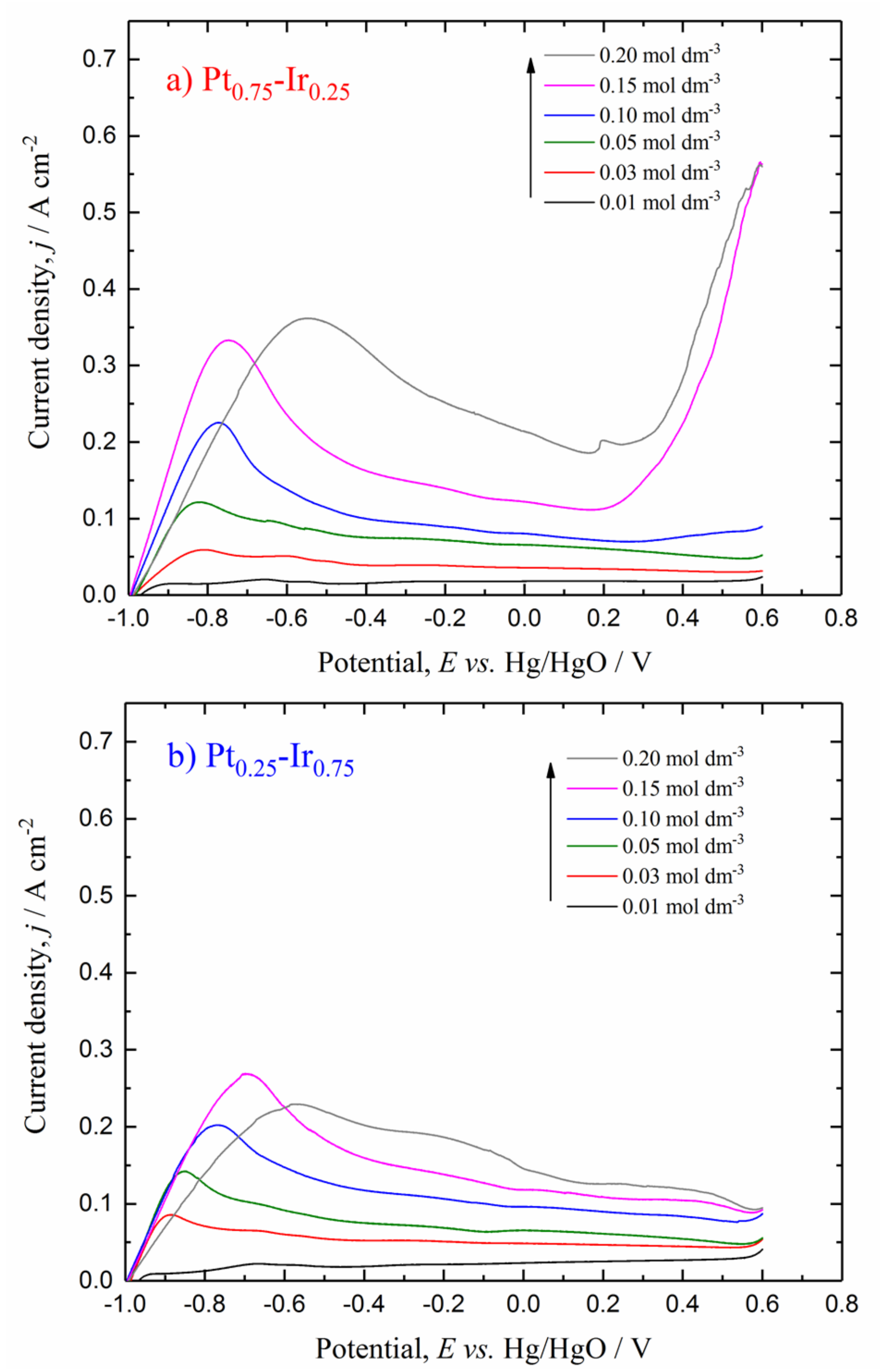

Figure 4.18. Linear voltammetry (-1 V to 0.6 V *vs.* Hg/HgO) of BH_4^- oxidation on a) $Pt_{0.75}$-$Ir_{0.25}$, b) $Pt_{0.25}$-$Ir_{0.75}$ on Ti (plate, 1 cm^2) using the three-electrode cell for the effect of borohydride concentration. Scan rate 100 mV s^{-1} at a controlled temperature of 294 K (21 ± 1 °C) in electrolyte consisted of different $NaBH_4$ in 2 mol dm^{-3} NaOH.

The reaction rate can be expressed as a kinetic current density (j/A cm^{-2}) given by Eq. (4.12) [219 220 92 119 209 217]:

$$j = yc^{\beta} \tag{4.12}$$

Where y is a reaction constant and β is the order of the reaction for a bulk concentration (c mol cm^{-3}). The linear form of Eq. (4.12) is Eq. (4.13), which was used to estimate the reaction rate constants and the order of the borohydride oxidation reaction on Pt$_x$-Ir$_x$/Ti catalysts. The slopes and intercepts of the linear plots of ln$j$ *vs.* ln$c$, were obtained to determine β and y, respectively, from Figure 4.19:

$$\ln j = \ln y + \beta \ln c \tag{4.13}$$

The reaction orders at -0.2 V (a2) *vs.* Hg/HgO – where the current was taken for all curves in Figure 4.18a) and b) – were 0.82 and 0.69 for 75:25 and 25:75 alloys, respectively, while y values were equal to 198 and 60 A cm mol^{-1}. The calculations were also repeated for the electrode potentials 0.0 and +0.2 V. Table 4.3 and Table 4.4 summarise all values of β and y, respectively.

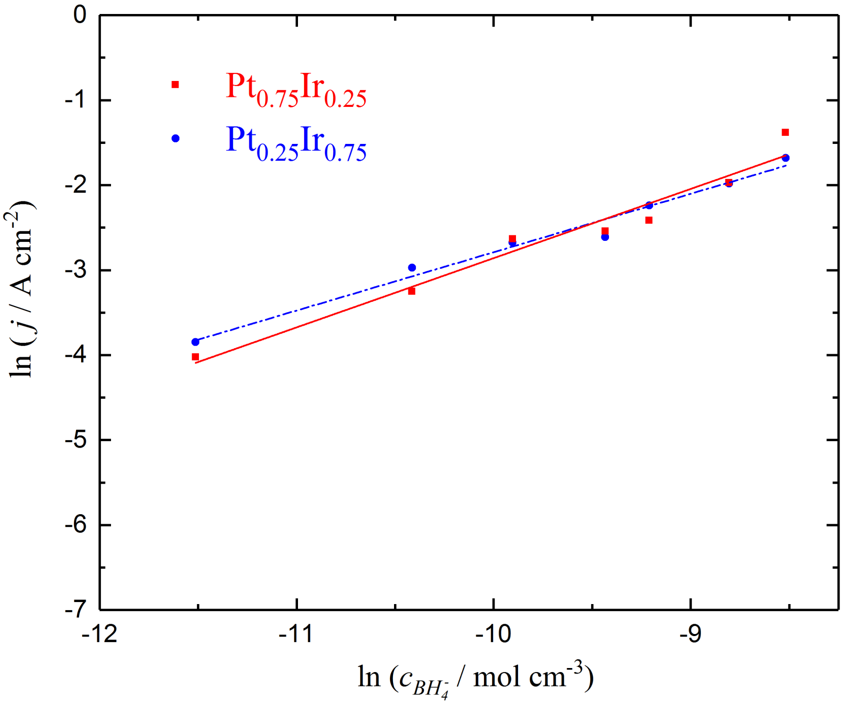

Figure 4.19. The kinetic current density *vs.* concentrations of NaBH$_4$ at -0.2 V (a2) *vs.* Hg/HgO collected from Figure 4.18 for Pt$_{0.75}$-Ir$_{0.25}$ and Pt$_{0.25}$-Ir$_{0.75}$ electrodes.

Table 4.3. The reaction orders, β, of BH_4^- at different potentials of Pt_x-Ir_x electrodes.

Electrode	*E vs.* Hg/HgO		
	-0.2	0.0	+0.2
75 25	0.82	0.76	0.73
25 75	0.69	0.59	0.53

Table 4.4. The reaction constants values, *y*, at different potentials of Pt_x-Ir_x electrodes.

Electrode	*E vs.* Hg/HgO		
	-0.2	0.0	0.2
75 25	198	106	77
25 75	60	22	11

In all cases, $Pt_{0.75}$-$Ir_{0.25}$ presented approximately a first-order reaction, and its reaction constants were more than three times larger than those of the $Pt_{0.25}$-$Ir_{0.75}$ electrode at -0.2 V *vs.* Hg/HgO. Even though Santos and Sequeira [209] mentioned that undertaking voltammograms in hydrodynamic conditions could be affected by other parameters (but have not determined them), they advised – among others [204 51 191 198] – to undertake the CV tests using the RDE technique. Therefore, it is useful to employ the data from Chapter 5, where the mass transport has been studied in detail using different anode structures of Ti materials coated with $Pt_{0.75}$-$Ir_{0.25}$ catalyst to confirm the reaction order results obtained here.

The limiting current densities were obtained at a mean linear flow velocity of 3.8 cm s^{-1} using chronoamperometry measurements (at 0.2 V *vs.* Hg/HgO) on $Pt_{0.75}$-$Ir_{0.25}$/Ti mesh for concentrations from 2 to 18 mmol dm^{-3} BH_4^- + 2 mol dm^{-3} NaOH (Figure 5.11b). By using the same technique of applying Eq. (4.13) and getting the limiting currents from the chronoamperometry data shown in Figure 5.11b, the reaction order of borohydride oxidation rate was calculated from the linear slope in Figure 4.20 to be 1.03 for $Pt_{0.75}$-$Ir_{0.25}$/Ti mesh. The agreement between the two methods (hydrodynamic and non-hydrodynamic conditions) is generally good and aligns with the literature. A range of reaction orders (0.83–1.11) was reported [119] using a $Pt_{0.75}$-$Co_{0.25}$/C RDE (1200 rpm) in solutions from 0.01 to 0.09 mol dm^{-3} BH_4^- + 2 mol dm^{-3} NaOH. The authors [119] found consistency between the reaction order obtained from CV RDE data and those obtained from CV (diffusion control) data (β = 0.85 to 0.91). They observed that the current trend with increasing BH_4^- concentration was similar in both methods, meaning the CV data (in natural diffusion control) leads to a good agreement with the RDE data (via convection-diffusion) in terms of the reaction order calculation, as seen from this research and the cited publications. Gyenge [49] compared the limiting current obtained from Pt in 0.03 and 0.3 mol dm^{-3} BH_4^- solutions (with the presence of 1.5 × 10^{-3} mol dm^{-3} thiourea). The current was ten times greater with 0.3 mol dm^{-3} BH_4^-, suggesting a first-order reaction rate, but the author did not apply any equation to calculate β.

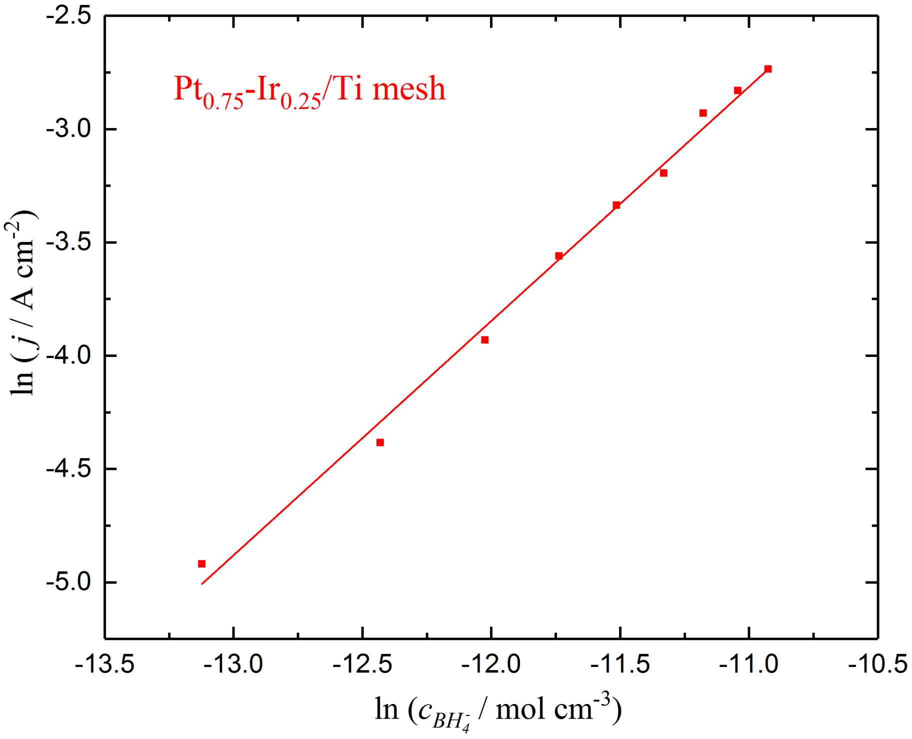

Figure 4.20. The logarithmic plot of the current densities and the different borohydride concentrations from Figure 5.11b). The limiting current *vs.* different borohydride concentrations was obtained from chronoamperometry (+0.2 V *vs.* Hg/HgO) on a Pt-Ir/Ti mesh (8.55 cm^2) working electrode for a half-cell operating at 296 K. The electrolyte composition was $x \times 10^{-3}$ mol dm^{-3} $NaBH_4$ in 2 mol dm^{-3} NaOH. The mean linear fluid velocity was 3.8 cm s^{-1}. The Pt/Ti mesh counter electrode was in 2 mol dm^{-3} NaOH.

Cheng and Scott [92] have also confirmed that (first-order) at 1000 rpm and onset potential of 0.45 V *vs.* Hg/HgO using an Au RDE in 0.27 to 2.65 mol dm^{-3} borohydride solutions (2.5 mol dm^{-3} NaOH). An Au electrode was also used in a different study [209]; however, CV experiments were carried out in natural diffusion conditions. The authors [209] found that the reaction order of the BH_4^- oxidation (at 0.0 *vs.* SCE and a scan rate of 2 V s^{-1}) laid between 0.82 and 1.25 for a range of solution temperatures (25–65 ºC). Lately, Oliveira et al. [217] obtained the average reaction order of Pt-Cu/mesoporous carbon nitride to be 0.87. In short, it can be concluded that the borohydride process is a first-order reaction.

4.3.9. The mass-transport coefficient – the influence of flow velocity

Figure 4.21a) and b) present the effects of changing the mean linear flow velocity, v (cm s^{-1}), on the current density, j (A cm^{-2}), gained from the $Pt_{0.75}$-$Ir_{0.25}$/Ti and $Pt_{0.25}$-$Ir_{0.75}$/Ti electrocatalysts, respectively. Figure 4.5 shows the single flow cell that was used to investigate the two anodes with a projected area of 9 cm^2. Figure 4.21a) and b) present the mass control region (steady-state), where the current remains approximately unchanged ($I = I_L$; limiting current) at $t > 25$ s, which represents the maximum reaction rate [175] of borohydride oxidation for Pt_x-Ir_x/Ti as well. The limiting current densities, j_L, were obtained using the average of the last ten current records (at $t > 25$ s) for each flow velocity in Figure 4.21 (a & b) and plotted in Figure 4.22a). This plot (log-log) illustrates increasing j_L in both electrodes with respect to the mean flow velocity. Although $Pt_{0.25}$-$Ir_{0.75}$ has a lower j_L than $Pt_{0.75}$-$Ir_{0.25}$, the slope of $Pt_{0.25}$-$Ir_{0.75}$ was higher, and, as a result, its j_L exceeded the current obtained from $Pt_{0.75}$-$Ir_{0.25}$ at a high flow velocity (> 8 cm s^{-1}). This result could be attributed to the surface roughness of $Pt_{0.25}$-$Ir_{0.75}$, as seen in Figure 4.7c) and d), which might cause a turbulent flow at higher v. At this stage, it is valuable to determine the mass-transfer coefficients, k_m (cm s^{-1}), of the two alloys by the following relationship [175 221]:

$$k_m = \frac{I_L}{zFAc} \tag{4.14}$$

Where A (cm^2) is the active surface area of the plate electrode (assumed to be 9 cm^2) and z is the stoichiometric number of electrons exchanged in the system. Accordingly, Figure 4.22b) shows the log-log plot of k_m with respect to the electrolyte mean flow velocity for the two Pt_x-Ir_x alloys. The curve of each k_m *vs.* v of $Pt_{0.75}$-$Ir_{0.25}$ and $Pt_{0.25}$-$Ir_{0.75}$, at steady-state conditions, can be expressed by the following equations:

$$k_{m,\ Pt_{0.75}-Ir_{0.25}} = 0.8\times10^{-3}v^{0.38} \qquad (4.15)$$

$$k_{m,\ Pt_{0.25}\text{-}Ir_{0.75}} = 0.6\times10^{-3}v^{0.54} \qquad (4.16)$$

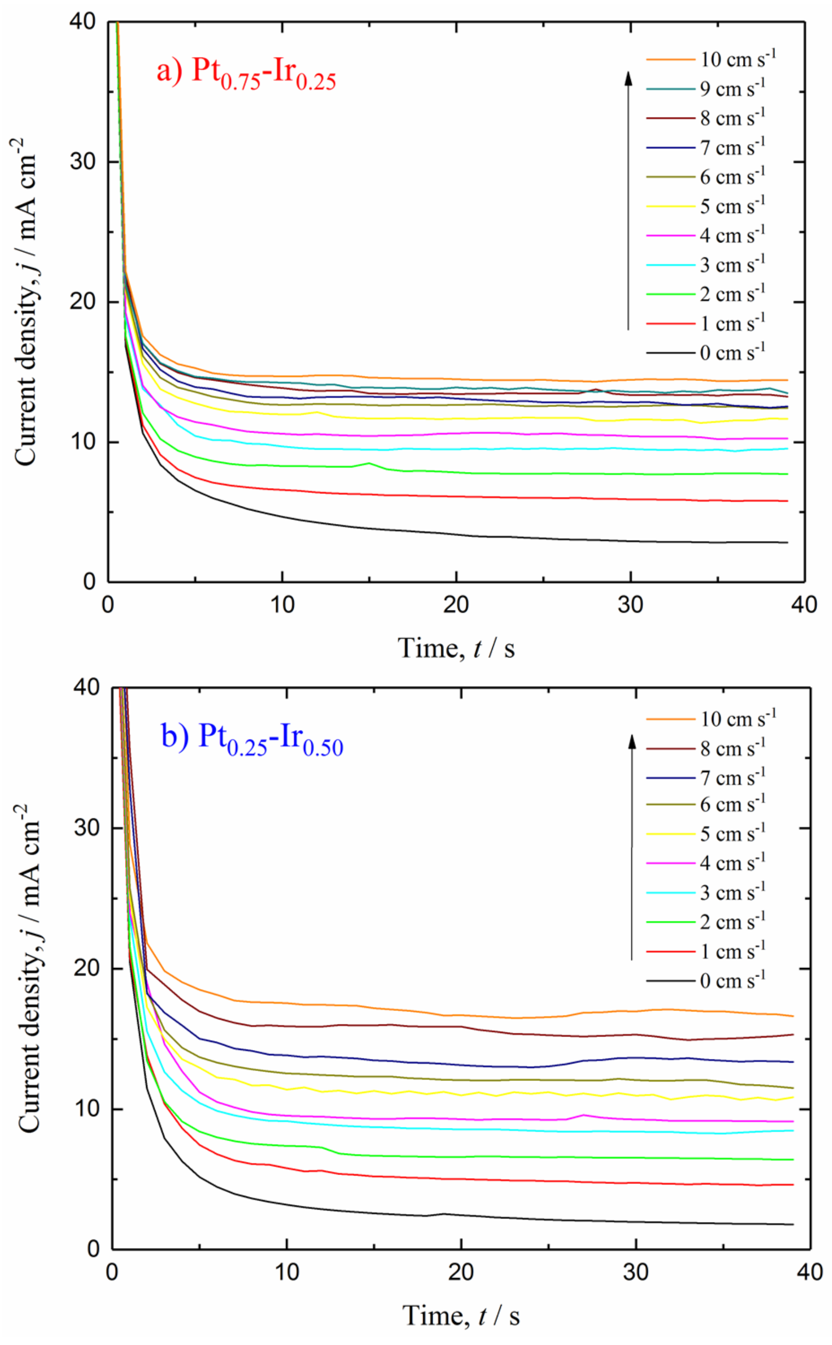

Figure 4.21. Chronoamperometry (at +0.2 V *vs.* Hg/HgO, 40 s) with different mean linear flow velocities of a single cell operating at 298 K. The anolyte consisted of 0.01 mol dm^{-3} $NaBH_4$ in 2 mol dm^{-3} NaOH (0.18 dm^{-3}) and 2 mol dm^{-3} NaOH Catholyte (0.18 dm^{-3}). The anodes were a) $Pt_{0.75}$-$Ir_{0.25}$ and b) $Pt_{0.25}$-$Ir_{0.75}$ on Ti plat (9 cm^2) and the cathode was Pt supported on Ti mesh (9 cm^2).

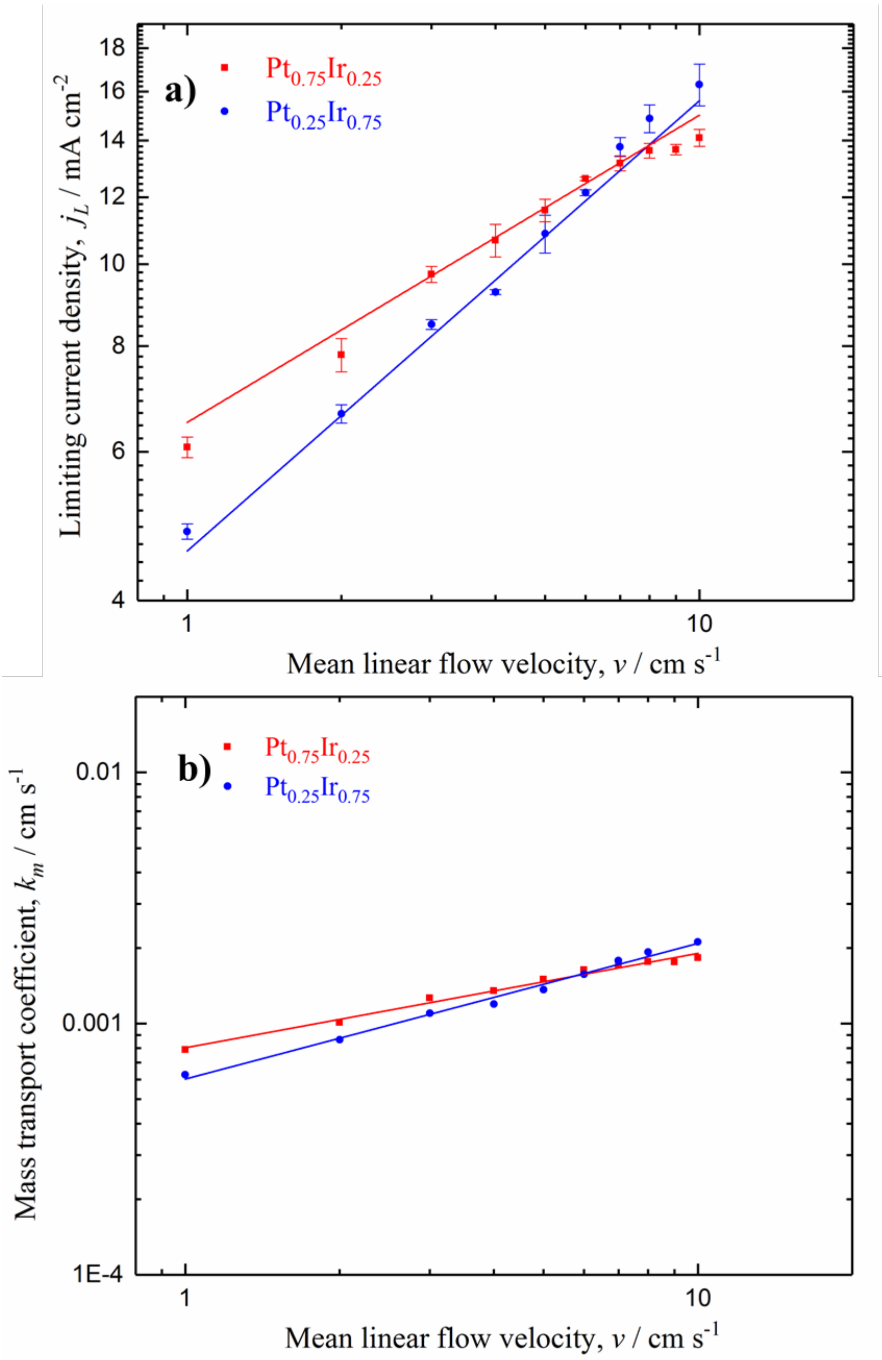

Figure 4.22. The a) limiting current density (at 0.2 V *vs.* Hg/HgO) and b) mass-transport coefficient *vs.* linear flow velocity using Pt$_{0.75}$-Ir$_{0.25}$/Ti and Pt$_{0.25}$-Ir$_{0.75}$/Ti anode catalysts (Ti plate, 9 cm^2). The anolyte consisted of 0.01 mol dm^{-3} NaBH$_4$ + 2 mol dm^{-3} NaOH and 2 mol dm^{-3} NaOH catholyte at 298 K.

As can be seen from Eq. (4.15) and Eq. (4.16), the flow velocity order of Pt$_{0.25}$-Ir$_{0.75}$ (0.54) is 40% higher than that of Pt$_{0.75}$-Ir$_{0.25}$ (0.38). However, the latter has a larger mass transfer coefficient (33%, 0.8×10^{-3} cm s^{-1}) than Pt$_{0.25}$-Ir$_{0.75}$ (0.6×10^{-3} cm s^{-1}). In general, the two catalysts have approximately similar k_m, which was expected, as a similar substrate was used (Ti plate). However, the $Pt_{0.75}$-$Ir_{0.25}$ electrode could present a slightly faster mass transport of BH_4^- ions only at lower flow velocity ($v < 6$ cm s^{-1}) and the $Pt_{0.25}$-$Ir_{0.75}$ at a higher ($v > 6$ cm s^{-1}), which may be due to the microsurfaces of the two electrodes. It has become obvious that DBFC system is dominated by the mass transfer of BH_4^- rather than the electron transfer as k_a larger than k_m.

4.3.10. Polarisation curves – the influence of temperature on a single cell

The schematic experimental system of the DBFC can be seen in Figure 4.5. The influence of the temperature on the polarisation and power density using $Pt_{0.75}$-$Ir_{0.25}$ and $Pt_{0.25}$-$Ir_{0.75}$ anodes was studied at 298 K (25 ^oC) and 333 K (60 ^oC), as shown in Figure 4.23. The electrolyte on the anode side consisted of 1 mol dm^{-3} $NaBH_4$ + 4 mol dm^{-3} NaOH, while the cathode solution (Pt/Ti mesh) was 1 mol dm^{-3} H_2O_2 + 1 mol dm^{-3} HCl, the two of which were separated by the CEM Nafion® 115. As was discussed in the literature review, this membrane allows only protons to crossover (in this case, Na^+). The rate of applied current density was 5 mA cm^{-2} min^{-1} from 0 to 250 mA cm^{-2} for less than 50 minutes. The power densities were calculated by multiplying the applied current densities and the measured cell potential (Figure 4.23). The two electrodes showed an OCP of about 1.8 V, which is approximately 1.2 V lower (40%) than the theoretical value of the $NaBH_4 \| H_2O_2$ cell [3.02 V, Eq. (2.18)] probably due to the mixed potentials at the anode and cathode electrodes caused by the reaction of intermediate products in the two compartments (see Chapter 6 for more detail). The OCP must also be decreased by the liquid junction potential (~826 mV) [162] [222] between the catholyte (pH ~ 0) and anolyte (pH ~ 14) solutions.

Table 4.5 summarises the temperature effects on the peak power densities, the cell potentials and current densities at the peak power densities of Pt_x-Ir_x/Ti anodes in the DBFC. The maximum power density of $Pt_{0.75}$-$Ir_{0.25}$ was practically double the maximum of $Pt_{0.25}$-$Ir_{0.75}$ in both cases of 298 K and 333 K. For example, at 333 K, the peak power density of $Pt_{0.75}$-$Ir_{0.25}$ was 84 mW cm^{-2}, while it was 40.7 mW cm^{-2} in the case of $Pt_{0.25}$-$Ir_{0.75}$. This result is evidence that DBFCs using $Pt_{0.75}$-$Ir_{0.25}$/Ti anode catalyst performed better. Increasing the temperature from 298 K to 333 K improved the maximum power density dramatically by *ca.* 70% (50 to 84 mW cm^{-2}) with $Pt_{0.75}$-$Ir_{0.25}$ and 50% (26.7 to 40.7 mW cm^{-2}) with $Pt_{0.25}$-$Ir_{0.75}$. Under a 100 mA cm^{-2} load with the $Pt_{0.75}$-$Ir_{0.25}$ anode, the fuel cell provided a cell potential of only 0.30 V (30 mW cm^{-2}) at 298 K, while at 333 K a cell potential of 0.82 V (82 mW cm^{-2}) was measured. As was mentioned before, only Gyenge et al. have studied Pt-Ir with a catalyst load of 1:1 [69]. The authors used double the borohydride concentration than that used here (2 mol dm^{-3} $NaBH_4$ + 2 mol dm^{-3} NaOH). Their oxidant was O_2 (200 cm^3 min^{-1}), which is known experimentally to be lower (1.64 V theoretical cell potential) in terms of power density and cell efficiency than hydrogen peroxide, as the latter has a faster reduction rate and higher cell voltage (3.02 V) [24]. They measured the cell voltage using Pt:Ir (50:50) at 0.1 V (10 mW cm^{-2}) and 0.53 V (53 mW cm^{-2}) at 298 K and 333 K, respectively, under 100 mA cm^{-2}. Even though they used a higher catalyst load (5 mg cm^{-2}, while 2 mg cm^{-2} was used in the current study), the cell power in the present work obtained using a $Pt_{0.75}$-$Ir_{0.25}$ anode was up to three times higher than the results of Gyenge et al. for the cell operated under 100 mA cm^{-2} at 298 K.

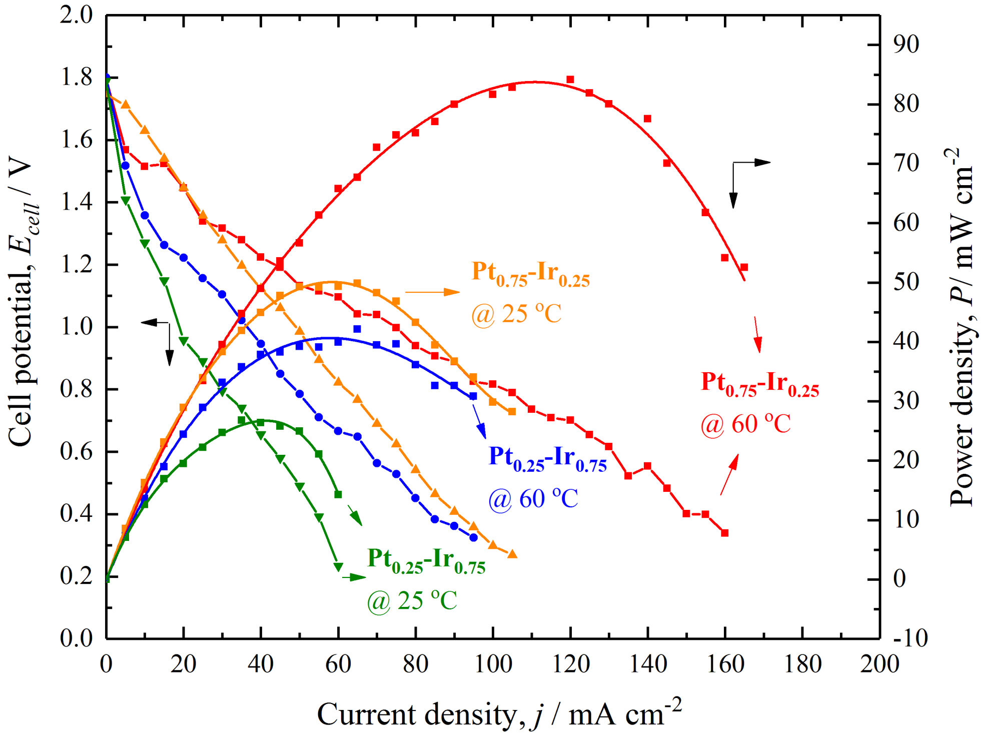

Figure 4.23. The effect of the operation temperature on cell polarisation and the power density curves of the $NaBH_4$‖H_2O_2 cell using $Pt_{0.75}$-$Ir_{0.25}$/Ti and $Pt_{0.25}$-$Ir_{0.75}$/Ti anode catalysts (Ti plate, 9 cm^2). The anolyte consisted of 1 mol dm^{-3} $NaBH_4$ + 4 mol dm^{-3} NaOH and 1 mol dm^{-3} H_2O_2 + 1 mol dm^{-3} HCl catholyte at a scan rate of 5 mA cm^{-2} min^{-1} and a mean linear fluid velocity of 3 cm s^{-1} at 298 K (25 °C) and 333 K (60 °C).

Table 4.5. The temperature effects on $Pt_{0.75}$-$Ir_{0.25}$ and $Pt_{0.25}$-$Ir_{0.75}$ anodes in the DBFC.

	$Pt_{0.75}$-$Ir_{0.25}$		$Pt_{0.25}$-$Ir_{0.75}$	
	298 K	333 K	298 K	333 K
Open-circuit potential / V	1.80	1.80	1.75	1.79
Peak power density / mW cm^{-2}	50	84	26.7	40.7
Cell potential at peak power density / V	0.85	0.75	0.64	0.7
Current density at peak power density / mA cm^{-2}	58.5	111	41.3	57.8

However, the differences in the catalyst composition, catholyte solution and cell operation conditions could explain the difference in cell performance. Yi et al. [73] tested a single cell using Pt, $Pt_{0.75}$-$Zn_{0.25}$, $Pt_{0.67}$-$Zn_{0.33}$ and $Pt_{0.50}$-$Zn_{0.50}$ as anode materials and Pt as a cathode (all electrodes had a 0.9 mg cm^{-2} catalyst load supported by Vulcan XC-72R carbon). The anolyte solution was composed of 1 mol dm^{-3} $NaBH_4$ + 3 mol dm^{-3} NaOH, while a 2 mol dm^{-3} H_2O_2 + 0.5 mol dm^{-3} H_2SO_4 was used as a catholyte. A Nafion® 117 membrane separated the two electrolytes. The OCP was 1.7 V, which was lower than that obtained in the present work (1.8 V). The authors [73] reported that the peak power densities using Pt, $Pt_{0.75}$-$Zn_{0.25}$, $Pt_{0.67}$-$Zn_{0.33}$ and $Pt_{0.50}$-$Zn_{0.50}$ were 42.8 mW cm^{-2} (39.6 mA cm^{-2}), 66.3 mW cm^{-2} (69.8 mA cm^{-2}), 79.9 mW cm^{-2} (79.5 mA cm^{-2}) and 59.5 mW cm^{-2} (65.0 mA cm^{-2}), respectively, at 298 K, which suggests using Pt alloys with 67:33 Pt:Zn. Others have examined many Pt-M alloys (M=Zn [73], Sn [117], Co [128], Cu [127] [130] and Fe [223]) and found that bimetallic catalysts are more active and improve the performance of DBFCs more than monometallic Pt catalysts. Generally, in all five studies, the Pt-M/C showed the highest catalytic activity for the BOR when the ratio of Pt:M was 67:33 rather than 80:20, 75:25, 50:50 or 100:0 (Pt), the last of which was the worst catalyst. Even though $Pt_{0.75}$-$Ir_{0.25}$ – which is studied here – showed promising activity, a further investigation of Pt:Ir catalysts needs to be made to find the optimal bimetallic catalyst ratio for borohydride systems.

4.3.11. The cell stability test

In order to confirm the high electrocatalytic activity of a $Pt_{0.75}$-$Ir_{0.25}$/Ti plate anode towards borohydride electro-oxidation, the short-term stability of the single cell shown in Figure 4.5 was studied. Figure 4.24 shows the cell voltage recorded over a continuous operating period of about 75 minutes at a constant current load of 25 mA cm^{-2} of the

DBFC using Pt_x-Ir_x anodes at 298 K (25 °C). The cell exhibited a relatively stable performance with both $Pt_{0.75}$-$Ir_{0.25}$ and $Pt_{0.25}$-$Ir_{0.75}$ anodes. The operating potential with the $Pt_{0.75}$-$Ir_{0.25}$ anode presented a little decay (1.38 V to 1.19 V over 75 min), while, for the $Pt_{0.25}$-$Ir_{0.75}$ anode, the cell voltage had slightly higher fluctuation around 1.0 V over the tested period. The fluctuation of the cell potential could be attributed to the oxygen escape from the cathode by the decomposition H_2O_2 [see Eq. (2.12)] or/and the evolution of H_2 from BH_4^- hydrolysis at the anode surface. O_2 and H_2 gas bubbles could also accumulate on the surfaces of the catalysts and hinder [145] the transferring of the primary reactants (BH_4^- or H_2O_2), which could be the cause of potential loss [224].

Long-term stability test can be done using larger volume of electrolytes, or periodically refreshing the solutions. However, some studies showed good cell stabilities for a more extended period [(90 h) [85], (25 h) [130]] using Pt alloys. For example, Ma et al. [85] evaluated the performance of Ni-Pt/C and Ni-Pd/C (both catalysts 25:1) as potential anodes for DBFCs. The test was carried out under 50 mA cm^{-2} in a period of about 100 hours at 298 K. The anode electrolyte contained 1.32 mol dm^{-3} BH_4^- + 2.5 mol dm^{-3} NaOH (5 cm^3 min^{-1}) and the catholyte was humidified oxygen (0.15 dm^3 min^{-1}), and a Nafion® 212 membrane separated the two solutions.

The cell started with a low potential of 0.68 V ($BH_4^- \| O_2$ cell), and it lost around 0.1 V over 90 hours of continuous operation. The authors observed the gradual decline and mentioned many possible reasons, such as the dissolution and agglomeration of the anode catalysts, the poisoning of active anode sites, deactivation of cathode and ion exchange membrane by sodium hydroxide and sodium carbonate (formed from the CO_2 in the ambient air).

Cheng and Scott [87] evaluated the durability at 20 mA cm^{-2} for 50 hours of titanium mesh–supported Au and Ag anodes (3D) in a DBFC, the performances of which were compared with two carbon-supported catalysts. Even though Au was expected to be more stable than Pt, the authors reported double the decline in the cell potential of all Au and Ag (mesh and carbon) electrodes of Ma et al.’s [85] results, who used a Pt alloy for a longer time period. For example, the cell voltage of Cheng and Scott’s DBFC with a Au/Ti mesh anode declined by approximately 0.2 V within 50 h (from 0.68 V to 0.48 V). They [87] attributed this decline to the same factors that were mentioned by Ma et al. [85], which caused a gradual deterioration in the Au and Ag electrodes. However, replacing H_2O_2 for O_2 as an oxidant could prevent sodium carbonate formation; using a AEM so that OH^- will migrate, not Na^+, could also be a solution. Cheng and Scott observed that 3D electrodes presented somewhat good stability – 50% higher in terms of the current densities – and power densities around 20% greater than those of Au/C and Ag/C (2D).

These findings led the current author to evaluate the performance of a $Pt_{0.75}$-$Ir_{0.25}$ catalyst with different Ti structures from an electrochemical engineering perspective, as $Pt_{0.75}$-$Ir_{0.25}$ showed promising kinetic parameters and cell performance. To the best of the author's knowledge, however, no publication has ever presented mass-transfer measurements of borohydride ions using different 3D electrodes, which can potentially further improve the DBFC and which are considered in next chapter.

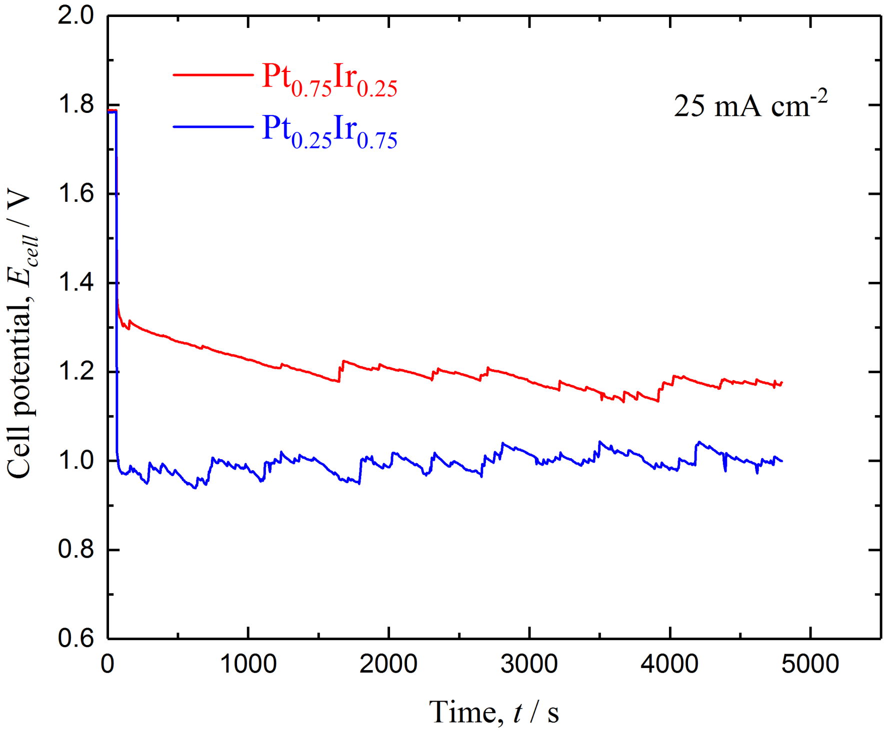

Figure 4.24. The stability of the $NaBH_4 \| H_2O_2$ cells using $Pt_{0.75}$-$Ir_{0.25}$/Ti and $Pt_{0.25}$-$Ir_{0.75}$/Ti plate anode catalysts (9 cm^2) and Pt/Ti mesh as a cathode operating at a current density of 25 mA cm^{-2} at 25 °C. The anolyte consisted of 1 mol dm^{-3} $NaBH_4$ + 4 mol dm^{-3} NaOH (0.2 dm^3) and the catholyte consisted of 1 mol dm^{-3} H_2O_2 + 1 mol dm^{-3} HCl (0.2 dm^3). The mean linear fluid velocity was 1 cm s^{-1}.

4.4. Conclusion

In summary, the $Pt_{0.75}$-$Ir_{0.25}$/Ti and $Pt_{0.25}$-$Ir_{0.75}$/Ti anodes were prepared, characterised and evaluated for DBFCs. The two electrocatalysts presented activity towards direct oxidation of BH_4^-, along with its hydrolysis. The Pt_x-Ir_x catalysts also showed high activity towards the HOR due to the fully-dissociative adsorption of BH_4^- over the surface of the examined catalysts at low potentials. CV measurements of Pt_x-Ir_x showed four anodic peaks in sodium borohydride alkaline solutions. Among the catalysts investigated, the bimetallic $Pt_{0.75}$-$Ir_{0.25}$/Ti catalyst demonstrated both the highest BOR current densities and the most number of electrons exchanged. Its reaction rate was faster and its activation energy was lower than $Pt_{0.25}$-$Ir_{0.75}$/Ti. Table 4.6 summarises the kinetics parameters and electrochemical measurements.

Table 4.6. The summary of the electrocatalyst parameters of $Pt_{0.75}$-$Ir_{0.25}$ and $Pt_{0.25}$-$Ir_{0.75}$.

Parameters	Anode catalyst		Conditions at
	$Pt_{0.75}$-$Ir_{0.25}$	$Pt_{0.25}$-$Ir_{0.75}$	
Apparent activation energy, E_a^{app} / kJ mol^{-1}	18.6	28	0.2 V *
Charge transfer coefficient, α	0.59	0.42	peak a2
Total number of electrons exchanged, z	5.3	3.7	peak a2
Standard heterogeneous rate constant, k_s / cm s^{-1}	0.1×10^{-10}	5×10^{-15}	peak a2
Heterogeneous rate constant, k_a / cm s^{-1}	0.40	0.55	-0.2 V
	0.37	0.64	0.0 V
	0.38	0.41	+0.2 V
The reaction orders, β	0.82	0.69	-0.2 V
The reaction constants, y	198	60	-0.2 V
Mass-transfer coefficient, $k_m(v)$ / cm s^{-1}	$0.8\times10^{-3}v^{0.38}$	$0.6\times10^{-3}v^{0.54}$	+0.2 V
Peak power density / mW cm^{-2}	84	40.7	333 K
Cell potential at peak power density / V	0.75	0.7	
Current density at peak power density / mA cm^{-2}	111	57.8	

*All potentials *vs.* Hg/HgO

Chapter 5: Mass-Transfer Measurements at Porous 3D Platinum-Iridium/Titanium Electrodes in Direct Borohydride Fuel Cell

The volumetric mass-transport coefficients ($k_m A_e$) for borohydride ion oxidation at various titanium three-dimensional (3D) electrode structures in a rectangular flow channel were determined by applying chronoamperometry tests in a single electrochemical flow cell. The 3D electrodes used for the oxidation of borohydride in alkaline media included flat, mesh, micromesh, fine mesh and felt coated with $Pt_{0.75}$-$Ir_{0.25}$ alloy catalysts. These five electrodes were prepared, characterised and evaluated by using different electrochemical techniques.

5.1. Introduction

The advantages of the direct borohydride fuel cell (DBFC, $NaBH_4 \| H_2O_2$) include high theoretical cell potential (2.11 V) [29] and specific energy density (*ca.* 12 kW h kg^{-1}) from a liquid fuel at 25 °C. The possibility of achieving high energy density in this system has attracted academic and industrial interest for applications in portable electronic devices, transportation, space and underwater vehicles [29 28 24]. The anodic oxidation of borohydride ions in an aqueous alkaline solution can occur directly at a wide range of anode catalysts to release a maximum of eight electrons [88 12]:

$$BH_4^- + 8OH^- \rightarrow BO_2^- + 6H_2O + 8e^- \qquad E^o_{Anode} = -1.24\ vs.\ \text{SHE} \tag{5.1}$$

This reaction coupled with the cathodic reduction of H_2O_2 in alkaline media, Eq. (5.2), can provide a theoretical cell potential of 2.11 V [29 63]:

$$4H_2O_2 + 8e^- \rightarrow 8OH^- \qquad E^o_{cathode} = 0.87\ \text{V}\ vs.\ \text{SHE} \tag{5.2}$$

Many advantages of employing 3D materials have been observed [225] [177] [226] for FCs as the following:

1. Allowing high residence time (space-time yield) [176] [227], which might help to consume the hydrogen generated in the anode by the borohydride hydrolysis [Eq. (2.2)] during the heterogeneous reaction [142]; enhancing the fuel utilisation efficiency.
2. The porous 3D electrodes can provide a highly active area per unit electrode volume which is expected to reduce the cell volume and electrode costs [102] by minimising the amount of noble metal required [48] and fully utilising the active site.
3. Developing turbulent flow, which enhances the mass-transport conditions close to the electrode surface [149].
4. They are mechanically robust and perform remarkably due to the quick release of by-product gases, preventing the active sites from attracting gas bubbles and becoming blocked [101] [102].

Many materials were used to investigate the effectiveness of 3D electrodes in DBFCs, such as nickel [102], copper [150], reticulated vitreous carbon (RVC) [88] and titanium [87]. Borohydride oxidation on gold nanoparticles/nanotubular titanate oxide presented the double performance of that from a Au/C [151] in agreement with [153]. Titanium mesh coated with Au (4 cm^{-2}) revealed significant power densities – 50% higher at 85 ^{o}C – than those obtained with Au/C [87]. Titanium supporter is promising material because of their acceptable conductivity (2.1×10^6 S m^{-1}, Alfa Aesar data sheet) compared to carbon (0.07×10^6 S m^{-1} at 293 K), high mechanical and electrochemical stability (unlike carbon in high alkaline solution), open structure and ease of manufacturing [63]. However, Ti should be coated to avoid developing titanium oxides, which create a non-conductive layer (insulating oxide layer).

Several limitations restrict the rapid development of DBFC technology. One of the major challenges is finding cost-effective electrocatalysts for borohydride oxidation that can minimise the hydrolysis of borohydride and increase its selectivity and reaction rate. Another challenge is to find electrode support structures and architectures which improve mass-transfer rates and can be scaled up. In this research, titanium materials were considered as substrates due to the above advantages. They were coated with Pt-Ir (75:25) to investigate the oxidation of borohydride ions on 3D electrodes. This chapter seeks to improve DBFC performance by evaluating well-defined 3D anode structures using the limiting current technique to characterise their mass-transfer properties. The limiting current technique [185] [183] [228] [229] [182] represents the maximum possible rate of electrochemical reactions on the electrode surface, under complete mass-transport control, at a given mean linear flow velocity [230]. In the mass-transfer controlled region, the current depends on the rate of the supply of electroactive species to the electrode, which can be determined by the volumetric mass-transport coefficient ($k_m A_e$):

$$k_m A_e = \frac{I_L}{zFcV_e} \tag{5.3}$$

Where k_m (cm s^{-1}) is the mass-transport coefficient, A_e (cm^{-1}) is the active electrode area per unit of electrode volume, I_L (A) is the limiting current, F is Faraday's constant (96485 C mol^{-1}), c (mol cm^{-3}) is the concentration of the electroactive species (BH_4^-) in the bulk electrolyte, V_e (cm^{-3}) is the electrode volume and z is the number of electrons exchanged in the reaction. The number of electrons was assumed to be 8 based on the stoichiometric anode electrode reaction in Eq. (5.1).

5.2. Experimental details

5.2.1. Electrode preparation and characterisation

In this study, 2D and 3D electrodes were used for the oxidation of borohydride, including flat, mesh, micromesh, fine mesh and felt-coated electrodes with $Pt_{0.75}$-$Ir_{0.25}$ alloy catalysts. Figure 5.1 shows titanium anodes coated with Pt-Ir (2 mg cm^{-2}): (a) flat, (b) mesh, (c) micromesh, (d) fine mesh and (e) felt. The counter electrode (f) was the Pt/Ti mesh (2 mg cm^{-2}, the same one was used in Chapter 4). All the electrodes were constructed in-house from commercially available Ti materials and coated by a commercial supplier (Magneto Special Anodes B.V.). The deposition method of the six electrodes was described thoroughly in Chapter 4 (section 4.2.1). The physical characteristics of these anodes are listed in Table 5.1. The porosity of the electrodes was measured volumetrically by measuring the amount of liquid filling the void space within the solid structures. Scanning electron microscopy (SEM) was carried out using a JSM-6500F field emission electron microscope (JEOL Inc, USA).

The Pt-Ir/Ti plate electrode (9 cm^2) in Figure 5.1a) was formed with a thickness of 0.9 mm and a 99.7 wt.% of pure titanium (Alfa Aesar Ltd., UK) coated with Pt-Ir catalyst (75:25 for all working electrodes in this work). The electrode was tested with three stacked, inert polypropylene mesh turbulence promoters (TPs, 1.3 mm thickness, LWD 8.0 mm and SWD 6.8 mm). The used TP can be seen in Figure 4.6 and the plot of standard dimension abbreviations of mesh in Figure 4.1. Its effect on electrochemical flow cells was discussed in Chapter 2.

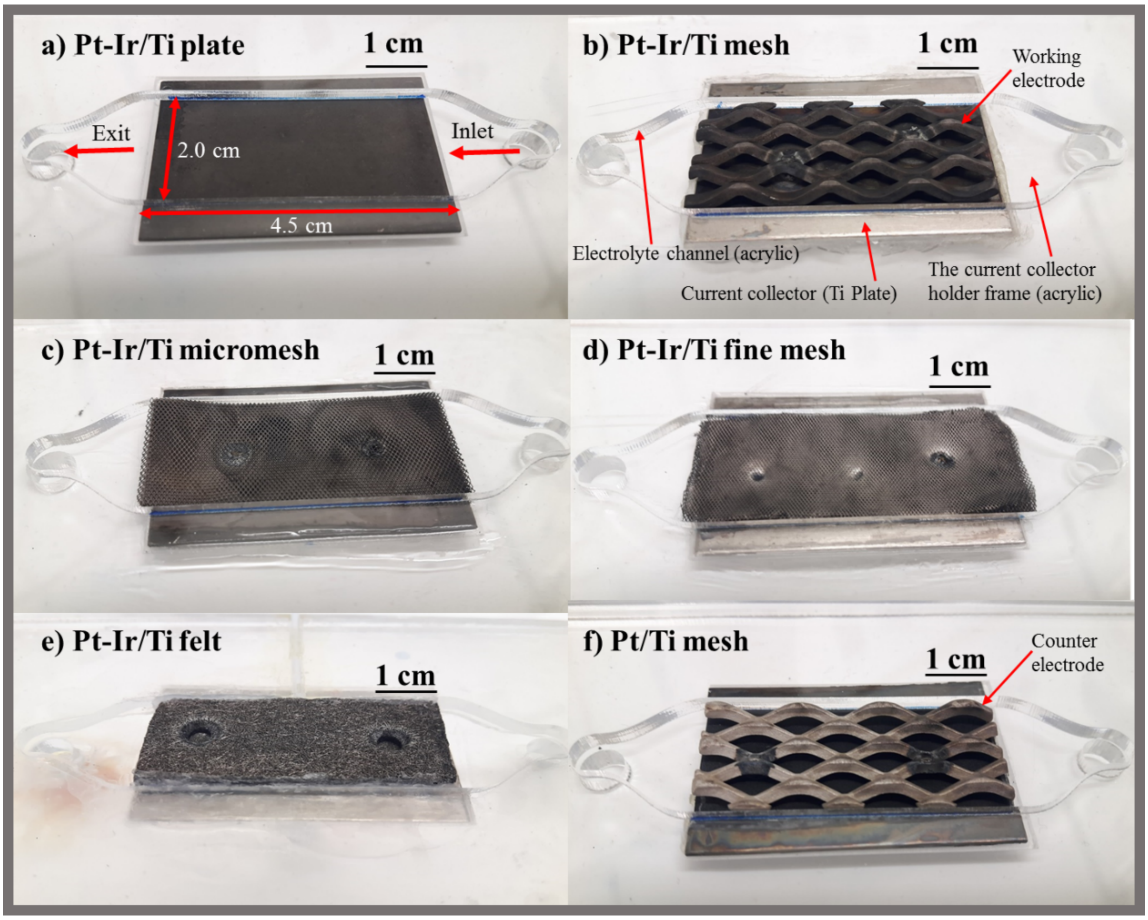

Figure 5.1. Various electrode materials spot-welded into a Ti plate and placed in a current collector holder frame a) Pt-Ir/Ti plate, b) Pt-Ir/Ti mesh, c) Pt-Ir/Ti micromesh, d) Pt-Ir/Ti fine mesh, e) Pt-Ir/Ti felt and f) Pt/Ti mesh (the counter electrode).

The Pt-Ir/Ti mesh in Figure 5.1b) was only one mesh (3 mm thickness, strand width 2 mm, LWD 12.5 mm, SWD 7.0 mm) spot-welded to a Ti plate (0.9 mm thickness) to form an overall 19 mm × 45 mm × 3 mm (8.55 cm^2) electrode. An inert polypropylene mesh stacked on the surface of the Pt-Ir/Ti mesh electrode was used as a TP to evaluate its effect on the mass-transport rate.

Fifteen identical Ti micromeshes (170 µm thickness, LWD 1.0 mm, SWD 0.670 mm) (Dexmet Co., USA) were coated with a Pt-Ir/Ti micromesh and spot-welded to a Ti plate, forming a 20 mm × 45 mm × 2.4 mm (9 cm^2) electrode, as seen in Figure 5.1c). The Ti fine mesh electrode (Dexmet Co., USA) was formed from 30 identical expanded titanium fine meshes (50 µm thickness, strand width 0.15 mm, LWD 0.79 mm, SWD 0.46–0.61 mm) and then coated with Pt-Ir and finally spot-welded to a Ti plate to be 20 mm × 45 mm × 2 mm (9 cm^2), as seen in Figure 5.1d).

The Pt-Ir/ Ti felt (3.6 mm thickness, 19 mm × 45 mm area) (NV Bekaert SA, Belgium) was also connected to a Ti current collector plate at two spot-welded points, as seen in Figure 5.1e). For the counter electrode, Pt/Ti mesh (3 mm thickness, strand width 2 mm, LWD 12.5 mm, SWD 7.0 mm) was spot-welded to a Ti plate, as seen in Figure 5.1f). The five anode electrodes were investigated using the single flow cell that is shown in Figure 4.5 (the hydraulic circuit) and explained in Chapter 4 (section 4.2.4.); the expanded view of the cell can be seen in Figure 4.3 (described in the same section).

5.2.2. Flow dispersion measurements

A perturbation-response technique was used to obtain the flow dispersion curves by carrying out electrochemical measurements, namely, chronoamperometry. Normally, the conductivity of the electrolyte is monitored at the cell outlet, while a saturated solution [such as potassium chloride (KCl)] is manually injected through the electrolyte inlet. Because an alternating-current (AC) conductivity meter connected to a chart reader was not available, the experiment was conducted with electrochemical measurements instead. In the experiment, deionised water at 288 K (15 ºC) was passed through the anode compartment (a single pass), while a 2 mol dm^{-3} NaOH electrolyte was circulated in the cathode compartment by a peristaltic pump, as seen in Figure 4.5.

Table 5.1. Characteristics of Pt-Ir /Ti anode electrodes used in this study.

Electrode type	**Number of electrodes**	**Breadth, B/ cm**	**Height, S/ cm**	**Length, cm**	**Equivalent diameter, $d_e=2BS/(B+S)$/ cm**	**Dimensionless length, $L_e= d_e/L$**	**Aspect ratio $\gamma=S/B$**	**Volumetric porosity, ε**	**Projected area, A/ cm^2**	**Electrode volume, V_e / cm^3**
plate + TP	1 + 3 TP	2	0.39	4.5	0.653	0.145	0.195	0.73	9	3.51
mesh	1	1.9	0.3	4.5	0.518	0.115	0.158	0.725	8.55	2.57
mesh +TP	1 + 1 TP	1.9	0.43	4.5	0.701	0.156	0.226	0.683	8.55	3.68
micromesh	15	2	0.24	4.5	0.429	0.095	0.120	0.53	9	2.16
fine mesh	30	2	0.2	4.5	0.364	0.081	0.100	0.82	9	1.80
felt	1	1.9	0.36	4.5	0.605	0.135	0.189	0.8	8.55	3.08

The current was measured *vs.* time using a chronoamperometry test (at +0.2 V *vs.* Hg/HgO) to obtain the borohydride oxidation current curve at different flow velocities (2, 4, 6 and 10 cm s^{-1}). After 10 s, a concentrated borohydride solution of 2.5 mol dm^{-3} $NaBH_4$ + 2 mol dm^{-3} NaOH was injected manually (0.5 cm^{-3}) by a syringe for 1–2 s into the distilled water at the inlet. The measurements were performed with a working electrode of $Pt_{0.75}$-$Ir_{0.25}$/Ti plate and Pt/Ti mesh cathode.

5.2.3. Limiting current *vs.* velocity

The aim of the experiments is to find the optimal performance factor, k_mA_e, for all five fabricated Pt-Ir/Ti working electrodes (Figure 5.1a-e) using the limiting current technique. The rectangular-channel flow cell, as seen in Figure 4.5, was used for the chronoamperometry measurements of the limiting current of the borohydride oxidation. The Autolab digital potentiostat was connected to the Pt-Ir/Ti working electrodes, while a platinised titanium (Pt/Ti) mesh supported by one TP was used as a counter electrode. The two compartments were separated by a CEM (Nafion® 115). Polytetrafluoroethylene (PTFE) tubing (1 mm internal diameter) was fitted to the anode compartment as a Luggin capillary to measure the potential of the anode *vs.* Hg/HgO. Small hydrogen bubbles were observed coming from the decomposing anolyte; the gas may have blocked the ionic contact between the working and reference electrodes through the Luggin capillary, causing fluctuation and inconsistency in the electrode potential measurements. Therefore, the reference electrode reservoir and electrolyte tank were connected by PTFE tubing (2 mm internal diameter; the orange line in Figure 4.5) to circulate the electrolyte and continuously remove any gas bubbles using the peristaltic pump. The mean linear flow rates of the working and counter electrode compartments were the same. To smooth outflow pulsation during the experiments, pressure pulse dampeners were fitted to the hydraulic circuit. A thermostatic water bath was used to control the electrolyte temperature.

Chronoamperometry was used on all five Pt-Ir/Ti working electrodes, to measure the limiting current *vs.* time (s) at a linear flow velocity ranging from 1 to 16 cm s^{-1}. The electrode potential was stepped from the open-circuit potential (OCP) to +0.2 V *vs.* Hg/HgO in an electrolyte of 0.01 mol dm^{-3} $NaBH_4$ and 2 mol dm^{-3} NaOH at 296 K. The counter electrode compartment contained 2 mol dm^{-3} NaOH. The summary of electrolyte properties and experimental conditions are shown in Table 5.2. The limiting current values were obtained based on the average of ten records from 25 to 35 s. Each chronoamperometry measurement was repeated three times at each flow velocity and the average limiting current was obtained *vs.* mean linear flow velocity.

Table 5.2. Characteristics of the electrolyte and process conditions.

Property	**Value**
Anolyte solution	0.01 mol dm^{-3} NaBH$_4$ 1.5 dm^3 of 2.0 mol dm^{-3} NaOH
Catholyte solution	350 cm^3 of 2.0 mol dm^{-3} NaOH
Kinematic viscosity of electrolyte, ν	0.02 cm^2 s^{-1} [198]
Diffusion coefficient of BH$^-_4$, *D*	2.23×10^{-5} cm^2 s^{-1} [198]
Schmidt number, *Sc*, *ν*/*D*	862
Range of mean linear velocity, *v*	0–16 cm s^{-1}
Temperature	296 K

5.2.4. Limiting current *vs.* concentration

The volumetric mass-transfer coefficient can also be obtained by measuring the limiting current of different borohydride concentrations (*c*) based on Eq. (5.3). Therefore, the chronoamperometry experiment (at +0.2 V *vs.* Hg/HgO) was also performed in the same flow cell arrangement (Figure 4.5) described in the previous section. It consisted of Pt-Ir/Ti mesh as the working electrode which was connected to the reference electrode Hg/HgO and Pt/Ti mesh as the counter electrode. A dilution series of borohydride solutions was prepared: 0, 2, 4, 6, 8, 10, 12, 14, 16 and 18 × 10^{-3} mol dm^{-3} NaBH$_4$ in 2 mol dm^{-3} NaOH. The volume of both electrolyte tanks was 250 cm^3 and $v = 3.8$ cm s^{-1} at 296 K.

5.2.5. Cell polarisation

The polarisation experiments were performed on a single flow cell. The cell potential and power density *vs.* current density were measured for all Pt-Ir/Ti anode electrodes. The rate of applied current density was 5 mA cm^{-2} min^{-1} from 0 to 140 mA cm^{-2}. The cell arrangement was like that shown in Figure 4.5; the cell was connected to a BST8-A3 battery analyser (MTI, USA) and disconnected from the reference electrode. The anolyte vessel (250 cm^{-3}) contained a solution of 2.5 mol dm^{-3} $NaBH_4$ in 2 mol dm^{-3} NaOH, while the catholyte (250 cm^{-3}) had 0.75 mol dm^{-3} H_2O_2 in 2 mol dm^{-3} NaOH (both at 296 K). The peristaltic pump recirculated the electrolytes at a 4 cm s^{-1} linear flow velocity.

5.3. Results and discussion

5.3.1. Characterisation of the electrodes

All SEMs are presented at magnifications of 1 mm and 100 µm. Figure 5.2a) and 5.2b) show SEM images of the Ti plate coated with Pt-Ir, which exhibited the homogeneity of the alloy. The Pt-Ir/Ti micromesh (Figure 5.2c and 5.2d) and fine mesh (Figure 5.2e and 5.2f) electrodes also showed uniform, compact Pt-Ir coatings. Even though the 15 Ti micromesh sheets were spot-welded to a Ti plate and then coated, all layers presented a homogenous, uniform deposition (see Figure 5.2c and 5.2d).

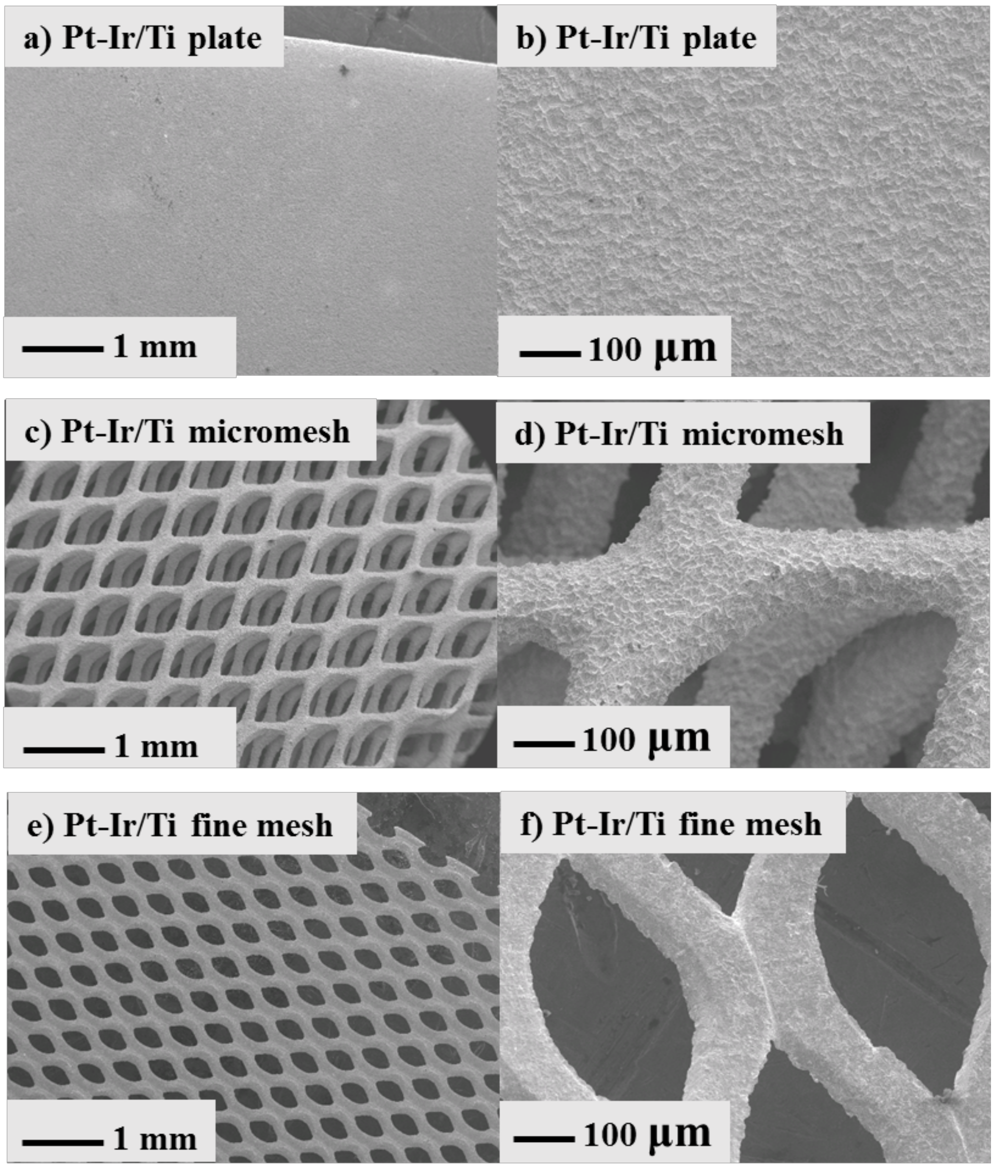

Figure 5.2. SEM images of the three Ti materials supporting Pt-Ir used as anode : a-b) the Pt-Ir/Ti plate, c-d) the Pt-Ir/Ti micromesh and e-f) the Pt-Ir/Ti fine mesh.

Figure 5.3a) and 5.3b) display the SEM images of uncoated felt which were compared with the coated one, as can be seen in Figure 5.3c) and 5.3d). The internal and external fibres appear to be uniformly covered with Pt-Ir catalysts with some agglomeration. The morphology of the Pt-Ir/Ti mesh, seen in Figure 5.3e, presents a well-coated surface. However, the Pt/Ti mesh (cathode) shows black spots, especially at the edges, which might represent the non-uniform distribution of Pt over the Ti surface because of uneven current distribution during the electrodeposit of Pt.

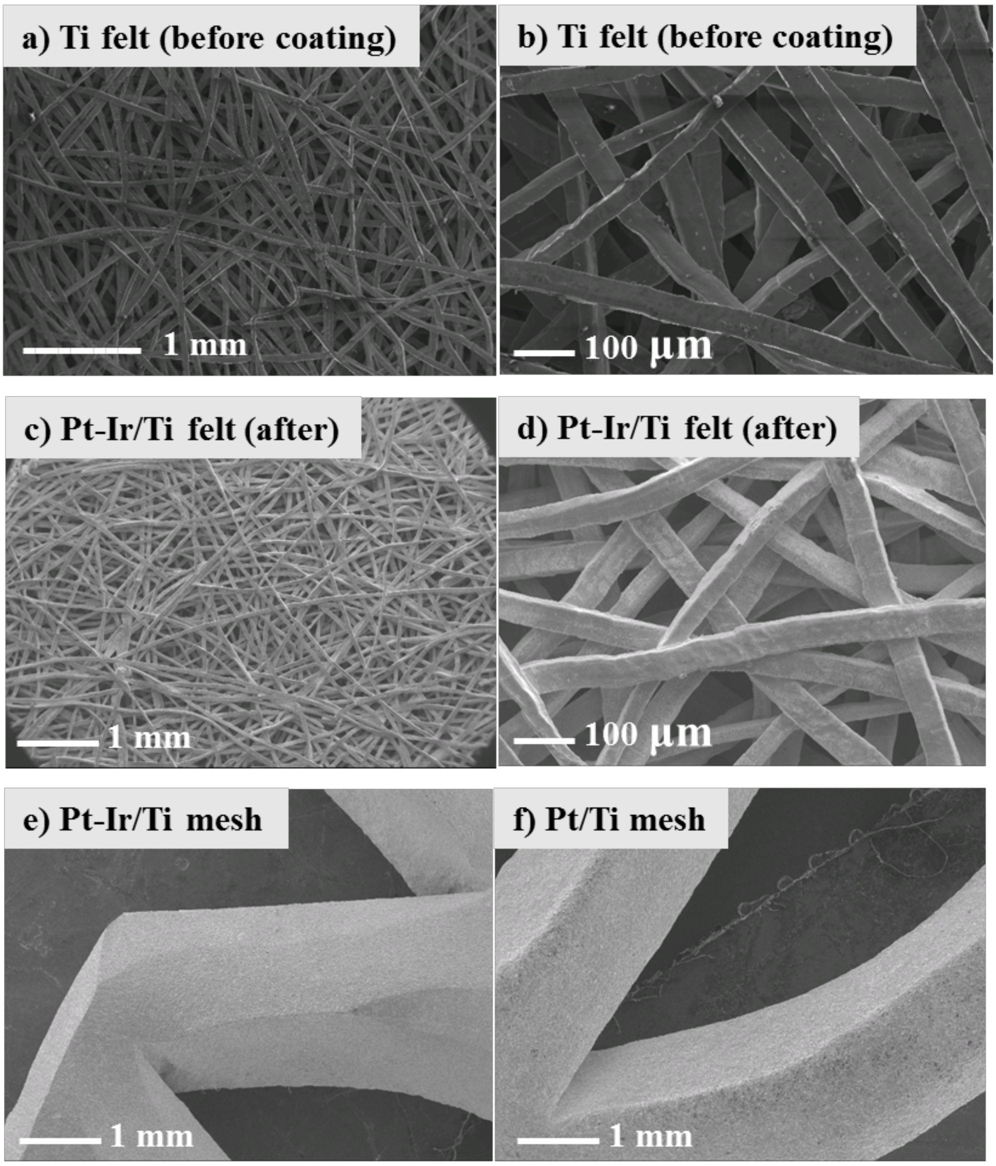

Figure 5.3. SEM images showing the surface morphologies of a-b) Pt-Ir/Ti felt before coating, c-d) Pt-Ir/Ti felt after coating, e) Pt-Ir/Ti mesh (felt and mesh anodes) and f) Pt/Ti mesh, which was used as a counter electrode.

5.3.2. Flow dispersion

The curves in Figure 5.4 show the current variations from borohydride oxidation at different mean linear flow velocities of the electrolyte. The graph presents one peak for all velocities; only a small shoulder was observed in the case of 2 cm s^{-1}. The total charge transferred per single injection (0.5 cm^3 of 2.5 mol dm^{-3} $NaBH_4$ + 2 mol dm^{-3}) at the inlet, Q (C), can be obtained by integrating the area under the curve:

$$Q = \int I dt \tag{5.4}$$

The total mass of BH_4^- consumed, m (g), can thus be calculated by the following:

$$m = \frac{QM_w}{zF} \tag{5.5}$$

Where z is the total number of electrons ($8e^-$), M_w is the molar mass of $NaBH_4$ (37.83 g mol^{-1}) and F is Faraday's constant (96485 C mol^{-1}). Figure 5.5 illustrates that the total mass-consumption of borohydride ions increases as flow velocity decreases, which was expected due to the rise of the borohydride residence time in the cell – see Eq. (5.6). Less than 0.15% of borohydride ions were consumed per pass per injection.

$$\tau_T = \frac{V_T}{Q_V} \tag{5.6}$$

Where τ_T (s) is the mean residence time in a reservoir containing a certain volume, V_T (cm^3), of electrolyte, and Q_V (cm^3 s^{-1}) is the electrolyte volumetric flow rate. The time needed to consume borohydride ions in a chronoamperometry test is much higher than the residence time of an electrolyte in the cell. For example, the current gained from borohydride oxidation at a velocity of 2 cm s^{-1} took around 30 s (see Figure 5.4); however, the theoretical residence time of the electrolyte was 2.25 s (see Figure 5.5). This difference could be attributed to the injection time, which was relatively slow (1–2 s). Moreover, the adsorbed ions on the electrode surface may have required a specific depletion time. As has been found in this research, the standard heterogeneous rate constant, k_s, was found to be very slow (0.1×10^{-10} cm s^{-1}) at the Pt-Ir/Ti plate electrodes

(Chapter 4). It is worth repeating this experiment with a 3D electrode to investigate this hypothesis.

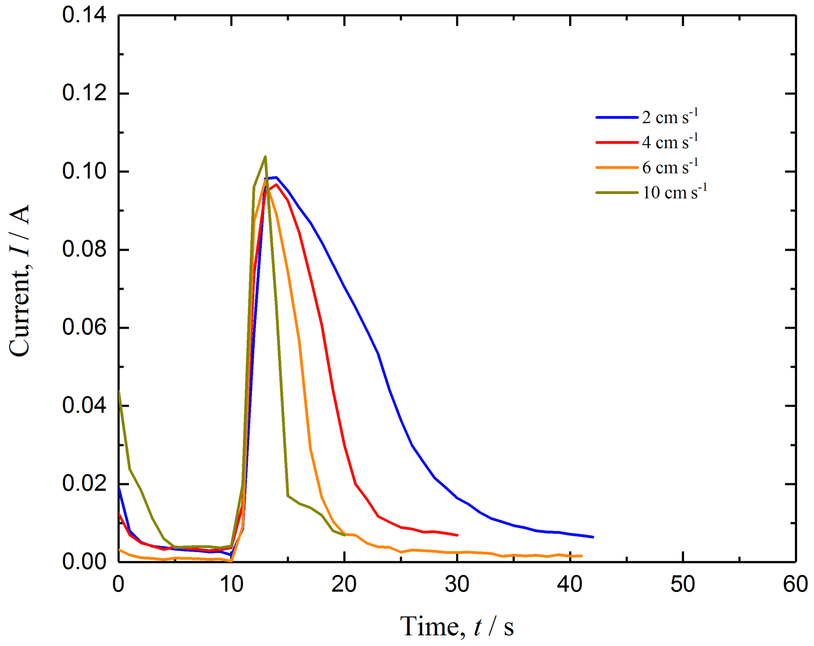

Figure 5.4. Flow dispersion curves of chronoamperometry (+0.2 V *vs.* Hg/HgO) of borohydride oxidation at different flow rates at 15 °C. A saturated borohydride solution of 2.5 mol dm^{-3} $NaBH_4$ + 2 mol dm^{-3} NaOH was injected manually (0.5 cm^{-3}) after 10 s of running the test at the inlet of electrolyte, which contained distilled water. The working electrode was a Pt-Ir/Ti plate and the counter electrode was Pt supported on Ti mesh.

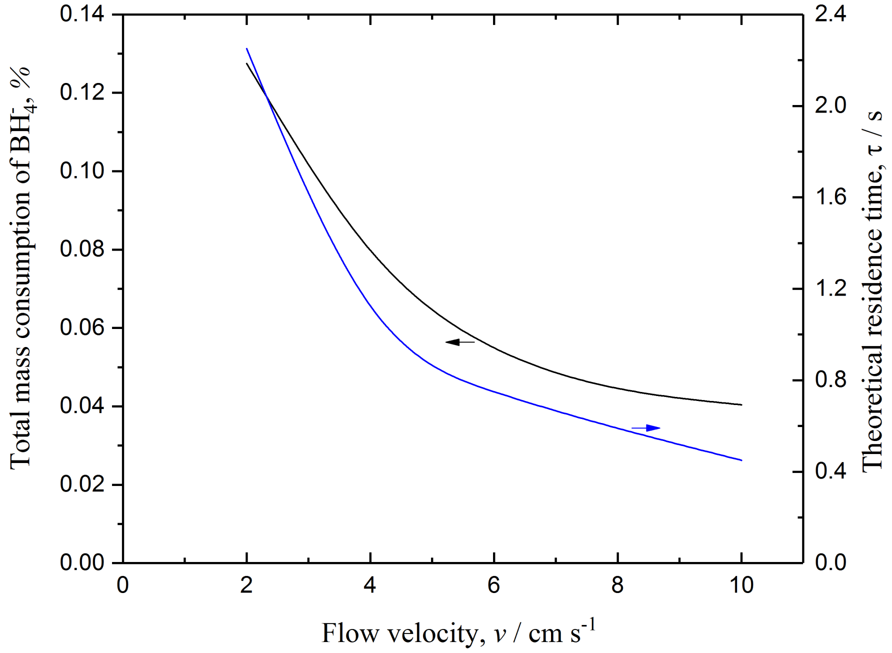

Figure 5.5. Mean linear flow velocities *vs.* total mass consumption of BH_4^- per a single pass and the theoretical residence time of the electrolyte in the cell at 15 °C. The data was calculated from Figure 5.4.

5.3.3. Linear sweep and chronoamperometry experiments

To determine the electrode overpotential value to carry out chronoamperometry measurements of the limiting current, polarisation curves were obtained using a gold RDE, as shown in Figure 5.6. The limiting current (plateau) of the borohydride oxidation was observed in the mass-transfer controlled region between -0.1 and 0.30 V *vs.* Hg/HgO. All electrode rotating speeds represented the limiting current plateau in a similar region. The applied potential value of +0.2 V *vs.* Hg/HgO was used in the chronoamperometry experiments with all anode electrodes (shown in Figure 5.1) for the sake of consistency.

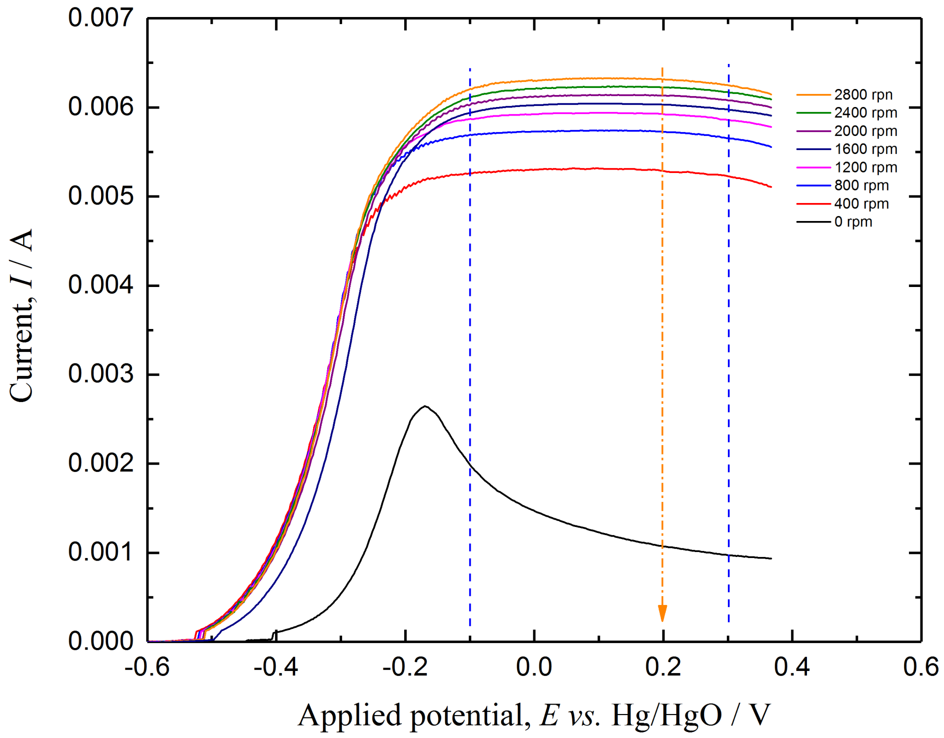

Figure 5.6. The linear sweep voltammetry (LSV) of a gold planar electrode (0.125 cm^2) at different rotation speeds in a solution containing 0.018 mol dm^{-3} in $NaBH_4$ in 2 mol dm^{-3} NaOH at 23 °C. The counter electrode was Pt mesh (1 cm^2) in a three-electrode cell.

The limiting current plateaus were obtained for the oxidation of borohydride ions on all anodes (Table 5.1) as a function of the mean linear flow velocity. As a sample, Figure 5.7 presents the chronoamperometry measurements of the borohydride oxidation on the Pt-Ir/Ti mesh [the large mesh is shown in Figure 5.1b)]. All the responses showed well-defined limiting current plateau which increased with the mean linear flow velocity. When the potential stepped from the OCP (-0.97 V) to +0.2 V *vs*. Hg/HgO in Figure 5.7, the current rapidly accelerated for all mean linear velocities due to the charge of the double layer and the oxidation of the borohydride ions on the electrode surface [175] [144]. The current then decreased to the steady-state value, i.e. the limiting current value, I_L.

The borohydride concentration for these experiments was 0.01 mol dm^{-3}, as higher concentrations caused fluctuation (oscillation) of the limiting current measurements, possible because of the hydrogen gas bubbling in the channel due to borohydride hydrolysis. This $NaBH_4$ concentration was found to be suitable for all tested electrodes. Fluctuations in the measurements were also observed at higher mean linear velocities, as can be seen from the slightly larger error bars in Figure 5.8a) and 5.8b).

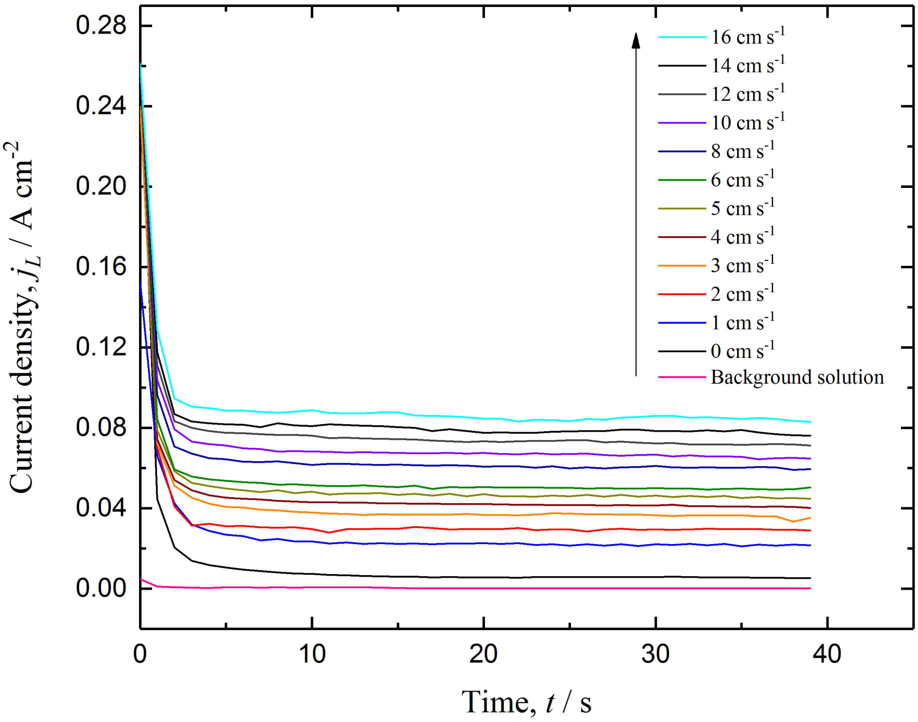

Figure 5.7. Chronoamperometry (at +0.2 V *vs.* Hg/HgO) with different mean linear flow velocities of a half-cell operating at 23 °C. The anolyte consisted of 0.01 mol dm^{-3} $NaBH_4$ in 2 mol dm^{-3} NaOH and 2 mol dm^{-3} NaOH in the counter electrode compartment. Both the anode and counter electrode were Pt-Ir/Ti meshes.

5.3.4. Limiting current and enhancement factor

Figure 5.8a) shows the limiting current density as a function of the mean linear flow velocities for the plate and mesh electrodes in the presence and absence of a TP, using chronoamperometry at a constant potential of +0.2 V *vs.* Hg/HgO in solutions consisting of 0.01 mol dm^{-3} $NaBH_4$ in 2 mol dm^{-3} NaOH. Figure 5.8b) compares the data obtained from the micromesh, fine mesh and felt electrodes to the results of the plate electrode.

All the curves show the expected increase in limiting current as the mean linear electrolyte flow rate increased. As seen in Figure 5.8, the felt and fine mesh electrodes showed the highest currents, followed by the micromesh, the mesh with one TP, the mesh without a TP, the plate with three TPs and the plate without a TP, sequentially. The average limiting currents measured at a low flow velocity of 2 cm s^{-1} were 5, 10, 24, 30, 116, 222 and 473 mA cm^{-2} for the plate, the plate + 3 TPs, the mesh, the mesh + 1 TP, the micromesh, the fine mesh and the felt, respectively. At the highest mean flow velocity used (16 cm s^{-1}), the average limiting current values were 19, 32, 64, 84, 295, 1088 and 1254 mA cm^{-2}, respectively. The productivity of the porous electrodes improved dramatically, even under high mass-transfer conditions in which the electrolyte might bypass the electrodes.

The plate electrode presented a linear relationship between the limiting current and the mean linear flow velocity, while the other electrodes followed a logarithmic relationship. A change of slope was observed at $v > 8$ cm s^{-1} for the felt, the micromesh, the plate + 3 TPs, the mesh and the mesh + 1 TP, whereas the change occurred at $v > 12$ cm s^{-1} for the fine mesh; these phenomena appear to be caused by some flow bypass in the cell. In this case, increasing the mean linear flow velocity does not improve the limiting current, as the mass-transport of the borohydride ions towards the electrode surface does not increase.

The enhancement factor, δ, can be used to compare the increase of the limiting current in a porous material in relation to the flat electrode [230], as expressed by the following:

$$\delta = \frac{I_{L,\ porous}}{I_{L,\ plate}} = \frac{k_m A_{e,\ porous}}{k_m A_{e,\ plate}} \qquad (5.7)$$

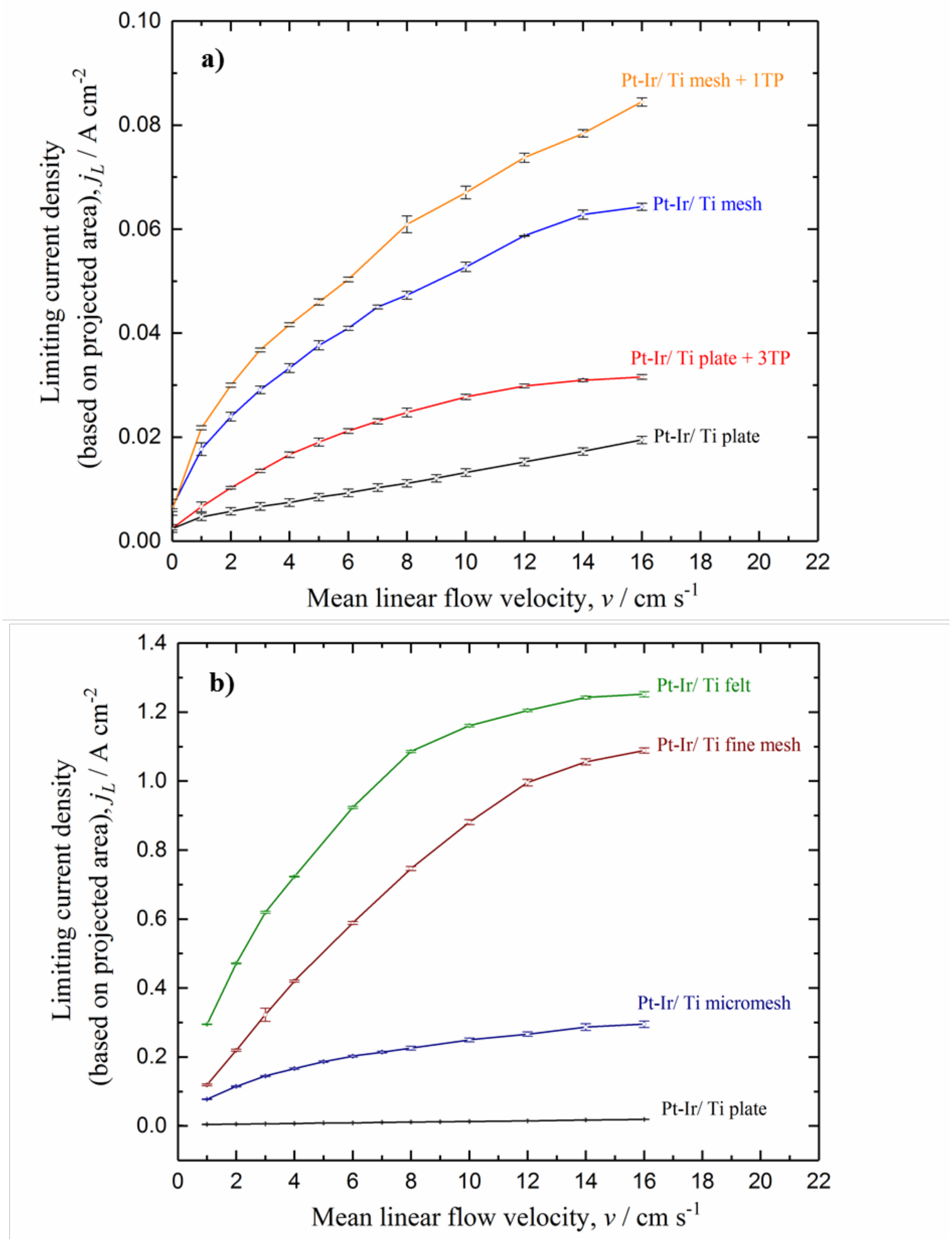

Figure 5.8. The limiting current density *vs.* the mean linear velocity obtained from chronoamperometry (at +0.2 V *vs.* Hg/HgO) for various Pt-Ir/Ti anode structures. The electrolyte consisted of 0.01 mol dm^{-3} $NaBH_4$ in 2 mol dm^{-3} NaOH at 23 °C. The counter electrode was Pt/Ti mesh in 2 mol dm^{-3} NaOH.

Figure 5.9a) shows δ *vs.* the mean linear velocity past the mesh electrode, the plate electrode with three TPs and the mesh electrode with one TP. Interestingly, in the presence of a TP, the currents extracted from the plate and mesh electrodes more than doubled. At low flow rates (e.g. 4 cm s^{-1}), which are favourable because they lower the pumping cost, the δ values were 2.2, 4.5 and 5.6 for the plate + 3 TPs, the mesh and the mesh + 1 TP stack, respectively. These were the maximum values for flow rates ranging from 1 to 16 cm s^{-1}.

At velocities above 8 cm s^{-1}, δ decreased with increasing electrolyte velocity. This decline was observed for all 3D electrodes in Figure 5.9a) and 5.10b), which can be attributed to the bypass of electrolyte mentioned previously. It is expected that δ can reach unity at a sufficiently high electrolyte flow rate. Griffiths et al. [230] studied the effect of both mass transport and pressure drop at higher flow velocities in the FM01-LC cell using the reduction of ferricyanide ions to ferrocyanide ions at a nickel cathode. The authors found that δ could reach one at 33 cm s^{-1} based on the linear correlation between the mass-transport enhancement and the mean linear electrolyte velocity, suggesting that there is no benefit to installing a TP in the system above this value.

Figure 5.9b) demonstrates the enhancement factor of the felt, fine mesh and micromesh electrodes, where a similar decline was observed at higher velocities (v > 8 cm s^{-1}); however, these electrodes show an enormous enhancement factor. The δ values of the micromesh, fine mesh and felt were 22, 57 and 88 (at 4 cm s^{-1}), respectively. The optimal values of the enhancement factor were 23 (4 cm s^{-1}), 67 (8 cm s^{-1}) and 100 (at 6 cm s^{-1}) for these electrodes in agreement with the literature. For example, the performance of nickel, including expanded metal grids and a nickel foam, has been investigated by Brown et al. [183] using an FM01-LC cell during the oxidation of alcohols and synthesis of carboxylic acids. The authors concluded that the use of 3D electrodes could enhance the overall reaction rate by a factor of up to 100. Similar results have been achieved in the present work for the BOR in a small DBFC at 23 ºC using a felt electrode.

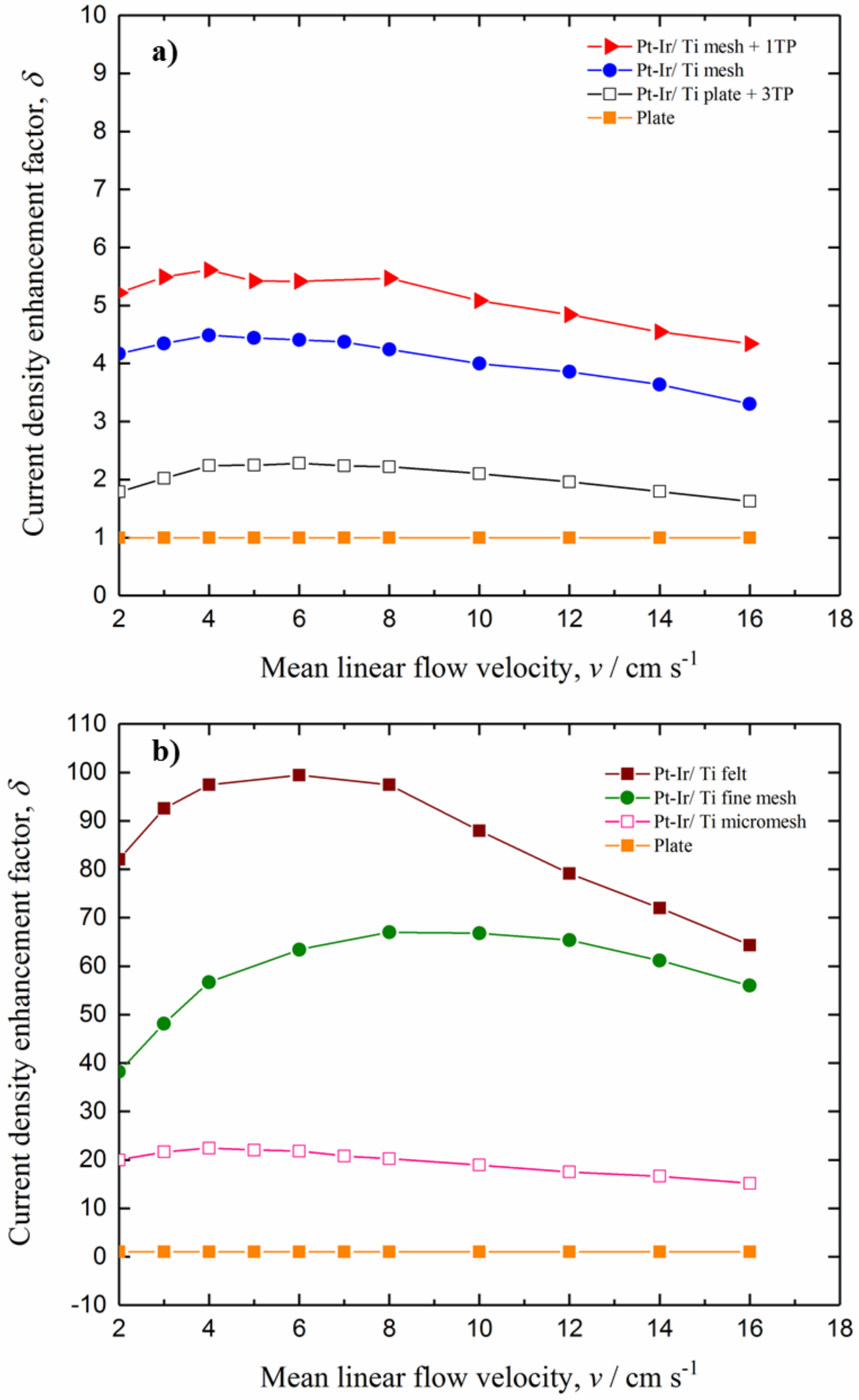

Figure 5.9. The enhancement factor *vs.* the mean linear velocity for various Pt-Ir/Ti anode materials. The electrolyte composition was 0.01 mol dm^{-3} $NaBH_4$ in 2 mol dm^{-3} NaOH at 296 K.

5.3.5. Volumetric mass-transport coefficient, k_mA_e, and Reynolds number

A log-log plot in Figure 5.10a) shows a range of k_mA_e values, calculated using Eq. (5.3), as a function of electrolyte flow velocity for several types of Ti materials coated with Pt-Ir, in the presence and the absence of TPs. The figure also shows the data from other flow cell systems, which have been taken from the literature. Figure 5.10b) presents a log-log plot of the k_mA_e values against Reynolds number, using Eq. (5.8), where it shows a fully developed laminar flow curves for all 3D Pt-Ir/Ti electrodes in comparison with the flat electrode.

$$Re=\frac{vd_e}{\nu} \tag{5.8}$$

The k_mA_e values obtained from Eq. (5.3) are under limiting current conditions in the mass-transfer controlled region. In all cases, the mass-transport rate, k_mA_e, increases towards the electrode surface, along with the electrolyte velocity and the Reynolds number. The fine mesh and felt materials show appreciably higher performance than the mesh + 1 TP and the plate + 3 TP electrodes. However, porous electrodes suffer from non-uniform potential and current density distribution in contrast to 2D electrodes, which might cause a lack of current efficiency and selectivity, especially for reactions that are highly potential-dependent [175 231].

Table 5.3 shows the values of the empirical constants p and q ($k_mA_e = pv^q$), Eq. (2.36), which was explained in Chapter 2, can characterise the performance of all the electrodes at steady-state conditions. The q value of the plate electrode increased by 10% in the presence of 3 TPs, in contrast to an empty channel. However, the q values of the mesh electrode and the mesh + 1 TP are almost equivalent. The fine mesh electrode presented the highest power value: $q = 0.82$.

Regarding p values, which are related to the active areas of electrodes, the mass-transport rate of the plate + 3 TPs, the mesh, the micromesh, the fine mesh and the felt were increased by 1.3, 4, 24, 45 and 65 times, respectively, in contrast to a plate electrode in an empty channel.

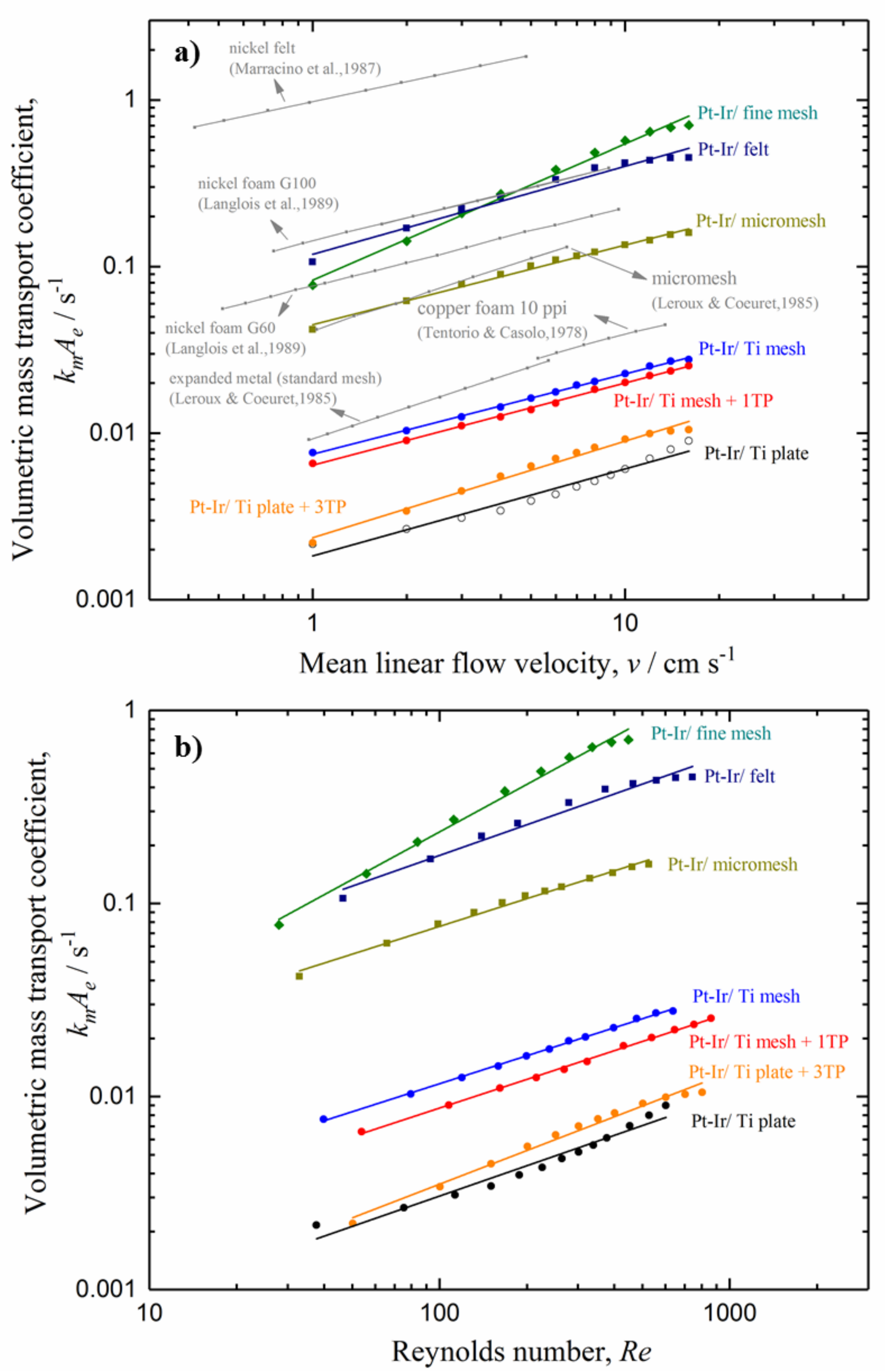

Figure 5.10. The electrode performance factor $k_m A_e$ for the oxidation of borohydride ions as a function of the a) electrolyte mean linear velocity and b) Reynolds number for different electrode structures (double logarithmic plot). The electrolyte consisted of 0.01 mol dm^{-3} $NaBH_4$ in 2 mol dm^{-3} NaOH at 296 K. The counter electrode was Pt/Ti mesh in 2 mol dm^{-3} NaOH. The materials compared in a) are (1) nickel felt [177], (2) nickel foam G100 [176], (3) nickel foam G60 [176], (4) micromesh [232], (5) 10 ppi copper foam [226] and (6) standard mesh [232].

Table 5.3. The empirical constants from the measurements of the mass-transport limiting currents for the oxidation of borohydride in 0.01 mol dm^{-3} $NaBH_4$ in 2 mol dm^{-3} NaOH at 296 K for various 3D Pt-Ir/Ti electrodes, presented as an empirical power law, $k_mA_e = p\ v^q$.

Electrode	***p***	***q***
Ti plate	1.83×10^{-3}	0.52
Ti plate + 3TP	2.36×10^{-3}	0.58
Ti mesh	7.48×10^{-3}	0.48
Ti mesh + 1TP	6.43×10^{-3}	0.49
Ti micromesh	4.48×10^{-2}	0.48
Ti fine mesh	8.28×10^{-2}	0.82
Ti felt	1.19×10^{-1}	0.53

These results mean that the electrode structure can have a strong influence on the electrode performance, which agrees with Freitas et al.'s [233] observation that, not only is the electrocatalyst important, but the electrode structure also has a decisive influence on the borohydride oxidation process. The *p* value of the flat electrode (1.3) in the presence of TPs is close to the values of 1.4 and 1.7 obtained by Recio et al. [173] with a mirror-polished nickel electrode in a rectangular flow cell (9 cm^2) and Brown et al. [184] with a nickel electrode in the FM01 electrolyser, respectively, for the reduction of ferricyanide ions.

To the best of the authors' knowledge, no data of the mass-transport coefficient for borohydride oxidation have been found for such 3D materials (3D Ti structures coated with Pt-Ir) with which the present work could compare its results. From a materials perspective, several 3D electrodes have been reported using other model reactions, namely, the reduction of ferricyanide to ferrocyanide in a laboratory-scale electrochemical cell, such as an FM01-LC reactor (projected area 4 cm × 16 cm) [230] [184] [183]. The electrolytes typically contained 1×10^{-3} mol dm^{-3} $K_3Fe(CN)_6$ with at least a fourfold excess of $K_4Fe(CN)_6$ in 1 mol dm^{-3} KOH [183]. Various materials were selected in the comparison made in Figure 5.10a). The performance (k_mA_e *vs.* v) of the Pt-Ir/Ti micromesh electrode agreed with those reported on expanded micromesh stainless steel

[232]; see Figure 5.10a, no. 4). The data obtained with the Pt-Ir/Ti fine mesh electrode are comparable to nickel foams, particularly G100 ($\varepsilon = 0.97$, thickness 2.1 mm) [176], as shown in Figure 5.10a, no. 2). The volumetric mass-transfer coefficient of the Pt-Ir/Ti mesh (present work) was lower by approximately 67% than the data obtained from standard mesh metal (No. 6) [232] and 10 ppi copper foam (No. 5) [226] at 4 cm s^{-1}. Nickel felt ($\varepsilon = 0.95$, thickness 1.4 mm) [177] shows better mass-transport performance (1.7 s^{-1}) than the Ti felt's 0.5 s^{-1} ($\varepsilon = 0.8$ in the present work). This superiority may be due to the difference in the open area; however, the compressibility of the felt and its texture are misleading [176], since they can increase the pressure drop, leading to a greater pumping power requirement.

5.3.6. Characterisation of mass transport by varying BH_4^- concentration

Another technique to determine the limiting current was used to study the effects of various borohydride-ion concentrations on the limiting current and k_mA_e. Figure 5.11a) illustrates well-defined limiting current plateaux of different borohydride concentrations for the Pt-Ir/Ti mesh electrode at a flow velocity of 3.8 cm s^{-1}. The mesh electrode has been selected to represent the 3D electrode material. As borohydride concentration increased, small gas bubbles of hydrogen were sometimes observed that temporarily blocked the Luggin capillary tube. This gas explains the fluctuation in the limiting current plots. Therefore, the data in Figure 5.11a) have been smoothed over. Figure 5.11b) shows the influence of the borohydride (BH_4^-) concentration on the limiting current value. The limiting current of the mesh electrode follows an apparently linear relationship with the BH_4^- concentration, which is evident from Eq. (5.3), as discussed at the beginning of this chapter.

$$I_L = k_m A_e z F c V_e \tag{5.3}$$

The volumetric mass-transport coefficient remained relatively constant (0.0157 s^{-1}) with respect to BH_4^- concentration, as can be seen in Figure 5.12. In this case, the limiting current rose due to the increasing number of borohydride ions while the mass-transport rate towards the electrode remained constant because the flow velocity (3.8 cm s^{-1}) and the electrode structure remained fixed. The average value of k_mA_e with various BH_4^-

concentrations reveals an acceptable agreement (9%) and 1.4% difference (0.0159 s^{-1}) at a concentration of 0.01 mol dm^{-3} BH_4^-, as seen in Figure 5.12, in comparison with the k_mA_e value obtained (0.0144 s^{-1}) using different flow velocities (Figure 5.10).

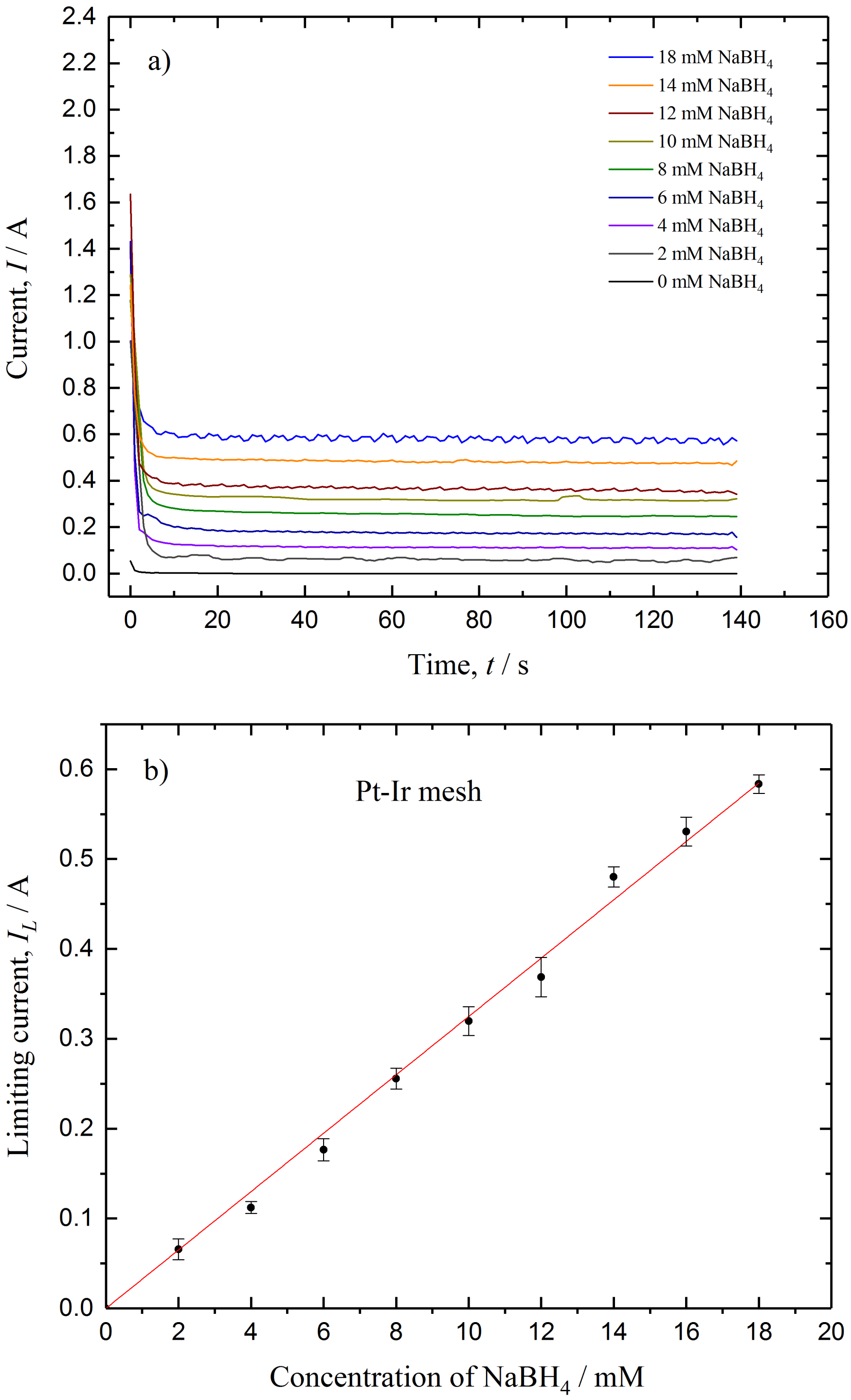

Figure 5.11. a) Chronoamperometry (+0.2 V *vs.* Hg/HgO) on a Pt-Ir/Ti mesh working electrode for a half-cell operating at 296 K. b) The limiting current *vs.* different borohydride concentrations. The electrolyte composition was $x \times 10^{-3}$ mol dm^{-3} $NaBH_4$ in 2 mol dm^{-3} NaOH. The mean linear fluid velocity was 3.8 cm s^{-1}. The counter electrode was Pt/Ti mesh in 2 mol dm^{-3} NaOH.

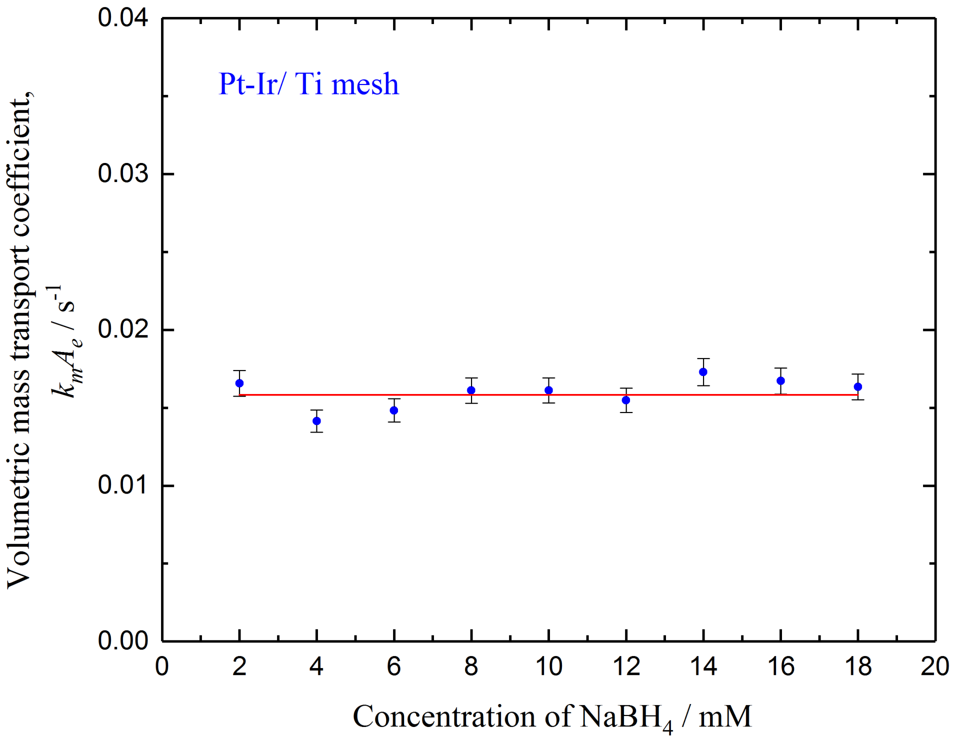

Figure 5.12. The electrode volumetric mass-transport coefficient, $k_m A_e$, for the oxidation of borohydride ions as a function of the borohydride concentration for a half-cell containing Pt-Ir/Ti mesh as the working electrode at 296 K. The electrolyte composition was $x \times 10^{-3}$ mol dm^{-3} $NaBH_4$ in 2 mol dm^{-3} NaOH. The mean linear fluid velocity was 3.8 cm s^{-1}. The counter electrode was Pt/Ti mesh in 2 mol dm^{-3} NaOH.

5.3.7. Performance of a single cell using all electrodes

Fuel cell (FC) tests were run on a single cell (Figure 4.5) using different Pt-Ir/Ti anodes at 296 K. Figure 5.13 displays the typical polarisation and power density curves. All electrodes exhibited an open-circuit cell potential of about 0.97 V apart from the felt electrode, which was slightly higher at 1.0 V. This is approximately 1.11 V lower (by more than 50%) than the theoretical value of the $NaBH_4 \| H_2O_2$ cell (2.11 V) in an alkaline solution, and 0.64 V lower (40%) than the $NaBH_4 \| O_2$ cell (1.64 V). The deviation can probably be attributed to a mixed potential at the two electrodes caused by the intermediate oxidation products of the BOR – such as H_2 (-0.828 *vs.* SHE), as shown in Eq. (2.4) – that are generated at the anode by the hydrolysis in Eq. (2.2). The deviation could also be attributed to the mixed cathode potentials in its compartment, involving the reduction of oxygen – [Eq. (2.8)] (0.4 V *vs.* SHE) [71] – that decomposed from hydrogen peroxide – [Eq. (2.12)], particularly in an alkaline medium – and the direct reduction of hydrogen peroxide – [Eq. (5.2)] (0.87 *vs.* SHE) [29] [65].

All current *vs.* potential curves in Figure 5.13 show a nearly linear response and continuous falling of the cell potential with the current density, indicating a strong dominance of ohmic resistance in the cell [29]. From Figure 5.13a) and 5.13b), the power density for studied electrodes increases in the following sequence: plate < micromesh < mesh < felt < mesh + 1 TP < fine mesh. The maximum power density for the Pt-Ir/Ti fine mesh was 44.5 mW cm^{-2} at a current density of 100 mA cm^{-2} and 0.44 V cell voltage.

The felt and micromesh electrodes in Figure 5.13b) did not perform as well as their higher surface areas would suggest, especially in comparison with the mesh electrode. For the felt electrode, significant hydrogen gas bubbles were observed during the experiment, indicating that HOR ($2e^-$) was occurring, which might explain the potential losses. Stroman et al. [234] developed a 2D DBFC model to investigate the major losses (activation, ohmic and concentration). They revealed that the largest losses come from the anode concentration and the cathode activation. Moreover, the current and potential distribution of the felt and micromesh electrodes might be non-uniform due to their structure, which may affect the reaction kinetics.

The main aim of this chapter is to study the mass transport of BH_4^- to the anode surface and the effect of the anode structure on DBFCs; however, the power achieved from the cell obtained here is relatively low compared to the reported power of such a system. This could be referred to as the activity of the Pt-Ir electrode towards BH_4^- hydrolysis and HOR, which affected the cell efficiency. However, a fine mesh substrate can be used when an efficient electroactive catalyst is found. The performance of the DBFC with Pt-Ir as an anode can be improved by using acidic media in the cathodic compartment and by optimising the operating conditions of the flow cell, such as anolyte composition, which have been considered in the following chapter. Another engineering design aspect that should be considered is the use of bipolar plate materials, flow fields and manifold design. Sanili et al. [235] evaluated DBFC performance by considering these design parameters. The power density was 67 mW cm^{-2} using parallel flow–channel bipolar plates with composite graphite, 87 mW cm^{-2} with sintered graphite and 93 mW cm^{-2} using a serpentine flow field.

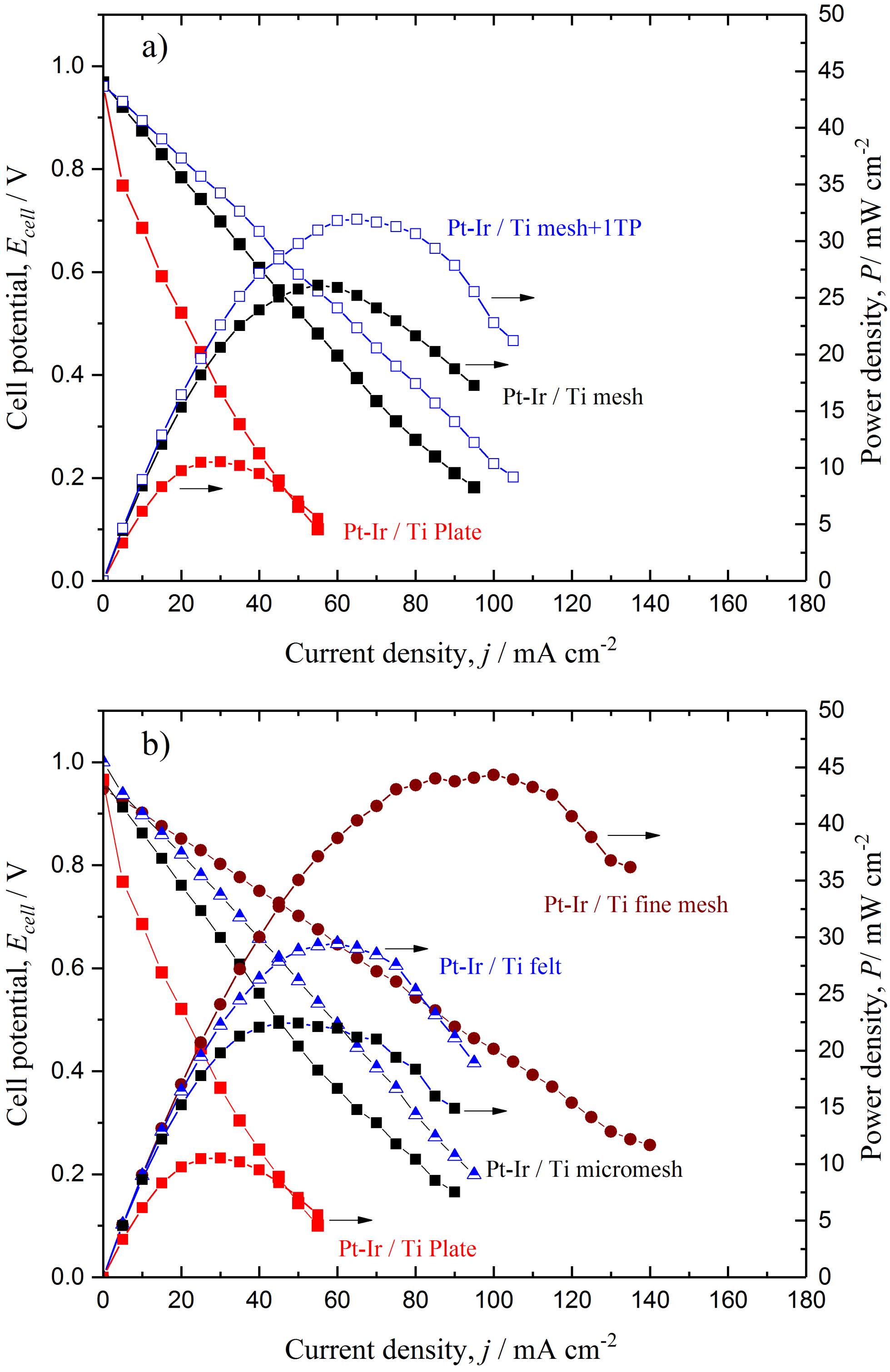

Figure 5.13. The effect of the electrode structure on the polarisation and power density curves for a single cell employing a Pt-Ir/Ti anode of selected materials and a Pt/Ti mesh cathode. The anolyte consisted of 2.5 mol dm^{-3} $NaBH_4$ + 2 mol dm^{-3} NaOH and the catholyte consisted of 0.75 mol dm^{-3} H_2O_2 + 2 mol dm^{-3} NaOH. The mean linear fluid velocity was 4 cm s^{-1} at 296 K.

5.3.8. The design equations of a unit cell and the prediction of borohydride conversion

It is crucial both to know the reactant conversion in any chemical reactor involving 3D electrodes and to relate it to its characteristic design (k_mA_e, L) – that was estimated in this chapter along with the process conditions (v, Q_V) [149]. To improve the overall fractional conversion of the electrochemical reactor. Two simple modes of operation could be considered: batch recirculation of the electrolyte through the cell via a reservoir, Figure 5.14a), and the single-pass mode using a cascade of identical cells in a series, Figure 5.14b) [175].

Assuming that the system used in this study conforms with the plug-flow in a batch recycle system, applying an overall mass balance on the system and knowing the characteristics of each electrode (k_mA_e, L) allow the prediction of the concentration decay in the reservoir over time (t). Therefore, at steady-state conditions (v, Q_V), the following expression could be used for the batch recycle mode of operation [175 236 237]:

$$C_{(out,\ t)} = C_{(in,0)}\, exp\left[\frac{-t}{\tau_T}\left(1 - exp\left(\frac{-\ k_m A}{Q_V}\right)\right)\right] \tag{5.9}$$

Where $C_{(in,0)}$ and $C_{(out,t)}$ are the inlet BH_4^- concentrations (mol cm^{-3}) initially and at time t, Q_V (cm^3 s^{-1}) is the electrolyte volumetric flow rate and τ_T (s) is the mean residence time from Eq. (5.6) in a reservoir containing a certain volume, V_T (cm^3), of electrolyte.

The active electrode area, A (cm^{-2}), and the volumetric flow rate, Q_V, through a porous electrode, can be obtained by Eq. (2.26) and Eq. (2.31), respectively. The electrode volume, V_e (cm^3), could be calculated by Eq. (5.10), where A_x (cm^2) is the electrode cross-sectional area and L is the length of the electrode.

$$V_e = A_x L \tag{5.10}$$

The substitution of Eq. (2.26), Eq. (2.31) and Eq. (5.10) into Eq. (5.9) followed by a rearrangement gives the following equation:

$$c_{(out,\ t)}=c_{(in,0)}\ exp\left[\frac{-t}{\tau_T}\left(1-exp\left(\frac{-k_m A_e L}{v\varepsilon}\right)\right)\right] \tag{5.11}$$

The fractional conversion of BH_4^- for all electrodes in the system at *t* time is the following:

$$X_{BH_4^-(t)}=\frac{\left(c_{(in,0)}-c_{(out,t)}\right)}{c_{(in,0)}} \tag{5.12}$$

Figure 5.14b shows a cascade mode of n_e identical plug-flow reactors. The overall fractional conversion by a single pass can be described by the following expression [144]:

$$X_{BH_4^-}=1-exp\left(\frac{-n_e k_m A_e L}{v\varepsilon}\right) \tag{5.13}$$

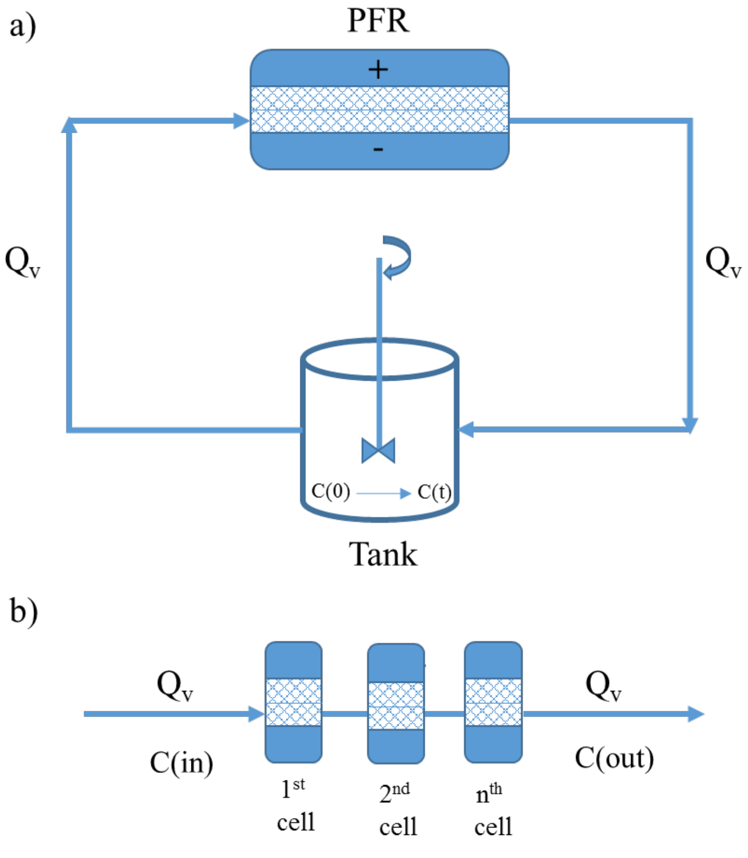

Figure 5.14. Two modes of operation of an electrochemical cell: a) the batch recycle mode and b) a cascade of a number of identical cells in a series flow.

5.3.8.1. Batch recycle mode

The borohydride concentration decays in the electrolyte tank (1.5 dm^3) – due to the electro-oxidation of BH_4^- in the cell-generating current (see the flow circuit in Figure 5.14a) – was calculated using Eq. (5.11) for all Pt-Ir/Ti anode materials at a mean electrolyte flow velocity of 10 cm s^{-1}. The fractional conversion was obtained by Eq. (5.12).

Figure 5.15a) and 5.15b) show the expected conversion and concentration of BH_4^- overtime for the plate, the plate + 3 TPs, the mesh electrode and the mesh + 1 TP. The performance of the micromesh, the fine mesh and the felt electrode can also be seen in Figure 5.16a) and 5.16b). The depletion time of (0.01 mol dm^{-3}) borohydride was only approximately 2 h for the felt and fine mesh electrodes, followed by the micromesh electrode (4.6 h), while the other electrode geometries required more than 30 h to consume the BH_4^- completely, even in the presence of the TPs. In the case of operating a highly porous electrode in which the concentration drops off quite rapidly, the electrolyte needs to have a high volume or will need refurbishment.

Figure 5.17a) and 5.17b) display the calculated number of cycles required for the circulation and utilisation of borohydride ions dissolved in the solution (0.01 mol dm^{-3}). The batch recycle system was considered, as seen in Figure 5.14a), at a flow rate of 10 cm s^{-1} for all electrodes. The number of cycles in the tank can be extracted from Eq. (5.14), which is based on the residence time of the electrolyte in the reservoir (V_T = 1.5 dm^3) as follows:

$$No\ of\ cycles = \frac{t}{\tau_T} \tag{5.14}$$

The results revealed that the mesh and the mesh + 1 TP required around 300 cycles, whereas the plate and the plate with three TPs required more than double that. The mesh electrode needed a lower number of cycles than the mesh + 1 TP because of its larger volumetric mass-transport coefficient. The fine mesh electrode presented the best performance (20 cycles only), followed by the felt and micromesh electrodes (27 and 50 cycles, respectively). Minimising the number of cycles in the borohydride system will reduce the operating expenses and allow it to compete with other efficient technologies.

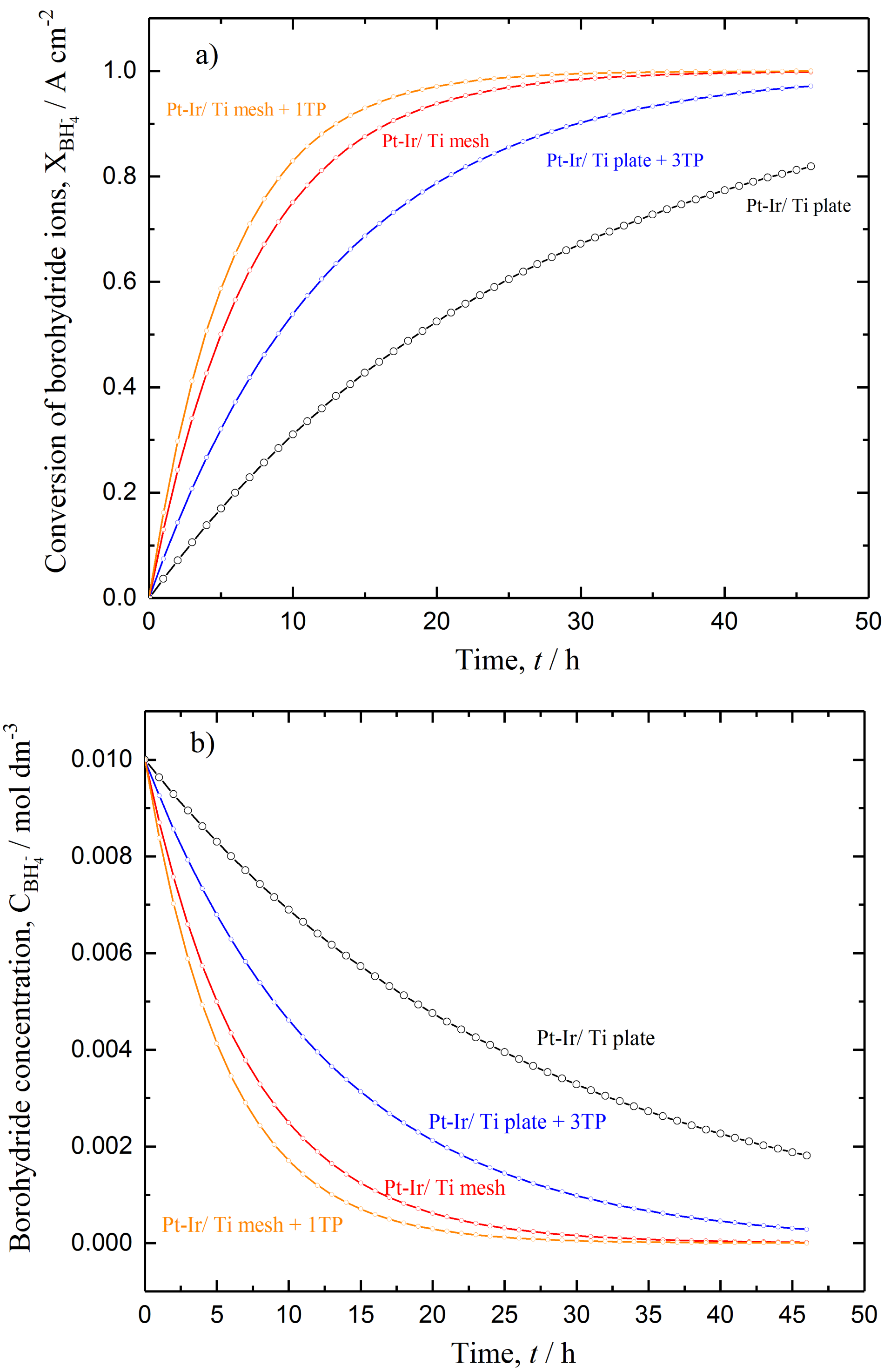

Figure 5.15. a) The borohydride concentration *vs.* time and b) the conversion of borohydride *vs.* time for the plate, the plate + 3 TP, the mesh and the mesh + 1 TP electrodes at a mean linear flow velocity of 10 cm s^{-1}. The electrolyte solution was 1.5 dm^3 consisting of 0.01 mol dm^{-3} $NaBH_4$ in 2 mol dm^{-3} NaOH at 296 K.

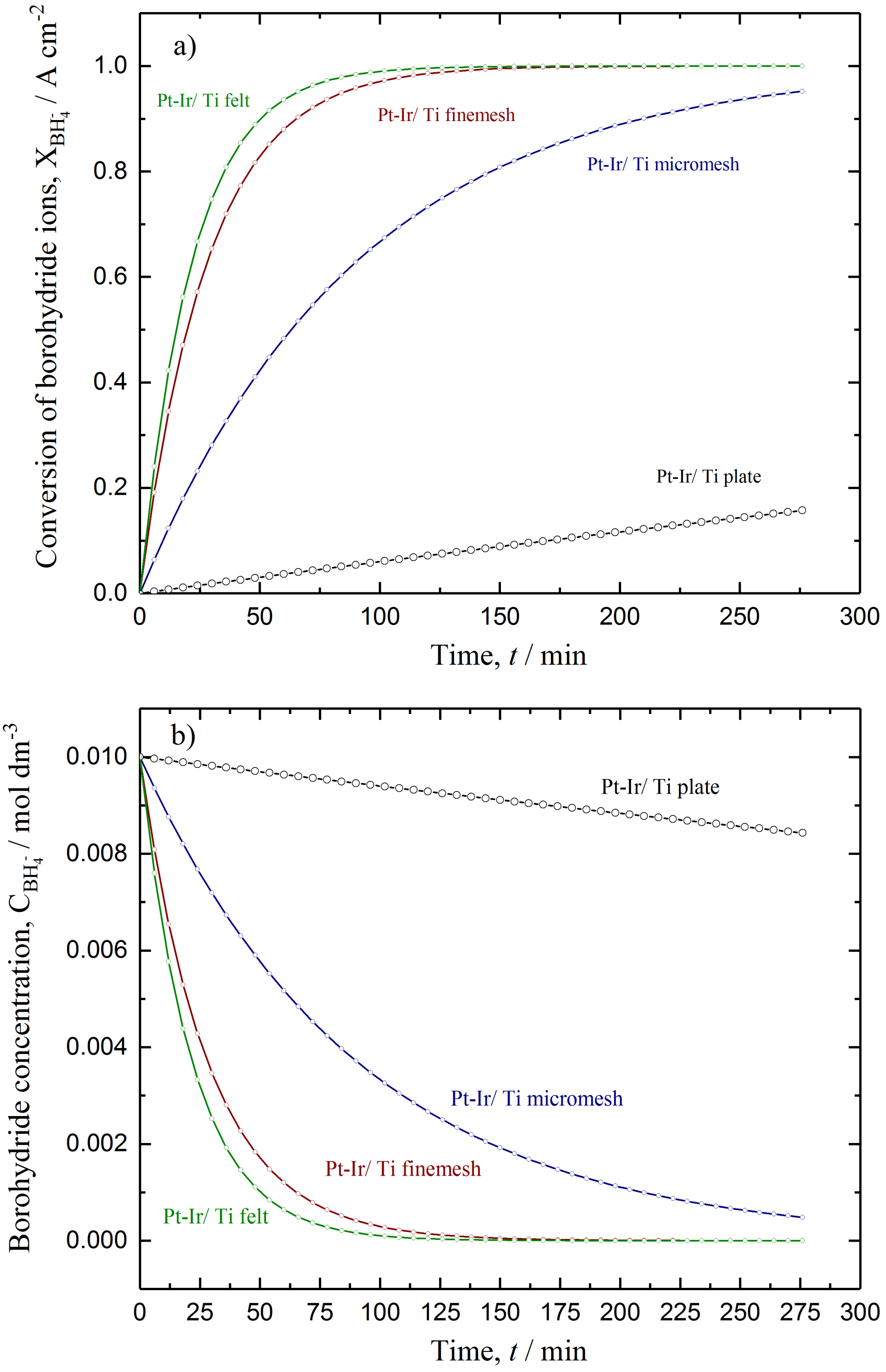

Figure 5.16. a) The borohydride concentration *vs.* time and b) the conversion of borohydride *vs.* time for the plate, the micromesh, the fine mesh and the felt electrodes at a mean linear flow velocity of 10 cm s^{-1}. The electrolyte solution was 1.5 dm^3 consisting of 0.01 mol dm^{-3} $NaBH_4$ in 2 mol dm^{-3} NaOH at 296 K.

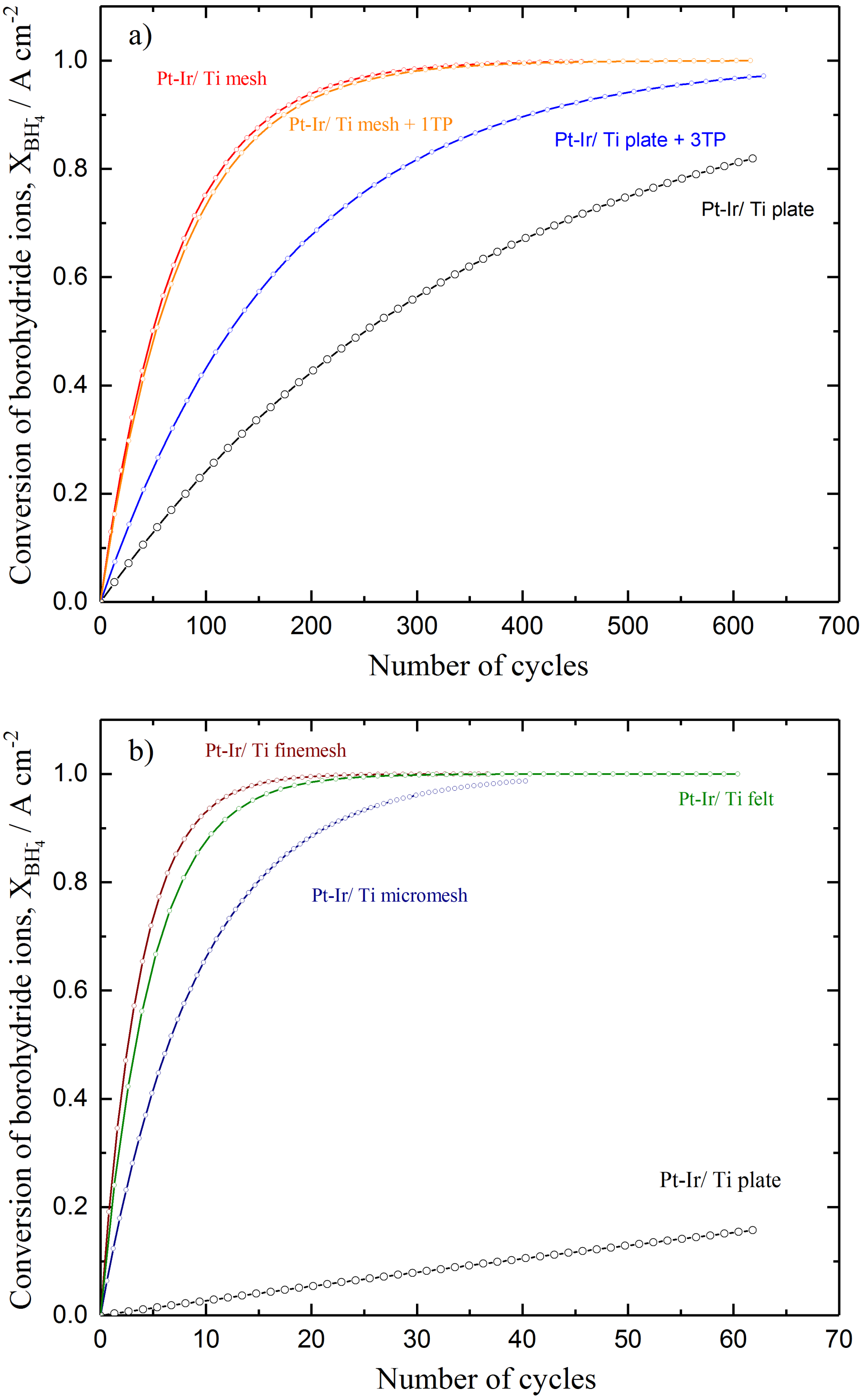

Figure 5.17. The conversion of borohydride ions *vs.* the number of cycles through the tank for different anode materials at a mean linear flow velocity of 10 cm s^{-1}. The electrolyte consisted of 0.01 mol dm^{-3} $NaBH_4$ in 2 mol dm^{-3} NaOH at 296 K. a) Plate, plate + 3 TP, mesh and mesh + 1 TP electrodes. b) Fine mesh, felt and micromesh electrodes.

5.3.8.2. Cascade mode of n_e identical electrodes

The second operation mode that could be considered is a cascade of n_e identical single-pass plug-flow reactors placed in a series electrolyte flow: see the schematic in Figure 5.14b. This model is typically used to reduce investment and maintenance costs [144], i.e. withdrawing one cell without shutting down the whole system. The main benefit of this scheme is its ability to provide high overall conversion [144].

The overall fractional conversions were obtained using Eq. (5.13). The dimensionless performance factor $k_m A_e L/v\varepsilon$ was used to compare the overall fractional conversion of all electrodes, under complete mass-transport control, as shown in Figure 5.18a and 5.18b. If 10 identical electrodes were employed using the existing electrode materials, the expected overall conversion would be as follows: 95% (fine mesh), 90% (felt), 68% (micromesh), 13% (mesh), 12% (mesh + 1 TP), 5.5% (plate + 3 TPs) and 2.7% (plate) at an electrolyte flow rate of 10 cm s^{-1}. The fine mesh electrode exhibited excellent performance in all aspects of borohydride oxidation in the DBFC compared to the other electrode materials, making it a candidate for further improvements, such as optimising the operating conditions (e.g. the temperature of the electrolyte, its composition and flow rate).

5.4. Conclusion

The volumetric mass-transport coefficients ($k_m A_e$), sometimes called the performance factor, of five fabricated $Pt_{0.75}$-$Ir_{0.25}$/Ti working electrodes, were evaluated with the limiting current technique using a single flow cell. The chronoamperometry technique was applied on them to measure the limiting current *vs.* time (s) with various linear flow velocities. All the results showed well-defined limiting current plateaux increasing with the mean linear flow velocity. The felt and fine mesh electrodes showed the highest activity, followed by the micromesh, the mesh with one TP, the mesh, the plate with three TPs and the plate electrode, sequentially.

The enhancement factors, δ, were also evaluated for all electrodes. In the presence of a TP, the currents extracted from the plate and mesh electrodes were more than doubled.

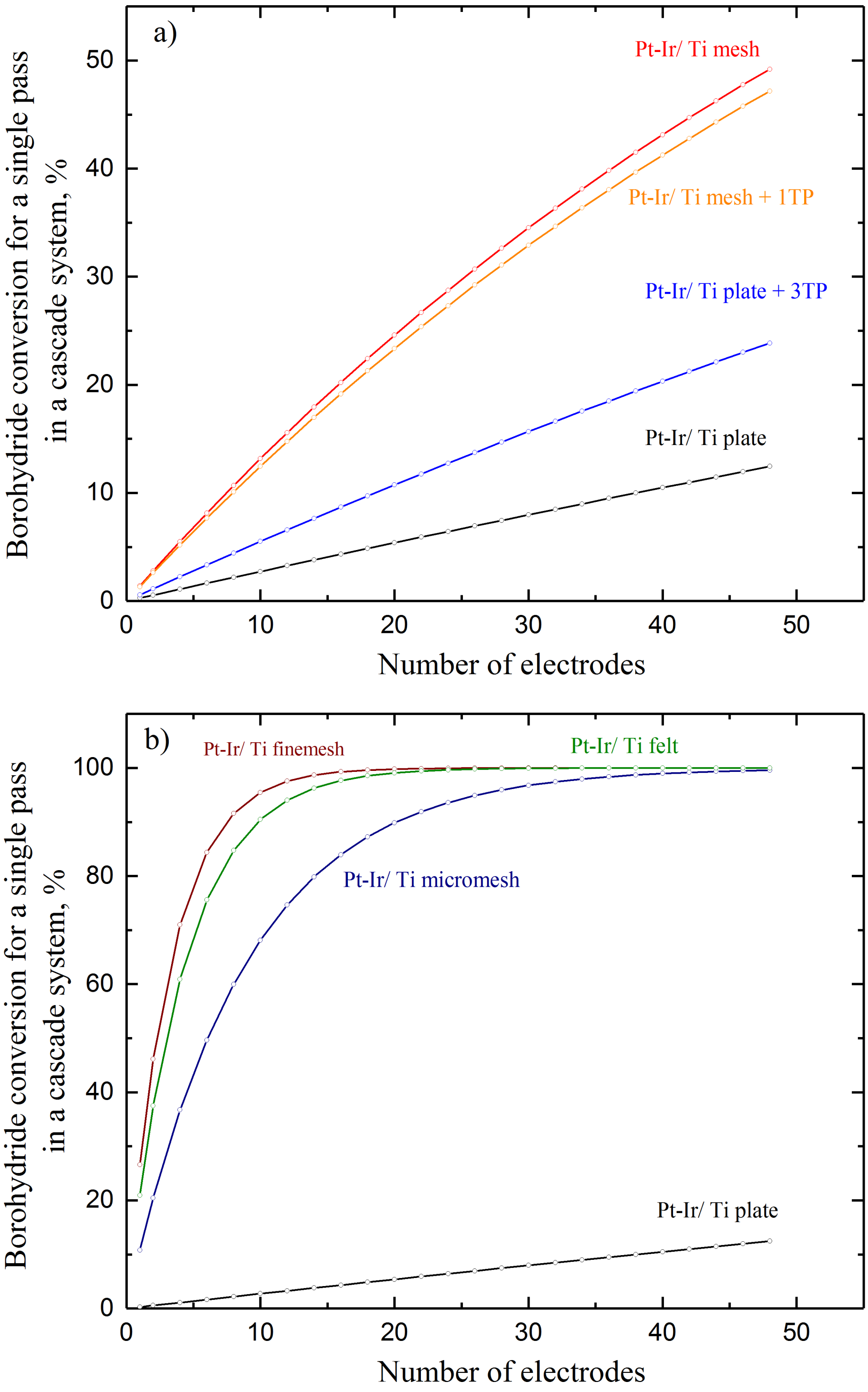

Figure 5.18. The conversion of borohydride ions *vs.* the number of electrodes for different anode materials at a mean linear flow velocity of 10 cm s^{-1}. The electrolyte consisted of 0.01 mol dm^{-3} $NaBH_4$ in 2 mol dm^{-3} NaOH at 296 K. a) Plate, plate + 3 TP, mesh and mesh + 1 TP electrodes. b) Fine mesh, felt and micromesh electrodes.

At a low flow rate (e.g. 4 cm s^{-1}), which is favourable because it lowers pumping costs, the δ values were 2.2, 4.5 and 5.6 for the plate + 3 TPs electrode, the mesh electrode and the mesh + 1 TP stack, respectively. However, the felt, fine mesh and micromesh electrodes also showed a marked enhancement, their δ values being 97.8, 56.7 and 22.3 (at 4 cm s^{-1}), respectively. The optimal values of the enhancement factor were 99.5 (at 6 cm s^{-1}), 67 (8 cm s^{-1}) and 22.6 (4 cm s^{-1}) for these electrodes.

The volumetric mass-transport coefficients (k_mA_e) were obtained in the presence and the absence of TPs. They increased towards the electrode surface along with electrolyte velocity and the Reynolds number. The fine mesh and felt materials showed appreciably higher performance than the mesh and plate electrodes, even in the presence of TPs. The effects of changing the borohydride ion concentration on the limiting current and k_mA_e values were also investigated. The limiting current increased when the borohydride ions concentration rose, while the mass-transport rate towards the electrode remained constant. Therefore, the volumetric mass-transport coefficient remained relatively constant with respect to the BH_4^- concentration at a specific flow velocity.

An FC performance test was performed on a single cell using different Pt-Ir/Ti anodes at 296 K with the typical polarisation and power density curves. All j-E_{cell} curves showed a nearly linear response and continuous decreasing of the cell potential with the current density, which indicates a strong dependence on the ohmic resistance in the cell. The power density of the studied electrodes increased in the following sequence: plate < micromesh < mesh < felt < mesh + 1 TP < fine mesh. The maximum power density for the Pt-Ir/Ti fine mesh was 44.5 mW cm^{-2} at a current density of 100 mA cm^{-2} and a 0.44 V cell voltage.

The borohydride concentration decay in an electrolyte tank was calculated for all Pt-Ir/Ti anode materials at a mean electrolyte flow velocity of 10 cm s^{-1}. The fractional conversions were also obtained. The complete conversion of borohydride only required approximately two hours for the felt and fine mesh electrodes, followed by the micromesh electrode (4.6 h), whereas the other electrode geometries required more than 30 h to consume the BH_4^- completely (0.01 mol dm^{-3}), even in the presence of TPs. The number of cycles in the tank required for the circulation and utilisation of the borohydride ions in the batch recycle system was also obtained. The fine mesh electrode presented the best performance (20 cycles), followed by the felt and micromesh electrodes (27 and 50 cycles, respectively). It took over 300 cycles for the mesh electrode and more than 600 cycles for the plate electrode. Finally, the mode of a cascade of n_e identical electrodes placed in a series of electrolyte flow was considered. The overall fractional conversions were obtained for all electrodes under complete mass-transport control. If 10 identical electrodes were employed using the existing electrode materials, the expected overall conversion would be as follows: 95% (fine mesh), 90% (felt), 68% (micromesh), 13% (mesh), 12% (mesh + 1 TP), 5.5% (plate + 3 TPs) and 2.7% (plate) at an electrolyte flow rate of 10 cm s^{-1}. The fine mesh electrode showed the best performance of all the electrodes studied here. However, the effects of operating conditions (concentration, temperature, etc.) need to be investigated to find the conditions that maximise the power density of the $NaBH_4 \| H_2O_2$ flow cell, which is considered in the next chapter.

Chapter 6: The Effect of Operating Conditions on Direct $NaBH_4\|H_2O_2$ Fuel Cell Performance

In this chapter, the influences of different operational conditions on the performance of the direct sodium borohydride–hydrogen peroxide fuel cell (DBHPFC) were explored. The investigated cell consisted of a $Pt_{0.75}$-$Ir_{0.25}$/Ti anode catalyst and a Pt/Ti mesh cathode. The performance of the DBHPFC under these operational conditions was evaluated by recording the cell potential *vs.* current density using the battery analyser to apply a load on a single cell. The optimal power density, the cell voltage, the suitable anode structure and the adequate operating conditions were discovered.

6.1. Introduction

The use of DBHPFCs as power sources has many advantages, such as no carbon-monoxide poisoning of the cell during its operation (unlike direct methanol FCs [75]), high cell voltage (3.02 V) and high predicted specific energy (up to 17 kW h kg^{-1}) [12]. The anodic oxidation of borohydride ions is as follows:

$$BH_4^- + 8OH^- \rightarrow BO_2^- + 6H_2O + 8e^- \qquad E^o_{Anode} = -1.24 \textit{ vs. } \text{SHE} \qquad (6.1)$$

In practice, this reaction is unlikely to happen to a large extent, as it must compete with the spontaneous hydrolysis of borohydride:

$$BH_4^- + 2H_2O \rightarrow BO_2^- + 4H_2 \qquad (6.2)$$

In this case, as a consequence the actual anodic reaction of the competitive oxidation of BH_4^- and H_2 at the anode surface will be the following [61 199 58]:

$$BH_4^- + xOH^- \rightarrow BO_2^- + (x\text{-}2)\, H_2O + (4 - \frac{x}{2})\, H_2 + xe^- \qquad (6.3)$$

Where x is the practical number of electrons released by each borohydride ion and is also the number of hydroxide ions (OH^-) involved. Olu et al. [59] reported that there is no practical electrocatalyst able to oxidise BH_4^- without generating H_2 gas that escapes from its electrode during the operation. Every active catalyst of the borohydride oxidation reaction (BOR) generates H_2 by hydrolysis [142], as seen in Eq. (2.2). The authors [142] suggested one way to achieve near-zero H_2 evolution, which is both to use a catalyst (e.g. Pt) that is active towards the hydrogen oxidation reaction, HOR [Eq. (2.4)], and also to optimise the operating conditions.

Manipulating the operational conditions of DBHPFCs would improve their efficiency and overall performance. For example, the performance of DBHPFCs can improve by taking advantage of the pronounced thermal activation of their electrochemical reactions, as shown in Chapter 4. The cell power density with a $Pt_{0.75}$-$Ir_{0.25}$ anode increased by about 70% (50 to 84 mW cm^{-2}) when the temperature rose from 298 K to 333 K. However, elevating the temperature could also enhance BH_4^- crossover, its hydrolysis (H_2 evolution), membrane dehydration, and strengthening membrane resistance, all of which dramatically reduce system efficiency. Another manipulation that can improve the FC performance is increasing the BH_4^- concentration. Despite possibly encouraging the BH_4^- ions crossover to the cathode compartment (as the Pt cathode is active towards BH_4^-), it could also increase H_2 gas evolution, the bubbles from which would block more active sites, hinder ion movement in the anolyte [145], and reduce the fuel utilisation efficiency. Therefore, the influence of the operating conditions needs to be studied to optimise them and thus improve the performance of DBHPFCs with the use of the best anode catalyst ($Pt_{0.75}$-$Ir_{0.25}$) and the anode structures found in Chapters 4 and 5, respectively. In this work, the studied variable conditions include the following: the sodium borohydride concentration, the sodium hydroxide concentration, the catholyte background materials, the hydrogen peroxide concentration, the sulfuric acid concentration, the flow velocity, the temperature and the effects of ammonium hydroxide and sodium dodecyl sulphate (SDS) as additives. The appropriate operating conditions were determined and used to evaluate the stability of a DBHPFC with a suggested anode structure. In the end, the optimal power density, the cell voltage, the suitable anode structure and the adequate operating conditions were determined.

6.2. Experimental details

The single DBHPFC and its hydraulic circuit are the same as that used in the previous work, see Figure 4.5. The expanded view is presented in Figure 4.3. The flow cell preparation and its description have been explained thoroughly in Chapter 4 on sections 4.2.3 and 4.2.4, respectively.

A $Pt_{0.75}$-$Ir_{0.25}$ catalyst supported by a Ti plate (9 cm^2, 20 × 45 mm, 0.9 mm thick, 99.7%, Alfa Aesar) was used as an anode because of its high kinetics parameters and cell performance, as demonstrated in Chapter 4. The details of the coating method of $Pt_{0.75}$-$Ir_{0.25}$ alloy and its characterisation is described in sections 4.2.1. and 4.3.1., respectively. Platinised titanium mesh (Pt/Ti, 8.55 cm^2 geometrical area, Figure 5.1f) was used as a counter electrode. The counter electrode compartment contained a plastic inert mesh (Figure 4.6) as a turbulence promoter [TP, 1.3 mm thickness, 8.0 mm long-way distance between connected knots of diamond (LWD) and 6.8 mm short-way distance between connected knots of diamond (SWD)]. TPs are commonly used to enhance mass transport and impose current distribution uniformity [185]. The TP also usefully fills the gap between the cathode and the membrane, forcing the volumes of both the cathode and anode departments to stay equivalent during the compression of the cell parts. The mean linear flow velocity (v, cm s^{-1}) in both compartments was always set to be similar, which helps in this matter. A pump (323S/D, Watson-Marlow) with two heads was used to recirculate and control the flow rate of the electrolyte into the anode and cathode electrode compartments. The volume of the circulated electrolyte (reservoir) was 200 mL. The two compartments were separated by a CEM Nafion® 115 (Dupont Co, USA). A thermostatic water bath was employed to maintain the electrolyte temperature at the desired level during the experiments.

The materials and chemicals used for the experiments were as follows: sodium borohydride (99%, Sigma-Aldrich), sodium hydroxide (98%, Fisher Scientific UK), hydrogen peroxide (30%, Fisher Scientific UK), sulfuric acid (95%, Fisher Scientific UK), hydrochloric acid (36%, Fisher Scientific UK), phosphoric acid (85%, Fisher Scientific UK), ammonium hydroxide (30%, Fisher Scientific UK) and sodium dodecyl sulphate salt (SDS, 98.5%, Sigma-Aldrich).

Several solutions were prepared and examined under their corresponding sets of conditions, as listed in Table 6.1, to study the effects of different operational conditions on the performance of the DBHPFC. The table presents the 11 target parameters that were studied. The cell's potential *vs.* current density was recorded using a battery analyser (BST8-A3, MTI, USA). The rate of current density was 5 mA cm^{-2} min^{-1} from 0 to 280 mA cm^{-2}. For each j-E_{cell} experiment, new solutions were prepared immediately prior to the measurements to avoid the loss of BH_4^- from hydrolysis during solution storage. Each experiment was repeated three times to confirm the results. The outputs of the eleven parameters were plotted to show the polarisation curves and the power densities of each set of conditions that are provided in Table 6.1.

A stability test was done by applying a current density of 25 mA cm^{-2} (using the battery analyser) for about 1 h on the cell, which consisted of a $Pt_{0.75}$-$Ir_{0.25}$/Ti plate anode and a Pt/Ti mesh cathode at 25 ±1 ^{o}C. The anolyte composition was 0.5 M $NaBH_4$ + 4 M NaOH, and the corresponding catholyte was composed of 2 M H_2O_2 + 1.5 M H_2SO_4, and the mean linear fluid velocity was 2 cm s^{-1} (in this chapter; M = mol dm^{-3}).

Table 6.1. List of experimental tests that were used to obtain the polarisation and power density curves for each set of operational conditions.

Set	Effect of	Electrolyte compositions / M = mol dm^{-3}		Values of the variable parameter, x	Temperature, flow velocity	Electrodes	
		Fuel	Oxidant			Anode	Cathode
1	$NaBH_4$ concentration	x M $NaBH_4$+2 M NaOH	1 M H_2O_2 + 1 M HCl	x = 0.13, 0.25, 0.5, 1.0, 1.5, 2.0 M	25 °C , 3 cm s^{-1}	$Pt_{0.75}$-$Ir_{0.25}$/Ti plate	Pt/Ti mesh
2	NaOH concentration	0.5 M $NaBH_4$+ x M NaOH		x = 0.5, 1, 2, 4, 6, 8 M			
3	Catholyte background material	0.5 M $NaBH_4$ + 4 M NaOH	1 M H_2O_2 + 1 M x	x = 1.0 M $\begin{cases} H_2SO_4 \\ H_3PO_4 \\ HCl \\ NaOH \end{cases}$			
4	H_2SO_4 concentration		1 M H_2O_2 + x M H_2SO_4	x = 0.5, 1.0, 1.5, 2.0 M			
5	H_2O_2 concentration		x M H_2O_2 + 1.5 M H_2SO_4	x =0.25, 0.5, 1, 1.5, 2.0 M			
6	Mean flow velocity		2 M H_2O_2 + 1.5 M H_2SO_4	x = 0.5, 1, 2, 3, 4, 6 cm s^{-1}	25 °C , x cm s^{-1}		
7	Temperature			x = 25, 35, 45, 55, 65 °C	x °C , 2 cm s^{-1}		
8	Ammonium hydroxide, NH_4OH			x = 0, 1.0 M NH_4OH	25 °C , 2 cm s^{-1}		
9	SDS additive /x wt%			x = 0, 0.01, 0.001, 0.0001 wt.% SDS			
10	Anode structure			x = plate, mesh, fine mesh		$Pt_{0.75}$-$Ir_{0.25}$/Ti x	
11	Highly porous felt	0.25 M $NaBH_4$+4 M NaOH 0.5 M $NaBH_4$+4 M NaOH		x = plate, felt; with & without 0.01 wt.% SDS		$Pt_{0.75}$-$Ir_{0.25}$/Ti x	

6.3. Results and discussion

6.3.1. The effect of borohydride concentration

The influence of $NaBH_4$ concentration on the performance of DBHPFCs is presented in Figure 6.1. It illustrates the curves of the cell potential and its corresponding power density against the current density measured at 0.13, 0.25, 0.5, 1.0, 1.5 and 2.0 M $NaBH_4$ in 2 M NaOH at 25 °C and a mean linear flow velocity of 3 cm s^{-1}. In the catholyte compartment, the concentration of H_2O_2 and its associated background material (HCl) were maintained at 1 M. The arrows next to the power density and cell polarisation curves in Figure 6.1 (and all figures in this chapter) indicate the corresponding *x* and *y* axes. The cell showed a slightly less positive open-circuit potential (OCP) of 1.71 V to 1.77 V with increasing BH_4^- concentrations from 0.13 M to 2.0 M, which were relatively high.

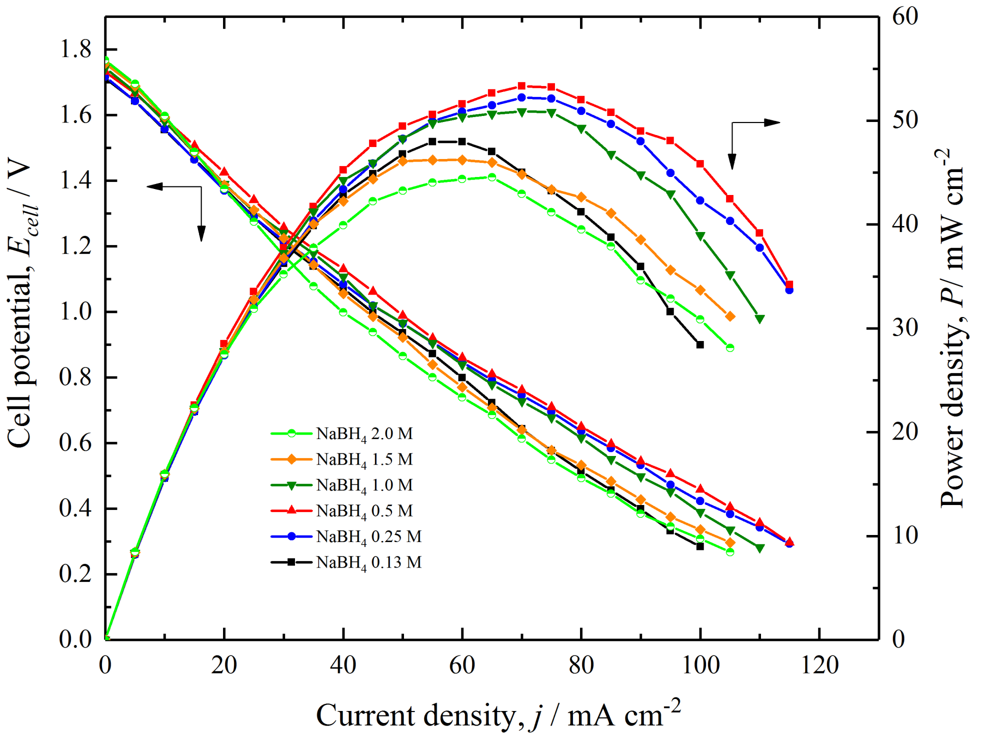

Figure 6.1. The effect of $NaBH_4$ concentration on the cell voltage and power density of the DBHPFC. Anode: $Pt_{0.75}$-$Ir_{0.25}$/Ti plate (9 cm^2). Cathode: Pt/Ti mesh (8.55 cm^2). Fuel: *x* M $NaBH_4$ + 2 M NaOH. Oxidant: 1 M H_2O_2 + 1 M HCl. Flow velocity: 3 cm s^{-1}. Temperature: 25 °C.

According to the Nernst equation [Eq. (6.4)], the open-circuit electrode potential of the half-cell reaction [Eq. (6.1)] depends on the electrolyte solution. The potential of the anode would increase; hence, the OCP would be higher with high BH_4^- concentration.

$$E=E^o+\frac{RT}{8F}\ ln\frac{(c_{BH_4^-})\times(c_{OH^-}^8)}{(c_{BO_2^-})} \tag{6.4}$$

Even though the OCP values (~1.74 V) of the electro-motive force at the equilibrium of all solutions were reasonable in comparison to the standard cell potential of a $BH_4^-\|O_2$ cell (1.64 V), they were lower (by 41%) than that estimated theoretically for an acidic $BH_4^-\|H_2O_2$ cell [3.02 V; see Eq. (2.18)]. This result aligns with previously reported OCP results (1.75 V) [28] (1.74) [238] and could be attributed to the mixed potentials from the simultaneous oxidation of BH_4^- ions and H_2 at the anode and the competition between H_2O_2 and O_2 to be reduced at the cathode [239] [161] [71]. Furthermore, in a system where an extreme pH gradient exists, an electrolyte junction potential would definitely develop across the membrane, in turn reducing the OCP (59 mV/pH unit, 826 mV) [162] [222].

Figure 6.1 reveals that neither low nor high BH_4^- concentrations benefit the cell voltage or power density, which is the reason the concentration needs to be optimised for this electrode (as the concentration depends on the electrodes used). High concentration would improve the transport of the reactants (BH_4^-, Na^+) and the reaction kinetics rate [Eq. (4.12)], however, it might lead to BH_4^- crossover and its hydrolysis [211], as H_2 evolution is strongly dependent on the $BH_4^-\|OH^-$ ratio [239]. For practical comparison, the maximum power density of a 2.0 M $NaBH_4$ solution (Figure 6.1) is 45 mW cm^{-2} at 0.69 V with a discharge current density of 65 mA cm^{-2}, while, with 0.5 M $NaBH_4$, the power density was 53 mW cm^{-2} (17% higher) at a 0.76 V cell voltage and 70 mA cm^{-2}. Using a low $NaBH_4$ concentration would cause higher fuel utilisation (which agrees with other research [61]) and less poisoning of the cathode catalysts, increasing the FC performance when a 0.5 M $NaBH_4$ solution is used. From the perspective of cost and energy cell capacity, 0.5 M $NaBH_4$ seems the best concentration for the current of the DBHPFC; thus, it has been chosen for the remaining experiments.

6.3.2. The effect of sodium hydroxide concentration

Finding appropriate NaOH concentration is also an important aspect. Figure 6.2 demonstrates the cell performance at different NaOH compositions varied between 0.5 M and 8.0 M + 0.5 M $NaBH_4$ at 25 °C. The OCP increased from 1.66 V to 1.84 V with increasing NaOH concentration from 0.5 M to 8.0 M, respectively, which is in line with the Nernst equation [Eq. (6.4)]. Using less than 1 M NaOH led to a decrease in cell performance because of the BH_4^- hydrolysis rate increases as the pH decreases. However, a significant improvement (46%) in both the cell voltage and the power density were observed as the NaOH content in the fuel increased from 1.0 (39 mW cm^{-2}) to 4.0 M (57 mW cm^{-2}), which matches the findings of Santos et al. [238]. Increasing the NaOH concentration increases both the electrolyte conductivity and the borohydride stability [211]. The highest peak power density was found when 6.0 M NaOH was tested, which was around 58 mW cm^{-2} at 0.76 V and 75 mA cm^{-2}. This value was almost equivalent to that obtained from a 4.0 M NaOH solution, which was 57 mW cm^{-2} at the same cell potential and current density of 6.0 M NaOH.

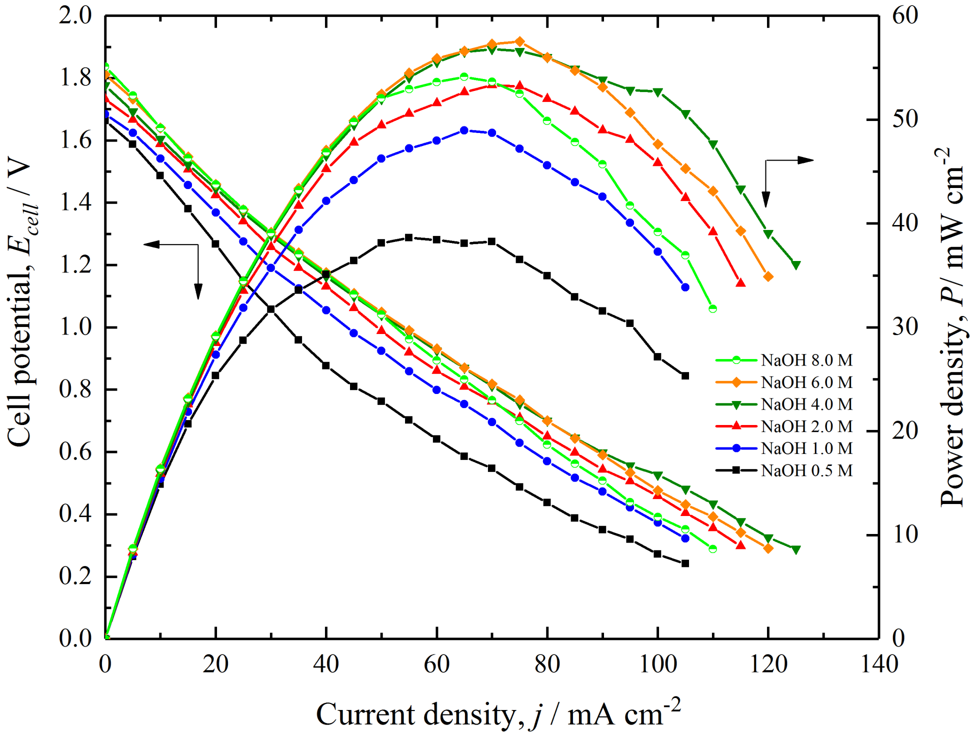

Figure 6.2. The effect of NaOH concentration on the cell voltage and power density of the DBHPFC. Anode: $Pt_{0.75}$-$Ir_{0.25}$/Ti plate (9 cm^2). Cathode: Pt/Ti mesh (8.55 cm^2). Fuel: 0.5 M $NaBH_4$ + x M NaOH. Oxidant: 1 M H_2O_2 + 1 M HCl. Flow velocity: 3 cm s^{-1}. Temperature: 25 °C.

A high NaOH concentration would increase the solution viscosity, which would then inhibit the movement capability of both the BH_4^- towards the anode active sites [41] [148] and also the Na^+ ions towards the cathode compartment [17], sinking the power efficiency. Using a NaOH concentration greater than 4.0 M did not appear to benefit the cell performance; as a result, the anolyte composition was fixed at 4.0 M NaOH + 0.5 M $NaBH_4$ for the remaining experiments.

6.3.3. The effect of catholyte background electrolyte

The performance of the DBHPFC when 1 M of different catholyte background electrolytes was used is shown in Figure 6.3, while the oxidant (H_2O_2) was kept at 1 M. The fuel was maintained at 0.5 M $NaBH_4$ + 4 M NaOH at 25 °C and a mean linear flow velocity of 3 cm s^{-1} in all the experiments. The investigated background materials included NaOH, sulfuric acid (H_2SO_4), hydrochloric acid (HCl) and phosphoric acid (H_3PO_4).

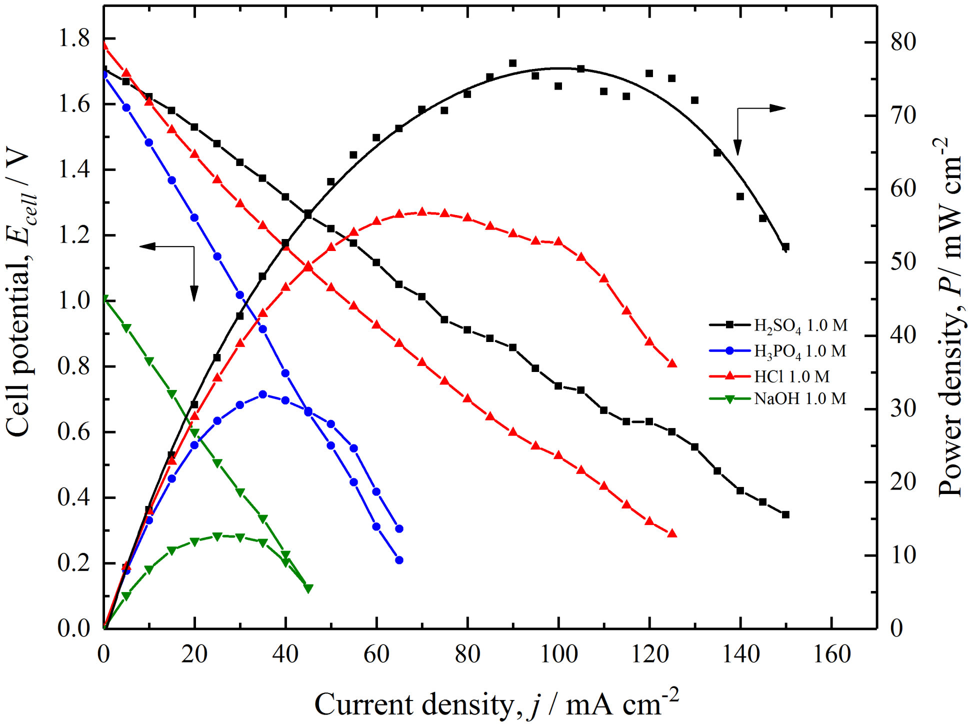

Figure 6.3. The effect of catholyte background materials on the cell voltage and power density of the DBHPFC. Anode: $Pt_{0.75}$-$Ir_{0.25}$/Ti plate (9 cm^2). Cathode: Pt/Ti mesh (8.55 cm^2). Fuel: 0.5 M $NaBH_4$ + 4 M NaOH. Oxidant: 1 M H_2O_2 + 1 M x. Flow velocity: 3 cm s^{-1}. Temperature: 25 °C.

Table 6.2. The pH and *pK* values of 1 M of different materials in the water at 25 °C [6].

Material	Dissociation step (*pK*)			
	pH	First	Second	Third
HCl	~ 0	-6.3	-	-
H_2SO_4	~ 0	-3.0 [240]	1.99	-
H_3PO_4	1.08	2.16	7.21	12.32
Na^+	14	14.8	-	-

A 1 M NaOH solution is a strong alkaline medium, while both HCl and H_2SO_4 are strongly acidic, unlike H_3PO_4, which is the weakest acid (see all pH levels in Table 6.2). Table 6.3 summarises the relevant data on the influence of electrolyte background materials on the investigated DBHPFC at 25 °C (taken from Figure 6.3). The highest OCP was 1.78 V for the catholyte solution of 1 M HCl, while the lowest was only 1.01 V (67% less) for the alkaline medium (NaOH). This result related to the difference in pH; as at a low pH the reduction has higher electrode potential (1.78 V *vs.* SHE, Eq. (2.15)).

Table 6.3. The effect of the catholyte (1 M concentration) on the DBHPFC at 25 °C.

	Catholyte			
	NaOH	H_3PO_4	HCl	H_2SO_4
Open-circuit potential / V	1.01	1.69	1.78	1.71
Peak power density / mW cm^{-2}	13	32	57	77
Cell potential at peak power density / V	0.28	0.71	0.82	0.73
Current density at peak power density / mA cm^{-2}	30	35	70	105

The maximum OCP of 1 M H_2SO_4 was lower (1.71 V) than that of 1 M HCl (1.78 V) probably due to, first, H_2SO_4 is poisoning the cathode; and second, the faster dissociation of HCl component (*pK* = -6.3) than H_2SO_4 (*pK* values from -3.0 to 1.99 between the first and second steps), as reported in Table 6.2. The *pK* indicates the speed and ease of a substance's dissociation in the water and its release of a proton (H^+ ions in case of an acid). The lower the value, the quicker the dissociation of the substance in water. The number of H^+ ions rises because of their fast transport, increasing both the electrolyte conductivity and the reduction rate of H_2O_2 (as it needs $8H^+$), which achieves a remarkable improvement in cell performance. The highest peak of power density was provided by the 1 M H_2SO_4 solution at 77 mW cm^{-2} and a cell potential of 0.73 V at 105 mA cm^{-2}. A little fluctuation in the cell voltage was observed, which could be related to the increasing H_2 evolution rate, as Li et al. [145] linked it with the increase of cell power density. Table 6.3 reveals that the alkaline solution (1 M NaOH) can only provide around 13 mW cm^{-2} of cell power density (0.28 V, 30 mA cm^{-2}), followed by 32 mW cm^{-2} (0.71 V, 35 mA cm^{-2}) and 57 mW cm^{-2} (0.82 V, 70 mA cm^{-2}) from the 1 M H_3PO_4 and 1 M HCl solutions, respectively. It has become obvious that H_2SO_4 should be selected for the remaining experiments; only a suitable concentration needs to be found, which is discussed in the next section.

6.3.4. The effect of sulfuric acid concentration

Figure 6.4 indicates the influence of the H_2SO_4 concentration on the cell potential and power density of the DBHPFC at 25 °C. It was observed that the OCP value was about 1.7 V for all studied solutions; that included 0.5, 1.0, 1.5 and 2.0 M H_2SO_4 in 1 M H_2O_2, while the rest of operating conditions were the same (as seen in Figure 6.4). The power density curve increased gradually with the H_2SO_4 concentration from 0.5 M to 1.5 M. Table 6.4 summarises the maximum power densities and the cell potentials for all curves. The 1.5 M H_2SO_4 concentration provided the most favourable cell voltage and power density, which were equal to 0.89 V and 83 mW cm^{-2}, respectively, at a current density load of 95 mA cm^{-2}. These data were approximately equal to those obtained with a 2.0 M H_2SO_4 solution. From an economic point of view, the 1.5 M H_2SO_4 concentration seems the best for the present DBHPFC; consequently, it has been selected for the remaining experiments.

Table 6.4. The effects of the H_2SO_4 concentration on the DBHPFC at 25 °C.

	H_2SO_4 concentration / M			
	0.5	1.0	1.5	2.0
Open-circuit potential / V	1.70	1.71	1.70	1.71
Peak power density / mW cm^{-2}	64	77	83	82
Cell potential at peak power density / V	0.81	0.73	0.89	0.87
Current density at peak power density / mA cm^{-2}	80	105	95	95

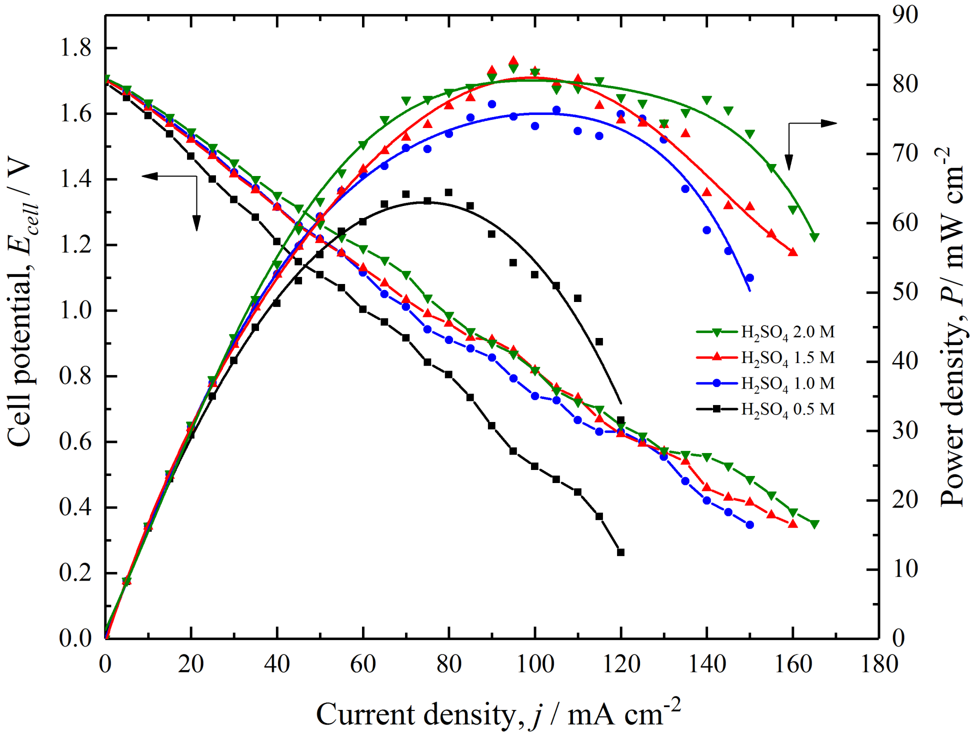

Figure 6.4. The effect of the H_2SO_4 concentration on the cell voltage and power density of the DBHPFC. Anode: $Pt_{0.75}$-$Ir_{0.25}$/Ti plate (9 cm^2). Cathode: Pt/Ti mesh (8.55 cm^2). Fuel: 0.5 M $NaBH_4$ + 4 M NaOH. Oxidant: 1 M H_2O_2 + x M H_2SO_4. Flow velocity: 3 cm s^{-1}. Temperature: 25 °C.

6.3.5. The effect of hydrogen peroxide concentration

According to the Nernst equation, the cathode voltage and the reaction rate that takes place on the cathode catalyst [Eq. (2.15)] are expected to increase with rising H_2O_2 concentration. The effect of the H_2O_2 concentration on cell performance is illustrated in Figure 6.5. The cell potential–current density polarisation curves appear nearly linear. The continuous decreasing (in all experiments) of the cell potential with the current density indicates the strong dominance of ohmic resistance in the DBHPFC (most likely in the electrolyte) and other chemical/electrochemical side reactions (e.g. BH_4^- hydrolysis). Increasing the H_2O_2 concentration from 0.25 M to 0.5 M significantly improved (35%) the cell power density from 68 mW cm^{-2} (0.91 V) at 75 mA cm^{-2} to 91 mW cm^{-2} (0.91 V) at 100 mA cm^{-2}, respectively. However, a further increase in the hydrogen peroxide concentration (> 0.5 M) decreased the OCP, the cell voltage and the power density, as can be seen in Figure 6.5 for concentrations of 1.0, 1.5 and 2.0 M. This behaviour could be attributed to the O_2 bubbles generated by the decomposition of H_2O_2

on the cathode sites [Eq. (2.16)] which would restrict the utilisation of the active surface area [241]. The cathode in this study is the Pt/Ti mesh (see Figure 5.1f), which is predicted to provide more surface area for the reactions to occur than a flat electrode. At a current load of 125 mA cm^{-2} (Figure 6.5), the cell voltage is 0.7 V with a corresponding peak power density of 88 mW cm^{-2} in the case of 2.0 M H_2O_2, whereas 0.5 M H_2O_2 provided 83 mW cm^{-2} and 0.67 V. The concentration of 2.0 M H_2O_2 was thus chosen as the oxidant concentration for the operation of the DBHPFC, the anolyte composition was fixed at 0.5 M $NaBH_4$ + 4 M NaOH and the oxidant was contained in 2.0 M H_2O_2 + 1.5 M H_2SO_4 for the remaining experiments.

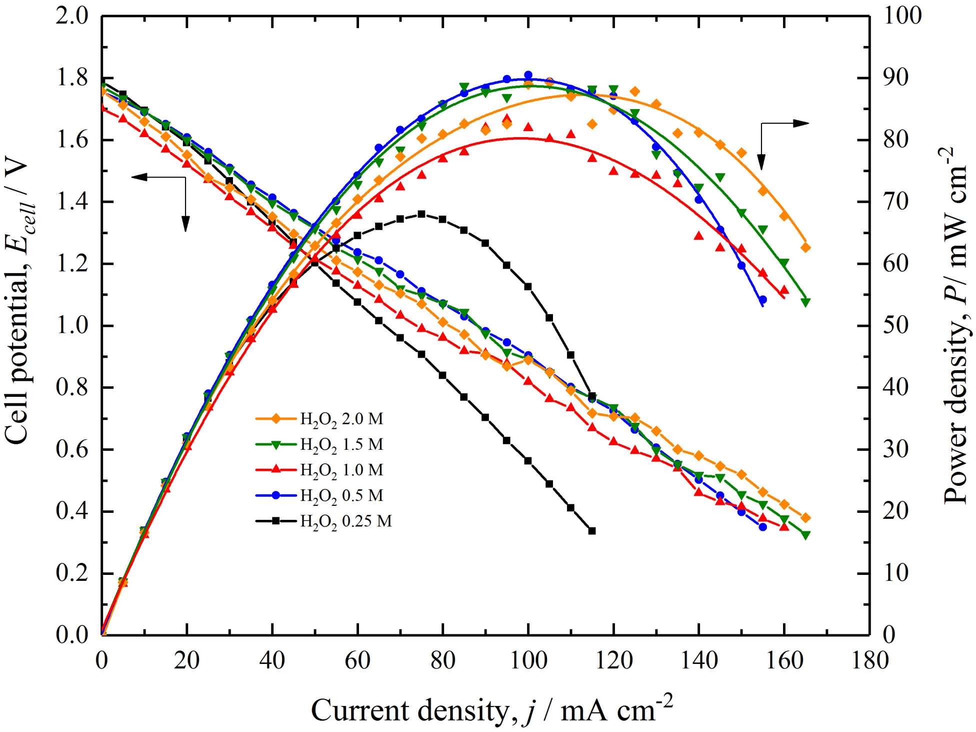

Figure 6.5. The effect of the H_2O_2 concentration on the cell voltage and power density of the DBHPFC. Anode: $Pt_{0.75}$-$Ir_{0.25}$/Ti plate (9 cm^2). Cathode: Pt/Ti mesh (8.55 cm^2). Fuel: 0.5 M $NaBH_4$ + 4 M NaOH. Oxidant: x M H_2O_2 + 1.5 M H_2SO_4. Flow velocity: 3 cm s^{-1}. Temperature: 25 °C.

6.3.6. The effect of mean linear flow velocity

The mean flow velocity, v (cm s^{-1}), of the electrolyte is another critical factor that affects the cell performance. Figure 6.6 plots the cell potential and the power density of the DBHPFC obtained at different mean linear electrolyte flow velocities of 0.5, 1, 2, 3, 4 and 6 cm s^{-1} at 25 °C using a fresh electrolyte for each experiment. It was observed that the flow velocity does not influence the OCP, as it generally hovers around 1.75 V for all variable velocities. This was expected, as no change in the electrolyte composition or in the other operating conditions should keep the thermodynamic equilibrium potentials of both the anode [Eq. (6.4)] and cathode reactions as they are. Figure 6.6 exhibits the continuous improvement on the FC performance as the flow velocity increased from 0.5 cm s^{-1} to 2 cm s^{-1}. The latter showed the best maximum power density, which was 93 mW cm^{-2} with a cell voltage of 0.8 V at 115 mA cm^{-2}. The rise of the mass transport of the reactants likely affected this improvement, as more BH_4^- and H_2O_2 were supplied to both the anode and cathode, respectively, enhancing the removal of H_2 bubbles from the anode and O_2 from the cathode [116]. The mass-transport aspect was discussed thoroughly in Chapter 5. Yang et al. [242] mentioned that a low linear flow velocity (0.5 cm s^{-1}, as in the present work) would encourage the crossover of the hydrogen peroxide and H^+ ions through the membrane, as the residence time of acid on contact with the base would increase while reducing the flow velocity. This phenomenon might explain the reduction of the cell performance at the mean flow velocity of 0.5 cm s^{-1}, where the peak power density was 75 mW cm^{-2} at a cell potential of 0.6 V and 125 mA cm^{-2} current density.

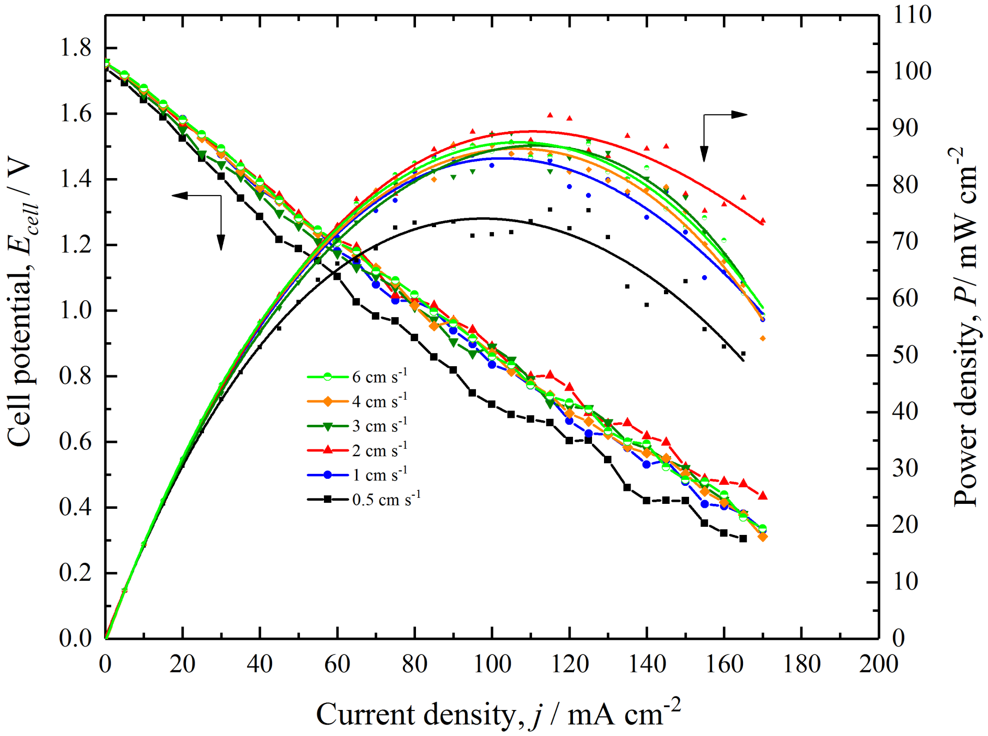

Figure 6.6. The effect of the mean linear flow velocity on the cell voltage and power density of the DBHPFC. Anode: $Pt_{0.75}$-$Ir_{0.25}$/Ti plate (9 cm^2). Cathode: Pt/Ti mesh (8.55 cm^2). Fuel: 0.5 M $NaBH_4$ + 4 M NaOH. Oxidant: 2 M H_2O_2 + 1.5 M H_2SO_4. Temperature: 25 °C.

Increasing the flow velocity more than 2 cm s^{-1}, however, did not improve the cell performance, as the hydrogen peroxide might be controlled by its reduction kinetics rate on the cathode [243] and the borohydride by its oxidation rate on the anode. Raising the flow rate may lead to greater bypass of the electrode surface by the electrolyte, which potentially decreases the cell performance. However, the type of flow field (configuration of the flow plate) in an electrochemical FC has a significant influence on the ratio of the performance improvement [244]. Increasing the flow velocity in one compartment may induce high pressure and force some species to crossover to the other compartment, affecting the DBHPFC performance. In order to minimise this effect, a one-head peristaltic pump (323S/D, Watson-Marlow) was used to maintain equivalent flow velocities in both compartments (as they have the same dimensions and distance of the pipes). The sealing materials were acceptable, as no leakage of the electrolyte was observed during the operation. High flow velocities of 3, 4 and 6 cm s^{-1} all showed reductions in the cell voltages and power densities than 2 cm s^{-1}, as the latter presented the best power density (93 mW cm^{-2}). For that reason, the velocity has been fixed at 2 cm s^{-1} in the remaining experiments, using the same conditions as those in Figure 6.6.

6.3.7. The effect of temperature

The variation of the power density and cell potential with respect to the current density at different cell operating temperatures are depicted in Figure 6.7 and summarised in Table 6.5. The table shows the OCP values, peak power densities and cell potential at their corresponding current density loads. The temperature was varied from 25 ^{o}C to 65 ^{o}C using a fuel containing 0.5 M $NaBH_4$ + 4 M NaOH and an oxidant of 2 M H_2O_2 + 1.5 M H_2SO_4 at $v = 2$ cm s^{-1}. The cell performance showed a strong dependence on the operating temperature and a considerable improvement as it increased. The peak power density increased from 93 to 162 mW cm^{-2} (~75%) when the temperature was elevated from 25 to 65 ^{o}C because of decreasing activation polarisation in the cell, as seen in the Arrhenius equation [Eq. (4.11)]. Elevating the operating temperature promotes (1) the kinetic rate of electrochemical reactions to take place on the anode and cathode, (2) the diffusion and mass-transfer coefficients of the chemical species and (3) the ionic conductivity of the anolyte and the membrane [141 138 142 143]. For example, it was found that increasing the temperature from 18 to 85 ^{o}C in the sodium hydroxide solution the conductivity rises three times [245] [138]. The conductivity of other DBHPFC components would exhibit similar effects at elevated temperature [138]. Parthasarathy et al. [141] attributed the increase of the conductivity on Nafion® membranes to rising temperature and water content, which they measured from 30 to 80 °C. However, above 70 °C, no considerable change in conductivity was observed, as the water uptake of the membrane reached its limit.

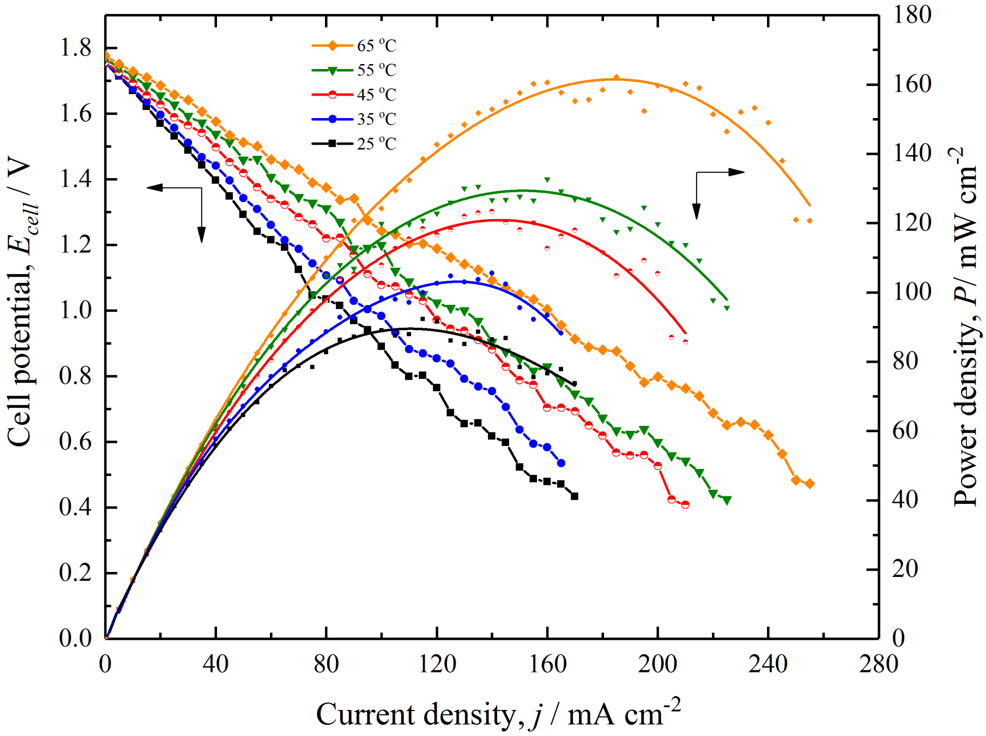

Figure 6.7. The effect of temperature on the cell voltage and power density of the DBHPFC. Anode: $Pt_{0.75}$-$Ir_{0.25}$/Ti plate (9 cm^2). Cathode: Pt/Ti mesh (8.55 cm^2). Fuel: 0.5 M $NaBH_4$ + 4 M NaOH. Oxidant: 2 M H_2O_2 + 1.5 M H_2SO_4. Flow velocity: 2 cm s^{-1}.

Table 6.5. The effect of temperature on the DBHPFC.

	Temperature / °C				
	25	35	45	55	65
Open-circuit potential / V	1.71	1.72	1.73	1.74	1.75
Peak power density / mW cm^{-2}	93	105	124	132	162
Cell potential at peak power density / V	0.80	0.76	0.88	0.83	0.88
Current density at peak power density / mA cm^{-2}	115	140	140	160	185

The improvement in these three parameters (kinetics, mass transfer and conductivity) leads to higher conversion rates of BH_4^- on the anode and the reduction of H_2O_2 on the cathode. Unfortunately, the increasing temperature also encourages crossover of borohydride ions and its hydrolysis on the anode side [138 145 148 101] and could even speed up the chemical decomposition of H_2O_2 [148 243 238], especially in an alkaline medium, which could cause considerable fuel loss. Moreover, the membrane may partially dry, creating a higher resistance in the DBHPFC and a reduction in output [138].

In general, the results showed that the DBHPFC could be operated with a wide range of temperatures, including room temperature. The cell was able to provide a maximum power density of about 162 mW cm^{-2} (E_{cell} = 0.88 V) at 185 mA cm^{-2} (65 °C), but at the expense of losing some of the fuel and oxidant. Therefore, perhaps operating at room temperature at a low concentration of BH_4^- and H_2O_2 is recommended in order to utilise the reactants more efficiently and decrease gas generation.

6.3.8. The effect of ammonium hydroxide additive

Ammonium hydroxide (NH_4OH) was proposed to be add 5 wt.% in the anolyte solution together with 10 wt.% $NaBH_4$ and 5 wt.% NaOH to dissolve the product of $NaBH_4$ oxidation, i.e. sodium metaborate ($NaBO_2$), and to minimise the borohydride hydrolysis [24 246]. The performance of the DBHPFC using fuel containing 1 M NH_4OH (~ 4 wt.%) in 0.5 M $NaBH_4$ + 4 M NaOH at 25 °C is presented in Figure 6.8. The rest of the operational conditions are the same and have been included in Figure 6.8. The presence of NH_4OH in the fuel decreased the peak power density by 33% (63 mW cm^{-2} and 0.82 V at 65 mA cm^{-2}) from the peak without it (93 mW cm^{-2} and 0.8 V at 115 mA cm^{-2}). These results indicate that ammonium hydroxide adversely affects the performance of DBHPFC. The ammonium hydroxide is a weak base, so it will not dissociate completely in an aqueous solution:

$$NH_4OH + H_2O \rightarrow NH_4^+ + 2OH^- \quad (6.5)$$

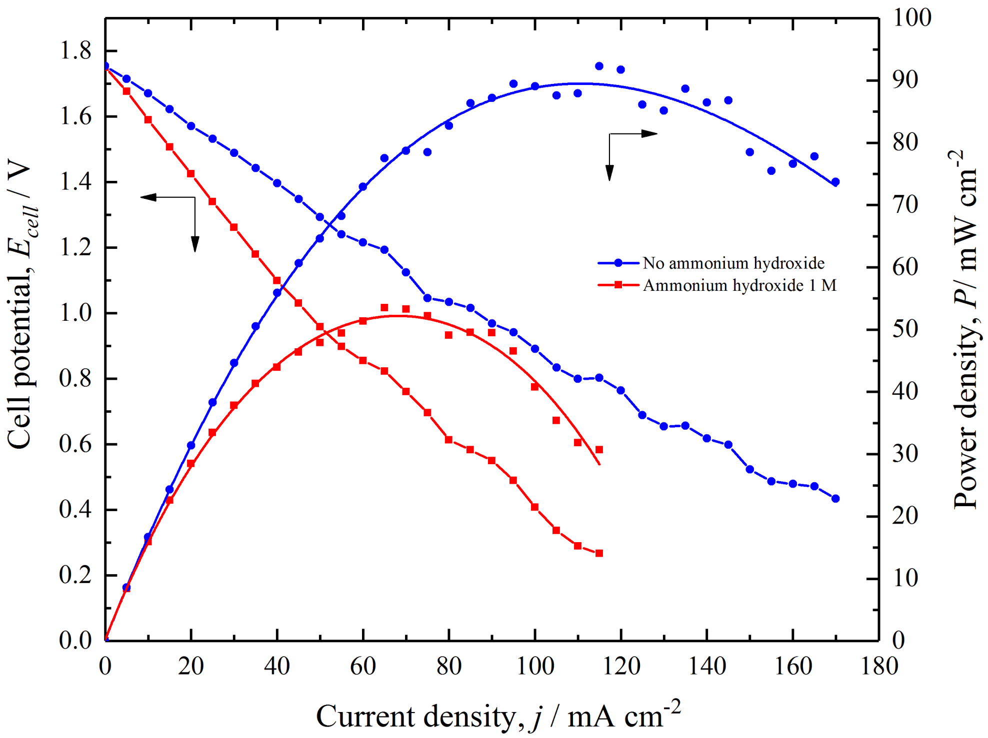

Figure 6.8. The effect of ammonium hydroxide (NH_4OH) on the cell voltage and power density of the DBHPFC. Anode: $Pt_{0.75}$-$Ir_{0.25}$/Ti plate (9 cm^2). Cathode: Pt/Ti mesh (8.55 cm^2). Fuel: 0.5 M $NaBH_4$ + 4 M NaOH + 1 M NH_4OH. Oxidant: 2 M H_2O_2 + 1.5 M H_2SO_4. Flow velocity: 2 cm s^{-1}. Temperature: 25 °C.

The ammonium ions act as a weak acid in water and dissociate to form ammonia and H^+ ions:

$$NH_4^+ \leftrightarrow NH_3 + H^+ \tag{6.6}$$

Ammonia may react with the protons of the Nafion® membrane to form NH_4^+ again, which might reduce the membrane conductivity and decrease the cell performance [247]. One of the challenges to $H_2 \| O_2$ proton exchange membrane (PEM) FCs is forming traces of NH_3 from the catalytic reaction of H_2 and N_2 [248]. Uribe et al. [248] found that high traces of ammonia levels (30–130 ppm in H_2 gas feed) for long exposure times to the anode severely cut cell performance, making DBHPFCs more attractive, since they apparently do not have gas impurities and poisoning species. Another possible reason for the drop in cell performance is the absorption of ammonia on the anode sites, which would minimise the direct oxidation of BH_4^-. However, ammonium hydroxide might help at a high level of borohydride concentration as more sodium metaborate will be produced and that needs further investigation. Generally, the results indicated that the associated adverse effects of adding ammonium hydroxide in the anolyte outmatched its beneficial effects, so it is not recommended for the current system.

6.3.9. The effect of sodium dodecyl sulphate additive

A small number of publications have reported on the use of additives to suppress the hydrolysis of BH_4^- [37 49 160 161], especially using sodium dodecyl sulphate (SDS) for the BH_4^- oxidation system [156]. Merino-Jimenez et al. [156] used a half-cell configuration to study the SDS effects on BH_4^- oxidation while, in the present work, it was investigated in a complete cell, which could provide more information for future applications. Figure 6.9 reveals the SDS influence on the polarisation curves of the DBHPFC obtained using SDS concentrations of 0.01, 0.001 and 0.0001 wt.% added to the fuel (see the figure caption).

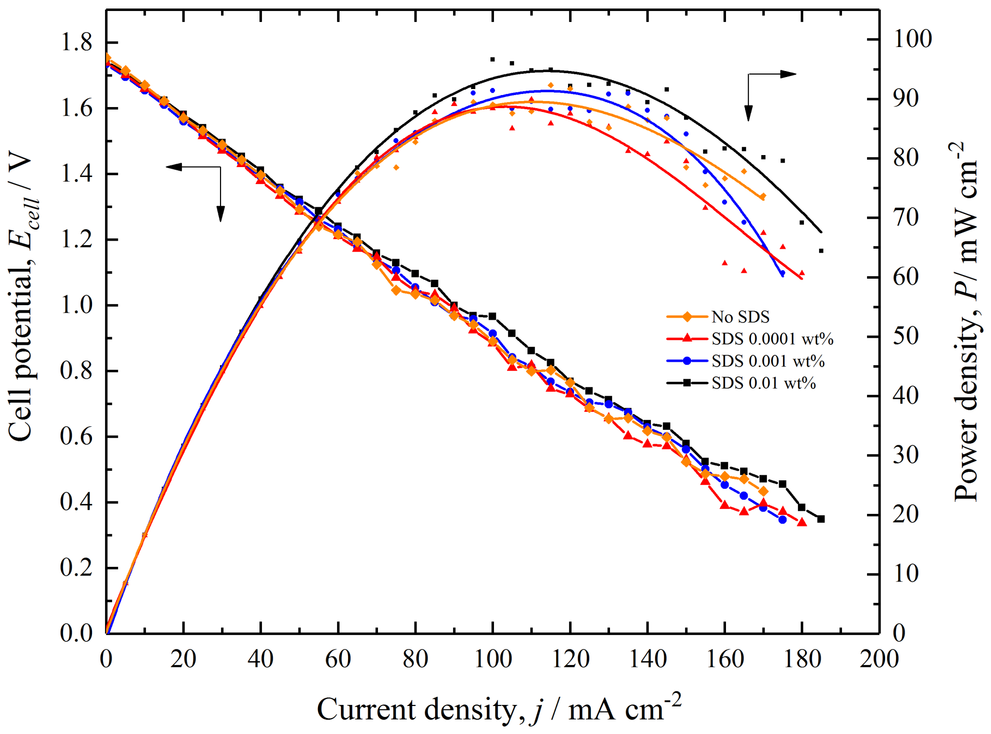

Figure 6.9. The effect of SDS on the cell voltage and power density of the DBHPFC. Anode: $Pt_{0.75}$-$Ir_{0.25}$/Ti plate (9 cm^2). Cathode: Pt/Ti mesh (8.55 cm^2). Fuel: 0.5 M $NaBH_4$ + 4 M NaOH + x wt.% SDS. Oxidant: 2 M H_2O_2 + 1.5 M H_2SO_4. Flow velocity: 2 cm s^{-1}. Temperature: 25 °C.

Increasing the SDS concentration from 0.001 to 0.01 wt.% showed a little improvement (3% at 0.01 wt.%) over the data obtained in the absence of surfactants. With 0.01 wt.% SDS, which was the best composition, the FC operated at 115 mA cm^{-2} and provided a cell potential of 0.83 V and only 95 mW cm^{-2} power density, compared to 92 mW cm^{-2} and 0.81 V at the same current density using the fuel without SDS. This enhancement on the cell performance has been referred to the inhibition of H_2 evolution [49] [160] [161], the improved diffusion coefficient of borohydride, the limiting current and the kinetic constants [156]. Some researchers [156] have suggested that the concentration of SDS should not exceed 0.001 wt.%; otherwise, it partially blocks the active sites and reduces the current density. However, the concentration of 0.01 wt.% worked well in the present study and showed increases in both the current cell voltage and power density. This finding may be attributed to the catalyst material that was used (gold) in the reference [156]. Further increasing the SDS concentration (> 0.01 wt.%) would probably affect the active catalyst sites and, as a consequence, reduce the cell performance; therefore, a high SDS concentration was not considered here. However, the use of 0.01 wt.% of SDS, as it presented a good performance, was recommended for the highly porous electrode, as can be seen in the section of 6.3.11.

6.3.10. The stability test of the DBHPFC under the optimal operating conditions

The operating stability test was also a crucial factor in confirming the durability and performance of the DBHPFC using the final optimal operating conditions. Figure 6.10 demonstrates the dependence of the cell potential on the operation time at a constant discharge current density of 25 mA cm^{-2} with the circulation of the electrolytes. The optimal operating conditions that have been found in this research (the blue curve) involved an anolyte containing 0.5 M $NaBH_4$ + 4 M NaOH and a catholyte containing 2 M H_2O_2 + 1.5 M H_2SO_4 at a mean linear flow velocity of 2 cm s^{-1} at 25 °C. The ohmic resistance in the cell and the side reactions that occur chemically and electrochemically could explain the drop in the OCP (1.71 V) from the maximum theoretical value of 3.02 V [Eq. (2.18)]. The average cell potential could continuously generate approximately 1.5 V and 38 mW cm^{-2} of power density during the one-hour operating period. The cell performance exhibited considerable stability using the optimal operating conditions; see Figure 6.10. This performance presented a remarkable improvement in the cell voltage

(25%, 1.5 V) and its stability, where the low cell voltage decay (or loss) and the less fluctuation were observed, in contrast to the cell output (1.2 V) under the initial conditions described in Chapter 4, which can be seen in Figure 6.10 (the red curve that was taken from Figure 4.24). The excellent stability is likely due to the optimised operating conditions that have been discovered in this study.

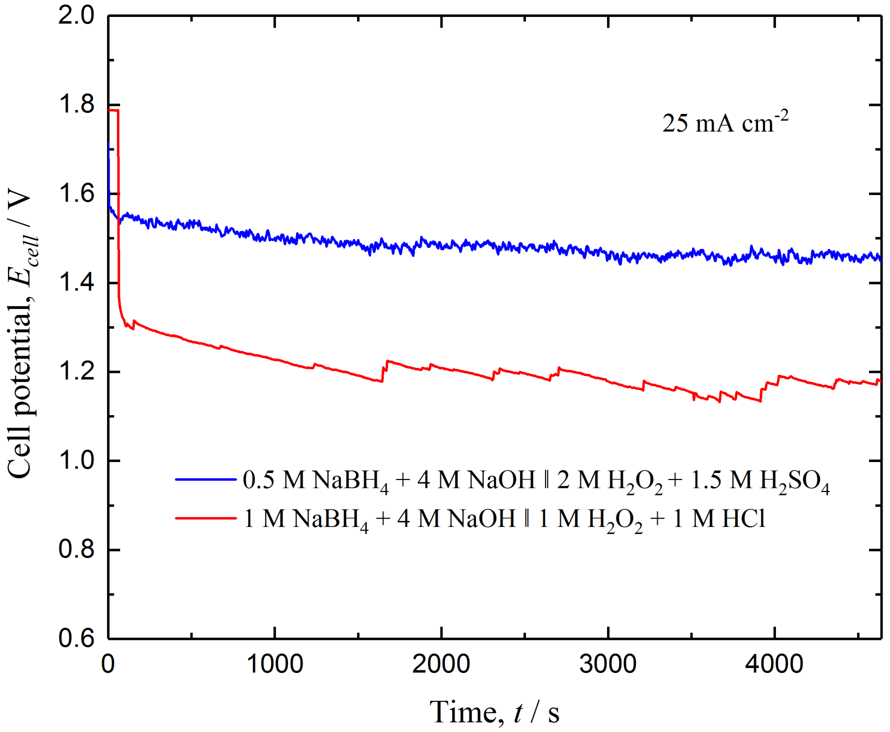

Figure 6.10. The stability of the $NaBH_4$‖H_2O_2 cells for about 1 h using $Pt_{0.75}$-$Ir_{0.25}$/Ti plate anode catalysts (9 cm^2) and Pt/Ti mesh (8.55 cm^2) as a cathode operating at a current density of 25 mA cm^{-2} at 25 ±1 °C. The mean linear fluid velocity was 2 cm s^{-1}.

The cell discharge capacity was calculated by multiplying the area under the curve (potential × time = 7257 V s) to the current load of 0.225 A (9 cm^2 electrode area) and divided by 3600 s, resulting in a cell energy capacity of 450 mW h and 300 mA h (for an average cell potential of 1.5 V). The expected FC life for the total weighted amount of $NaBH_4$ (3.783 g in 200 mL) was about 1.38 h [cell capacity (300 mA h) divided by the current load (225 mA)]. The specific energy was about 304 W h kg^{-1} (based on the total, 1.48 g BH_4^-, fuel weight) and the maximum power density was 93 mW cm^{-2} (at 115 mA cm^{-2}; see Table 6.5). Amendola et al. [91] reported 184 W h kg^{-1} and 20 mW cm^{-2} using gold-coated carbon silk in a borohydride-air cell (3.6 cm^2) at room temperature. In other words, the $Pt_{0.75}$-$Ir_{0.25}$/Ti plate catalyst provided better performance than the gold catalyst.

6.3.11. The effect of anode structure on the direct borohydride fuel cell

The best 3D electrodes (from Chapter 5), including the $Pt_{0.75}$-$Ir_{0.25}$/Ti fine mesh, the mesh and the felt electrodes (see their structures in Figure 5.1d, b and e, respectively), were examined using the optimal operating conditions that have been found for the plate electrode. The performance of the DBHPFC using the fine mesh and mesh anodes is displayed in Figure 6.11. The polarisation and power density curves were obtained using fuels of 0.5 M and 0.25 M $NaBH_4$ in 4 M NaOH, and the oxidant contained 2 M H_2O_2 in 1.5 M H_2SO_4 at a mean linear flow velocity of 2 cm s^{-1} at 25 °C.

It was surprising that the mesh and fine mesh performed worse than the plate electrode; see all the results summarised in Table 6.6. The maximum power density of the cell with an anode plate structure (93 mW cm^{-2}) is around 38–40% higher than when mesh (68 mW cm^{-2}) and fine mesh (66 mW cm^{-2}) electrodes were employed. This result could be attributed to an increased hydrolysis rate, the H_2 bubbles that were observed, and the HOR competing with the BOR, as 3D electrodes provide higher surface areas exposed to BH_4^- ions than plates, which reduces both the cell voltage and power output and, thus, fuel utilisation efficiency.

In order to confirm that increasing BH_4^- concentration was indeed reducing fuel utilisation efficiency, another electrolyte solution with a lower borohydride concentration of 0.25 M was tested. In this case, a little enhancement in the power density (6%, 70 mW cm^{-2}) and the cell potential (0.93 V) of fine mesh was observed, meaning that 3D electrodes with a low $NaBH_4$ concentration should be used – or an efficient catalyst active towards the direct electro-oxidation of BH_4^- should be found – to maximise the fuel utilisation efficiency.

It is worth to compare the data obtained from the final optimal operating conditions (Figure 6.11) with the that obtained from the initial conditions (Figure 5.13) for the 3D electrodes. As a result, under the optimal operating conditions, the maximum power density with the fine mesh electrode improved by 48% from 44.5 mW cm^{-2} (Figure 5.13b) to 66 mW cm^{-2} (Figure 6.11) and, with the mesh electrode, 170% from 25 mW cm^{-2} (Figure 5.13a) to 68 mW cm^{-2} (Figure 6.11). These results demonstrate the importance of optimising the operating conditions for the cell performance.

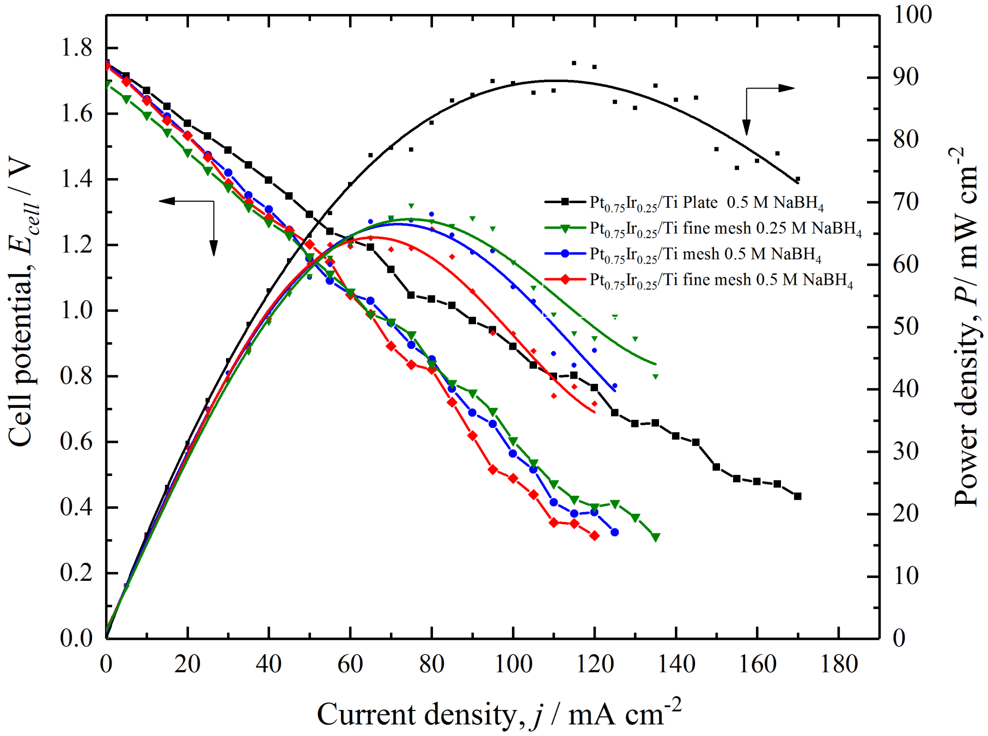

Figure 6.11. The effect of the anode structure on the cell voltage and power density of the DBHPFC. Anodes: $Pt_{0.75}$-$Ir_{0.25}$/Ti plate (9 cm^2), mesh (8.55 cm^2) and fine mesh (9 cm^2). Cathode: Pt/Ti mesh (8.55 cm^2). Fuel: 0.5 M $NaBH_4$ + 4 M NaOH. Oxidant: 2 M H_2O_2 + 1.5 M H_2SO_4. Flow velocity: 2 cm s^{-1}. Temperature: 25 °C.

Table 6.6. The effect of the anode structure on the $Pt_{0.75}$-$Ir_{0.25}$/Ti | 0.5 M $NaBH_4$ + 4 M NaOH ‖ 2 M H_2O_2 + 1.5 M H_2SO_4 | Pt cell at 25 °C.

	Anode structure			
	Plate	Mesh	Fine mesh	Fine mesh*
Open-circuit potential / V	1.75	1.75	1.75	1.69
Peak power density / mW cm^{-2}	93	68	66	70
Cell potential at peak power density / V	0.80	0.85	0.82	0.93
Current density at peak power density / mA cm^{-2}	115	80	80	75

*at 0.25 M $NaBH_4$

Figure 6.12 illustrates the polarisation and power density curves for the felt (highly porous) electrode using the same conditions as Figure 6.11 but with and without the presence of SDS additive (0.01 wt.%) to observe the fuel utilisation efficiency. The main results from Figure 6.12 were summarised in Table 6.7, where the cell performance showed significant improvement under the optimal operating conditions over the output from Figure 5.13b's conditions. The latter presents the maximum power density with felt as only 29 mW cm^{-2} at 0.5 V and a 60 mA cm^{-2} current load, while the power density soared by 83% under the optimal operating conditions to 53 mW cm^{-2} at a cell voltage of 0.83 V and 65 mA cm^{-2}. The anolyte composition of Figure 5.13b was 2.5 M $NaBH_4$ + 2 M NaOH, and the catholyte composition was 0.75 M H_2O_2 + 2 M NaOH with a mean linear flow velocity of 4 cm s^{-1} at 23 °C. A low borohydride concentration has been suggested with the fine mesh and mesh electrodes, however, with the felt electrode, the opposite was the case, as the cell performance decreased with minimising the BH_4^- content (50%) to 0.25 M; see Figure 6.12. That could be attributed to the larger area of it that could occupy the reactant species.

Section 6.3.9 demonstrated that adding SDS additive to the anolyte solution could benefit the DBHPFC performance. That was applicable with the felt electrode, with which the peak power density reached 77 mW cm^{-2} at 0.77 V and 100 mA cm^{-2}, a 45% improvement over the results with no SDS and 166% over the initial, non-tuned operating conditions. Even though the cost of 3D electrodes is higher, they could not compete with the plate electrode. That could be connected with the fuel decomposition on the highly porous electrodes. However, if a cost-effective and inactive catalyst towards BH_4^- hydrolysis is found, the mesh (Figure 5.1b) and fine mesh (Figure 5.1d) structures seem perfect for the DBHPFC because of their excellent performance with the Pt-Ir catalyst, which could outmatch the plate's performance.

Table 6.7. The effect of the felt anode on the $Pt_{0.75}$-$Ir_{0.25}$/Ti | 0.5 M $NaBH_4$ + 4 M NaOH ‖ 2 M H_2O_2 + 1.5 M H_2SO_4 | Pt cell at 25 °C.

	Plate	Felt	
	No SDS	No SDS	0.01 wt.% SDS
Open-circuit potential / V	1.75	1.73	1.75
Peak power density / mW cm^{-2}	93	53	77
Cell potential at peak power density / V	0.80	0.83	0.77
Current density at peak power density / mA cm^{-2}	115	65	100

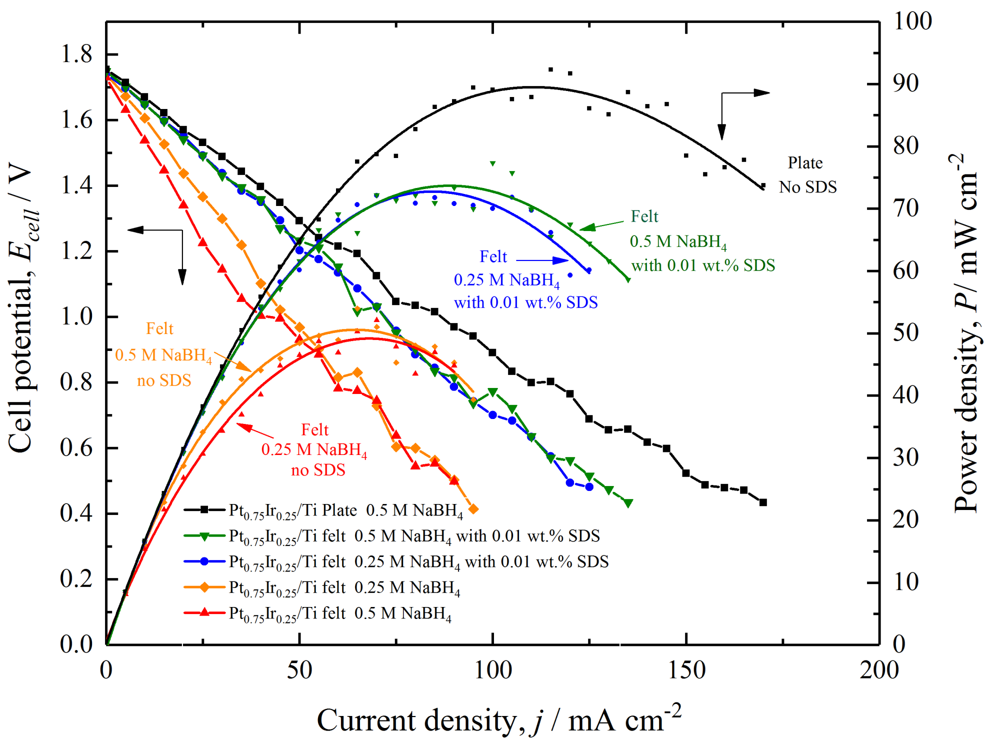

Figure 6.12. The performance of the highly porous felt anode electrode in the DBHPFC with and without 0.01 wt.% SDS. Anode: $Pt_{0.75}$-$Ir_{0.25}$/Ti felt (8.55 cm^2). Cathode: Pt/Ti mesh (8.55 cm^2). Fuel: 0.25 or 0.5 M $NaBH_4$ + 4 M NaOH. Oxidant: 2 M H_2O_2 + 1.5 M H_2SO_4. Flow velocity: 2 cm s^{-1}. Temperature: 25 ^{o}C.

6.4. Conclusion

The effects of the operation conditions on the DBHPFC performance were evaluated. The following are the most relevant results, where the improvement of cell power density due to the changing of the operating conditions is presented in Figure 6.13:

- Increasing the sodium borohydride concentration enhanced the cell performance due to the improvement in the transport of the reactants (i.e. BH_4^-, Na^+) and the reaction kinetics rate, however, increasing it beyond 0.5 M was not favourable to the DBHPFC, as it likely led to both more BH_4^- crossover and a greater BH_4^- hydrolysis rate.
- A significant improvement (46%) in the cell potential and the power density was observed by increasing the NaOH concentration from 1.0 to 4.0 M due to the enhancement in the electrolyte conductivity and the borohydride stability. Using less than 1 M NaOH reduced the cell performance because of a higher BH_4^-

hydrolysis rate, but more than 4.0 M NaOH created a highly viscous solution, affecting the ion mass transport.

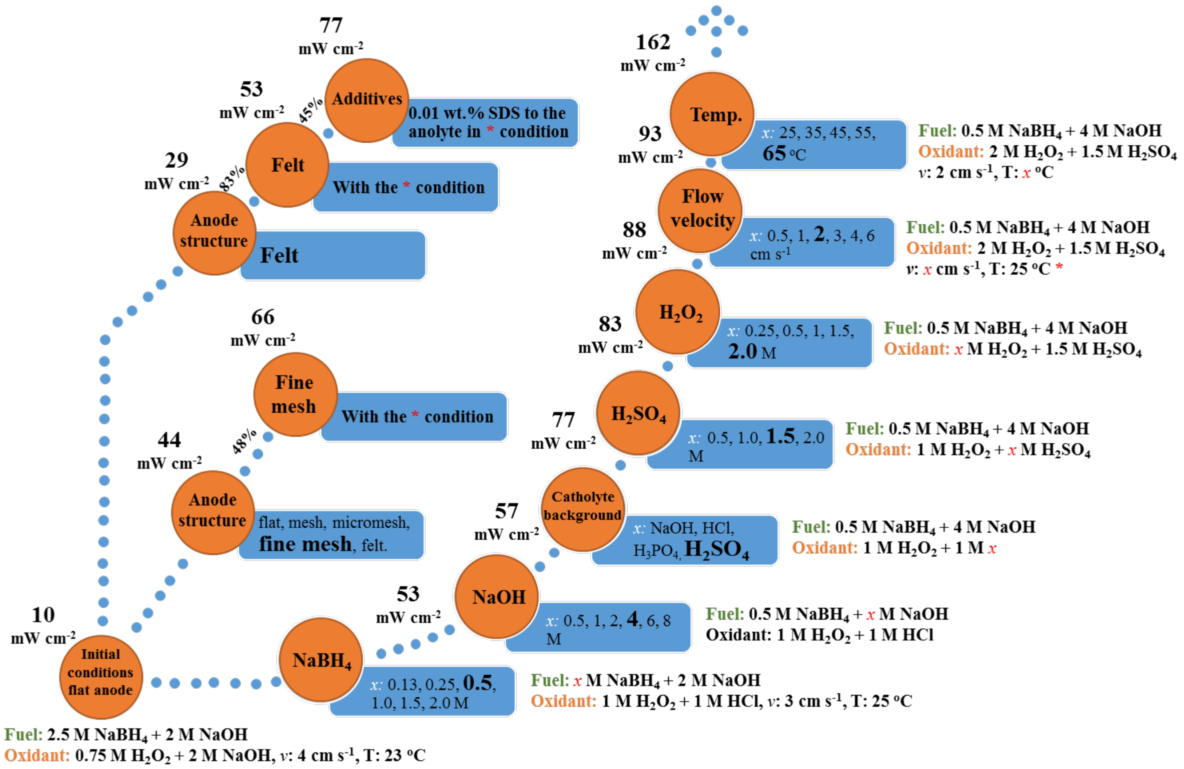

Figure 6.13. The improvement of power densities that were obtained from the direct borohydride fuel cell at different operating conditions and anode structures.

- Sulfuric acid is the proposed catholyte background material among sodium hydroxide, phosphoric acid and hydrochloric acid. The concentration of 1.5 M H_2SO_4 provided the most favourable cell voltage and power density (six times greater than that obtained from alkaline).
- Increasing the mean linear flow velocity from 0.5 to 2 cm s^{-2} presented a positive effect on the cell power density, which reached 93 mW cm^{-2} with a cell voltage of 0.8 V at 115 mA cm^{-2} for 2 cm s^{-2} at 25 °C. This improvement was due to greater mass-transport of the reactants, more BH_4^- and H_2O_2 being supplied to the anode and cathode, respectively, as well as the ease of removal of the H_2 bubbles from the anode and O_2 from the cathode.
- The cell performance showed a dependence on the operating temperature. The reaction kinetics at the anode and cathode were promoted at higher temperatures.

The peak power density increased dramatically from 93 to 162 mW cm^{-2} (double tilde 75%) when the temperature elevated from 25 to 65 °C.

- The presence of ammonium hydroxide (4 wt.%) in the fuel revealed a significant decrease of 33% in the peak power density, meaning that adversely affects DBHPFC performance.
- Adding SDS (0.01 wt.%) as a surfactant to the fuel showed considerable improvement, mainly when 3D electrodes were used. The enhancement on the cell performance was referred to inhibiting H_2 evolution and the improvement on the diffusion coefficient of borohydride, the limiting current and the kinetic constants. The peak power density of the felt electrode improved by 45%, reaching 77 mW cm^{-2} at 0.77 V and 100 mA cm^{-2}, over its performance with no SDS.
- The cell performance exhibited good operating stability under the optimal operating conditions, generating approximately 38 mW cm^{-2} power density at 1.5 V during the 1-h operating period. The cell discharge capacity was 450 mW h and 300 mA h. The specific energy was about 304 W h kg^{-1} (of BH_4^-) and the maximum power density was 93 mW cm^{-2} (at 115 mA cm^{-2}).
- 3D electrodes could not compete with the plate. However, if an efficient catalyst for the direct oxidation of BH_4^- is found, the mesh and fine mesh structures are suggested, as they are expected to outperform the plate because of their remarkable behaviour with the Pt-Ir catalyst.

Chapter 7: Conclusions and Future Work

The aim of the present study (as seen in Figure 7.1) was to increase the performance of a direct borohydride fuel cell (DBFC) in three stages. The first one was to study the borohydride oxidation kinetics on bimetallic Pt-Ir alloys (75:25 and 25:75) by a variety of electrochemical techniques (chapter 4). The second stage was using the optimal Pt-Ir composition, the outcome of the first stage, to find out the appropriate 3D anode design (chapter 5). The third stage was studying the performance of a practical DBFC at various operating conditions using the most promising anode materials from the second stage to maximise the cell power output (chapter 6). This is the first study reporting the BH_4^- oxidation parameters of Pt-Ir (75:25, 25:75) deposited on a Ti plate, the mass-transport measurements of 3D $Pt_{0.75}$-$Ir_{0.25}$/Ti materials in a DBFC and the cell performance under various operating conditions.

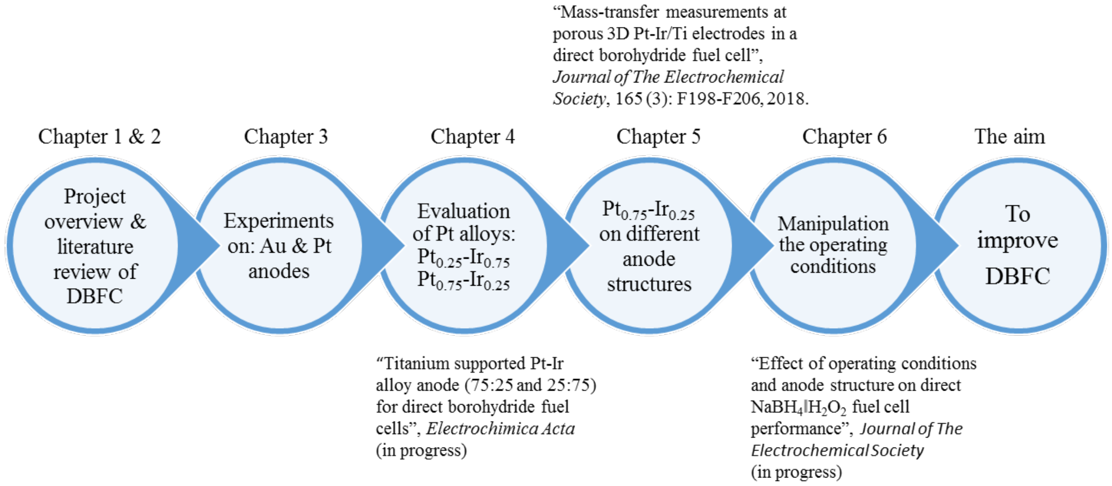

"Mass-transfer measurements at porous 3D Pt-Ir/Ti electrodes in a direct borohydride fuel cell", *Journal of The Electrochemical Society*, 165 (3): F198-F206, 2018.

"Titanium supported Pt-Ir alloy anode (75:25 and 25:75) for direct borohydride fuel cells", *Electrochimica Acta* (in progress)

"Effect of operating conditions and anode structure on direct $NaBH_4$‖H_2O_2 fuel cell performance", *Journal of The Electrochemical Society* (in progress)

Figure 7.1. The project sequence and the outcomes.

7.1. Conclusions

The conclusions of this research are listed here in order of relevance:

- A full DBFC setup was prepared and a single cell was designed and constructed.
- The half-cell test of the electrochemical oxidation of borohydride ions was carried out on Pt and Au anodes by cyclic voltammetry (CV), linear sweep voltammetry (LSV), and rotating disc–electrode (RDE) measurements. The Pt planar electrode showed higher activity towards BH_4^- oxidation at a much lower potential than Au.

- CV was used to quantify the concentration of sodium borohydride for an alkaline solution. The empirical linear relationship between the peak current (mA) and the borohydride concentration was obtained ($I_p = 0.182\ c_{BH_4}$) for a concentration ranging from 0 to 20 mmol dm^{-3} in 2 mol dm^{-3} NaOH using an Au planar electrode.
- Borohydride ions presented appreciable stability in an aqueous alkaline solution (2 mol dm^{-3} NaOH) over a 15-h test period using a concentration of 0.02 mol dm^{-3} BH_4^-. The stability study was performed using LSV to record the peak current using an Au electrode (2 mm diameter).
- Unreported anode catalysts of Pt alloy that included $Pt_{0.75}$-$Ir_{0.25}$ and $Pt_{0.25}$-$Ir_{0.75}$ deposited on a Ti plate were investigated for application in DBFCs. The two anodes were prepared, characterised and evaluated for direct BH_4^- oxidation. They presented higher activity towards direct oxidation of BH_4^- at a considerably lower potential than Au. The $Pt_{0.75}$-$Ir_{0.25}$ catalyst provided a power density of approximately 35% higher than the gold electrode. As the Pt-Ir is relatively very active for BH_4^- oxidation, its hydrolysis was also observed. Sodium dodecyl sulphate (SDS) additive was suggested to suppress the hydrolysis, as it had a significant beneficent influence (45% in the power density in case of felt anode).
- Among the catalysts that have been investigated, the bimetallic $Pt_{0.75}$-$Ir_{0.25}$/Ti plate anode demonstrated higher borohydride oxidation reaction (BOR) current densities, a higher number of electrons exchanged and a faster reaction rate than $Pt_{0.25}$-$Ir_{0.75}$/Ti.
- The required activation energy of $Pt_{0.75}$-$Ir_{0.25}$ was also lower (18.6 kJ mol^{-1}) than that of $Pt_{0.25}$-$Ir_{0.75}$ (28 kJ mol^{-1}). For the BOR, the value of the charge transfer coefficient, α, on the $Pt_{0.75}$-$Ir_{0.25}$/Ti plate was 0.59, while its value was 0.42 on the $Pt_{0.25}$-$Ir_{0.75}$ plate, which confirms that the system is irreversible.
- The total number of electrons exchanged, z, on $Pt_{0.75}$-$Ir_{0.25}$/Ti was 5.3 electrons at 294 K and 3.7 electrons for $Pt_{0.25}$-$Ir_{0.75}$/Ti. The standard heterogeneous rate constant, k_s, of the BOR was 5×10^{-10} cm s^{-1}, which suggests that the oxidation reaction was prolonged in $Pt_{0.25}$-$Ir_{0.75}$/Ti in contrast to $Pt_{0.75}$-$Ir_{0.25}$ (0.1×10^{-10} cm s^{-1}), however, it is relatively still lower than the reported. The reaction constant, y, of $Pt_{0.75}$-$Ir_{0.25}$ is three times that of $Pt_{0.25}$-$Ir_{0.75}$, and $Pt_{0.75}$-$Ir_{0.25}$'s reaction order, β, is closer to the unity, while it was 0.69 for $Pt_{0.25}$-$Ir_{0.75}$.

- The peak power density of the DBFC with $Pt_{0.75}$-$Ir_{0.25}$/Ti anode was about double that provided by the $Pt_{0.25}$-$Ir_{0.75}$/Ti under the same conditions.
- The mass-transport study for the DBFC was carried out, as no data had been published on it. The researcher has successfully reported the study [249] and the related data in 2018, as listed in the publication section.
- The volumetric mass-transport coefficients, k_mA_e, for five fabricated $Pt_{0.75}$-$Ir_{0.25}$/Ti working electrodes were evaluated by the limiting current technique. The mass-transport rate (the value of k_mA_e) increased towards the electrode surface along with the electrolyte mean flow velocity and the Reynolds number. The felt and fine mesh electrodes showed the highest rate of all the tested anodes.
- The enhancement factors, δ, were also evaluated for all electrodes. The optimal values of δ were 99.5 (at a flow rate of 6 cm s^{-1}), 67 (8 cm s^{-1}) and 22.6 (4 cm s^{-1}) for felt, fine mesh and micromesh, respectively. In the presence of turbulence promoters (TPs), the currents extracted from the plate and mesh electrodes more than doubled.
- The effects of various borohydride concentrations on the limiting current and k_mA_e values were examined. The limiting current increased when the concentration rose, but the volumetric mass-transport coefficient remained relatively constant with respect to the concentration at a specific flow velocity.
- The volumetric mass-transport coefficient of the reactants for all anode electrodes increased in the following sequence: plate < plate + 3 TP < mesh < micromesh < felt < fine mesh.
- The (calculated) complete conversion of borohydride was fast for the felt and fine mesh electrodes. For example, they required about only two hours to consume 0.01 mol dm^{-3} of BH_4^-, followed by the micromesh electrode (4.6 h), whereas the other electrode geometries required more than 30 h to consume BH_4^- completely, even in the presence of TPs.
- The number of cycles in a batch recycle system was calculated for all electrodes as well. The number of cycles indicates how many circulations the system requires to utilise the dissolved borohydride ions (0.01 mol dm^{-3}). The fine mesh electrode presented the best performance (20 cycles), followed by the felt and micromesh electrodes (27 and 50 cycles, respectively). However, it was estimated to take a

higher number of cycles if mesh (300 cycles) and plate (600 cycles) electrodes are used.

- The overall fractional conversions in a cascade system of n_e identical electrodes were evaluated as well. The fine mesh electrode showed a remarkable performance, followed by the felt and micromesh electrodes.
- The effects of the operating conditions on the performance of a DBHPFC using $Pt_{0.75}$-$Ir_{0.25}$ anode was studied. The power density improved dramatically by using suitable materials and determining the optimal values of the operating parameters.
- Using a low $NaBH_4$ concentration (≤ 0.5 M) would be beneficial for higher fuel utilisation and less poisoning of the cathode catalysts.
- Using less than 1.0 M NaOH as a background solution for $NaBH_4$ decreased the cell performance because a low pH value encourages BH_4^- hydrolysis. A solution containing more than 4.0 M NaOH is also not beneficial to the cell, as it creates a highly viscous solution, which decreases the movement capability of the ions towards the anode active sites. An improvement of 46% in the power density was recorded by increasing the NaOH concentration from 1.0 to 4.0 M. The anolyte with 4.0 M NaOH + 0.5 M $NaBH_4$ turned out to best suit the DBHPFC with a $Pt_{0.75}$-$Ir_{0.25}$ anode and a Pt cathode.
- Among the several catholyte background materials that have been studied, sulfuric acid (H_2SO_4) presented the best performance among sodium hydroxide, phosphoric acid and hydrochloric acid. It was found that a DBHPFC with a 1.5 M H_2SO_4 concentration provided the most favourable cell voltage and power density (83 mW cm^{-2}), as increasing the H^+ ions speeds up their transportation, increases the electrolyte conductivity and raises the reduction rate of H_2O_2. The power density of the DBHPFC with H_2O_2 in a strong acid (1.5 M H_2SO_4) was about six times that achieved with an alkaline background solution (13 mW cm^{-2}) under the same conditions.
- The external mechanical force also affects the cell output. Therefore, raising the mean linear flow velocity from 0.5 to 2 cm s^{-1} benefited the cell power density. Increasing the flow velocity beyond 2 cm s^{-1} did not benefit the cell performance, as the hydrogen peroxide might be controlled by its reduction kinetics rate on the cathode and the borohydride by its oxidation rate on the anode. The bypass of the

reactants is, perhaps, another possibility at a high flow rate (> 2 cm s^{-1}) and potentially reduces the cell performance.

- An improvement of 75% was measured in the power density of the DBHPFC when the temperature was elevated from 25 to 65 ^{o}C, meaning there is a strong dependence on the operating temperature in the DBHPFC system.
- The presence of an SDS surfactant (0.01 wt.%) in the fuel exhibited a considerable improvement, mainly when 3D electrodes were employed. However, adding ammonium hydroxide (4 wt.%) to the fuel revealed a significant decrease of 33% in the power density, meaning that it adversely affects the DBHPFC system.
- The optimal operating conditions found in this research are an anolyte of 0.5 M $NaBH_4$ + 4 M NaOH and a catholyte of 2 M H_2O_2 + 1.5 M H_2SO_4 at a mean linear flow velocity of 2 cm s^{-1} at 25 ^{o}C.
- The stability test of the DBHPFC exhibited a continuous generation of 38 mW cm^{-2} at 1.5 V during one hour of operating. The cell discharge capacity was 450 mW h and 300 mA h. The specific energy was about 304 W h kg^{-1} (of BH_4^-) and 93 mW cm^{-2} for the maximum power density (at 115 mA cm^{-2}).
- The performance of 3D electrodes could not compete with that presented by the plate anode. However, the fine mesh structure is suggested, based on the results of the mass-transport study (Chapter 5), when an efficient electroactive catalyst for the direct oxidation of BH_4^- is found.

7.2. Future work

Despite extensive work to commercialise DBFCs, several technological challenges that need to be overcome to reach theoretical power density values that are still far away. The performance of DBFCs can be improved by the following:

- Finding suitable flow field designs (such as serpentine [250 138 251]) for the electrolyte solution feed and comparing the results with a parallel flow field. Finding the optimal design would raise fuel utilisation efficiency by creating a uniform fuel distribution on the electrode surface.

- Depositing Au material on the fine mesh substrate and comparing the results with a Pt film electrode on the various structures and possibly an Ir film electrode are worth examining.
- Modelling the DBHPFC system using the research findings here (reaction parameters, electrode characterisations and mass-transport outputs) to study the effects of electrode structures and cell designs on its performance and the possibility of scale-up.
- Reducing both $NaBH_4$ hydrolysis and borohydride crossover.
- Investigating the precise mechanism of borohydride electro-oxidation on Pt-Ir electrode, which is still not fully understood.
- Long-term experimenting with DBHPFCs using 3D electrodes, carefully monitoring the H_2 and O_2 gases produced by the decomposition of $NaBH_4$ and H_2O_2, respectively, along with pH. A comparison between the rate of hydrogen evolution on 2D and 3D electrodes needs to be addressed using different 3D structures (felt, mesh, foam).

Appendix

Appendix I

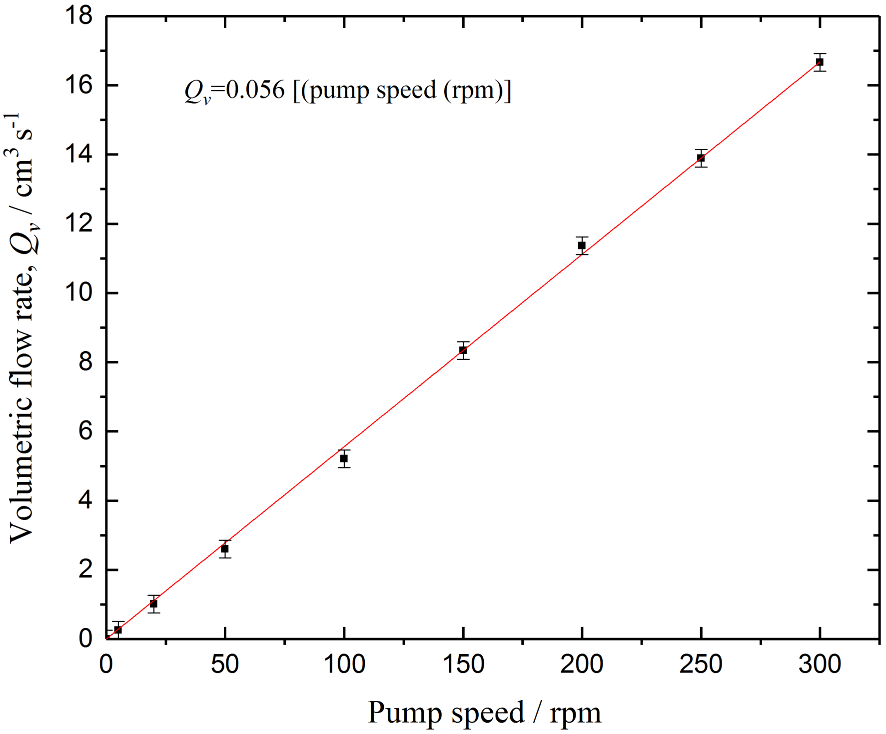

Figure A1. The calibration curve of volumetric flow rate, Q_V (cm^3 s^{-1}) *vs.* pump speed (rpm) for the pump (323S/D, 300 rpm) Watson-Marlow used in all experiments.

Appendix II

Table A1. EDS results using at different spot positions.

	Pt-Ir 75:25		Pt-Ir 25:75	
Spot No.	Pt	Ir	Pt	Ir
1	74.7	25.30	17.21	82.79
2	76.39	23.61	16.21	83.79
3	78	22.00	17.49	82.51
4	75.56	24.44	15.58	84.42
5	74.76	25.24	15.22	84.78
6	75.86	24.14	16.16	83.84
7	75.46	24.54	16.57	83.43
8	75.82	24.18	15.72	84.28
9	75.45	24.55	15.61	84.39
Average	75.78	24.22	16.20	83.80
	76	24	16	84

Appendix III

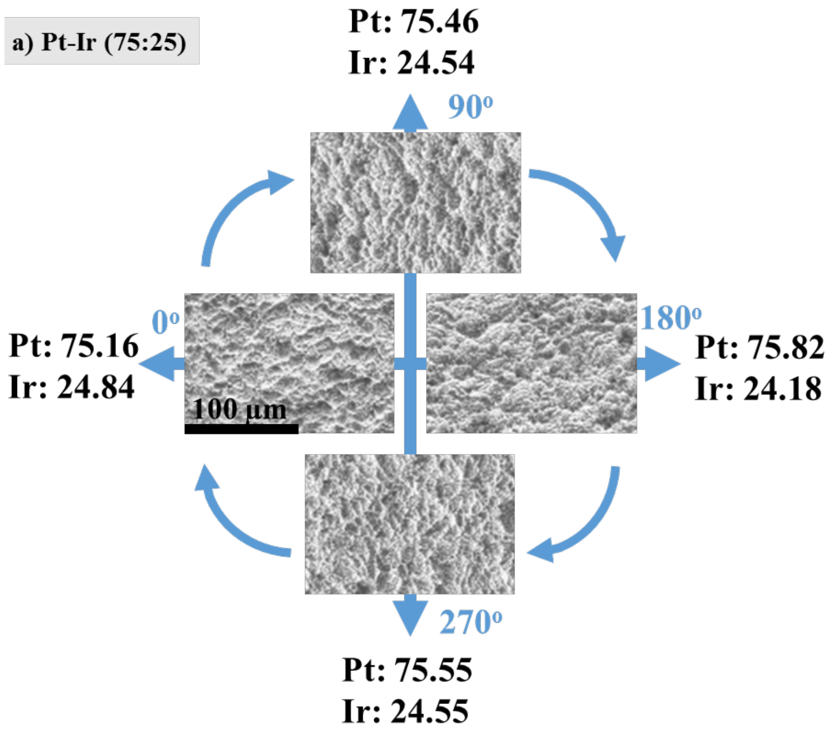

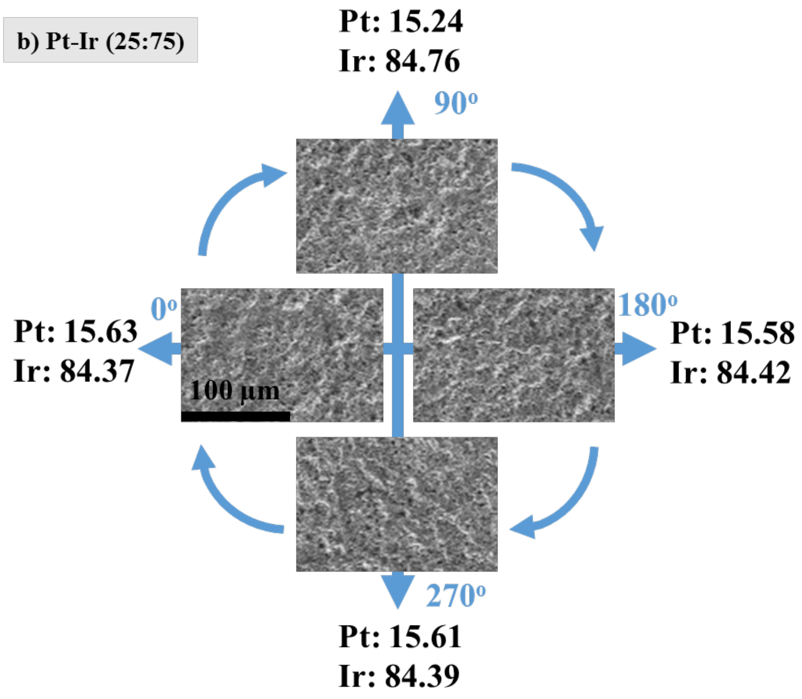

Figure A2. Effects of samples rotation on EDS results (atomic ratio of Pt-Ir): a) Pt-Ir (75:25) and b) Pt-Ir (25:75).

Appendix IV

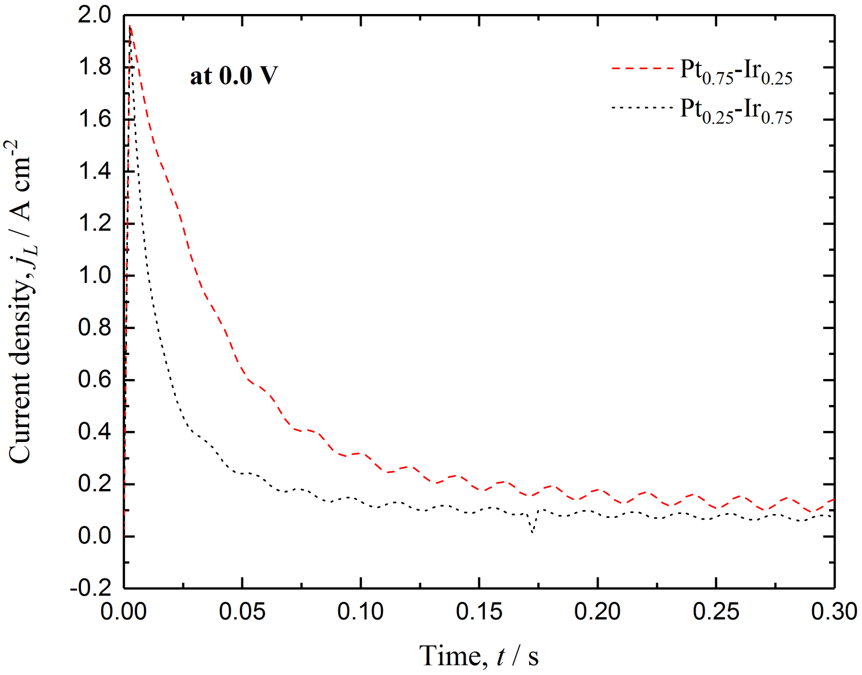

Figure A3. Chronoamperometry (from OCP to 0.0 V *vs.* Hg/HgO, 40 ms) of 0.03 mol dm^{-3} $NaBH_4$ in 2 mol dm^{-3} in the three-electrode cell using different Pt-Ir alloys. Pt mesh was the counter, and the temperature was controlled at 294 K (21 ±1 ^{o}C).

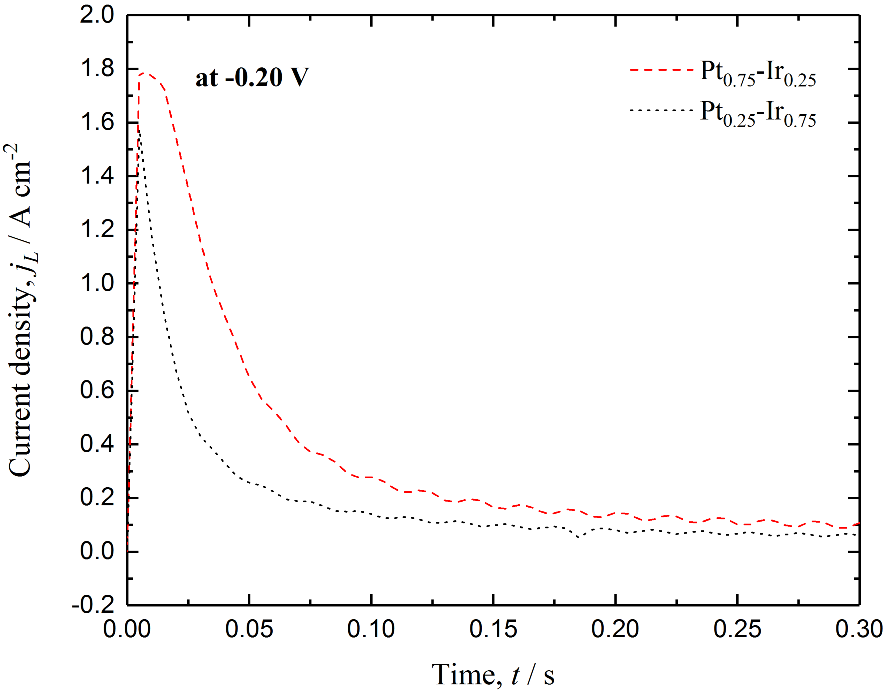

Figure A4. Chronoamperometry (from OCP to -0.2 V *vs.* Hg/HgO, 40 ms) of 0.03 mol dm^{-3} $NaBH_4$ in 2 mol dm^{-3} in the three-electrode cell using different Pt-Ir alloys. Pt mesh was the counter, and the temperature was controlled at 294 K (21 ±1 ^{o}C).

References

(1) Campen, A.; Mondal, K.; Wiltowski, T. Separation of Hydrogen from Syngas Using a Regenerative System. *Int. J. Hydrogen Energy* **2008**, *33* (1), 332–339. https://doi.org/10.1016/j.ijhydene.2007.07.016.

(2) Pison, G. The Population of the World (2019). *Popul. Soc.* **2019**, *569* (8), 1–8.

(3) Balat, M. Potential Importance of Hydrogen as a Future Solution to Environmental and Transportation Problems. *Int. J. Hydrogen Energy* **2008**, *33* (15), 4013–4029. https://doi.org/10.1016/j.ijhydene.2008.05.047.

(4) Lamy, C.; Coutanceau, C.; Leger, J.-M. The Direct Ethanol Fuel Cell: A Challenge to Convert Bioethanol Cleanly into Electric Energy. In *Catalysis for Sustainable Energy Production*; Wiley-VCH Verlag GmbH & Co. KGaA: Weinheim, Germany, 2009; pp 1–46. https://doi.org/10.1002/9783527625413.ch1.

(5) Barbaro, P.; Bianchini, C. *Catalysis for Sustainable Energy Production*; WILEY-VCH Verlag, 2009.

(6) Williams, M. L. CRC Handbook of Chemistry and Physics, 76th Edition. *Occup. Environ. Med.* **1996**, *53* (7), 504–504. https://doi.org/10.1136/oem.53.7.504.

(7) Ponce de León, C.; Walsh, F. C.; Bessette, R. R.; Patrissi, C. J.; Medeiros, M. G.; Rose, A.; Browning, D.; Lakeman, J. B.; Reeve, R. W. Recent Developments in Borohydride Fuel Cells; 2008; Vol. 15, pp 25–49.

(8) Ponce de Leon, C.; Walsh, F. C.; Pletcher, D.; Browning, D. J.; Lakeman, J. B. Direct Borohydride Fuel Cells. *J. Power Sources* **2006**, *155* (2), 172–181. https://doi.org/http://dx.doi.org/10.1016/j.jpowsour.2006.01.011.

(9) Stroman, R. O.; Jackson, G. S.; Garsany, Y.; Swider-Lyons, K. A Calibrated Hydrogen-Peroxide Direct-Borohydride Fuel Cell Model. *J. Power Sources* **2014**, *271*, 421–430. https://doi.org/http://dx.doi.org/10.1016/j.jpowsour.2014.07.139.

(10) Amendola, S. C.; Sharp-Goldman, S. L.; Janjua, M. S.; Spencer, N. C.; Kelly, M. T.; Petillo, P. J.; Binder, M. A Safe, Portable, Hydrogen Gas Generator Using Aqueous Borohydride Solution and Ru Catalyst. *Int. J. Hydrogen Energy* **2000**, *25* (10), 969–975. https://doi.org/http://dx.doi.org/10.1016/S0360-3199(00)00021-5.

(11) Ong, B. C.; Kamarudin, S. K.; Basri, S. Direct Liquid Fuel Cells: A Review. *Int. J. Hydrogen Energy* **2017**, *42* (15), 10142–10157. https://doi.org/10.1016/j.ijhydene.2017.01.117.

(12) Merino-Jiménez, I.; Ponce de León, C.; Shah, A. A.; Walsh, F. C. Developments in Direct Borohydride Fuel Cells and Remaining Challenges. *J. Power Sources* **2012**, *219*, 339–357. https://doi.org/http://dx.doi.org/10.1016/j.jpowsour.2012.06.091.

(13) Feng, R. X.; Dong, H.; Wang, Y. D.; Ai, X. P.; Cao, Y. L.; Yang, H. X. A Simple and High Efficient Direct Borohydride Fuel Cell with MnO2-Catalyzed Cathode. *Electrochem. commun.* **2005**, *7* (4), 449–452.

https://doi.org/http://dx.doi.org/10.1016/j.elecom.2005.02.023.

(14) Rude, L. H.; Nielsen, T. K.; Ravnsbæk, D. B.; Bösenberg, U.; Ley, M. B.; Richter, B.; Arnbjerg, L. M.; Dornheim, M.; Filinchuk, Y.; Besenbacher, F.; et al. Tailoring Properties of Borohydrides for Hydrogen Storage: A Review. *Phys. Status Solidi Appl. Mater. Sci.* **2011**, *208* (8), 1754–1773. https://doi.org/10.1002/pssa.201001214.

(15) Schlapbach, L.; Züttel, a. Hydrogen-Storage Materials for Mobile Applications. *Nature* **2001**, *414* (6861), 353–358. https://doi.org/10.1038/35104634.

(16) Schlesinger, H. I.; Brown, H. C.; Finholt, A. E.; Gilbreath, J. R.; Hoekstra, H. R.; Hyde, E. K. Sodium Borohydride, Its Hydrolysis and Its Use as a Reducing Agent and in the Generation of Hydrogen [1]. *J. Am. Chem. Soc.* **1953**, *75* (1), 215–219. https://doi.org/10.1021/ja01097a057.

(17) Celik, C.; Gul, F.; San, B.; Ibrahim, H. Effects of Operation Conditions on Direct Borohydride Fuel Cell Performance. *J. Power Sources* **2008**, *185*, 197–201. https://doi.org/10.1016/j.jpowsour.2008.06.066.

(18) Celik, C.; San, F. G. B.; Sarac, H. I. Influences of Sodium Borohydride Concentration on Direct Borohydride Fuel Cell Performance. *J. Power Sources* **2010**, *195* (9), 2599–2603. https://doi.org/10.1016/j.jpowsour.2009.11.093.

(19) Schlesinger, H. I.; Brown, H. C.; Abraham, B.; Bond, A. C.; Davidson, N.; Finholt, A. E.; Gilbreath, J. R.; Hoekstra, H.; Horvitz, L.; Hyde, E. K.; et al. New Developments in the Chemistry of Diborane and the Borohydrides. I. General Summary 1. *J. Am. Chem. Soc.* **1953**, *75* (1), 186–190. https://doi.org/10.1021/ja01097a049.

(20) Schlesinger, H. I.; Brown, H. C.; Finholt, A. E.; Gilbreath, J. R.; Hoekstra, H. R.; Hyde, E. K. Sodium Borohydride, Its Hydrolysis and Its Use as a Reducing Agent and in the Generation of Hydrogen 1. *J. Am. Chem. Soc.* **1953**, *75* (1), 215–219. https://doi.org/10.1021/ja01097a057.

(21) Richardson, B. S.; Birdwell, J. F.; Pin, F. G.; Jansen, J. F.; Lind, R. F. Sodium Borohydride Based Hybrid Power System. *J. Power Sources* **2005**, *145* (1), 21–29. https://doi.org/10.1016/j.jpowsour.2004.12.057.

(22) Wee, J. A Comparison of Sodium Borohydride as a Fuel for Proton Exchange Membrane Fuel Cells and for Direct Borohydride Fuel Cells. *J. Power Sources* **2006**, *155* (2), 329–339. https://doi.org/10.1016/j.jpowsour.2006.01.036.

(23) Santos, D. M. F.; Sequeira, C. A. C. Sodium Borohydride as a Fuel for the Future. *Renew. Sustain. Energy Rev.* **2011**, *15* (8), 3980–4001. https://doi.org/http://dx.doi.org/10.1016/j.rser.2011.07.018.

(24) Gu, L.; Luo, N.; Miley, G. H. Cathode Electrocatalyst Selection and Deposition for a Direct Borohydride/Hydrogen Peroxide Fuel Cell. *J. Power Sources* **2007**, *173* (1), 77–85. https://doi.org/10.1016/j.jpowsour.2007.05.005.

(25) Wee, J.-H. Which Type of Fuel Cell Is More Competitive for Portable Application: Direct Methanol Fuel Cells or Direct Borohydride Fuel Cells? *J. Power Sources* **2006**, *161* (1), 1–10. https://doi.org/10.1016/j.jpowsour.2006.07.032.

(26) Grinberg, V. a.; Mayorova, N. a.; Pasynskii, a. a. A Cluster Pt-Sn-Catalyst for the Ethanol Direct Oxidation. *Russ. J. Electrochem.* **2009**, *45* (12), 1321–1326. https://doi.org/10.1134/S1023193509120015.

(27) Broussely, M.; Archdale, G. Li-Ion Batteries and Portable Power Source Prospects for the next 5–10 Years. *J. Power Sources* **2004**, *136* (2), 386–394. https://doi.org/10.1016/j.jpowsour.2004.03.031.

(28) Miley, G. H.; Luo, N.; Mather, J.; Burton, R.; Hawkins, G.; Gu, L.; Byrd, E.; Gimlin, R.; Shrestha, P. J.; Benavides, G.; et al. Direct $NaBH_4/H_2O_2$ Fuel Cells. *J. Power Sources* **2007**, *165* (2), 509–516. https://doi.org/http://dx.doi.org/10.1016/j.jpowsour.2006.10.062.

(29) de León, C. P.; Walsh, F. C.; Rose, A.; Lakeman, J. B.; Browning, D. J.; Reeve, R. W. A Direct Borohydride—Acid Peroxide Fuel Cell. *J. Power Sources* **2007**, *164* (2), 441–448. https://doi.org/10.1016/j.jpowsour.2006.10.069.

(30) Lamy, C.; Lima, A.; LeRhun, V.; Delime, F.; Coutanceau, C.; Léger, J. M. Recent Advances in the Development of Direct Alcohol Fuel Cells (DAFC). *J. Power Sources* **2002**, *105* (2), 283–296. https://doi.org/10.1016/S0378-7753(01)00954-5.

(31) Scott, K.; Taama, W. .; Argyropoulos, P.; Sundmacher, K. The Impact of Mass Transport and Methanol Crossover on the Direct Methanol Fuel Cell. *J. Power Sources* **1999**, *83* (1–2), 204–216. https://doi.org/10.1016/S0378-7753(99)00303-1.

(32) Mochalov, K. N.; Khain, V. S.; Gil'manshin, G. G. Kinetic Studies on Intermediate Steps of BH4- Hydrolysis. *Kinet. Katal* **1965**, *6*, 541--544.

(33) Molina Concha, B.; Chatenet, M. Direct Oxidation of Sodium Borohydride on Pt, Ag and Alloyed Pt–Ag Electrodes in Basic Media. *Electrochim. Acta* **2009**, *54* (26), 6130–6139. https://doi.org/10.1016/j.electacta.2009.04.074.

(34) Retnamma, R.; Novais, A. Q.; Rangel, C. M. Kinetics of Hydrolysis of Sodium Borohydride for Hydrogen Production in Fuel Cell Applications: A Review. *Int. J. Hydrogen Energy* **2011**, *36* (16), 9772–9790. https://doi.org/http://dx.doi.org/10.1016/j.ijhydene.2011.04.223.

(35) Demirci, U. B. Direct Borohydride Fuel Cell: Main Issues Met by the Membrane–Electrodes-Assembly and Potential Solutions. *J. Power Sources* **2007**, *172* (2), 676–687. https://doi.org/10.1016/j.jpowsour.2007.05.009.

(36) Kojima, Y.; Haga, T. Recycling Process of Sodium Metaborate to Sodium Borohydride. *Int. J. Hydrogen Energy* **2003**, *28* (9), 989–993. https://doi.org/10.1016/S0360-3199(02)00173-8.

(37) Martins, J. I.; Nunes, M. C.; Koch, R.; Martins, L.; Bazzaoui, M. Electrochemical Oxidation of Borohydride on Platinum Electrodes: The Influence of Thiourea in Direct Fuel Cells. *Electrochim. Acta* **2007**, *52* (23), 6443–6449. https://doi.org/http://dx.doi.org/10.1016/j.electacta.2007.04.066.

(38) Wu, C.; Wu, F.; Bai, Y.; Yi, B.; Zhang, H. Cobalt Boride Catalysts for Hydrogen Generation from Alkaline NaBH 4 Solution. *Mater. Lett.* **2005**, *59* (14–15), 1748–1751. https://doi.org/10.1016/j.matlet.2005.01.058.

(39) Indig, M. E.; Snyder, R. N. Sodium Borohydride, An Interesting Anodic Fuel (1). *J. Electrochem. Soc.* **1962**, *109* (11), 1104–1106.

(40) Li, Z. P.; Liu, B. H.; Arai, K.; Asaba, K.; Suda, S. Evaluation of Alkaline Borohydride Solutions as the Fuel for Fuel Cell. *J. Power Sources* **2004**, *126* (1–2), 28–33. https://doi.org/10.1016/j.jpowsour.2003.08.017.

(41) Ponce de León, C.; Walsh, F. C.; Pletcher, D.; Browning, D. J.; Lakeman, J. B. Direct Borohydride Fuel Cells. *J. Power Sources* **2006**, *155* (2), 172–181. https://doi.org/http://dx.doi.org/10.1016/j.jpowsour.2006.01.011.

(42) Ritter, J. A.; Ebner, A. D.; Wang, J.; Zidan, R. Implementing a Hydrogen Economy. *Mater. Today* **2003**, *6* (9), 18–23. https://doi.org/10.1016/S1369-7021(03)00921-0.

(43) Zhang, Q.; Smith, G.; Wu, Y.; Mohring, R. Catalytic Hydrolysis of Sodium Borohydride in an Auto-Thermal Fixed-Bed Reactor. *Int. J. Hydrogen Energy* **2006**, *31* (7), 961–965. https://doi.org/http://dx.doi.org/10.1016/j.ijhydene.2005.07.008.

(44) Morris, J. H.; Gysling, H. J.; Reed, D. Electrochemistry of Boron Compounds. *Chem. Rev.* **1985**, *85* (1), 51–76. https://doi.org/10.1021/cr00065a003.

(45) Çelikkan, H.; Şahin, M.; Aksu, M. L.; Nejat Veziroğlu, T. The Investigation of the Electrooxidation of Sodium Borohydride on Various Metal Electrodes in Aqueous Basic Solutions. *Int. J. Hydrogen Energy* **2007**, *32* (5), 588–593. https://doi.org/10.1016/j.ijhydene.2006.06.065.

(46) Liu, B. H.; Suda, S. Hydrogen Storage Alloys as the Anode Materials of the Direct Borohydride Fuel Cell. *J. Alloys Compd.* **2008**, *454* (1–2), 280–285. https://doi.org/10.1016/j.jallcom.2006.12.034.

(47) Larminie, J.; Dicks, A. *Fuel Cell Systems Explained*, Second Edi.; John Wiley & Sons Ltd, Ed.; Chichester, England, 2003.

(48) Chen, H.; Chen, J.-T.; Shao, L.; Wang, L.; Fu, X.-Z.; Luo, J.-L. Minimum and Well-Dispersed Platinum Nanoparticles on 3D Porous Nickel for Highly Efficient Electrocatalytic Hydrogen Evolution Reaction Enabled by Atomic Layer Deposition. *Appl. Surf. Sci.* **2019**, *494*, 1091–1099. https://doi.org/10.1016/j.apsusc.2019.07.251.

(49) Gyenge, E. Electrooxidation of Borohydride on Platinum and Gold Electrodes: Implications for Direct Borohydride Fuel Cells. *Electrochim. Acta* **2004**, *49* (6), 965–978. https://doi.org/10.1016/j.electacta.2003.10.008.

(50) Mirkin, M. V. Borohydride Oxidation at a Gold Electrode. *J. Electrochem. Soc.* **1992**, *139* (8), 2212. https://doi.org/10.1149/1.2221204.

(51) Finkelstein, D. a; Mota, N. Da; Cohen, J. L.; Abruña, H. D. Rotating Disk Electrode (RDE) Investigation of BH_4^- and BH_3OH^- Electro-Oxidation at Pt and Au: Implications for BH_4^- Fuel Cells. *J. Phys. Chem. C* **2009**, *113* (45), 19700–19712. https://doi.org/10.1021/jp900933c.

(52) Elder, J. P.; Hickling, A. Anodic Behaviour of the Borohydride Ion. *Trans. Faraday Soc.* **1962**, *58*, 1852–1864. https://doi.org/10.1039/tf9625801852.

(53) Elder, J. P. Hydrogen Ionization in the Anodic Oxidation of the Borohydride Ion. *Electrochim. Acta* **1962**, *7* (4), 417–426. https://doi.org/10.1016/0013-4686(62)80030-9.

(54) Olu, P.-Y.; Bonnefont, A.; Rouhet, M.; Bozdech, S.; Job, N.; Chatenet, M.; Savinova, E. Insights into the Potential Dependence of the Borohydride Electrooxidation Reaction Mechanism on Platinum Nanoparticles Supported on Ordered Carbon Nanomaterials. *Electrochim. Acta* **2015**, *179*, 637–646. https://doi.org/10.1016/j.electacta.2015.02.158.

(55) Oliveira, V. L.; Sibert, E.; Soldo-Olivier, Y.; Ticianelli, E. A.; Chatenet, M. Borohydride Electrooxidation Reaction on Pt(111) and Pt(111) Modified by a Pseudomorphic Pd Monolayer. *Electrochim. Acta* **2016**, *190*, 790–796. https://doi.org/10.1016/j.electacta.2016.01.013.

(56) Molina Concha, B.; Chatenet, M.; Ticianelli, E. A.; Lima, F. H. B. In Situ Infrared (FTIR) Study of the Mechanism of the Borohydride Oxidation Reaction on Smooth Pt Electrode. *J. Phys. Chem. C* **2011**, *115* (25), 12439–12447. https://doi.org/10.1021/jp2002589.

(57) Concha, B. M.; Chatenet, M.; Coutanceau, C.; Hahn, F. In Situ Infrared (FTIR) Study of the Borohydride Oxidation Reaction. *Electrochem. commun.* **2009**, *11* (1), 223–226. https://doi.org/http://dx.doi.org/10.1016/j.elecom.2008.11.018.

(58) Grimmer, C.; Grandi, M.; Zacharias, R.; Cermenek, B.; Weber, H.; Morais, C.; Napporn, T. W.; Weinberger, S.; Schenk, A.; Hacker, V. The Electrooxidation of Borohydride: A Mechanistic Study on Palladium (Pd/C) Applying RRDE, 11B-NMR and FTIR. *Appl. Catal. B Environ.* **2016**, *180*, 614–621. https://doi.org/10.1016/j.apcatb.2015.07.028.

(59) Olu, P.-Y.; Bonnefont, A.; Braesch, G.; Martin, V.; Savinova, E. R.; Chatenet, M. Influence of the Concentration of Borohydride towards Hydrogen Production and Escape for Borohydride Oxidation Reaction on Pt and Au Electrodes – Experimental and Modelling Insights. *J. Power Sources* **2018**, *375*, 300–309. https://doi.org/10.1016/j.jpowsour.2017.07.061.

(60) Shah, A. A.; Singh, R.; de Leon, C. P.; Wills, R. G.; Walsh, F. C. Mathematical Modelling of Direct Borohydride Fuel Cells. *J. Power Sources* **2013**, *221*, 157–171. https://doi.org/10.1016/j.jpowsour.2012.07.083.

(61) Liu, B. H.; Li, Z. P.; Suda, S. Electrocatalysts for the Anodic Oxidation of Borohydrides. *Electrochim. Acta* **2004**, *49* (19), 3097–3105. https://doi.org/10.1016/j.electacta.2004.02.023.

(62) Chatenet, M.; Micoud, F.; Roche, I.; Chainet, E. Kinetics of Sodium Borohydride Direct Oxidation and Oxygen Reduction in Sodium Hydroxide Electrolyte. Part I. BH4- Electro-Oxidation on Au and Ag Catalysts. *Electrochim. Acta* **2006**, *51* (25), 5459–5467. https://doi.org/10.1016/j.electacta.2006.02.015.

(63) Ma, J.; Choudhury, N. A.; Sahai, Y. A Comprehensive Review of Direct Borohydride Fuel Cells. *Renew. Sustain. Energy Rev.* **2010**, *14* (1), 183–199. https://doi.org/http://dx.doi.org/10.1016/j.rser.2009.08.002.

(64) Li, Z. P.; Liu, B. H.; Arai, K.; Suda, S. A Fuel Cell Development for Using Borohydrides as the Fuel. *J. Electrochem. Soc.* **2003**, *150* (7), A868.

https://doi.org/10.1149/1.1576767.

(65) Raman, R. K.; Choudhury, N. A.; Shukla, A. K. A High Output Voltage Direct Borohydride Fuel Cell. *Electrochem. Solid-State Lett.* **2004**, *7* (12), A488–A491. https://doi.org/10.1149/1.1817855.

(66) Kiran, V.; Ravikumar, T.; Kalyanasundaram, N. T.; Krishnamurty, S.; Shukla, a. K.; Sampath, S. Electro-Oxidation of Borohydride on Rhodium, Iridium, and Rhodium–Iridium Bimetallic Nanoparticles with Implications to Direct Borohydride Fuel Cells. *J. Electrochem. Soc.* **2010**, *157* (8), B1201. https://doi.org/10.1149/1.3442372.

(67) Oh, T. H.; Jang, B.; Kwon, S. Estimating the Energy Density of Direct Borohydride–Hydrogen Peroxide Fuel Cell Systems for Air-Independent Propulsion Applications. *Energy* **2015**, *90*, 980–986. https://doi.org/10.1016/j.energy.2015.08.002.

(68) Liu, B. H.; Li, Z. P.; Suda, S. Anodic Oxidation of Alkali Borohydrides Catalyzed by Nickel. *J. Electrochem. Soc.* **2003**, *150* (3), A398. https://doi.org/10.1149/1.1553785.

(69) Gyenge, E.; Atwan, M.; Northwood, D. Electrocatalysis of Borohydride Oxidation on Colloidal Pt and Pt-Alloys (Pt-Ir, Pt-Ni, and Pt-Au) and Application for Direct Borohydride Fuel Cell Anodes. *J. Electrochem. Soc.* **2006**, *153* (1), A150. https://doi.org/10.1149/1.2131831.

(70) Jusys, Z.; Behm, R. J. Borohydride Electrooxidation over Pt/C, AuPt/C and Au/C Catalysts: Partial Reaction Pathways and Mixed Potential Formation. *Electrochem. commun.* **2015**, *60*, 9–12. https://doi.org/10.1016/j.elecom.2015.07.021.

(71) Ponce de León, C.; Walsh, F. C.; Patrissi, C. J.; Medeiros, M. G.; Bessette, R. R.; Reeve, R. W.; Lakeman, J. B.; Rose, A.; Browning, D. A Direct Borohydride–Peroxide Fuel Cell Using a Pd/Ir Alloy Coated Microfibrous Carbon Cathode. *Electrochem. commun.* **2008**, *10* (10), 1610–1613. https://doi.org/10.1016/j.elecom.2008.08.006.

(72) Merino-Jimenez, I.; Janik, M. J.; Ponce de Leon, C.; Walsh, F. C. Pd–Ir Alloy as an Anode Material for Borohydride Oxidation. *J. Power Sources* **2014**, *269*, 498–508. https://doi.org/10.1016/j.jpowsour.2014.06.140.

(73) Yi, L.; Wei, W.; Zhao, C.; Yang, C.; Tian, L.; Liu, J.; Wang, X. Electrochemical Oxidation of Sodium Borohydride on Carbon Supported Pt-Zn Nanoparticle Bimetallic Catalyst and Its Implications to Direct Borohydride-Hydrogen Peroxide Fuel Cell. *Electrochim. Acta* **2015**, *158*, 209–218. https://doi.org/10.1016/j.electacta.2015.01.111.

(74) Duan, D.; You, X.; Liang, J.; Liu, S.; Wang, Y. Carbon Supported Cu-Pd Nanoparticles as Anode Catalyst for Direct Borohydride-Hydrogen Peroxide Fuel Cells. *Electrochim. Acta* **2015**, *176*, 1126–1135. https://doi.org/10.1016/j.electacta.2015.07.118.

(75) Behmenyar, G.; Akın, A. N. Investigation of Carbon Supported Pd–Cu Nanoparticles as Anode Catalysts for Direct Borohydride Fuel Cell. *J. Power Sources* **2014**, *249*, 239–246. https://doi.org/10.1016/j.jpowsour.2013.10.063.

(76) Tiwari, A.; Nagaiah, T. C. Mesoporous Nitrogen-Rich Carbon as Metal-Free Anode Catalyst for Borohydride Fuel Cells. *Energy Technol.* **2016**, n/a-n/a. https://doi.org/10.1002/ente.201500472.

(77) Bayatsarmadi, B.; Peters, A.; Talemi, P. Catalytic Polymeric Electrodes for Direct Borohydride Fuel Cells. *J. Power Sources* **2016**, *322*, 26–30. https://doi.org/10.1016/j.jpowsour.2016.04.137.

(78) Santos, D. M. F.; Šljukić, B.; Amaral, L.; Macciò, D.; Saccone, A.; Sequeira, C. A. C. Nickel and Nickel-Cerium Alloy Anodes for Direct Borohydride Fuel Cells. *J. Electrochem. Soc.* **2014**, *161* (5), F594–F599. https://doi.org/10.1149/2.023405jes.

(79) Celik, C.; Boyaci San, F. G.; Sarac, H. I. Investigation of Ni Foam Effect for Direct Borohydride Fuel Cell. *Fuel Cells* **2012**, *12* (6), 1027–1031. https://doi.org/10.1002/fuce.201200002.

(80) Guo, M.; Cheng, Y.; Yu, Y.; Hu, J. Ni-Co Nanoparticles Immobilized on a 3D Ni Foam Template as a Highly Efficient Catalyst for Borohydride Electrooxidation in Alkaline Medium. *Appl. Surf. Sci.* **2017**, *416*, 439–445. https://doi.org/10.1016/j.apsusc.2017.04.193.

(81) Oshchepkov, A. G.; Braesch, G.; Ould-Amara, S.; Rostamikia, G.; Maranzana, G.; Bonnefont, A.; Papaefthimiou, V.; Janik, M. J.; Chatenet, M.; Savinova, E. R. Nickel Metal Nanoparticles as Anode Electrocatalysts for Highly Efficient Direct Borohydride Fuel Cells. *ACS Catal.* **2019**, *9* (9), 8520–8528. https://doi.org/10.1021/acscatal.9b01616.

(82) Santos, D. M. F.; Šljukić, B.; Amaral, L.; Milikić, J.; Sequeira, C. A. C.; Macciò, D.; Saccone, A. Nickel–Rare Earth Electrodes for Sodium Borohydride Electrooxidation. *Electrochim. Acta* **2016**, *190*, 1050–1056. https://doi.org/10.1016/j.electacta.2015.12.218.

(83) Duan, D.; Liang, J.; Liu, H.; You, X.; Wei, H.; Wei, G.; Liu, S. The Effective Carbon Supported Core–Shell Structure of Ni@Au Catalysts for Electro-Oxidation of Borohydride. *Int. J. Hydrogen Energy* **2015**, *40* (1), 488–500. https://doi.org/10.1016/j.ijhydene.2014.10.101.

(84) Li, B.; Yan, Q.; Song, C.; Yan, P.; Ye, K.; Cheng, K.; Zhu, K.; Yan, J.; Cao, D.; Wang, G. Reduced Graphene Oxide Foam Supported CoNi Nanosheets as an Efficient Anode Catalyst for Direct Borohydride Hydrogen Peroxide Fuel Cell. *Appl. Surf. Sci.* **2019**. https://doi.org/10.1016/j.apsusc.2019.06.110.

(85) Ma, J.; Sahai, Y.; Buchheit, R. G. Direct Borohydride Fuel Cell Using Ni-Based Composite Anodes. *J. Power Sources* **2010**, *195* (15), 4709–4713. https://doi.org/10.1016/j.jpowsour.2010.02.034.

(86) Liu, B. H.; Li, Z. P.; Higuchi, E.; Suda, S. Improvement of the Electrochemical Properties of Zr-Based AB2 Alloys by an Advanced Fluorination Technique. *J. Alloys Compd.* **1999**, *293*, 702–706. https://doi.org/10.1016/S0925-8388(99)00445-4.

(87) Cheng, H.; Scott, K. Investigation of Ti Mesh-Supported Anodes for Direct Borohydride Fuel Cells. *J. Appl. Electrochem.* **2006**, *36* (12), 1361–1366. https://doi.org/10.1007/s10800-006-9199-7.

(88) Ponce de León, C.; Kulak, A.; Williams, S.; Merino-Jiménez, I.; Walsh, F. C. Improvements in Direct Borohydride Fuel Cells Using Three-Dimensional Electrodes. *Catal. Today* **2011**, *170* (1), 148–154. https://doi.org/http://dx.doi.org/10.1016/j.cattod.2011.03.010.

(89) Duan, D.; Liu, H.; You, X.; Wei, H.; Liu, S. Anodic Behavior of Carbon Supported Cu@Ag Core–Shell Nanocatalysts in Direct Borohydride Fuel Cells. *J. Power Sources* **2015**, *293*, 292–300. https://doi.org/10.1016/j.jpowsour.2015.05.086.

(90) EG&G Technical Services, I. Fuel Cell Handbook. *Fuel Cell* **2004**, *7 Edition* (November), 1–352. https://doi.org/10.1002/zaac.200300050.

(91) Amendola, S. C.; Onnerud, P.; Kelly, M. T.; Petillo, P. J.; Sharp-Goldman, S. L.; Binder, M. A Novel High Power Density Borohydride-Air Cell. *J. Power Sources* **1999**, *84* (1), 130–133. https://doi.org/10.1016/S0378-7753(99)00259-1.

(92) Cheng, H.; Scott, K. Determination of Kinetic Parameters for Borohydride Oxidation on a Rotating Au Disk Electrode. *Electrochim. Acta* **2006**, *51* (17), 3429–3433. https://doi.org/10.1016/j.electacta.2005.09.038.

(93) Lima, F. H. B.; Pasqualeti, A. M.; Molina Concha, M. B.; Chatenet, M.; Ticianelli, E. A. Borohydride Electrooxidation on Au and Pt Electrodes. *Electrochim. Acta* **2012**, *84*, 202–212. https://doi.org/10.1016/j.electacta.2012.05.030.

(94) Atwan, M. H.; Macdonald, C. L. B.; Northwood, D. O.; Gyenge, E. L. Colloidal Au and Au-Alloy Catalysts for Direct Borohydride Fuel Cells: Electrocatalysis and Fuel Cell Performance. *J. Power Sources* **2006**, *158* (1), 36–44. https://doi.org/10.1016/j.jpowsour.2005.09.054.

(95) Yi, L.; Wei, W.; Zhao, C.; Tian, L.; Liu, J.; Wang, X. Enhanced Activity of Au-Fe/C Anodic Electrocatalyst for Direct Borohydride-Hydrogen Peroxide Fuel Cell. *J. Power Sources* **2015**, *285*, 325–333. https://doi.org/10.1016/j.jpowsour.2015.03.118.

(96) Tamasauskaite-Tamasiunaite, L.; Jagminiene, A.; Balčiunaite, A.; Zabielaite, A.; Žieliene, A.; Naruškevičius, L.; Vaičiuniene, J.; Selskis, A.; Juškenas, R.; Norkus, E. Electrocatalytic Activity of the Nanostructured Au-Co Catalyst Deposited onto Titanium towards Borohydride Oxidation. *Int. J. Hydrogen Energy* **2013**, *38* (33), 14232–14241. https://doi.org/10.1016/j.ijhydene.2013.08.101.

(97) Tamašauskaitė-Tamašiūnaitė, L.; Balčiūnaitė, A.; Zabielaitė, A.; Stankevičienė, I.; Kepenienė, V.; Selskis, A.; Juškėnas, R.; Norkus, E. Investigation of Electrocatalytic Activity of the Nanostructured Au–Cu Catalyst Deposited on the Titanium Surface towards Borohydride Oxidation. *J. Electroanal. Chem.* **2013**, *700*, 1–7. https://doi.org/10.1016/j.jelechem.2013.04.011.

(98) Duan, D.; Yin, X.; Wang, Q.; Liu, S.; Wang, Y. Performance Evaluation of Borohydride Electrooxidation Reaction with Ternary Alloy Au–Ni–Cu/C Catalysts. *J. Appl. Electrochem.* **2018**, *48* (7), 835–847. https://doi.org/10.1007/s10800-018-1208-0.

(99) Balčiūnaitė, A.; Tamašauskaitė-Tamašiūnaitė, L.; Santos, D. M. F.; Zabielaitė,

A.; Jagminienė, A.; Stankevičienė, I.; Norkus, E. Au Nanoparticles Modified Co/Titania Nanotubes as Electrocatalysts for Borohydride Oxidation. *Fuel Cells* **2017**, *17* (5), 690–697. https://doi.org/10.1002/fuce.201600168.

(100) Chatenet, M.; Lima, F. H. B.; Ticianelli, E. A. Gold Is Not a Faradaic-Efficient Borohydride Oxidation Electrocatalyst: An Online Electrochemical Mass Spectrometry Study. *J. Electrochem. Soc.* **2010**, *157* (5), B697–B704. https://doi.org/10.1149/1.3328179.

(101) Cao, D.; Gao, Y.; Wang, G.; Miao, R.; Liu, Y. A Direct $NaBH_4$–H_2O_2 Fuel Cell Using Ni Foam Supported Au Nanoparticles as Electrodes. *Int. J. Hydrogen Energy* **2010**, *35* (2), 807–813. https://doi.org/10.1016/j.ijhydene.2009.11.026.

(102) Cheng, K.; Cao, D.; Yang, F.; Zhang, D.; Yan, P.; Yin, J.; Wang, G. Pd Doped Three-Dimensional Porous Ni Film Supported on Ni Foam and Its High Performance toward NaBH4 Electrooxidation. *J. Power Sources* **2013**, *242*, 141–147. https://doi.org/10.1016/j.jpowsour.2013.05.070.

(103) Yang, F.; Cheng, K.; Mo, Y.; Yu, L.; Yin, J.; Wang, G.; Cao, D. Direct Peroxide–Peroxide Fuel Cell – Part 1: The Anode and Cathode Catalyst of Carbon Fiber Cloth Supported Dendritic Pd. *J. Power Sources* **2012**, *217*, 562–568. https://doi.org/10.1016/j.jpowsour.2012.07.019.

(104) Simões, M.; Baranton, S.; Coutanceau, C. Influence of Bismuth on the Structure and Activity of Pt and Pd Nanocatalysts for the Direct Electrooxidation of NaBH4. *Electrochim. Acta* **2010**, *56* (1), 580–591. https://doi.org/10.1016/j.electacta.2010.09.006.

(105) Oliveira, R. C. P.; Vasić, M.; Santos, D. M. F.; Babić, B.; Hercigonja, R.; Sequeira, C. A. C.; Šljukić, B. Performance Assessment of a Direct Borohydride-Peroxide Fuel Cell with Pd-Impregnated Faujasite X Zeolite as Anode Electrocatalyst. *Electrochim. Acta* **2018**, *269*, 517–525. https://doi.org/10.1016/j.electacta.2018.03.021.

(106) Zhou, Y.; Li, S.; Chen, Y.; Liu, Y. The High Utilization of Fuel in Direct Borohydride Fuel Cells with a PdNi x -B/Carbon Nanotubes-Catalysed Anode. *J. Power Sources* **2017**, *351*, 79–85. https://doi.org/10.1016/j.jpowsour.2017.03.056.

(107) Milikić, J.; Ćirić-Marjanović, G.; Mentus, S.; Santos, D. M. F.; Sequeira, C. A. C.; Šljukić, B. Pd/c-PANI Electrocatalysts for Direct Borohydride Fuel Cells. *Electrochim. Acta* **2016**, *213*, 298–305. https://doi.org/10.1016/j.electacta.2016.07.109.

(108) Cheng, H.; Scott, K.; Lovell, K. Material Aspects of the Design and Operation of Direct Borohydride Fuel Cells. *Fuel Cells* **2006**, *6* (5), 367–375. https://doi.org/10.1002/fuce.200500260.

(109) Abahussain, A. A.; de Leon, C. P.; Walsh, F. C. Mass-Transfer Measurements at Porous 3D Pt-Ir/Ti Electrodes in a Direct Borohydride Fuel Cell. *J. Electrochem. Soc.* **2018**, *165* (3), F198–F206. https://doi.org/10.1149/2.0751803jes.

(110) Molina Concha, B.; Chatenet, M. Direct Oxidation of Sodium Borohydride on Pt, Ag and Alloyed Pt-Ag Electrodes in Basic Media. Part II. Carbon-Supported Nanoparticles. *Electrochim. Acta* **2009**, *54* (26), 6130–6139.

https://doi.org/10.1016/j.electacta.2009.04.074.

(111) Briega-Martos, V.; Herrero, E.; Feliu, J. M. Borohydride Electro-Oxidation on Pt Single Crystal Electrodes. *Electrochem. commun.* **2015**, *51*, 144–147. https://doi.org/10.1016/j.elecom.2014.12.024.

(112) Finkelstein, D. A.; Letcher, C. D.; Jones, D. J.; Sandberg, L. M.; Watts, D. J.; Abruña, H. D. Self-Poisoning during BH 4 – Oxidation at Pt and Au, and in Situ Poison Removal Procedures for BH 4 – Fuel Cells. *J. Phys. Chem. C* **2013**, *117* (4), 1571–1581. https://doi.org/10.1021/jp308677f.

(113) Antolini, E.; Salgado, J. R. C.; Gonzalez, E. R. Carbon Supported Pt75M25 (M=Co, Ni) Alloys as Anode and Cathode Electrocatalysts for Direct Methanol Fuel Cells. *J. Electroanal. Chem.* **2005**, *580* (1), 145–154. https://doi.org/10.1016/j.jelechem.2005.03.023.

(114) İyigün Karadağ, Ç.; Behmenyar, G.; Boyacı San, F. G.; Şener, T. Investigation of Carbon Supported Nanostructured PtAu Alloy as Electrocatalyst for Direct Borohydride Fuel Cell. *Fuel Cells* **2015**, *15* (2), 262–269. https://doi.org/10.1002/fuce.201300060.

(115) Šljukić, B.; Milikić, J.; Santos, D. M. F.; Sequeira, C. A. C.; Macciò, D.; Saccone, A. Electrocatalytic Performance of Pt–Dy Alloys for Direct Borohydride Fuel Cells. *J. Power Sources* **2014**, *272*, 335–343. https://doi.org/10.1016/j.jpowsour.2014.08.080.

(116) Boyacı San, F. G.; Okur, O.; İyigün Karadağ, Ç.; Isik-Gulsac, I.; Okumuş, E. Evaluation of Operating Conditions on DBFC (Direct Borohydride Fuel Cell) Performance with PtRu Anode Catalyst by Response Surface Method. *Energy* **2014**, *71*, 160–169. https://doi.org/10.1016/j.energy.2014.04.037.

(117) Yi, L.; Liu, L.; Wang, X.; Liu, X.; Yi, W.; Wang, X. Carbon Supported Pt–Sn Nanoparticles as Anode Catalyst for Direct Borohydride–Hydrogen Peroxide Fuel Cell: Electrocatalysis and Fuel Cell Performance. *J. Power Sources* **2013**, *224*, 6–12. https://doi.org/10.1016/j.jpowsour.2012.09.082.

(118) Balčiūnaitė, A.; Sukackienė, Z.; Tamašauskaitė-Tamašiūnaitė, L.; Činčienė, Ž.; Selskis, A.; Norkus, E. CoB/Cu and PtCoB/Cu Catalysts for Borohydride Fuel Cells. *Electrochim. Acta* **2017**, *225*, 255–262. https://doi.org/10.1016/j.electacta.2016.12.155.

(119) Šljukić, B.; Milikić, J.; Santos, D. M. F.; Sequeira, C. A. C. Carbon-Supported Pt0.75M0.25 (M=Ni or Co) Electrocatalysts for Borohydride Oxidation. *Electrochim. Acta* **2013**, *107*, 577–583. https://doi.org/10.1016/j.electacta.2013.06.040.

(120) Jasinski, R. Fuel Cell Oxidation of Alakali Borohydrides. *Electrochem. Technol.* **1965**, *3* (1–2), 40.

(121) Durst, J.; Simon, C.; Siebel, A.; Rheinlander, P. J.; Schuler, T.; Hanzlik, M.; Herranz, J.; Hasche, F.; Gasteiger, H. A. Hydrogen Oxidation and Evolution Reaction (HOR/HER) on Pt Electrodes in Acid vs. Alkaline Electrolytes: Mechanism, Activity and Particle Size Effects. *ECS Trans.* **2014**, *64* (3), 1069–1080. https://doi.org/10.1149/06403.1069ecst.

(122) Mahmood, N.; Yao, Y.; Zhang, J.-W.; Pan, L.; Zhang, X.; Zou, J.-J. Electrocatalysts for Hydrogen Evolution in Alkaline Electrolytes: Mechanisms, Challenges, and Prospective Solutions. *Adv. Sci.* **2018**, *5* (2), 1700464. https://doi.org/10.1002/advs.201700464.

(123) Conway, B. E.; Jerkiewicz, G. Relation of Energies and Coverages of Underpotential and Overpotential Deposited H at Pt and Other Metals to the 'Volcano Curve' for Cathodic H2 Evolution Kinetics. *Electrochim. Acta* **2000**, *45* (25–26), 4075–4083. https://doi.org/10.1016/S0013-4686(00)00523-5.

(124) Bessette, R. R.; Cichon, J. M.; Dischert, D. W.; Dow, E. G. A Study of Cathode Catalysis for the Aluminium/Hydrogen Peroxide Semi-Fuel Cell. *J. Power Sources* **1999**, *80* (1–2), 248–253. https://doi.org/10.1016/S0378-7753(98)00265-1.

(125) Bessette, R. R.; Medeiros, M. G.; Patrissi, C. J.; Deschenes, C. M.; Lafratta, C. N. Development and Characterization of a Novel Carbon ® Ber Based Cathode for Semi-Fuel Cell Applications. *J. Power Sources* **2001**, *96*, 240–244.

(126) Luo, N.; Miley, G. H.; Kim, K.-J.; Burton, R.; Huang, X. NaBH4/H2O2 Fuel Cells for Air Independent Power Systems. *J. Power Sources* **2008**, *185* (2), 685–690. https://doi.org/http://dx.doi.org/10.1016/j.jpowsour.2008.08.090.

(127) Yi, L.; Hu, B.; Song, Y.; Wang, X.; Zou, G.; Yi, W. Studies of Electrochemical Performance of Carbon Supported Pt–Cu Nanoparticles as Anode Catalysts for Direct Borohydride–Hydrogen Peroxide Fuel Cell. *J. Power Sources* **2011**, *196* (23), 9924–9930. https://doi.org/10.1016/j.jpowsour.2011.08.063.

(128) Yi, L.; Liu, L.; Liu, X.; Wang, X.; Yi, W.; He, P.; Wang, X. Carbon-Supported Pt–Co Nanoparticles as Anode Catalyst for Direct Borohydride-Hydrogen Peroxide Fuel Cell: Electrocatalysis and Fuel Cell Performance. *Int. J. Hydrogen Energy* **2012**, *37* (17), 12650–12658. https://doi.org/10.1016/j.ijhydene.2012.06.065.

(129) Hjelm, R. M. E.; Garsany, Y.; Atkinson, R. W.; Stroman, R. O.; Swider-Lyons, K.; Lafforgue, C.; Chatenet, M. Sodium Borohydride Oxidation on Pt and/or Pd-Based Electrodes in Hydrogen Peroxide Direct Borohydride Fuel Cells (H 2 O 2 -DBFCs). *ECS Trans.* **2017**, *80* (8), 1033–1042. https://doi.org/10.1149/08008.1033ecst.

(130) Jing, L.; Zhao, Q.; Chen, S.; Yi, L.; Wang, X.; Wei, W. Nanoporous Carbon Supported Platinum-Copper Nanocomposites as Anode Catalysts for Direct Borohydride-Hydrogen Peroxide Fuel Cell. *Electrochim. Acta* **2015**, *171*, 96–104. https://doi.org/10.1016/j.electacta.2015.05.002.

(131) He, Y.; Zhu, C.; Chen, K.; Wang, J.; Qin, H.; Liu, J.; Yan, S.; Yang, K.; Li, A. Development of High-Performance Cathode Catalyst of Polypyrrole Modified Carbon Supported CoOOH for Direct Borohydride Fuel Cell. *J. Power Sources* **2017**, *339*, 13–19. https://doi.org/10.1016/j.jpowsour.2016.11.021.

(132) Raman, R. K.; Prashant, S. K.; Shukla, A. K. A 28-W Portable Direct Borohydride-Hydrogen Peroxide Fuel-Cell Stack. *J. Power Sources* **2006**, *162* (2 SPEC. ISS.), 1073–1076. https://doi.org/10.1016/j.jpowsour.2006.07.059.

(133) Cheng, H.; Scott, K. Investigation of Non-Platinum Cathode Catalysts for Direct

Borohydride Fuel Cells. *J. Electroanal. Chem.* **2006**, *596* (2), 117–123. https://doi.org/10.1016/j.jelechem.2006.07.031.

(134) Lin, L.; Qin, H.; Jia, J.; Ji, Z.; Chi, H.; Ni, H.; Wang, J.; He, Y.; Liu, J. FeS as a Promising Cathode Catalyst for Direct Borohydride Fuel Cells. *J. Alloys Compd.* **2018**, *769*, 136–140. https://doi.org/10.1016/j.jallcom.2018.07.269.

(135) Pourbaix, M. *Atlas of Electrochemical Equilibria in Aqueous Solutions*; Pergamon Press: New York, 1966.

(136) Horsfall, J. A.; Lovell, K. V. Comparison of Fuel Cell Performance of Selected Fluoropolymer and Hydrocarbon Based Grafted Copolymers Incorporating Acrylic Acid and Styrene Sulfonic Acid. *Polym. Adv. Technol.* **2002**, *13* (5), 381–390. https://doi.org/10.1002/pat.202.

(137) Choudhury, N. a.; Raman, R. K.; Sampath, S.; Shukla, a. K. An Alkaline Direct Borohydride Fuel Cell with Hydrogen Peroxide as Oxidant. *J. Power Sources* **2005**, *143* (1–2), 1–8. https://doi.org/10.1016/j.jpowsour.2004.08.059.

(138) Cheng, H.; Scott, K. Influence of Operation Conditions on Direct Borohydride Fuel Cell Performance. *J. Power Sources* **2006**, *160* (1), 407–412. https://doi.org/10.1016/j.jpowsour.2006.01.097.

(139) Liu, B. H.; Li, Z. P.; Arai, K.; Suda, S. Performance Improvement of a Micro Borohydride Fuel Cell Operating at Ambient Conditions. *Electrochim. Acta* **2005**, *50* (18), 3719–3725. https://doi.org/10.1016/j.electacta.2005.01.018.

(140) Šljukić, B.; Morais, A. L.; Santos, D. M. F.; Sequeira, C. A. C. Anion- or Cation-Exchange Membranes for NaBH4/H2O2 Fuel Cells? *Membranes (Basel).* **2012**, *2* (3), 478–492. https://doi.org/10.3390/membranes2030478.

(141) Parthasarathy, A.; Srinivasan, S.; Appleby, A. J. Temperature Dependence of the Electrode Kinetics of Oxygen Reduction at the Platinum/Nafion® Interface—A Microelectrode Investigation. *J. Electrochem. Soc.* **2006**, *139* (9), 2530. https://doi.org/10.1149/1.2221258.

(142) Olu, P.-Y.; Job, N.; Chatenet, M. Evaluation of Anode (Electro)Catalytic Materials for the Direct Borohydride Fuel Cell: Methods and Benchmarks. *J. Power Sources* **2016**, *327*, 235–257. https://doi.org/10.1016/j.jpowsour.2016.07.041.

(143) Beattie, P. D.; Basura, V. I.; Holdcroft, S. Temperature and Pressure Dependence of O2 Reduction at Pt | Nafion® 117 and Pt | BAM® 407 Interfaces. *J. Electroanal. Chem.* **1999**, *468* (2), 180–192. https://doi.org/10.1016/S0022-0728(99)00164-3.

(144) Pletcher, D. *A First Course in Electrode Processes*, second ed.; Royal Society of Chemistry, 2009.

(145) Li, Z. P.; Liu, B. H.; Zhu, J. K.; Suda, S. Depression of Hydrogen Evolution during Operation of a Direct Borohydride Fuel Cell. *J. Power Sources* **2006**, *163* (1 SPEC. ISS.), 555–559. https://doi.org/10.1016/j.jpowsour.2006.09.037.

(146) Wang, K.; Lu, J.; Zhuang, L. Direct Determination of Diffusion Coefficient for Borohydride Anions in Alkaline Solutions Using Chronoamperometry with Spherical Au Electrodes. *J. Electroanal. Chem.* **2005**, *585* (2), 191–196.

https://doi.org/10.1016/j.jelechem.2005.08.009.

(147) Koscher, G.; Kordesch, K. Can Refillable Alkaline Methanol–Air Systems Replace Metal–Air Cells? *J. Power Sources* **2004**, *136* (2), 215–219. https://doi.org/10.1016/J.JPOWSOUR.2004.03.005.

(148) Duteanu, N.; Vlachogiannopoulos, G.; Shivhare, M. R.; Yu, E. H.; Scott, K. A Parametric Study of a Platinum Ruthenium Anode in a Direct Borohydride Fuel Cell. *J. Appl. Electrochem.* **2007**, *37* (9), 1085–1091. https://doi.org/10.1007/s10800-007-9360-y.

(149) Pletcher, D.; Walsh, F. C. Three-Dimensional Electrodes. In *Industrial electrochemistry*; Genders, J. D., Weinberg, N. L., Eds.; The Electrosynthesis Company Inc.: Electrochemistry for a Clean Environment. New York, 1992; pp 51–100.

(150) Santos, D. M. F.; Eugénio, S.; Cardoso, D. S. P.; Šljukić, B.; Montemor, M. F. Three-Dimensional Nanostructured Ni–Cu Foams for Borohydride Oxidation. *Russ. J. Phys. Chem. A* **2015**, *89* (13), 2449–2454. https://doi.org/10.1134/S0036024415130336.

(151) Low, C. T. J.; Ponce de León, C.; Walsh, F. C. A Gold-Coated Titanium Oxide Nanotube Array for the Oxidation of Borohydride Ions. *Electrochem. commun.* **2012**, *22* (1), 166–169. https://doi.org/10.1016/j.elecom.2012.06.003.

(152) Santos, D. M. F.; A. Balčiūnaitė; Tamašauskaitė-Tamašiūnaitė, L.; Zabielaitė, A.; Jagminienė, A.; Stankevičienė, I.; Naujokaitis, A.; Norkus, E. AuCo/TiO2-NTs Anode Catalysts for Direct Borohydride Fuel Cells. *J. ofThe Electrochem. Soc.* **2016**, *163* (14), 1553–1557. https://doi.org/10.1149/2.0891614jes.

(153) Ponce de León, C.; Bavykin, D. V.; Walsh, F. C. The Oxidation of Borohydride Ion at Titanate Nanotube Supported Gold Electrodes. *Electrochem. commun.* **2006**, *8* (10), 1655–1660. https://doi.org/10.1016/j.elecom.2006.07.031.

(154) Friedrich, J. M.; Ponce-de-Leon, C.; Reade, G. W.; Walsh, F. C. Reticulated Vitreous Carbon as an Electrode Material N. **2004**, *561*, 203–217. https://doi.org/10.1016/j.jelechem.2003.07.019.

(155) Cheng, H.; Scott, K.; Christensen, P. A. Application of a Solid Polymer Electrolyte Reactor to Remove Nitrate Ions from Wastewater. *J. Appl. Electrochem.* **2005**, *35* (6), 551–560. https://doi.org/10.1007/s10800-005-1519-9.

(156) Merino-Jimenez, I.; Ponce de León, C.; Walsh, F. C. The Effect of Surfactants on the Kinetics of Borohydride Oxidation and Hydrolysis in the DBFC. *Electrochim. Acta* **2014**, *133*, 539–545. https://doi.org/http://dx.doi.org/10.1016/j.electacta.2014.04.061.

(157) Ang, X. D.; Ei, Y. W.; Shengshui, H. U. Effects of Surfactants on the Electroreduction of Dioxygen at an Acetylene Black Electrode. **2004**, *20* (February), 307–310.

(158) Demirci, U. B. Comments on the Paper "Electrooxidation of Borohydride on Platinum and Gold Electrodes: Implications for Direct Borohydride Fuel Cell" by E. Gyenge, Electrochim. Acta 49 (2004) 965: Thiourea, a Poison for the Anode Metallic Electrocatalyst of the Direct B. *Electrochim. Acta* **2007**, *52* (15), 5119–

5121. https://doi.org/10.1016/j.electacta.2006.12.024.

(159) Wang, K.; Lu, J.; Zhuang, L. A Mechanistic Study of Borohydride Anodic Oxidation. *Catal. Today* **2011**, *170* (1), 99–109. https://doi.org/10.1016/j.cattod.2010.12.023.

(160) Celik, C.; Boyaci San, F. G.; Sarac, H. I. Improving the Direct Borohydride Fuel Cell Performance with Thiourea as the Additive in the Sodium Borohydride Solution. *Int. J. Hydrogen Energy* **2010**, *35* (16), 8678–8682. https://doi.org/10.1016/j.ijhydene.2010.04.150.

(161) Jamard, R.; Latour, A.; Salomon, J.; Capron, P.; Martinent-Beaumont, A. Study of Fuel Efficiency in a Direct Borohydride Fuel Cell. *J. Power Sources* **2008**, *176*, 287–292. https://doi.org/10.1016/j.jpowsour.2007.10.036.

(162) Harvey, D. *Modren Analytical Chemistry*; McGraw-Hill Higher Education, 2000.

(163) Vittal, R.; Gomathi, H.; Kim, K. J. Beneficial Role of Surfactants in Electrochemistry and in the Modification of Electrodes. *Adv. Colloid Interface Sci.* **2006**, *119* (1), 55–68. https://doi.org/10.1016/j.cis.2005.09.004.

(164) Kojima, Y.; Haga, T. Recycling Process of Sodium Metaborate to Sodium Borohydride. *Int. J. Hydrogen Energy* **2003**, *28* (9), 989–993. https://doi.org/10.1016/S0360-3199(02)00173-8.

(165) Lang, C.; Jia, Y.; Liu, J.; Wang, H.; Ouyang, L.; Zhu, M.; Yao, X. $NaBH_4$ Regeneration from $NaBO_2$ by High-Energy Ball Milling and Its Plausible Mechanism. *Int. J. Hydrogen Energy* **2017**, 1–9. https://doi.org/10.1016/j.ijhydene.2017.04.014.

(166) Huang, M.; Zhong, H.; Ouyang, L.; Peng, C.; Zhu, X.; Zhu, W.; Fang, F.; Zhu, M. Efficient Regeneration of Sodium Borohydride via Ball Milling Dihydrate Sodium Metaborate with Magnesium and Magnesium Silicide. *J. Alloys Compd.* **2017**, *729*, 1079–1085. https://doi.org/10.1016/j.jallcom.2017.09.262.

(167) Chen, W.; Ouyang, L. Z.; Liu, J. W.; Yao, X. D.; Wang, H.; Liu, Z. W.; Zhu, M. Hydrolysis and Regeneration of Sodium Borohydride ($NaBH_4$) – A Combination of Hydrogen Production and Storage. *J. Power Sources* **2017**, *359*, 400–407. https://doi.org/10.1016/j.jpowsour.2017.05.075.

(168) Zhong, H.; Ouyang, L.; Liu, J.; Peng, C.; Zhu, X.; Zhu, W.; Fang, F.; Zhu, M. Sodium Borohydride Regeneration via Direct Hydrogen Transformation of Sodium Metaborate Tetrahydrate. *J. Power Sources* **2018**, *390* (March), 71–77. https://doi.org/10.1016/j.jpowsour.2018.04.037.

(169) Linehan, S. W.; Chin, A. A.; Allen, N. T.; Butterick, R.; Kendall, N. T.; Klawiter, I. L.; Lipiecki, F. J.; Millar, D. M.; Molzahn, D. C.; November, S. J.; et al. Low-Cost Precursors to Novel Hydrogen Storage Materials https://digital.library.unt.edu/ark:/67531/metadc845615/.

(170) Hal, C. Electrolytic Process for the Production of Alkali Metal Borohydrides, 1973.

(171) Kibar, M. E.; Akın, A. N. A Novel Process for CO2 Capture by Using Sodium Metaborate. Part I: Effects of Calcination. *Environ. Sci. Pollut. Res.* **2018**, *25* (4), 3446–3457. https://doi.org/10.1007/s11356-017-0644-4.

(172) Cañizares, P.; García-Gómez, J.; Fernández de Marcos, I.; Rodrigo, M. a.; Lobato, J. Measurement of Mass-Transfer Coefficients by an Electrochemical Technique. *J. Chem. Educ.* **2006**, *83* (8), 1204. https://doi.org/10.1021/ed083p1204.

(173) Recio, F. J.; Herrasti, P.; Vazquez, L.; Ponce de León, C.; Walsh, F. C. Mass Transfer to a Nanostructured Nickel Electrodeposit of High Surface Area in a Rectangular Flow Channel. *Electrochim. Acta* **2013**, *90*, 507–513. https://doi.org/10.1016/j.electacta.2012.11.135.

(174) Selman, J. R.; Tobias, C. W. Mass-Transfer Measurements by the Limiting-Current Technique. In *Advances in Chemical Engineering*; Thomas B. Drew John W. Hoopes and Theodore Vermeulen BT - Advances in Chemical Engineering, G. R. C., Ed.; Academic Press, 1978; Vol. 10, pp 211–318. https://doi.org/10.1016/S0065-2377(08)60134-9.

(175) Walsh, F. *A First Course in Electrochemical Engineering*; Electrochemical Consultancy: Hants, England, 1993.

(176) Langlois, S.; Coeuret, F. Flow-through and Flow-by Porous Electrodes of Nickel Foam. II. Diffusion-Convective Mass Transfer between the Electrolyte and the Foam. *J. Appl. Electrochem.* **1989**, *19* (1), 51–60. https://doi.org/10.1007/BF01039389.

(177) Marracino, J. M.; Coeuret, F.; Langlois, S. A First Investigation of Flow-through Porous Electrodes Made of Metallic Felts or Foams. *Electrochim. Acta* **1987**, *32* (9), 1303–1309. https://doi.org/10.1016/0013-4686(87)85059-4.

(178) Brunauer, S.; Emmett, P. H.; Teller, E. Adsorption of Gases in Multimolecular Layers. *J. Am. Chem. Soc.* **1938**, *60* (2), 309–319. https://doi.org/10.1021/ja01269a023.

(179) Sing, K. The Use of Nitrogen Adsorption for the Characterisation of Porous Materials. *Colloids Surfaces A Physicochem. Eng. Asp.* **2001**, *187–188*, 3–9. https://doi.org/10.1016/S0927-7757(01)00612-4.

(180) Walsh, F.; Reade, G. Design and Performance of Electrochemical Reactors for Efficient Synthesis and Environmental Treatment. Part 1. Typical Reactors and Their Performance. *Analyst* **1994**, *119* (5), 791–796.

(181) Brown, C. J.; Walsh, F. C.; Pletcher, D. Mass Transfer and Pressure Drop in a Laboratory Filterpress Electrolyser. *Chem. Eng. Res. Des.* **1995**, *73* (A2).

(182) Arenas, L. F.; Ponce de León, C.; Walsh, F. C. Mass Transport and Active Area of Porous Pt/Ti Electrodes for the Zn-Ce Redox Flow Battery Determined from Limiting Current Measurements. *Electrochim. Acta* **2016**, *221*, 154–166. https://doi.org/10.1016/j.electacta.2016.10.097.

(183) Brown, C. J.; Pletcher, D.; Walsh, F. C.; Hammond, J. K.; Robinson, D. Studies of Three-Dimensional Electrodes in the FMO1-LC Laboratory Electrolyser. *J. Appl. Electrochem.* **1994**, *24* (2), 95–106. https://doi.org/10.1007/BF00247779.

(184) Brown, C. J.; Pletcher, D.; Walsh, F. C.; Hammond, J. K.; Robinson, D. Studies of Space-Averaged Mass Transport in the FM01-LC Laboratory Electrolyser. *J. Appl. Electrochem.* **1993**, *23* (1), 38–43. https://doi.org/10.1007/BF00241573.

(185) Brown, C. J.; Walsh, F. C.; Hammond, J. K.; Robinson, D. Local Mass Transport Effects in the FMO1 Laboratory Electrolyser. *J. Appl. Electrochem.* **1992**, *22*, 613–619. https://doi.org/10.1007/BF01092609.

(186) Leroux, F.; Coeuret, F. Flow-by Electrodes of Ordered Sheets of Expanded Metal-I. Mass Transfer and Current Distribution. *Electrochim. Acta* **1985**, *30* (2), 159–165.

(187) Martins, M.; Šljukić, B.; Sequeira, C. A. C.; Metin, Ö.; Erdem, M.; Sener, T.; Santos, D. M. F. Biobased Carbon-Supported Palladium Electrocatalysts for Borohydride Fuel Cells. *Int. J. Hydrogen Energy* **2016**, 1–9. https://doi.org/10.1016/j.ijhydene.2016.04.039.

(188) Martins, J. I.; Nunes, M. C. Comparison of the Electrochemical Oxidation of Borohydride and Dimethylamine Borane on Platinum Electrodes: Implication for Direct Fuel Cells. *J. Power Sources* **2008**, *175* (1), 244–249. https://doi.org/10.1016/j.jpowsour.2007.09.028.

(189) JAKSIC, M.; JOHANSEN, B.; TUNOLD, R. Electrochemical Behaviour of Platinum in Alkaline and Acidic Solutions of Heavy and Regular Water. *Int. J. Hydrogen Energy* **1993**, *18* (10), 817–837. https://doi.org/10.1016/0360-3199(93)90136-X.

(190) Lam, V. W. S.; Gyenge, E. L. High-Performance Osmium Nanoparticle Electrocatalyst for Direct Borohydride PEM Fuel Cell Anodes. *J. Electrochem. Soc.* **2008**, *155* (11), B1155. https://doi.org/10.1149/1.2975191.

(191) Chatenet, M.; Molina-Concha, M. B.; Diard, J. P. First Insights into the Borohydride Oxidation Reaction Mechanism on Gold by Electrochemical Impedance Spectroscopy. *Electrochim. Acta* **2009**, *54* (6), 1687–1693. https://doi.org/10.1016/j.electacta.2008.09.060.

(192) Rostamikia, G.; Janik, M. J. First Principles Mechanistic Study of Borohydride Oxidation over the Pt(111) Surface. *Electrochim. Acta* **2010**, *55* (3), 1175–1183. https://doi.org/10.1016/j.electacta.2009.10.002.

(193) Rostamikia, G.; Janik, M. J. Direct Borohydride Oxidation: Mechanism Determination and Design of Alloy Catalysts Guided by Density Functional Theory. *Energy Environ. Sci.* **2010**, *3* (9), 1262. https://doi.org/10.1039/c0ee00115e.

(194) Rostamikia, G.; Mendoza, A. J.; Hickner, M. A.; Janik, M. J. First-Principles Based Microkinetic Modeling of Borohydride Oxidation on a Au(111) Electrode. *J. Power Sources* **2011**, *196* (22), 9228–9237. https://doi.org/10.1016/j.jpowsour.2011.07.042.

(195) Elder, J. P.; Hickling, A. Anodic Behaviour of the Borohydride Ion. *Trans. Faraday Soc.* **1962**, *58*, 1852–1864. https://doi.org/10.1039/tf9625801852.

(196) Nagle, L. C.; Rohan, J. F. Nanoporous Gold Anode Catalyst for Direct Borohydride Fuel Cell. *Int. J. Hydrogen Energy* **2011**, *36* (16), 10319–10326. https://doi.org/10.1016/J.IJHYDENE.2010.09.077.

(197) Simões, M.; Baranton, S.; Coutanceau, C. Electrooxidation of Sodium Borohydride at Pd, Au, and Pd x Au 1− x Carbon-Supported Nanocatalysts. *J.*

Phys. Chem. C **2009**, *113* (30), 13369–13376. https://doi.org/10.1021/jp902741z.

(198) Chatenet, M.; Molina-Concha, M. B.; El-Kissi, N.; Parrour, G.; Diard, J. P. Direct Rotating Ring-Disk Measurement of the Sodium Borohydride Diffusion Coefficient in Sodium Hydroxide Solutions. *Electrochim. Acta* **2009**, *54* (18), 4426–4435. https://doi.org/10.1016/j.electacta.2009.03.019.

(199) Šljukić, B.; Santos, D. M. F.; Sequeira, C. a. C.; Banks, C. E. Analytical Monitoring of Sodium Borohydride. *Anal. Methods* **2013**, *5* (4), 829. https://doi.org/10.1039/c2ay26077h.

(200) Mirkin, M. V; Bard, A. J. Voltammetric Method for the Determination of Borohydride Concentration in Alkaline Aqueous Solutions. *Anal. Chem.* **1991**, *63*, 532–533. https://doi.org/10.1021/ac00005a030.

(201) El, H. Ç.; Ikkan, ˙; Aydin, H.; Levent Aksu, M. The Electroanalytical Determination of Sodium Borohydride Using a Gold Electrode. *Turk J Chem* **2005**, *29*, 519–524.

(202) Mclafferty, J.; Tokash, J.; Zhang, Y.-C.; Coulson, W. J.; Macdonald, D. D. Electroanalysis of the Borohydride Ion. **2007**, *2* (29), 19–25. https://doi.org/10.1149/1.2815946.

(203) Colominas, S.; McLafferty, J.; Macdonald, D. D. Electrochemical Studies of Sodium Borohydride in Alkaline Aqueous Solutions Using a Gold Electrode. *Electrochim. Acta* **2009**, *54* (13), 3575–3579. https://doi.org/10.1016/j.electacta.2009.01.021.

(204) Krishnan, P.; Yang, T. H.; Advani, S. G.; Prasad, A. K. Rotating Ring-Disc Electrode (RRDE) Investigation of Borohydride Electro-Oxidation. *J. Power Sources* **2008**, *182* (1), 106–111. https://doi.org/10.1016/j.jpowsour.2008.03.064.

(205) Chandler, G. K.; Genders, J. D.; Pletcher, D. Electrodes Based on Noble Metals. *Platin. Met. Rev.* **1997**, *41* (2), 54–63.

(206) Newbury, D. E.; Ritchie, N. W. M. Is Scanning Electron Microscopy/Energy Dispersive X-Ray Spectrometry (SEM/EDS) Quantitative? *Scanning* **2013**, *35* (3), 141–168. https://doi.org/10.1002/sca.21041.

(207) Santos, D. M. F.; Saturnino, P. G.; Macciò, D.; Saccone, A.; Sequeira, C. A. C. Platinum-Rare Earth Intermetallic Alloys as Anode Electrocatalysts for Borohydride Oxidation. *Catal. Today* **2011**, *170* (1), 134–140. https://doi.org/10.1016/j.cattod.2011.03.037.

(208) Bard, A. J.; Faulkner, L. R. *Electrochemical Methods Fundamentals and Applications*, Second ed.; John Wiley & Sons: New York, 2001. https://doi.org/10.1146/annurev.matsci.30.1.117.

(209) Santos, D. M. F.; Sequeira, C. A. C. Cyclic Voltammetry Investigation of Borohydride Oxidation at a Gold Electrode. *Electrochim. Acta* **2010**, *55* (22), 6775–6781. https://doi.org/10.1016/j.electacta.2010.05.091.

(210) Cardoso, D. S. P.; Santos, D. M. F.; Šljukić, B.; Sequeira, C. A. C.; Macciò, D.; Saccone, A. Platinum-Rare Earth Cathodes for Direct Borohydride-Peroxide Fuel Cells. *J. Power Sources* **2016**, *307*, 251–258. https://doi.org/10.1016/j.jpowsour.2015.12.131.

(211) Haijun, W.; Cheng, W.; Zhixiang, L.; Zongqiang, M. Influence of Operation Conditions on Direct NaBH4/H2O2 Fuel Cell Performance. *Int. J. Hydrogen Energy* **2010**, *35* (7), 2648–2651. https://doi.org/10.1016/j.ijhydene.2009.04.020.

(212) Tanaka, N.; Tamamushi, R. Kinetic Parameters of Electrode Reactions. *Electrochim. Acta* **1964**, *9* (7), 963–989. https://doi.org/10.1016/0013-4686(64)85045-3.

(213) B. E. Conway. *Electrochemical Data*; Elsevier, Ed.; Elsevier: Amsterdam, 1952.

(214) Parsons, R. *Handbook of Electrochemical Data*; Butterworths: London, 1959.

(215) Bard, A. J.; Lund, H. *Encyclopedia of the Electrochemistry of the Elements*; Marcel Dekker: New York, 1986.

(216) Santos, D. M. F.; Sequeira, C. A. C. Chronopotentiometric Investigation of Borohydride Oxidation at a Gold Electrode. *J. Electrochem. Soc.* **2010**, *157* (1), F16–F21. https://doi.org/10.1016/j.electacta.2010.05.091.

(217) Oliveira, R. C. P.; Sevim, M.; Šljukić, B.; Sequeira, C. A. C.; Metin, Ö.; Santos, D. M. F. Mesoporous Graphitic Carbon Nitride-Supported Binary MPt (M: Co, Ni, Cu) Nanoalloys as Electrocatalysts for Borohydride Oxidation and Hydrogen Evolution Reaction. *Catal. Today* **2019**. https://doi.org/10.1016/J.CATTOD.2019.09.006.

(218) Oliveira, R. C. P.; Milikić, J.; Daş, E.; Yurtcan, A. B.; Santos, D. M. F.; Šljukić, B. Platinum/Polypyrrole-Carbon Electrocatalysts for Direct Borohydride-Peroxide Fuel Cells. *Appl. Catal. B Environ.* **2018**, *238*, 454–464. https://doi.org/10.1016/j.apcatb.2018.06.057.

(219) Atkins, P. *Physical Chemistry*, 7th ed.; Oxford University Press, 2003.

(220) Yeager, E.; Zurilla, R. W. Rotating Disc and Ring-Disc Techniques. *Symp. Electrochem. Process.* **1967**, 66.

(221) Pletcher, D.; Walsh, F. . C. *Industrial Electrochemistry*, Second edi.; Springer Netherlands: Dordrecht, 1993. https://doi.org/10.1007/978-94-011-2154-5.

(222) Chatenet, M. Tailoring Membranes. *Nat. Energy* **2019**, *4* (4), 261–262. https://doi.org/10.1038/s41560-019-0348-8.

(223) Yi, L.; Yu, B.; Yi, W.; Zhou, Y.; Ding, R.; Wang, X. Carbon-Supported Bimetallic Platinum − Iron Nanocatalysts: Application in Direct Borohydride/Hydrogen Peroxide Fuel Cell. *ACS Sustain. Chem. Eng.* **2018**. https://doi.org/10.1021/acssuschemeng.7b04438.

(224) Yilmaz, E. S.; Canan, B.; Günlü, G.; Sanli, A. E. Effects of Power Control Techniques on Hydrogen and Oxygen Evolution in Direct Borohydride Peroxide Fuel Cells. *Int. J. Hydrogen Energy* **2017**, *42* (4), 2617–2625. https://doi.org/10.1016/j.ijhydene.2016.05.045.

(225) Langlois, S.; Coeuret, F. Flow-through and Flow-by Porous Electrodes of Nickel Foam. I. Material Characterization. *J. Appl. Electrochem.* **1989**, *19* (1), 43–50. https://doi.org/10.1007/BF01039389.

(226) Tentorio, A.; Casolo-Ginelli, U. Characterization of Reticulate, Three-Dimensional Electrodes. *J. Appl. Electrochem.* **1978**, *8*, 195–205.

(227) Ralph, T.; Hitchman, M.; Millington, J.; Walsh, F. C. Mass Transport in an Electrochemical Reactor and Its Enhancement by Turbulence Promoters. *Electrochim. Acta* **1996**, *41* (4), 591–603.

(228) Trinidad, P.; Walsh, F. C. Hydrodynamic Behaviour of the FM01-LC Reactor. *Electrochim. Acta* **1996**, *41* (4 SPEC. ISS.), 493–502. https://doi.org/10.1016/0013-4686(95)00335-5.

(229) Taama, W. M.; Plimley, R. E.; Scott, K. Mass Transfer Rates in a DEM Electrochemical Cell. *Electrochim. Acta* **1996**, *41* (4), 543–548.

(230) Griffiths, M.; Ponce de León, C.; Walsh, F. C. Mass Transport in the Rectangular Channel of a Filter-Press Electrolyzer (the FM01-LC Reactor). *AIChE J.* **2005**, *51* (2), 682–687. https://doi.org/10.1002/aic.10311.

(231) Walsh, F.; Reade, G. Design and Performance of Electrochemical Reactors for Efficient Synthesis and Environmental Treatment. Part 2. Typical Reactors and Their Performance. *Analyst* **1994**, *119* (5), 797–803. https://doi.org/10.1039/AN9941900797.

(232) Leroux, F.; Coeuret, F. Flow-by Electrodes of Ordered Sheets of Expanded Metal-II. Potential Distribution for the Diffusional Regime. *Electrochim. Acta* **1985**, *30* (2), 167–172. https://doi.org/10.1016/0013-4686(85)80077-3.

(233) Freitas, K. S.; Concha, B. M.; Ticianelli, E. A.; Chatenet, M. Mass Transport Effects in the Borohydride Oxidation Reaction - Influence of the Residence Time on the Reaction Onset and Faradaic Efficiency. *Catal. Today* **2011**, *170* (1), 110–119. https://doi.org/10.1016/j.cattod.2011.01.051.

(234) Stroman, R. O.; Jackson, G. S. Modeling the Performance of an Ideal NaBH4–H2O2 Direct Borohydride Fuel Cell. *J. Power Sources* **2014**, *247*, 756–769. https://doi.org/http://dx.doi.org/10.1016/j.jpowsour.2013.08.100.

(235) Sanli, A. E.; Gordesel, M.; Yilmaz, E. S.; Ozden, S. K.; Gunlu, G.; Uysal, B. Z. Performance Improvement in Direct Borohydride/Peroxide Fuel Cells. *Int. J. Hydrogen Energy* **2017**, *42* (12), 8119–8129. https://doi.org/10.1016/j.ijhydene.2016.08.105.

(236) Walker, A. T. S.; Wragg, A. A. The Modelling of Concentration—Time Relationships in Recirculating Electrochemical Reactor Systems. *Electrochim. Acta* **1977**, *22* (10), 1129–1134. https://doi.org/10.1016/0013-4686(77)80051-0.

(237) Ford, W. P. J.; Walsh, F. C.; Whyte., I. Simplified Batch Reactor Models for the Removal of Metal Ions from Solution. *Inst. Chem. Eng. Symp. Ser.* **1992**, *127*, 111–126.

(238) Santos, D. M. F.; Saturnino, P. G.; Lobo, R. F. M.; Sequeira, C. A. C. Direct Borohydride/Peroxide Fuel Cells Using Prussian Blue Cathodes. *J. Power Sources* **2012**, *208*, 131–137. https://doi.org/10.1016/j.jpowsour.2012.02.016.

(239) Jamard, R.; Salomon, J.; Martinent-Beaumont, A.; Coutanceau, C. Life Time Test in Direct Borohydride Fuel Cell System. *J. Power Sources* **2009**, *193* (2), 779–787. https://doi.org/10.1016/j.jpowsour.2009.03.057.

(240) Dawoud, B.; Amer, E.; Gross, D. Experimental Investigation of an Adsorptive Thermal Energy Storage. *Int. J. energy Res.* **2007**, *31* (August 2007), 135–147.

https://doi.org/10.1002/er.

(241) Cao, D.; Chen, D.; Lan, J.; Wang, G. An Alkaline Direct NaBH4–H2O2 Fuel Cell with High Power Density. *J. Power Sources* **2009**, *190* (2), 346–350. https://doi.org/10.1016/j.jpowsour.2008.12.134.

(242) Yang, F.; Cheng, K.; Liu, X.; Chang, S.; Yin, J.; Du, C.; Du, L.; Wang, G.; Cao, D. Direct Peroxide–Peroxide Fuel Cell – Part 2: Effects of Conditions on the Performance. *J. Power Sources* **2012**, *217*, 569–573. https://doi.org/10.1016/J.JPOWSOUR.2012.06.079.

(243) Lei, T.; Tian, Y. M.; Wang, G. L.; Yin, J. L.; Gao, Y. Y.; Wen, Q.; Cao, D. X. An Alkaline Al-H2O2 Semi-Fuel Cell Based on a Nickel Foam Supported Co3O4 Nanowire Arrays Cathode. *Fuel Cells* **2011**, *11* (3), 431–435. https://doi.org/10.1002/fuce.201000168.

(244) Carton, J. G.; Olabi, A. G. Design of Experiment Study of the Parameters That Affect Performance of Three Flow Plate Configurations of a Proton Exchange Membrane Fuel Cell. *Energy* **2010**, *35* (7), 2796–2806. https://doi.org/10.1016/J.ENERGY.2010.02.044.

(245) Hine, F. *Electrode Processes and Electrochemical Engineering*; Plenum Press: New York, 1985.

(246) Kim, K.; Bernas, R.; Luo, N.; Yang, X.; Miley, G. A Novel Anode Electrode for Direct Borohydride Fuel Cell Preparation of Anode. *TechConnect Briefs* **2009**, *3*, 179–182.

(247) Rajalakshmi, N.; Jayanth, T. T.; Dhathathreyan, K. S. Effect of Carbon Dioxide and Ammonia on Polymer Electrolyte Membrane Fuel Cell Stack Performance. *Fuel Cells* **2003**, *3* (4), 177–180. https://doi.org/10.1002/fuce.200330107.

(248) Uribe, F. A.; Gottesfeld, S.; Zawodzinski, T. A. Effect of Ammonia as Potential Fuel Impurity on Proton Exchange Membrane Fuel Cell Performance. *J. Electrochem. Soc.* **2002**, *149* (3), A293. https://doi.org/10.1149/1.1447221.

(249) Abahussain, A. A.; de Leon, C. P.; Walsh, F. C. Mass-Transfer Measurements at Porous 3D Pt-Ir/Ti Electrodes in a Direct Borohydride Fuel Cell. *J. Electrochem. Soc.* **2018**, *165* (3), F198–F206. https://doi.org/10.1149/2.0751803jes.

(250) Kim, C.; Kim, K.-J.; Ha, M. Y. Performance Enhancement of a Direct Borohydride Fuel Cell in Practical Running Conditions. *J. Power Sources* **2008**, *180* (1), 154–161. https://doi.org/10.1016/j.jpowsour.2008.01.042.

(251) Yang, H.; Zhao, T. S. Effect of Anode Flow Field Design on the Performance of Liquid Feed Direct Methanol Fuel Cells. *Electrochim. Acta* **2005**, *50* (16–17), 3243–3252. https://doi.org/10.1016/j.electacta.2004.11.060.